

# LASER WELDING OF SHEET STEEL

A thesis presented for the Doctor of Philosophy at the  
University of Liverpool

by

Geoff Shannon, BEng (Hons)

1993

1993.

## ACKNOWLEDGEMENTS

I would like to thank my supervisors Professor W.M Steen and Mr. B.D Eccleston in providing constant support and helpfull advice during the project. Also, Mr. G. Szotts-Pollak, Van Leer (Netherlands), who gave great assistance in the formulating and the analysis of the statistical experimentation. Mr. J. Murray, Van Leer UK, who made an invaluable contribution to the design of the pre-production welding jig

Next the laboratory members, who provided an extremely relaxed, yet productive working atmosphere. Oh, and some seriously partying. So, by "name" past and present; Mr. Steve "the man" Plant, Mr. Jack "its in my loft" Frith, Mr. Andy "scally" Snaylem, Mr Geoff "cigar" Southern, Dr. William "billy whizz" O'Niell, Dr. Nicola "manic" Mckeown, Miss Sarah "gossip" Sharkey, Mr. Mathew "dealer" Murphy, Mr. Martin "IBM" Sparkes, Dr Rehan Akhter, Dr. Fiona Fellows, Dr. Lin li, Dr. Lu Zu, Dr Mathew Ellis, and last but by no means least Mrs Andrea Dearden, Mrs Heather Garnett and Mrs Jenny. Special thanks to Miss Karen "the prof" Williams for providing a computer (cheque in the post), information, references and upto date lab gossip.

As major support in social activities "The Boys from Biochemistry" were the business, and in particular, Dr. Andy Stephen - my partner in crime at Liverpool for six years man and boy.

A special thanks to Claire, and all my family in their support, and the occasional financial contribution over the last four years.

The support of the Science and Engineering Research Council and the Van Leer organisation in providing funding is greatly acknowledged. A further thanks goes to SERC, and Mr Peter Goodyear for the loan of the Ekatpro high speed video camera.

## ABSTRACT

An investigation was undertaken into the laser butt welding of drum quality sheet steel (BS 1449:CR2) and the feasibility of a production laser welder.

A fractional factorial experimental design is used to establish the significance of nine identified welding parameters, including interactions, to the responses of weld dimensions and weld strength. Based on these results a statistical model is formulated.

Optimisation studies are carried out on the laser power, weld speed and position of focus. The orientation of the workpiece to the laser beam, shielding gas composition and gas delivery are covered in depth. Individual parameter specification for optimised weld quality and reliability is given.

A major study of the effect of edge preparation on weld quality is undertaken, comparing bead on plate, milled and guillotine edges. Specific weld faults, weld dimensions, weld appearance and tolerances are presented.

A number of in-process weld monitoring systems are identified and extensively tested for weld fault identification, ease of use and reliability.

A high speed video camera (1000 frames per second) was used to investigate high speed welding, in particular the humping phenomenon. The onset of humping is delayed by a proposed modification of the welding set-up, specifically by angling the workpiece and offsetting the beam from the weld centreline. Throughout the research the high speed video provided useful quantitative information regarding the temporal behaviour of both the plasma and melt pool during welding.

The design, construction and testing of a semi-automated welding jig was completed. A marked improvement was observed in weld reliability due to the consistent fit-up achieved. Considerations for a production system are discussed and the economic feasibility of a laser drum welder is proven.

Dedicated to Mum and Dad



“You can’t always get what you want, but if you try sometimes you just might find you get what you need”.

The Rolling Stones

# TABLE OF CONTENTS

Acknowledgements

Abstract

**INTRODUCTION** 1

**CHAPTER ONE: LITERATURE SURVEY**

1.1 Laser fundamentals	5
1.1.1 Solid state lasers	5
1.1.2 Gas lasers	6
1.1.2.1 The carbon dioxide laser	6
1.1.2.2 The carbon monoxide laser	8
1.1.2.3 The chemical oxygen iodine laser	8
1.1.2.4 The excimer laser	8
1.2 LASER PARAMETERS	9
1.2.1 Power	9
1.2.2 Mode structure	10
1.2.3 $M^2$ factor	11
1.2.4 Polarisation	12
1.2.5 Wavelength	13
1.3 BEAM FOCUSING SYSTEM	14
1.3.1 Focal length	14
1.3.2 Position of focus	15
1.3.3 Material selection for optics	16
1.4 LASER-WORKPIECE INTERACTION	17
1.4.1 Absorptivity	17
1.4.2 Thermal effects	18
1.4.3 Workpieec traverse speed	19
1.4.4 Effect of gas shielding on the welding process	19
1.4.5 Joint geometry	21
1.4.6 Laser-plasma interaction	22
1.4.7 Optical feedback	24
1.5 DYNAMICS OF LASER WELDING	25
1.5.1 Keyhole/melt pool stability	25

1.5.2 Gravity	26
1.5.3 Weld solidification ripple	27
1.5.4 Thin sheet discontinuities	28
1.6 LASER SAFETY	29
FIGURES	30-43
REFERENCES	44

## CHAPTER TWO: EXPERIMENTAL DESIGN, METHOD AND ANALYSIS

2.1 EXPERIMENTAL STRATEGY	48
2.2 EXPERIMENTAL DESIGN	49
2.3 EXPERIMENTAL ARRANGEMENT	51
2.3.1 Processing lasers	51
2.3.2 Beam delivery system	51
2.3.3 Sample clamping and movement	52
2.3.4 Shielding gas delivery	52
2.3.5 Establishing the focal position	53
2.3.6 Alignment of the processing beam	53
2.3.7 Mode selection, tuning and quality	54
2.3.8 High speed video set-up	55
2.3.9 Weld monitoring set-up	55
2.4 EVALUATION AND TESTING	56
2.4.1 Metallurgy	56
2.4.2 Optical microscopy	56
2.4.3 Joining efficiency	56
2.4.4 Melting efficiency	57
2.4.5 Specific energy	58
2.4.6 Measurement of the fusion zone area	58
2.4.7 Tensile testing	58
2.4.8 Erichsen test	59
2.4.9 Weld quality	59
2.4.10 Microhardness measurement	59
2.4.11 Corrosion resistance	60
FIGURES	61-68

## CHAPTER THREE: PROCESSING: RESULTS AND DISCUSSION

3.1 INTRODUCTION	69
3.2 RESULTS AND DISCUSSION - PART 1	70
3.2.1 Identification of statistically significant welding variables	70
3.2.1.1 Speed and power	70
3.2.1.2 Focal length	72
3.2.1.3 Position of focus	73
3.2.1.4 Mode structure	76
3.2.1.5 Polarisation	78
3.2.1.6 Side angle weld orientation	79
3.2.1.7 Normal angle weld orientation	82
3.2.2 Weld profiles	83
3.2.3 Weld surface characterisation	86
3.2.4 Weld fault categorisation	88
3.2.4.1 Porosity	88
3.2.4.2 Cracking/incomplete fusion	90
3.2.4.3 Carbide formation	90
3.2.4.4 Surface defects	91
3.2.5 Comparison between bead on plate and butt welds	91
3.2.6 Mechanical testing	92
3.2.6.1 Tensile test	92
3.2.6.2 Erichsen test	92
3.2.6.3 Microhardness test	93
3.2.6.4 Corrosion resistance	94
3.2.7 Weld quality assessment	94
3.2.8 Statistical modelling	95
3.3 RESULTS - PART 2	97
3.3.1 Weld assist gas	97
3.3.2 Normal angle orientation	99
3.3.3 Side angle orientation	99
3.3.4 Position of focus	100
3.3.5 Edge preparation and fit-up	100
3.4 DISCUSSION -PART2	101
3.4.1 Weld assist gas	101
3.4.2 Normal angle orientation	104

3.4.3	Side angle orientation	106
3.4.4	Position of focus	106
3.4.5	Edge preparation and fit-up	107
3.4.6	Investigation of the humping effect	109
3.4.6.1	Experimental arrangement to observe weld formation	110
3.4.6.2	Results of the filming	111
3.4.6.3	Discussion of the high speed videos	112
3.4.7	The application of a mathematical model	114
	FIGURES	117-144
	REFERENCES	145

## **CHAPTER FOUR: IN-PROCESS WELD MONITORING**

4.1	INTRODUCTION	148
4.2	WELDING SENSOR SURVEY	149
4.2.1	Laser beam monitoring	149
4.2.2	Melt pool monitoring	150
4.2.3	Plasma monitoring	151
4.3	SELECTION OF IN-PROCESS WELD MONITORS	152
4.3.1	Dual wavelength optical sensors	152
4.3.2	Acoustic emission nozzle	154
4.3.3	Plasma charge monitor	155
4.4	RESULTS AND DISCUSSION	157
4.4.1	Dual wavelength optical sensors	157
4.4.2	Plasma charge monitor and acoustic emission nozzle	158
4.4.3	Reliability and ease of implementation	159
4.4.4	Weld sensor recommendation	160
4.5	FURTHER CHARACTERISATION OF OPTICAL SENSORS	160
4.5.1	Real time weld diagnostic system	160
4.5.2	Predictive nature of the sensors	161
	FIGURES	163-169
	REFERENCES	170

## **CHAPTER FIVE: LASER WELDING SYSTEM**

5.1	INTRODUCTION	172
5.2	SEMI-AUTOMATED LABORATORY WELDING SYSTEM	172

5.2.1	Fit-up and joint positiong	173
5.2.2	Focusing optics	174
5.2.3	Gas delivery system	175
5.2.4	Clamping units and datum bar	175
5.2.5	Welding system control unit	176
5.2.6	Edge preparation and fit-up	176
5.2.7	Weld quality assurance	177
5.2.8	Experimental trials	177
5.3	PRODUCTION SYSTEM RECOMMENDATIONS	178
5.3.1	Discussion of the production system	178
5.3.2	Economic feasibility	180
	FIGURES	181-186
	REFERENCES	187
<b>CHAPTER SIX: CONCLUSION</b>		<b>188</b>
<b>FUTURE WORK</b>		<b>190</b>
<b>APPENDICES</b>		
	APPENDIX A: Stat-ease statistical software and design matrix report	191
	APPENDIX B: A summary of the statistical data analysis	201
	APPENDIX C: Mechanical testing data	207
	APPENDIX D: Quadrant sensor specification and circuit design.	212

## INTRODUCTION

The project was conceived to investigate the feasibility and the economic viability of laser welding the longitudinal side seam of the Van Leer 1 mm thick 210 litre steel drum.

The Van Leer organisation was founded in The Netherlands, originally specialising in the manufacture of steel drums for the chemical and oil industries. Over the years the world wide success attained in this area has lead to a significant expansion, both geographically and in product diversity. Today, Van Leer is the premier steel drum manufacturer and is rapidly developing in the field of plastic container fabrication for both industrial and domestic markets. The importance placed on the need for research on advancing technology was the key to the initiation of this project.

Originally, the manufacture of drums was by hand, by skilled workman. In later years came the introduction of electrical resistance welding. This process has remained largely unchanged, with the original AC supplies now replaced by more efficient DC power supplies. Until the development of laser welding no alternative existed to warrant changes to the established system.

The discovery of the laser by Maiman in 1960 heralded the start of a manufacturing revolution which was not realised until the early 1980's. The principle manufacturing application of the laser was and still is the cutting of metal. Industry has now focused on the laser welding process as the latest advanced manufacturing tool. Laser welding has become, on the back of well documented research, an accepted manufacturing process. Adopted by, in particular, large scale automotive companies for reasons of performance and unique manufacturing techniques

So, what is a laser ? - consider the acronym, Light Amplification through

Stimulated Emission of Radiation. The laser is an energy converter. Electrical, chemical or other form of energy is used to excite a medium which decays by stimulated emission as opposed to spontaneous emission to give a near parallel, coherent beam of radiation of high spectral purity. This radiant beam can be shaped or focused to give an exact amount of energy which can be precisely delivered to the target in order to achieve the required operation, be it cutting, welding or surface treatment.

The generation of a laser beam results from the controlled excitation of a selected lasing medium, the most common of these being CO<sub>2</sub> and Nd:YAG (Neodymium in a Yttrium Aluminium Garnet crystal). The "beam" characteristics are high monochromaticity, high power densities, temporal and spatial stability. These two different types of laser medium exhibit different beam and processing characteristics. The CO<sub>2</sub> laser is the most common industrial welding laser largely for reasons of maximum output power capabilities (up to 24 kW). The Nd:YAG however has two strong factors in its favour; the shorter wavelength offers more efficient optical energy transfer to the workpiece and a flexible fibre-optic cable can be used for beam delivery.

There are two fundamental modes of welding; conduction and penetration welds. The dividing line between these modes is the formation of a fine hole by vaporisation known as the "keyhole". Conduction welding conditions are such that little vaporisation of the material occurs, producing a typically wide shallow weld pool. Conversely, the penetration welding mode, as the name suggests, offers deep and narrow welds. This is a direct result of the formation of the keyhole. In this mode the typical surface power densities are in the region of 10<sup>6</sup> W/cm<sup>2</sup>. The general advantages of laser welds over other conventional welds are their high integrity, autogenous nature, relatively small thermal input, and high processing speeds.

The present technique used by Van Leer to weld the drums is Electrical



Resistance Welding (ERW). This is a process which uses high currents to melt the metal and then pressure to “mash” the joint together to form the weld in a process known as forge welding. The result is a lap weld that is highly dependent on the contact between the welding wheels. As a consequence of the lap geometry the thickness at the weld is increased by approximately 1.7 times the thickness of the drum. This increase in thickness causes problems in the formability of the weld, which has a tendency to tear apart. This is especially a problem when sealing the top and the base of the drum . This ERW welding method has remained largely unchanged simply because there had been no viable alternative.

When considering laser welding in comparison with electrical resistance there are several specific advantages -

- 1) Improved weld quality.
- 2) Low energy input of 5 kW compared to 250 kVA.
- 3) Butt weld configuration leading to a saving of material.
- 4) No weakening at start and finish of the weld.
- 5) The drum enclosure insertion (emptying/refilling fitting) can be made in weld seam.
- 6) Butt configuration presents an improved surface condition for internal lacquering and external paint spraying.
- 7) Better quality control and more flexibility.
- 8) Minimal level of operator education.
- 9) Laser generator and optical system are environmentally safe, and can be encapsulated for minimum interference by personnel.

This listing indicates the potential advantages of laser welding technology. The prime objective is to produce a quality drum, at high production rates. The target for the welding speed was set at between 150-200 mm/s (9-12 m/min.).

The project objective was to achieve a foundation of laser welding research

from which the specific applications could be assessed. Thus, the initial work was followed by both optimisation and further in-depth research studies. Encompassed within the project are two specific areas, worthy of specific mention due to their importance; (i) are the fit-up and edge quality required to produce the target speed whilst retaining consistent weld quality and (ii) the formulation of a quality weld assessment criteria.

# CHAPTER ONE

## LITERATURE SURVEY

### 1.1 LASER FUNDAMENTALS

The laser beam represents a powerful processing tool due to its capability of delivering a large amount of energy concentrated in such a way as to produce surface melting and vaporisation. As the beam has no defined physical form but merely an energy content it is very flexible, with the main recognised forms of processing being welding, cutting and surface treatment. Any of these mentioned *processes* are dependent on several main areas defining each individual process summarised in figure 1.1.

In all lasers the basic construction is identical; firstly some form of excitation is required, together with an amplifying medium located between mirrors to produce the lasing action and lastly an optical resonator which focuses the lasing action of the medium in order to generate the high energy beam. This means the resonator design is largely responsible for propagation characteristics of the laser beam. There are five types of laser which produce sufficient power for material processing - the solid state, CO<sub>2</sub>, CO, COIL and excimer gas lasers.

#### 1.1.1 Solid State Lasers

This type of laser as the name suggests incorporates a solid amplifying medium composed of active Nd<sup>3+</sup> ions suspended in a transparent host material of yttrium aluminium garnet (YAG), glass, YLF and many other alternatives. The excitation for the medium had initially been provided by a helical Xenon flashlamp as in Maiman first working laser (1960), now this is likely to be superseded by diode laser

pumping. Amplification is achieved through multiple reflections of the laser light back and forth between the cavity mirrors through the medium. The useful beam energy emerges from the partially reflective output window (95% reflective).

The maximum power achievable at this wavelength of 1.06  $\mu\text{m}$  is 400 W per YAG rod, this power availability is limited by the cooling of the rod. Commercially available YAG lasers incorporate multirod amplifier/oscillator systems that offer up to 2.4 kW. The cooling of the rods may be improved with the development of slab YAG crystals which provide improved power due to symmetrical cooling. The pumping of the medium with a diode also reduces the heating affect and also promises to give greater power and the control of the energy distribution within the beam. The lasing wavelength of this type of laser allows the use of fibre optics in the delivery of the beam to the workpiece area giving the possibility non-linear delivery paths and the ability to link several lasers together allowing multi-kilowatt CW processing.

### 1.1.2 Gas Lasers

#### 1.1.2.1 *The Carbon Dioxide laser*

The gas laser has several advantages over the solid state; increased efficiency due to the lasing mechanism with in the gas medium, greater available power resulting from replenishment of the medium, ease of resonator design as this is no longer constrained by a solid medium, control over the discharge stability and free propagation of the laser beam within the cavity. The principle gas laser for industrial application today is the carbon dioxide laser although the laser is called a CO<sub>2</sub> laser, Nitrogen and Helium gases are present (CO<sub>2</sub>:N<sub>2</sub>:He::12:18:70) increasing the efficiency of the lasing process by collision energy transfer and enhanced cooling respectively as seen in Figure 1.2a.

The basis of the lasing process is through the phenomenon of stimulated emission , a mechanism whereby carbon dioxide molecules stored in the metastable level, through D.C. or RF excitation under low pressure conditions emit photons

when stimulated by an identical photon. Once the plasma has been formed through the excitation, an individual molecule loses its energy by collision with the walls of the cavity or through spontaneous emission. The photon of light produced by spontaneous emission of 10.6  $\mu\text{m}$  wavelength is emitted in any random direction however one will eventually travel in the direction of the optical axis. This photon may be diffracted out of the system or may collide with an already excited molecule - in this case the molecule returns to the lower energy level in doing so emits a photon of identical wavelength, phase and direction. The two photons now travel back and forth through the cavity generating more photons from other excited molecules resulting in an extremely rapid amplification process. The lasing wavelength incorporates a range of 9-11 microns with 10.6 micron being the most common.

There are four classes of carbon dioxide lasers-

- 1) Sealed - The laser contains a static gas mixture within a single sealed tube, with cooling being provided by conduction through the tube walls. The uses of this laser are mostly for requirements of low power and high beam stability (up to 100 W) , used mostly for medical, military and diagnostic purposes.
- 2) Slow Flow - The laser gas mixture pumped through cavity therefore overcoming gas decomposition problems, the cooling being achieved by conduction through the discharge tube walls to a water jacket. The power is a function of discharge tube length, typically around 50 W/m with maximum powers upto 1.5 kW for normal commercial lasers allowing cutting and welding of sheet metal plus low speed surface treatment.
- 3) Fast Axial Flow - The flow of the laser gas mixture is near sonic speeds, the increase flow rate gives higher powers and cooling of the mixture by forced convection increases the lasing efficiency to about 15 %, compared to the theoretical maximum of 45 % which is the quantum efficiency. The power is a function of the discharge length and, due to the forced convective cooling the tube diameter, offering

upto 1 kW/m. Typical industrial laser are of 5 - 10 kW providing the welding and cutting of thick sections or the high speed processing of sheet metal.

4) Transverse-Flow - In this case the gas mixture flows perpendicular to the optical oscillation direction and electrode discharge, cooling is therefore improved allowing compact high power lasers. The current powers available are upto 24 kW the applications of these very high powers being the processing of sections of around 10 cm thickness.

#### **1.1.2.2 *The Carbon Monoxide laser***

One of the most recent development in the high power regime is the CO laser, operating at around 5 microns. This gas laser having an identical generation mechanism to the CO<sub>2</sub> fast axial flow laser. The lasing process has a quantum efficiency of nearly 100% double that of the CO<sub>2</sub>, however the process only occurs effectively at about 200 K. [3]. The shorter wavelength of the CO laser is hoped to provide for a more efficient processing of material, similar to the solid state laser, but offer power capabilities of the existing CO<sub>2</sub>.

#### **1.1.2.3 *The Chemical Oxygen-Iodine laser***

The so-called COIL laser combines the power capabilities of the gas lasers with the fibre delivery possibilities of the solid state lasers. The laser operates continuously in the near infra-red at 1.3 microns, and is currently at the 1 kW mark [4].

#### **1.1.2.4 *The Excimer laser***

This laser operates in the ultra-violet region from 172 nm to 354 nm depending on the active medium, usually a combination of an inert gas and a halide. The combination of only the two forms when in the excited state producing an excited complex molecule, the molecule rapidly falls back to the lower ground state emitting laser radiation and effectively in the same instance dissociating. The excimer laser

can only operate in pulsing mode, being capable of delivering nano second discharge times reaching peak powers of gega watt proportion. The uses of the excimer lasers are in mainly in the ablation and marking of materials.

## 1.2 LASER PARAMETERS

From an observers standpoint the laser simply provides the heat source required for the welding operation with the power of the laser the only apparent beam variable. The true story is that it is slightly more complicated with the distribution of energy in the beam, the mode structure, playing an important role in determining the irradiance of the focussed beam. The importance of the mode structure is highlighted by the existance of factor which defines the quality of the mode- the  $M^2$  concept. Another relevant beam characteristic is its polarisation which together with the wavelength of the laser are linked to the absorption of the beam at the workpiece. When considering long beam paths (over 5 m) the actual propagation of the beam becomes important, the beam will be expanding over the distance with the power attenuation related to variable conditions along the atmospheric delivery path.

### 1.2.1 Power

Power represents one of the most important and fundamental parameters of laser welding, directly controlling the energy input into the material. The effect of this particular factor with respect to weld penetration has been investigated in many previous studies, originally by Baarsden (1973)[5] seen in Figure 1.2a with the high speed welding of low rimmed carbon sheet steel and later by Dawes and Watson (1985)[16] in the processing of similar material. The results of which show the depth to be directly proportional to the input power and that for a given thickness the maximum welding speed increases with increasing power.

The power is obviously related to the joining efficiency of the operation [6], if an arbitrary process efficiency is to be maintained then there is a certain power level below which this is not possible. Figure 1.3b shows the logarithmic relationship due to the fact that the speed term is included in the joining efficiency equation.

### 1.2.2 Mode Structure

The mode of the laser is described as the spatial distribution of energy across the beam, perpendicular to the propagation direction [8]. It is basically a standing transverse electromagnetic wave which can be thought of as representing the power distribution across the beam.

This mode is fixed by the design of the laser cavity incorporating such factors as the alignment of the cavity mirrors, their radius of curvature and spacing and the bore of the discharge tube. By choosing suitable values of these factors a mode can be generated according to the requirements of the process.

These mode structures are known as Transverse Electromagnetic Modes, and are universally shorthanded to  $TEM_{pq}$  where p and q are the number of nodes contained within two specified directions. These directions can be described by two coordinate systems firstly rectangular and secondly cylindrical. In the rectangular coordinate system p and q are the nodes in two orthogonal directions. The cylindrical and more widely used system describes p and q as the nodes in the radial and angular directions respectively. A few examples are given in Figure 1.4 of the more common structures for both coordinate systems.

The welding process prefers the lower mode structures, in particular  $TEM_{00}$ ,  $TEM_{01}$  and  $TEM_{01*}$  (cylindrical) as these provide smaller focussed spot size than higher modes with comparable optics see section 1.2.4. Just to note the latter mode is made up from the oscillation between two orthogonal  $TEM_{01}$  modes. Experimentation has proved that the Gaussian mode gives greatest penetration for a



given power, speed and thickness [9] as it provides the greatest power density available for the focussing optics used. The intensity distribution of a Gaussian mode is described by a simplification of the Laguerre-Gaussian Distribution Function -

$$I_r = I_0 \exp [ -2r^2 / r_0^2 ] \quad (1.1)$$

where  $I_0$  = Intensity at the beam centre (W/m<sup>2</sup>)

$r_0$  = Raw beam radius.(m)

$r$  = Distance from centre.(m)

$I_r$  = Intensity at distance  $r$  from the centre.(W/m<sup>2</sup>)

This intensity distribution is very important in laser welding though it is interesting to note that longitudinal electromagnetic modes also exist creating a standing wave along the optical axis, however the affect of different longitudinal modes on the welding process is not a consideration.

### 1.2.3 M<sup>2</sup> Factor

Recognising the important role the mode plays in the welding process the M<sup>2</sup> factor was introduced to act as a guide to the quality of the mode structure. The basic idea behind this quality factor is that it relates the working beam to that of a perfect Gaussian beam generated under the same resonator design and conditions [12]. This comparison is achieved simply by a ratio of the ideal and working beams divergence shown schematically in Figure 1.6. Thus -

$$M^2 = \theta_w / \theta_g \quad (1.2)$$

where  $\theta_w$  = Working beam divergence.

$\theta_g$  = Equivalent Gaussian divergence.

The divergence of the working beam can be measured and the ideal is given by equations describing the propagation of a Gaussian beam through space [10]. This quality measurement is an important concept in laser welding and cutting processes standardising a previously non-quantified variable which effects the process to a high degree.

The importance of beam quality on processing is emphasised if one considers the that minimum spot size is directly related to  $M^2$  and even more significantly that the maximum intensity is directly related to  $M^4$ .

#### 1.2.4 Polarisation

Laser radiation consists of a stream of electromagnetic waves, the electric and magnetic wave components being orthogonal but are vectors in space at right angles to the direction of propagation. When all of the main portion of the radiation has the electric vector in the same orientation the beam is said to be polarised. The laser cavity is an optical amplifier and hence tends to produce polarised beams, there are three forms of polarisation governed by the distribution of the electric and magnetic waves perpendicular to the direction of propagation.

If the cavity has similar losses for all planes of polarisation then the beam is randomly polarised however this is an unstable system for material processing. Usually laser cavities contain folded mirrors to stabilise one orientation of polarisation the beam is now plain polarised. When considering cutting and welding plain polarisation causes process variation subject to the direction of movement therefore many industrial lasers are fitted with a circular polariser. This consists of mirror angled at 45 degrees with a 1/4 wavelength film the reflected electromagnetic waves form a helix in the direction of propagation.

The effect of polarisation on laser welding is related to the absorption mechanism. At lower processing speeds the keyhole can be thought of as a cylinder filled with plasma, the beam is absorbed by the plasma and reradiated to the

workpiece heating of material ahead of the beam is purely by conduction only. In this case polarisation has no effect. Increasing the processing speed moves the keyhole towards the melt front until such time as the beam is directly incident on the melt front. The absorption of the beam energy at the molten wall is a function of the orientation of the electromagnetic waves. Polarisation perpendicular to the direction of welding has an electric vector oscillating at right angles along the surface therefore the interaction causes the free electrons to vibrate in a similar direction. Parallel polarisation has the vector oscillating into to the workpiece causing electron vibration to be effectively out of the surface. Looking at the two cases it is likely the latter has the higher absorption level of the incident radiation.

This effect only becomes apparent at incident angles greater than 30 degrees, which is particularly relevant in high speed thin gauge welding [13]. Beyer *et al* (1986)[12] showed that by orientating the electromagnetic field in the direction of welding enhanced penetration is achieved. Figure 1.7 shows that the onset of this effect occurs around 50 mm/s for the processing conditions described, where a change in absorption mechanisms is observed from the plasma within the keyhole to the front cavity wall.

### 1.2.5 Wavelength

The absorptivity of a material is largely dependent on the wavelength of the incident radiation, as shown in figure 1.8. Shorter wavelengths giving higher energy coupling, this is most significant when processing highly reflective metals such as copper. Where the YAG and Excimer lasers can be used in processing, the CO<sub>2</sub> laser beam merely scratches the surface unless outrageously large power densities are used. In the case of mild steel no such problem exists, once the keyhole is established the area of interest is the dynamic absorption during the welding process. In this situation there are two particular areas are of interest, firstly; the role of the plasma and secondly; the absorption of the beam at the front wall. It has been

shown that the absorptivity of the plasma,  $\alpha$ , simply considering the inverse bremsstrahlung absorption relates to the radiation wavelength thus,

$$\alpha = f(\lambda^2) \quad (1.3)$$

Which gave lasers upto the 5 micron wavelength region (Excimer, YAG and CO lasers) an extreme advantage with the CO<sub>2</sub> laser having an absorption coefficient 100 times larger than an equivalent YAG laser. Matsunawa and Ohnawa (1991)[14] investigated beam losses using YAG laser on titanium targets discovering 30% of the incident radiation was being scattered away from the target as a result of Rayleigh scattering due to ultra fine particles, these particles forming from condensation of evaporated atoms. This loss associated with the shorter wavelength laser was equivalent to the bremsstrahlung loss of the CO<sub>2</sub> laser for the material used. Therefore although the shorter wavelength laser shows better absorption characteristics, the advantage in the dynamic welding situation may not be as great as previously thought.

### 1.3 BEAM FOCUSsing SYSTEM

#### 1.3.1 Focal Length

In order for the laser beam to be of use as a processing tool the raw beam is focussed to a spot achieving the power density required for the welding operation. The focal length of the focussing system fixes the minimum spot size and the depth of focus of the beam at the workpiece. The raw beam is not focussed to a point but is diffraction limited, the size of the spot for a Gaussian mode is described by -

$$d_f = 2.44 \lambda F M^2 \quad (1.4)$$

where  $d_f$  = Beam diameter.(mm)

$F$  = F-number (focal length/raw beam diameter) (mm)

$M^2$  = Quality factor (no units)

$\lambda$  = Laser radiation wavelength (mm)

The inclusion of the quality factor in the equation underlines the effect of the incident beam dimensions, increasing the mode order causing an increase in the focussed spot size. The distribution of power in the spot is known as the “Fraunhofer” diffraction pattern, the central maximum contains about 86% of the total power and also defines the measurement of the spot size - that diameter which contains  $1/e^2$  of the total power. Immediately above and below the point of focus there is only a small change this is the depth of focus, defined as the distance over which the spot size changes by 5%. The depth of focus is simplified for a diffraction limited spot for a Gaussian beam:

$$Z_f = 1.48 F^2 \lambda \quad (1.5)$$

where  $F$  = F number (Focal length/Diameter of raw beam)

The optimal selection of the focal length is related to the thickness of material to be welded. For thin plate and sheet metal processing shorter focal lengths are preferred [17] with around 60 mm recommended for the welding of 1 mm thick sheets. The choice should be such that the depth of focus is around the same thickness of the section to be welded [16].

### 1.3.2 Position of Focus

The position of focus dictates the location of the maximum power density with respect to the workpiece and the intensity distribution through the material thickness, thus controlling the penetration limit and the weld profile.

The problem to be overcome is having sufficient power density at the surface

to generate the keyhole whilst the distribution of the power through the section gives the required penetration. This situation was originally investigated by Engel (1976)[18], shown in figure 1.10, and later summarised by Steen (1992)[47] for different F numbers. Several authors have suggested the position of focus should be about 1 mm below the surface [18, 19] with Wilgoss *et al* (1979)[17] showing this to be so in the welding of 6 mm thick stainless steel. In the welding of sheet metal the use of shorter focal length optics mean tighter tolerances on the position of focus due to the decreased depth of focus. Akhter (1990)[48] in the welding of 1mm thick steel preferred the focus to be at the surface. In association to simply deciding the position of focus according to the thickness a further consideration is the joint geometry in the welding area, Kawai *et al* (1984)[19] performed butt welding of 0.75 mm thick mild steel stated the position of focus to be 2.5 mm below the surface in order to overcome fitup tolerances and variable edge quality.

### **1.3.3 Material Selection for Optics**

When considering a focussing system the main factors are the transmissive qualities at the operating wavelength of the laser, in this case 10.6 microns, with regard to beam absorption, the raw beam focusibility and the materials hydroscopic nature. The potassium chloride crystal is most commonly used in the form of a plano-convex shape offering average performance at low cost. Higher quality materials exist in the form of zinc selenide and gallium arsenide which naturally offer improved all round performance but at a cost of about 8 times that of the KCl.

When using high powered lasers of 5 kW and over, lens systems are unable to function at these higher power densities, therefore mirror systems must be used plus the advantages of no aberration, high durability and convenient focus setup (as lens focus may vary from one to another by upto 2 mm). In its simplest form this could just be a single off axis parabolic or a combination of several mirrors depending on the beam delivery constraints. The construction of the mirrors is

dependent on the required power handling capabilities, upto 2 kW a base material of copper or aluminium with a nickel/gold coating on the reflective surface. Over 2 kW the base material remains to provide heat conduction away from the surface normally to circulating water in the back of the mirror but the coating is gold only or may be just the base material itself.

## 1.4 LASER - WORKPIECE INTERACTION

### 1.4.1 Absorptivity (or reflectivity)

In the low intensity region around  $10^4$  W/cm<sup>2</sup>, below the materials melting point, absorptivity is largely dependent on the materials surface conditions and the incident laser wavelength. With increasing intensities in the region of  $10^6$  W/cm<sup>2</sup> the absorption becomes more dependent on the level of the laser intensity itself, even to the extent that it is independent of the processing wavelength [21] this corresponds to the onset of plasma formation. The mechanism of the transfer of energy to the workpiece is fairly complex therefore a summary is presented.

The mechanism involves photon/electron/lattice phonon interactions; the electrons are promoted to the Fermi level through photon collision, these conduction electrons move randomly within the skin depth  $d$ , where  $d = 1/\alpha$  (mm), until losing its energy through collision with a phonon (heating process). The relaxation time, i.e. time taken in between electron-phonon interaction, is dependent on the electron mean free path and impurities within the bulk material. So the phonon population increases, as the temperature increases, leading to a continual reduction in the relaxation time and an increase in the absorption. If one considers the time taken for this to occur is of the order  $10^{-13}$  s there is an extremely rapid rate of energy transfer to the target, and as long as there is sufficient intensity melting, boiling and evaporation will occur. Figure 1.12 shows the relative speed of events associated

with the optical energy deposition and the dynamic welding process.

Figure 1.11a and b shows this effect of increasing absorptivity with laser intensity and the corresponding increase in penetration depth. The sudden fall of reflectivity at around  $10^6 \text{ W/cm}^2$  is mainly due to the formation of the keyhole. This is the region for most welding processes [21]. Further to this the absorption (or reflection) is highly dependent on the surface condition of the metal, as shown in figure 1.13. There are two basic theories covering absorptivity; Plasma and Fresnel. The Fresnel absorption is modelled by the Drude theory which calculates the photon/electron interaction in a solid. Plasma absorption is due to the photon absorption by free electrons in the plasma.

#### 1.4.2 Thermal effects

It was seen in Section 1.4.1 that the absorptivity depends upon the free electrons in the material and the surface shape. The free electron density is proportional; to the electrical conductivity of the material which by the Wiedermann Franz principle is related to the thermal conductivity - being dependent in the energy transfer from the same source. As this energy is absorbed so it will be conducted away according to the principle held in Fouriers First Law of heat conduction.

$$Q = -k A dT/dx \quad (1.8)$$

where  $Q$  = Rate of energy transfer (W/s)

$k$  = Thermal conductivity

$A$  = Cross-sectional area

$dT/dx$  = Temperature gradient (K/m).

By assuming the energy from the laser was absorbed along a line source into the material (a simulation of the keyhole for thin materials) Swifthook and Gick developed Rosenthal's solution (1947)[22] and showed that for high speed welding



there is a limiting melting efficiency of 48.3% defined by -

$$P = 2 vwt (\rho C_p T_m) \quad (1.9)$$

where P = Power (kW)

v = Speed (cm/s)

w = Weld width (cm)

t = Weld thickness (cm)

$\rho$  = Material density (Kg/m<sup>3</sup>)

$C_p$  = Specific heat capacity (kJ/Kg/C)

$T_m$  = Latent heat of melting.

The melting efficiency was defined as the energy required to melt the weld nugget/energy absorbed.

### 1.4 3 Workpiece traverse speed

The relationship between traverse speed and the penetration is indicated by Swifthook and Gick's equation 1.9 quoted in the previous section. This inverse relationship is reported by many authors [5, 6, 7, 18] shown in figure 1.14. Provided the penetration can be achieved satisfactory weld bead shapes can only be found in a limited range of speed and power. Mazumder (1983)[11] plotted the extent of the optimal welding region and Albright has mapped out weld bead profiles and pool shapes discussed further in Section 1.5.4.

### 1.4.4 Effect of Gas Shielding on the Welding Process

During the welding process it is necessary to use a gas blanket and jet to perform a series of functions; prevent the weld from oxidising, control the extent of plasma formation and lastly to protect the welding optics from spattered weld metal. The

selection of the gas is only half the problem, the design and positioning of the gas delivery must be tailored in such a way that all three of the above requirements are optimised for the specific welding problem.

Seaman (1977)[23] carried out the first work on the effect of different shielding gases on penetration. The results showed Helium to be the most effective in plasma suppression and therefore increased welding depth. This relates to the higher ionisation potential of helium (24.46 eV) in comparison with air and other gases, thus raising the power density for plasma formation. Another gas of interest was argon; this has a lower ionisation energy than helium (15.68 eV), making welding at low speeds impossible due to beam blocking. However it was found to be particularly useful at higher processing speeds where plasma blocking does not present a problem, but actually may increase coupling and as well as preventing oxidation. Seaman came to the conclusion that best results were achieved with a mixture of the two; 90%Helium and 10% Argon.

Beyer *et al* (1983)[24] considered a further possibility of using nitrogen gas, which possesses better plasma suppressing characteristics than argon whilst from a commercial standpoint is better value than helium. Beyer also carried out work on the effect of different gas flow rates, showing the welding depth to be a function of individual flow rates, as shown in figure 1.15. In particular, that argon has a critical value at which plasma is readily formed and that helium plasma suppression ability decreased over a certain flow rate which corresponded to the critical value of the argon - around 40 l/min. for the processing conditions. From Beyer's results it can be observed that the increase in penetration achieved by increasing the flow rate from 0 to 80 l/min. is only a few percent. Miyamoto *et al* (1984)[25] showed the delivery pressure of the assist gas must be higher than the pressure within the cavity in order to produce a smooth weld, any value over this causes a humping bead. Further experimentation was carried out by Heiple *et al* (1983)[38], investigating the addition of oxygen to the shielding gas. By adding a

critical amount whilst welding certain metals enhanced penetration occurred with no detrimental effects to the mechanical properties of the metal.

More recently Chrysler, who are introducing extensive tailored blank facilities using laser welding have designed a welding shroud using CO<sub>2</sub> gas thus reducing the cost of the shield gas by a factor of five.

Traditionally the delivery of the gas was simply through a coaxial nozzle, Locke *et al* (1968)[6, 7] discovered that the use of a side jet parallel to the workpiece angled across the direction of welding greatly increased achievable penetration by up to 40% particularly at low speeds. A later development was the 'plasma disruption jet' which is positioned at 45 degrees following the weld. The location of the jet in relation to the keyhole is extremely critical around 0.5 mm in any direction [26], incorrect location causes a plasma or 'nail head' bead.

McCay *et al* (1990)[26] showed that a critical delivery pressure exists in order to achieve a sound and smooth weld, highlighting the importance of flow rate, pipe bore and jet positioning. More recently a new design of nozzle has been produced by Sutcliffe *et al* (1992)[27] which incorporates an aerodynamic window to protect the focussing optics from particles from the workpiece and vaporised metal, a side jet is used to provide cross-flow of up to 208 l/min. into the cylindrical nozzle with a conical tip. This arrangement also seems to show reduced porosity (88% less by area) in the welding of 6 mm thick aluminium alloy.

#### 1.4.5 Joint Geometry

Within the area of welding there are numerous types of weld geometry however in the manufacture of drums only two are relevant the butt and lap welds. The latter is largely connected with the existing production technique therefore only the former is of interest, the factor of importance in butt welding is the quality of the interface resulting from the method of cutting. Kawai *et al* (1986)[19] showed that laser cut interfaces with near parallel sides achieved nearly double the speed

achieved with guillotine cut edges, this is largely due to the lack of material volume in the weld zone with the sheared edges and the problem of the beam passing through the joint. In previous literature (Industrial laser handbook) the vertical misalignment tolerance is quoted as 25 % of the sample thickness otherwise penetration does not occur, also the gap thickness should be less than half the beam diameter (Industrial Laser Handbook) - summarised in figure 1.17.

Another crucial aspect of the interfaces is the uniformity of the profile through the thickness and along the length of the weld.

#### **1.4.6 Laser - Plasma Interaction**

When a laser is incident on a material of sufficient intensity the material will experience melting, boiling and evaporation. This extremely rapid heating process leads the materials absorptivity, typically for mild steel, to jump from around 10 to 90% with the formation of the keyhole in a matter of milliseconds [30].

With the onset of evaporation shock waves are generated at the material surface due to the pressure difference caused by the high temperature gradient between the target and the ambient surroundings. These waves radiate outwards effectively 'dragging' the vaporised metal particles into an area above the weld. The area immediately above the interaction point contained within the beam experiences power densities of  $10^6$  W/cm<sup>2</sup>, in association with the added input of free electrons from the metal vapour, avalanche ionisation together with multi-photon absorption cause a breakdown of the ambient gases (air is normally  $10^9$  W/cm<sup>2</sup> breakdown intensity) occurs leading to the formation of a plasma. The plasma is initiated when free charges are generated at a rate sufficient to produce a free charge density which will absorb the incident radiation.

On ignition the plasma begins to absorb the radiation from the incoming beam and, via inverse bremsstrahlung re-radiates this absorbed radiation as a black body spectrum - this describes the Laser Supported Absorption wave (LSA) [32]. The

absorption wave can either be a Laser Supported Combustion wave (LSC) or a Laser Supported Detonation wave (LSD) depending on processing conditions. The LSA wave moves into the area shocked by the precursor pressure wave, if the wave is subsonic and less than the gas particle velocity it is a LSC shown schematically in figure 1.18. If the the wave is supersonic moving with the gas particles it is a LSD.

The LSC wave is typically produced with a power density of around  $10^6$  W/cm<sup>2</sup>, whereas the LSD occurs at higher threshold around  $10^9$  W/cm<sup>2</sup>. Considering the laser welding power regimes the LSC is more applicable and by its nature more desirable; remaining coupled to the workpiece, being more transparent and of larger dimensions.

The important question is the usefulness of the plasma, it does provide 'enhanced coupling' however theoretical losses of 3.65 kW/cm<sup>2</sup> have been reported [32] in beam attenuation. The absorptivity of the plasma results from plasma oscillation expressed as -

$$\omega_p^2 = (n_e e^2) / (\epsilon_0 m_e) \quad (1.6)$$

where  $\omega_p$  = plasma frequency (1/s).

$n_e$  = electron number density (m<sup>-3</sup>).

$m_e$  = mass of electron (Kg).

$e$  = electronic charge (C).

$\epsilon_0$  = dielectric constant.

The plasma frequency is expressed in terms of the high concentration electrons contained with in its volume, around  $10^{24}$  m<sup>-3</sup>, as the like charged electrons repel one another (long range coulomb effect) chain reactions are set up producing an overall oscillatory system. The incident radiation will pass through the plasma if the plasma frequency is less than the laser frequency ( $\omega$ ), however if the plasma frequency is greater than the laser frequency the radiation is reflected or totally absorbed to be re-radiated [16]. More recently Ducharme *et al* (1992)[33]

predicted that the defocusing of the beam in the plasma produces welding interruptions. Furthermore, by this mechanism the welding action is terminated before the critical electron density, therefore preventing any reflection of the beam by the plasma.

Dixon and Lewis (1984)[34] showed that by angling the sample to be welded the number of initiated Laser Supported Combustion waves reaching critical density ( $w = w_p$ ) is reduced. They reasoned that the wave moved directly along the beam axis whereas the plasma propagated normal to the workpiece, thus reducing the role played by the plasma in contributing energy to the wave to an extent where fewer reached the critical density.

However it is not possible to eliminate plasma altogether [11] therefore no matter how standardised the welding process the plasma phenomena will always be present.

#### 1.4.7 Optical Feedback

The welding process requires processing in and around the focus area of the beam, in doing so and dependent on the reflection coefficient and target positioning a part of the laser radiation is reflected back into the laser cavity [36]. This effectively enlarges the laser cavity as the processing optics, target and laser output mirror form an optical resonator which is linked to the actual laser resonator.

The effect of this feedback is to produce spiking of the intensity distribution in the beam, the extent and behaviour of this intensification are related to the relaxation times of the CO<sub>2</sub> molecules. The strongest spiking occurs when the target is in focus, the effect on processing is still unclear although an obvious result must be variable penetration and possible intermittent processing, the extent can be minimised using higher intensities and thinner gauge material.

## 1.5 DYNAMICS OF LASER WELDING

### 1.5.1 Keyhole/Melt pool Stability

Once the keyhole has been established and the welding process starts an equilibrium exists between the molten pool and keyhole, the fluid flow in the melt pool tending to obliterate the plasma filled keyhole which is maintained by the recoil pressure of evaporating metal. The absorption mechanism within the keyhole and transference of heat between the laser beam/plasma/molten metal/solid is an extremely complex problem as yet to be solved satisfactorily.

The shape and behaviour of the keyhole and melt pool has been studied by Siekmann and Morijn (1970)[36] and Arata and Mijamoto (1978)[37] respectively. Figure 1.19 shows that with increasing processing speed the keyhole becomes angled backwards losing penetration depth, Arata used tracers elements to show the increase in the melt pool length at higher speeds highlighting pool instability. Associated with large melt pool lengths at high processing speeds was the fact that the weld profiles showed very low aspect ratios having large surface width but very little penetration. Later this was explained by Chan *et al* (1989) as very steep surface temperature gradients were setup between the beam centre and outer edges of the melt pool thus creating strong sideways convective forces.

This effect was investigated by Heiple and Burgardt (1985)[38] showing that the use of Group VI elements created positive temperature effects thus effectively reversing the thermocapillary flow inwards towards the heat source transporting thermal energy down the central axis of the weld pool along the interface. The problem is incorporating the required doping elements in the material or the use of additions to the welding gases such as Sulphur dioxide.

The dynamic welding situation - the relationship between absorbed energy, plasma generation and molten fluid flow has been investigated by Gatzweiler *et al* (1989)[40] and Arata *et al* (1978)[39]. Gatzweiler considered two situations; full

and partial penetration, the former is most relevant in this case. The extent of the plasma above and below the keyhole was measured by photodiodes is shown in figure 1.20 showed a period variation in the readings from above and below are almost perfectly out of phase exhibiting alternate high and low pressure readings, the surface leading. The melt pool thus modulates according to the these pressure variations, the whole process being controlled by the absorption and evaporation rate at the leading edge.

### 1.5.2 Gravity

Laser welding in reduced and increased gravity was originally attempted by Duley and Mueller (1990)[41] using polymers with a 25 W CO<sub>2</sub> laser and later by Workmann and Kauler (1990)[42] using the same NASA KC - 135 microgravity aeroplane investigating the effect on 0.127 mm thick 304 stainless steel processing with an 18 W Nd:YAG laser. Both sets of results were not particularly significant apart from the observed change in the wave structure on the trailing edge of the keyhole. The welding of the steel resulted in a 50% improvement in penetration under reduced gravity conditions the explanation offered being that a higher surface curvature can be maintained thus reducing the width, however the total weld volume remains constant leading to the increased depth.

Welding under hypo and hyper gravity conditions is somewhat unpractical however the direction of the gravity component acting on the melt pool can be varied according to the angle and orientation of the welding [41, 11]. Foley and Banas (1984)[43] found with increasing speed welding with the sample directly overhead of the beam offered greatest penetration all other possibilities caused melt pool instabilities as the gravity component was not acting along the beam path. Mazumder (1983)[11] preferred welding in the vertical plane.



### 1.5.3 Weld Solidification Ripple

Any laser welded sample has a characteristic surface solidification pattern, as shown in figure 1.21. If one examines the longitudinal section a rippling effect is apparent, in some cases a periodic variation in the weld width occurs. The surface topography and the mechanisms causing these variations has been investigated by several authors attempting to explain the fluid mechanics behind the rippling.

There are three types of ripple that occur; 1. a fine ripple of 5 - 15  $\mu\text{m}$  wavelength which is present at all speeds, 2. a coarser ripples of about 100  $\mu\text{m}$  and 3. in more critical cases an undercutting effect with central humping.

Cline and Anthony (1977)[46] thought the main driving force was surface tension caused by the steep thermal gradients within the pool, this however did not hold at higher speeds or explain the intermittent flow required for ripple formation. Copley *et al* (1981)[44] attributed the coarser rippling to variable power coupling, Moore *et al* (1978)[44] reported that melt pool depression caused by vapour pressure variations produced the rippling effect. Ishizaki (1980)[45] modelled the fine ripples on the assumption of a period oscillation of the liquid contact angle at the solidification front which was confirmed by Hawkes *et al* (1983)[44] using high speed photography. They showed the fine rippling to be independent of fluid flow conditions and was most noticeable with increasing power densities. The idea of the bow wave theory first suggested by Moore was taken a stage further by Hawkes, suggesting that a stern wave was propagated towards the back of the melt pool when the bow wave reached a critical size. This would cause the melt to be sloshed back and forward under the waves own momentum, providing for oscillatory melt flow conditions possible setting up a standing solidification wave. Traces of forward flow were discovered by EDAX scans confirming the theory.

These suggested mechanisms have been partly proved. However, it is almost impossible to define an exact mechanism: with respect to absorption conditions, vapour pressure, material properties and contact angles is almost impossible.

#### 1.5.4 Thin Sheet discontinuities

The welding of sheet metal has certain weld defects particular to this gauge of sample ( $\leq 1$  mm), the defects have been recently documented by Albright and Chaing (1990)[49]; lower speeds resulting in cutting and hole formation, higher speeds causing 'snaking' or 'ropey' beads in extreme cases a longitudinal humping effect, the results mapped out in figure 1.23.

At lower speed and moderate power, drop out of the weld material is experienced due to sagging of the melt pool under the gravitational force of its own mass overcoming the opposing forces of surface tension. This effect is accentuated by the coaxial shielding gas jet which impinges normally on the pool thus increasing the total downward force.

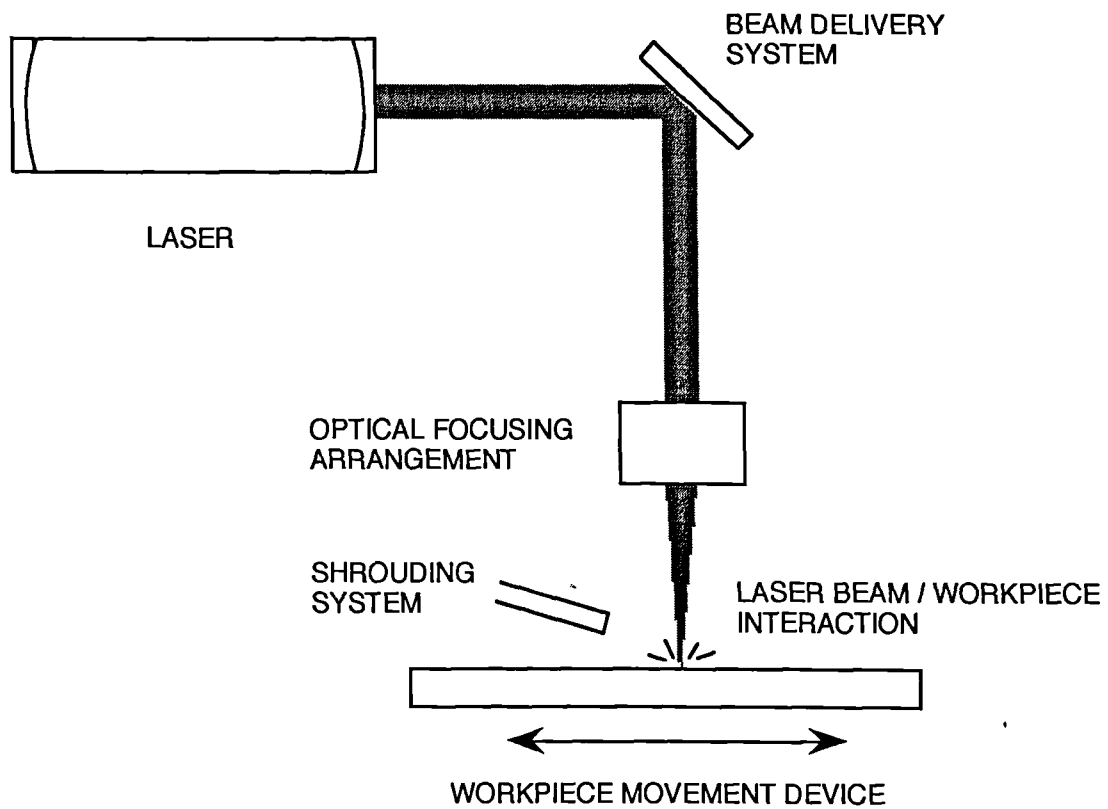
As the speed exceeds the sound weld threshold for the conditions the melt pool elongates, through penetration becomes occasional and eventually non-existent leading to instabilities in the melt pool as modelled by Gratzke *et al* (1991)[48]. The effect on the solidification process is that the molten metal does not have sufficient time to reach equilibrium position before solidifying producing narrow weld widths and undercutting at the edges, characteristically showing a wavy centreline. Further increases in the speed to around 500 mm/s (20 m/min.) for 1mm thick steel causes the phenomenon of "humping" to occur - this is the longitudinal height variation of the solidified weld metal. The reasons for this phenomenon are still unclear, in traditional welding techniques it was thought pressure instability arising from changes in surface tension and pool curvature lead to a "pinch" effect resulting in hump formation [46]. A more recent explanation suggests that as the molten material is swept around the keyhole it becomes greatly accelerated and tunnelled up and along the back of the keyhole directed down the weld centreline [44]. The metal quickly solidifies into the "hump" as this represents the minimum surface energy shape.

## 1.6 LASER SAFETY

Considering the nature of the laser beam, it is invisible contains many kilowatts of power and travels at  $300 \times 10^6$  m/s. Therefore any contact cannot be avoided once the danger has arisen and results in severe burning at best.

During any form of processing protective glasses should be worn at all times, these can be either plastic or glass. The hazard of an "escape" of the beam from the defined path or from reflection from the workpiece must be guarded against, particularly when taking beam prints or aligning the beam, and when angling or in the use of highly reflective samples. It is advised that the use of beam blocking be employed when, for any reason, the protective beam path covers have to be removed (eg fire bricks). When one is moving around the laser, a constant awareness must be maintained of where the beam path is and the presence of other people around the processing area. It must be remembered when working with high power lasers, the noise is sometimes deafening, therefore communication becomes impossible. A further danger exists from the close proximity of high voltage elements, extreme care must be taken when close to the laser head. Lastly, when and during firing of the laser all the above should be taken into account.

The implementation of a laser safety standard in the United Kingdom is currently under BS 7192:1989.



**Figure 1.1** Schematic diagram of the important areas of laser processing covered in the first chapter.

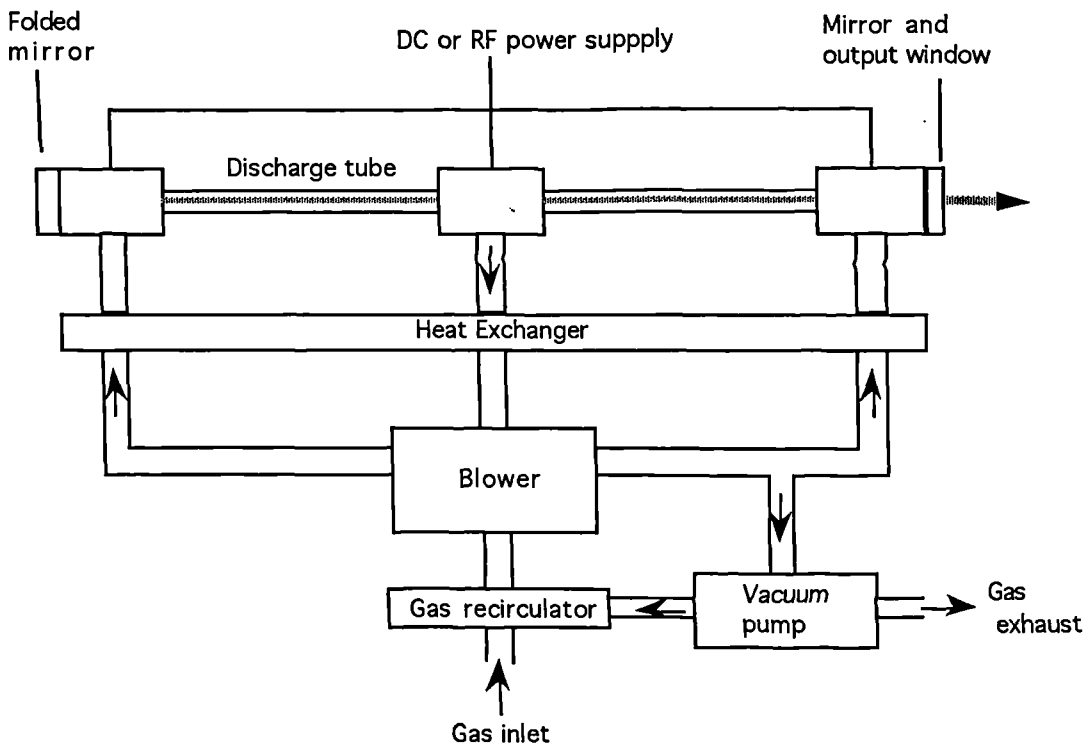
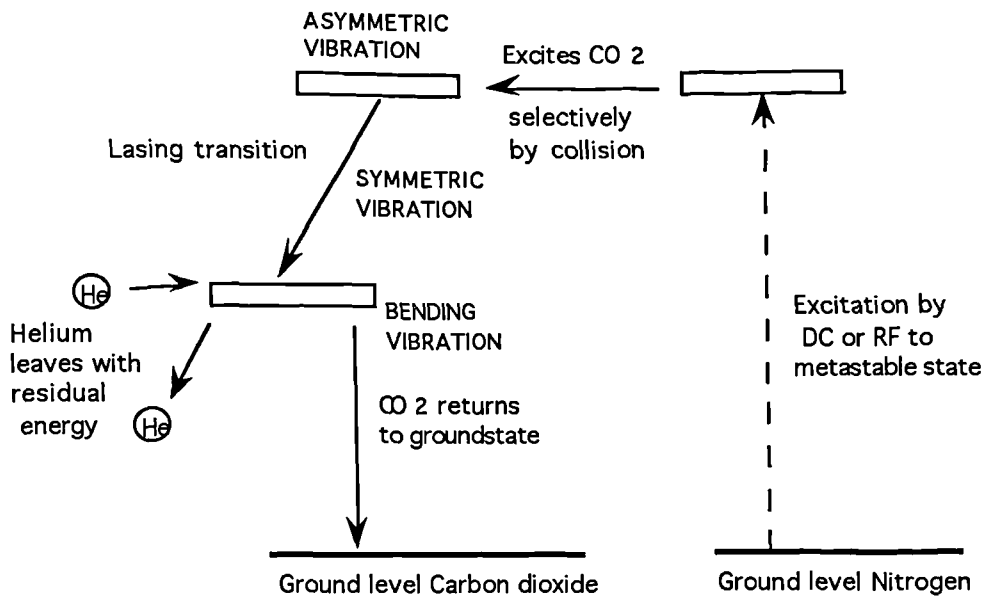


Figure 1.2a Intermolecular mechanism of lasing action b Schematic operational layout of a Fast Axial Flow Laser, arrows indicating direction of gas flow.

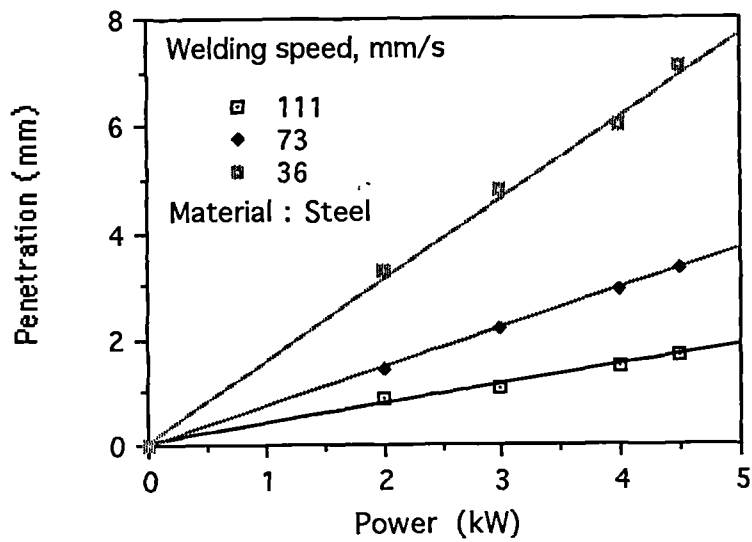
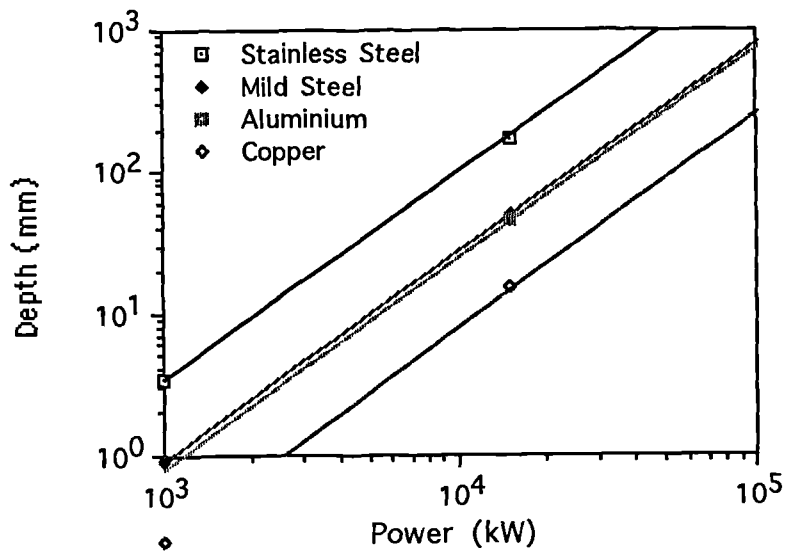


Figure 1.3a Minimum power for efficient welding (Locke *et al* 1972)[6]. 1.3 b Weld bead penetration as a function of laser power at various speeds on mild steel sheet (Baarsden *et al* 1973)[5].

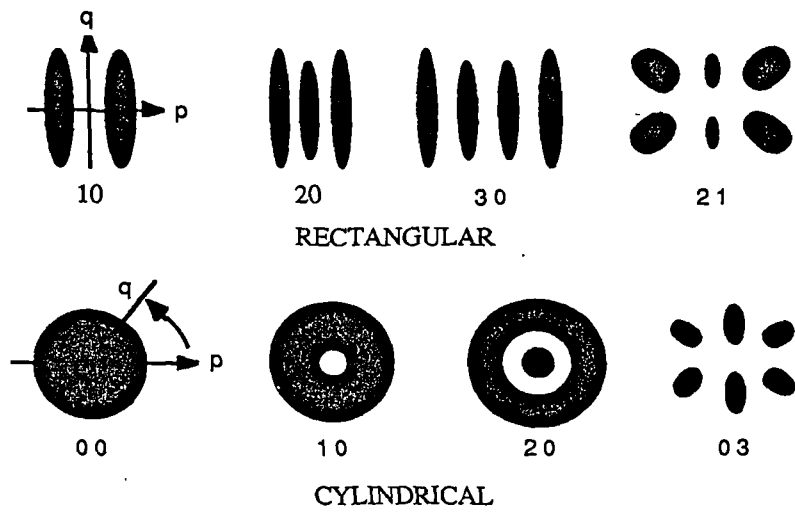


Figure 1.4 Common processing modes represented in Rectangular and Cylindrical Coordinate systems.

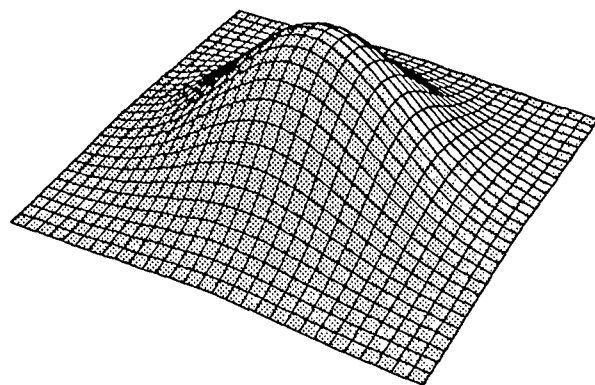


Figure 1.5 The optimal welding mode  $TEM_{00}$  showing the three dimensional intensity distribution.

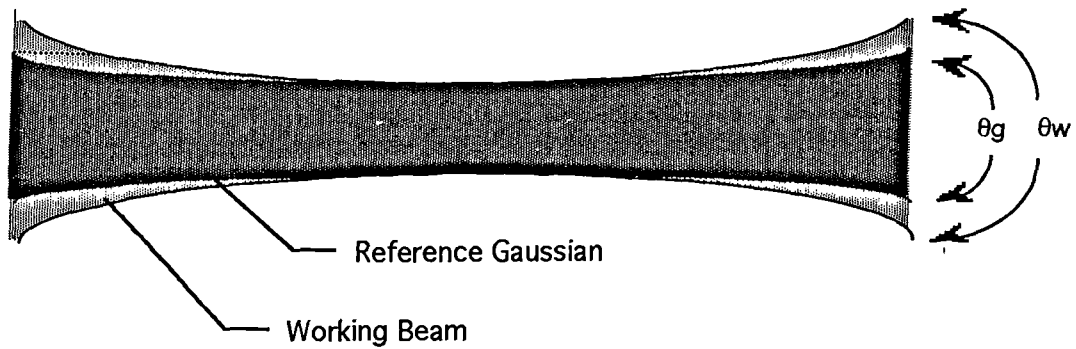


Figure 1.6 Schematic representation of the  $M^2$  factor method of mode superposition.

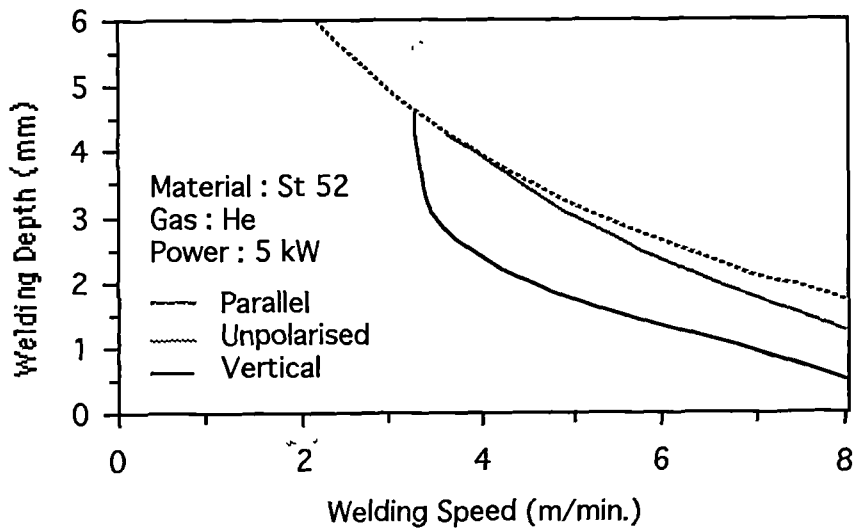


Figure 1.7 The effect of polarisation becomes apparent with increasing speed, as plasma absorption threshold is reached with Fresnel absorption becoming dominant (Beyer 1986)[12].



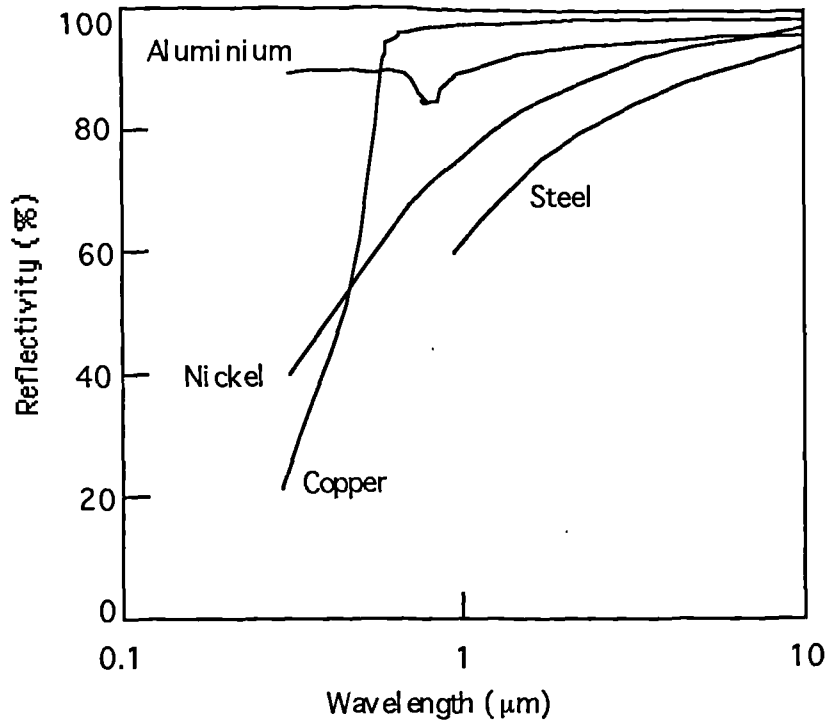


Figure 1.8 The reflectivity of various metals as a function of wavelength.

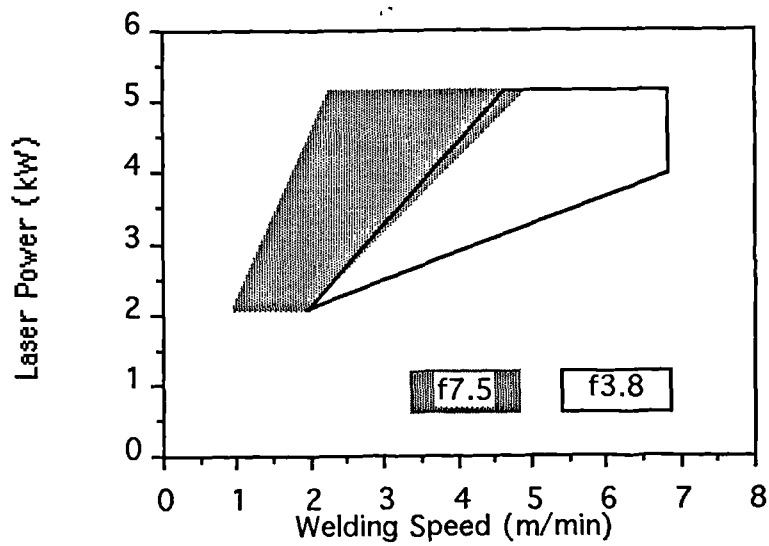
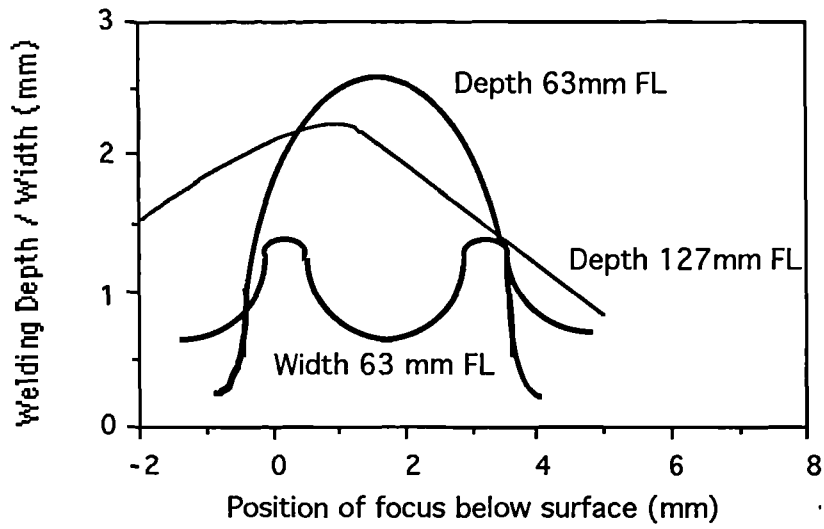
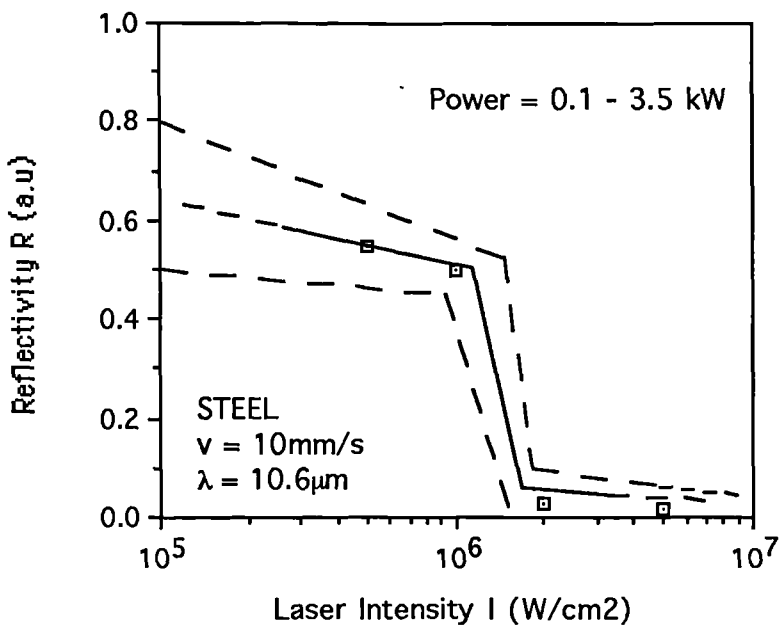


Figure 1.9 Processing window for full penetration of 2mm thick mild steel for different focal lengths (Dawes and Watson 1983)[16].

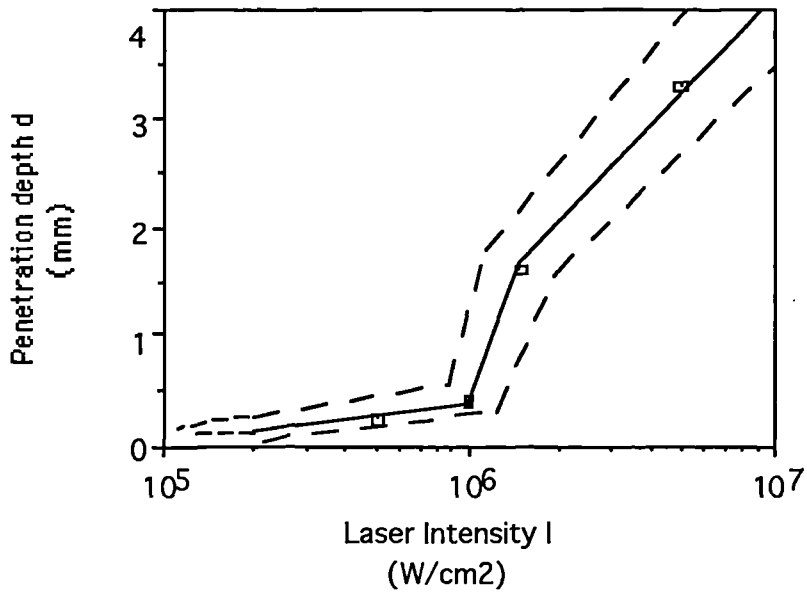


**Figure 1.10** Effect of the position of focus on weld dimensions on mild steel at 22mm/s and 1.5 kW power (Engel 1977)[18].



**(a)**

**1.11 a** Welding depth as a function of intensity (Beyer 1986)[12]



(b)

Figure 1.11b Reflectivity as a function of intensity at different powers.(Beyer 1986)[12].

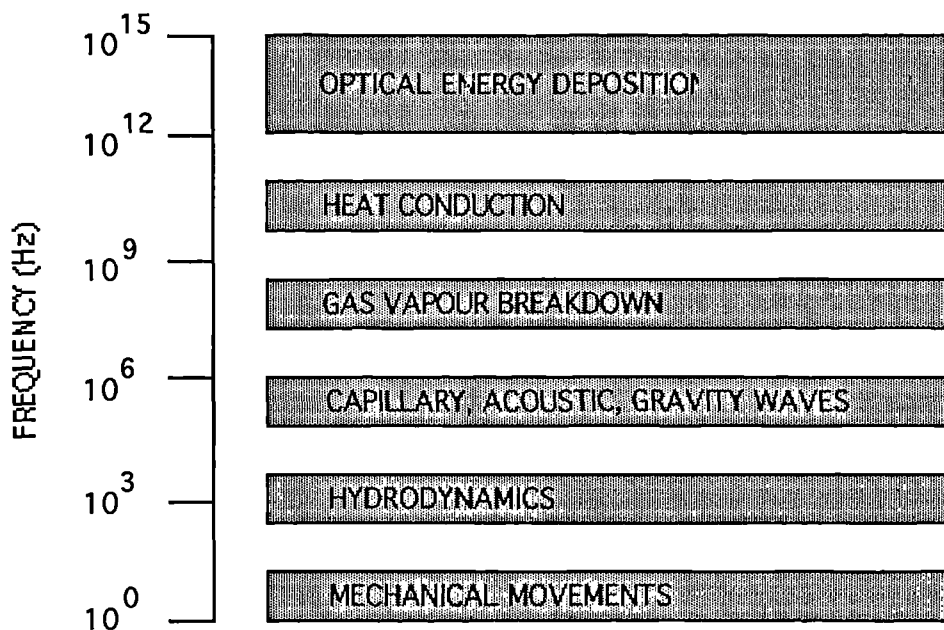


Figure 1.12 Summary of interaction relaxation times involved in the optical energy deposition into the workpiece (Kreutz 1988)[29].

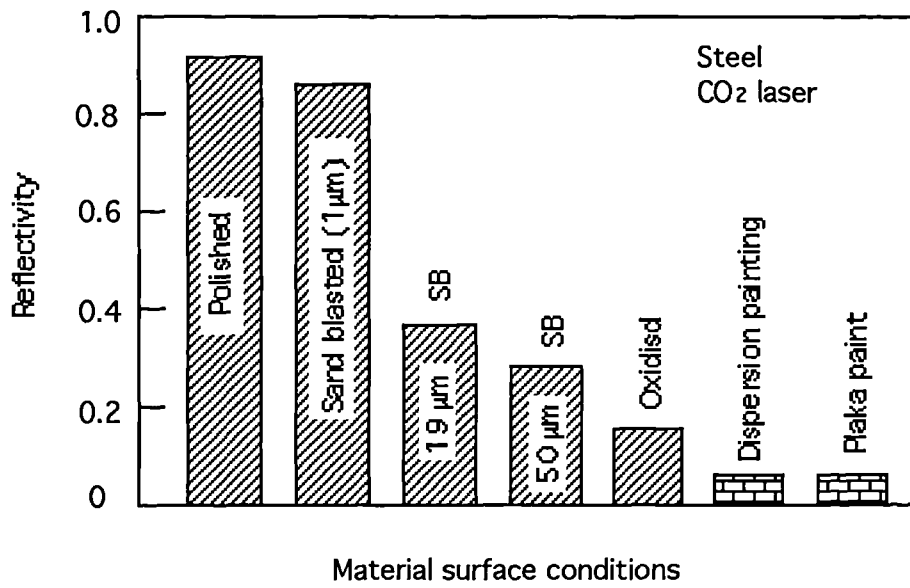


Figure 1.13 The effect of surface finish on the absorption of 10.6 micron laser radiation (Kreutz 1987)[29]

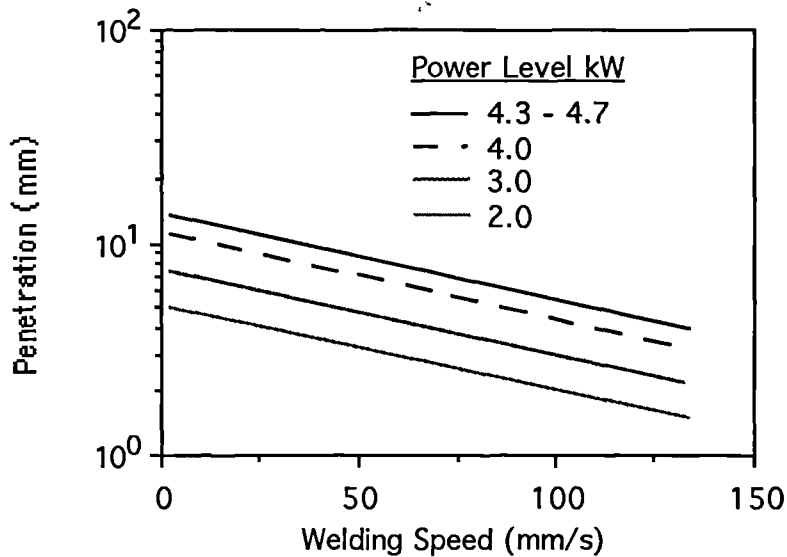


Figure 1.14 Weld bead penetration as a function of welding speed at various power levels (Baarsden *et al* 1973)[5].

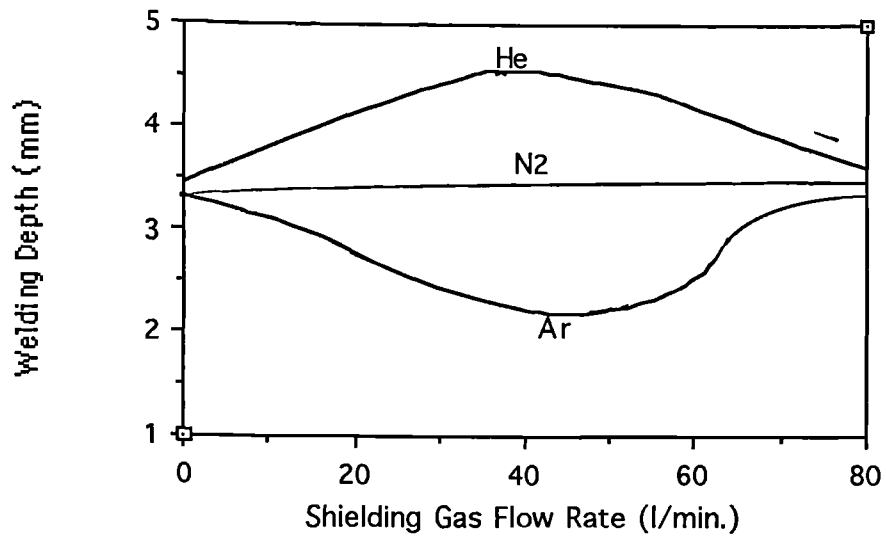


Figure 1.15 Relationship between gas flow and welding depth, showing the critical flow rates for Argon and Helium (Beyer *et al* 1983)[24].

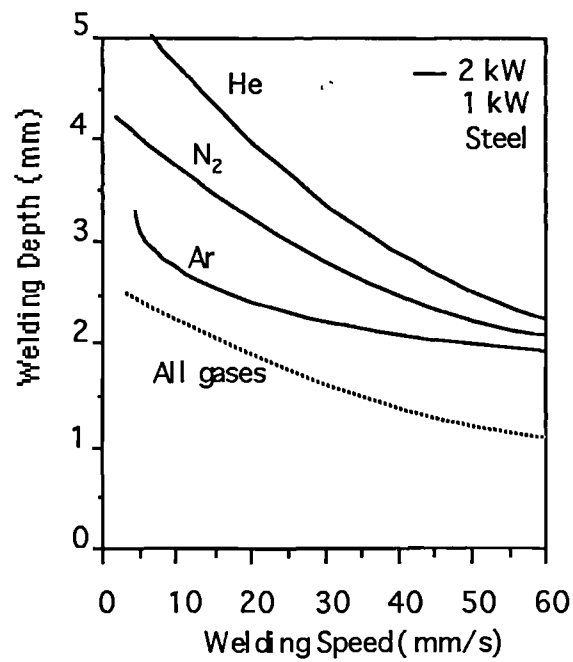


Figure 1.16 Achievable Welding depths of various gas types as a function of power (Beyer *et al* 1983)[24].

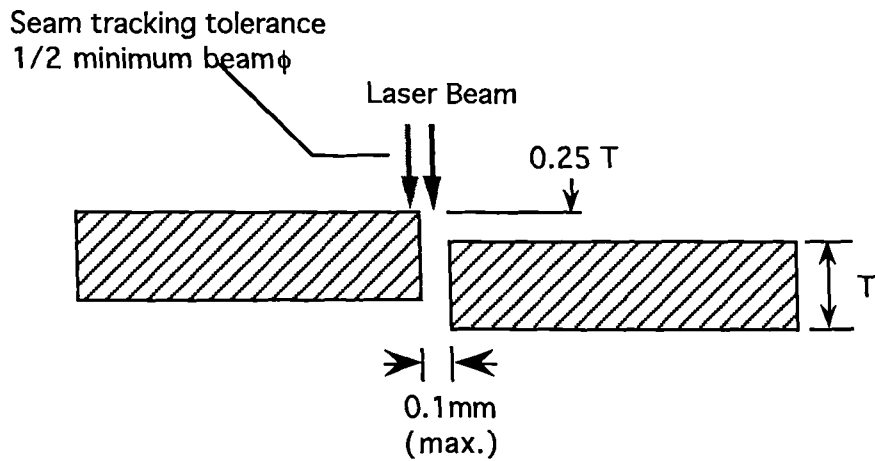


Figure 1.17 Standard fit-up and alignment tolerances for laser butt welding.

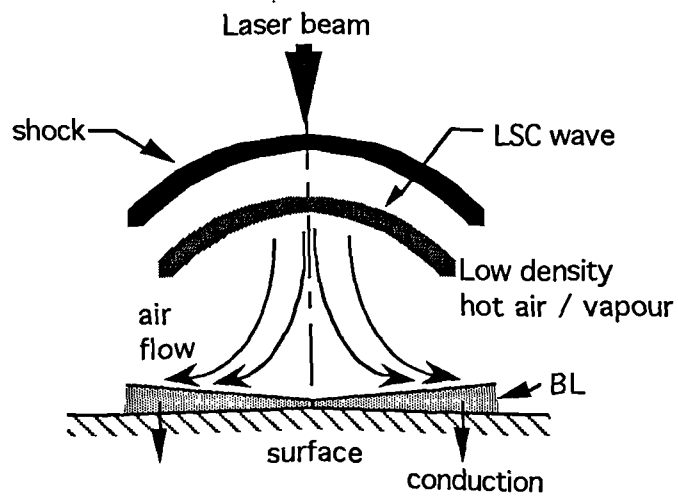
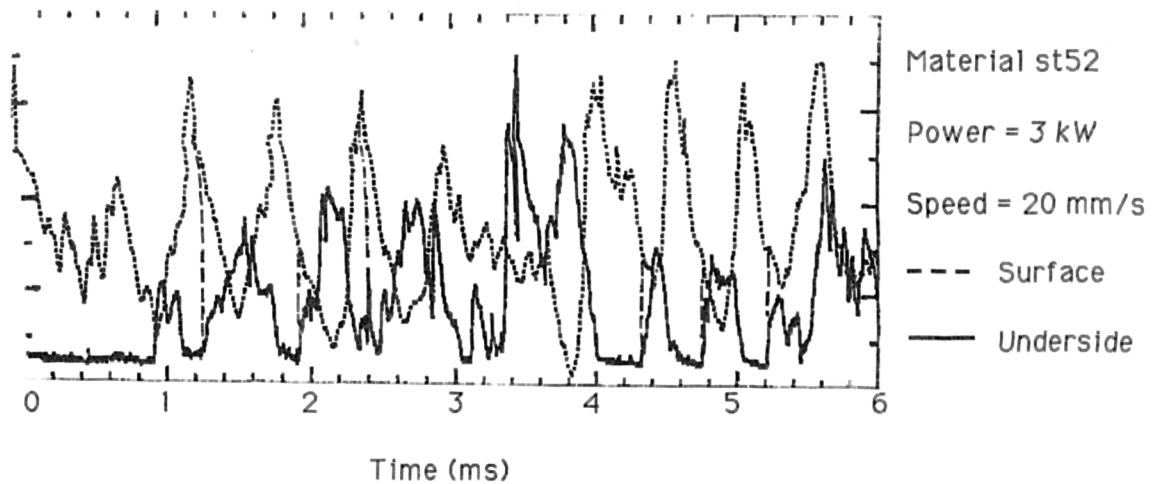


Figure 1.18 Schematic diagram of the generation of a Laser Supported Combustion wave (Pirri et al 1977).



**Figure 1.16** Keyhole shape during the welding of a seam, increasing velocity from left to right. Extreme left  $v = 0$  (Siekmann and Morijn 1968).



**Figure 1.20** Trace showing the variation with time of surface and underside plasma densities, note the period oscillation of both traces almost perfectly out of phase (Gatzweiler *at al* 1989).

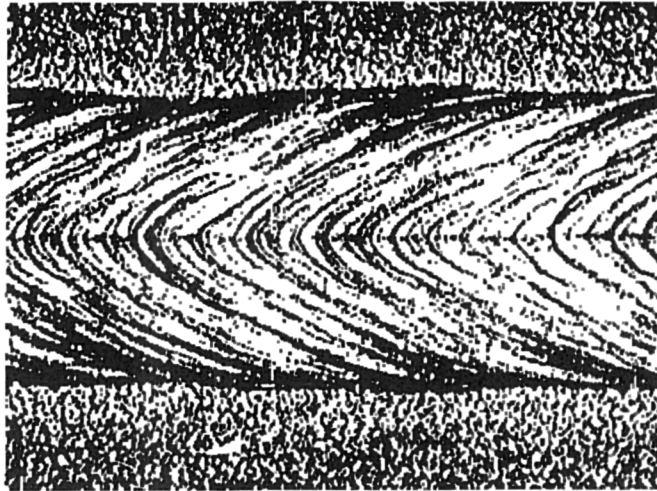


Figure 1.21 Periodical surface roughness also highlighting low frequency width ripple of a welding seam (Beyer *et al* 1987)[34]

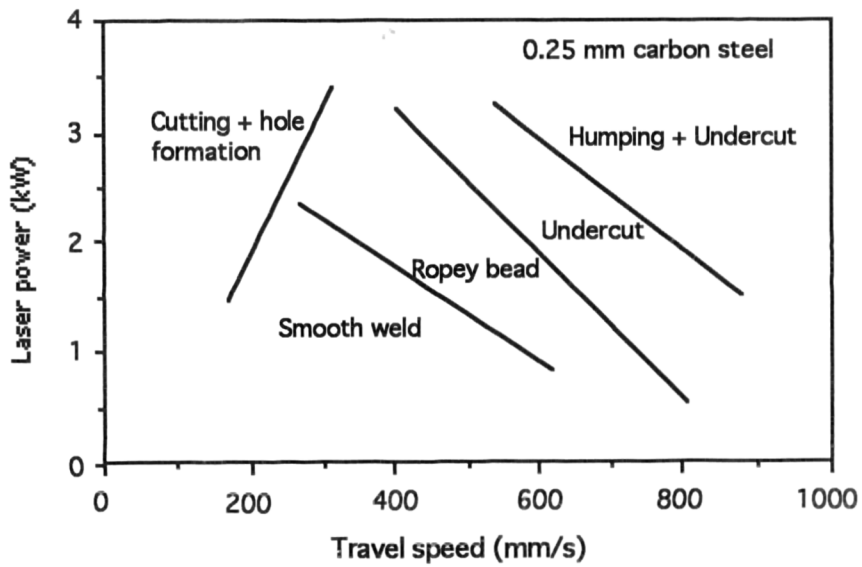
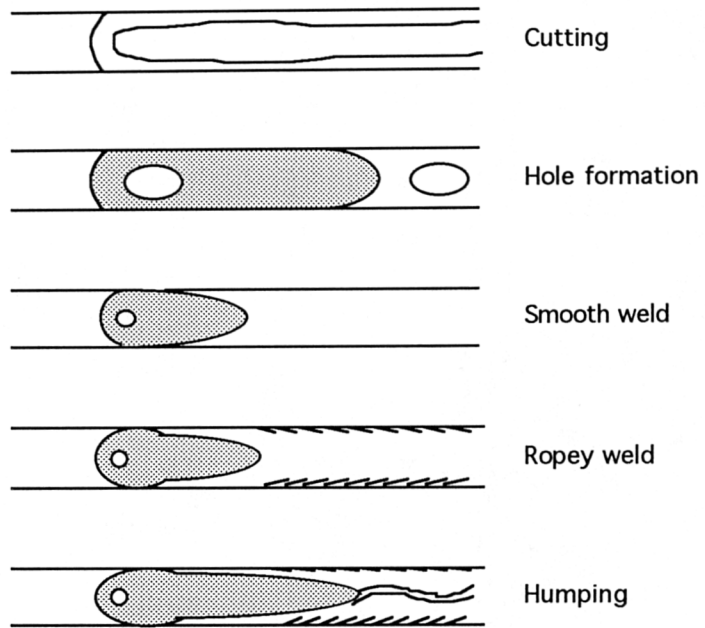


Figure 1.22 Map of weld bead profiles as functions of welding speed and power for 0.25 thick carbon steel. (Albright and Chaing 1990)[45].





**Figure 1.23** Shape of the melt pool as a function of increasing velocity (Albright and Chaing 1990)[45]

## REFERENCES

1. Schawlow, A.L. "Advances in Optical Masers". Scientific America July 1963.
2. Crafer, R.C. and Oakley, P.J. "Design Principles of High Power CO<sub>2</sub> Laser".  
Welding Institute Bulletin Vol. 22 October, 1981.
3. Maisenhalder, F. "High Power CO lasers". Proceedings SPIE Volume 650  
High Power Lasers and their Industrial Applications, 15 - 18 April  
Innsbruck 1986.
4. Wani, F., Naitou, T., Iizuka, M., Tsuji, H. and Fujii, H. "Development of 1 kW  
VW Iodine Laser for Industrial Use". Proceedings of Laser Advanced  
Materials Processing (LAMP), 1992, pp127-132.
5. Baardsen, E.L., Schmatz, D.J. and Bisaro, R.E. "High speed welding of sheet  
steel with a CO<sub>2</sub> laser". Welding Journal April 1973.
6. Locke, V.E., Hoag, E.D. and Hella, R.A. "Deep Penetration Welding with High  
Power Laser". IEEE Journal of Quantum Electronics, QE-8 No.2 1972.
7. Locké, V.E. and Hella, R.A. "Metal Processing with a High Power CO<sub>2</sub> Laser".  
IEEE Journal of Quantum Electronics, QE-10 No. 2 1974.
8. Breck Hitz, C. "Review of Laser Modes - A Lasers Transverse and  
Longitudinal Modes Affect the Output Beam". Laser and Applications  
November 1985.
9. Sharpe, M., Steen, W.M., Henry, P. and Lim, G.M. "An Analysis of the Effect of  
Mode Structure on Laser Material Processing". Laser 83 Opto-elektronik  
Munich 1983.
10. Weichel, H and Pedrotti, L. S. "A Summary of Useful Laser Equations - An  
LIA Report". Electro-Optical Systems Design Volume 8, 22 - 36 July  
1976.
11. Mazumder, J. "Laser welding". Chapter 3 Laser materials processing (Ed)  
M. Bass North-Holland Publishing Co. (USA) 1983. (References therein)
12. Beyer, E., Behler, K and Herziger, G. "Influence of laser beam polarisation  
in Welding". Proc. 5th Int. Conf. Lasers in Manufacturing, September 1986,  
pp233-240.
13. Miyamoto, I., Marou, H and Arata, Y. "Beam Absorption Mechanism in Laser  
Welding". SPIE Vol. 668, 1986.
14. Matsunawa, A and Ohnawa, T. "Beam-Plume Interactions in Laser Materials  
Processing". Trans. of JWRI, Volume 20, No. 1, 1991.
15. Duhamel, R.F. "Laser Welding of X-65 Oil and Gas Transmission Pipe". Proc.  
of International Congress on the Applications of Lasers and Electro-Optics,

- (ICALEO), 1986.
16. Dawes,C.J. and Watson,M.N. "CO<sub>2</sub> Laser Welding of Deep Drawing Steel Sheet and Microalloyed Steel Plates.' Lasers in America Vol 38 ICALEO, 1983, pp73 -79.
  17. Willgoss,R.A., Megaw,J.H.P.C. and Clark,J.N. "Assessing the Laser Power for Plant Welding". Welding and Metal Fabrication, March 1979.
  18. Engel, S, L. Laser Focus February 1976.
  19. Kawai, Y., Aihara, M., Ishii,K., Tabuchi, M. and Sakai, H. "Developement of Laser Welidng for strip Processing Line". Kawasaki Steel Technical Report, No. 10, Dec. 1984, pp39-46.
  20. Kocher, E., Tsuiudi, L., Steffen, J. and Herziger, G. "Dynamics of Laser Processing in Transparent Media". IEEE Quantum Electronics Volume 8, 1972, pp120 - 125.
  21. Herziger, G. "Physics of Laser Material Processing". Proc. of SPIE Volume 650 High power lasers and their indusrial applications, 1986, pp188 - 194.
  22. SwifTHOOK and Gick. Welding Research Supplement, November 1973, p492 - 298s.
  23. Seaman, F. D. "The Role of Shielding Gas in High Power CO<sub>2</sub> Laser Welding". SME Technical Report 1977.
  24. Beyer, E., Herziger, G., Petschke, U., Sokolowski, W. "Influence of Shelding Gas in Laser Beam Welding". Optoelectronics in Engineering, Vol. 6, 1983, pp259-263.
  25. Miyamoto,I.Marou,H. and Arata,Y. "The Role of Assist Gas in CO<sub>2</sub> Laser Welding". Laser in America, ICALEO Vol. 44, 1984, pp68 - 75.
  26. McCay, M. H., McCay, T., Sharpe, M., Dahotre, N. "Gas Assisted Heat Transfer Effects in Laser Welding Iconel 718". Published in Joining Sciences, 1992.
  27. Sutliff, D. R., McCay, T. D., McCay, M. H and Sharp, M. C. "A LASer Welding Nozzle for Beam Delivery Optics Protection". Welding Journal, June 1992, pp219-224s.
  28. Rossler,D.M. "An Introduction to the Laser Processing of Materials". Industrial Laser Handbook, edited by D. Belforte and M. Levitt, Tulsa, 1986.
  29. Megaw, J. H. P. C, Hill, M., Johnson. 'Laser Welding of Steel plates with Unmachined Edges". Proc. Inst. Met. Conf. Joining of Metals - practice and performance 1981.
  30. Kreutz,E.W. "Physical Requirements for Lasers in Processing.' Proc. 4<sup>th</sup>

- Int. Conf. Lasers in Manufacturing, 1987, pp263 - 278. ( References therein )
31. Dixon, R. D. and Lewis, G. K. "The Influence of a Plasma during Laser Welding". Laser Institute of America, ICALEO Volume 38, 1987, pp44 - 49.
  32. Kapadia, P., Ducharme, R. Dowden, J. "An integrated Mathematical Model of the Keyhole and weldpool in the Laser Welding of Thin Metals Sheets". Proc. of ICALEO, Orlando, 1992.
  33. Ducharme, R, Kapadia,P and Dowden, J. "A Mathematical Model of the Defocusing of Laser Light Above a Workpiece in Laser Materials Processing". Proc. of ICALEO, 1992, pp187-197.
  34. Dixon, R. D. and Lewis, G. K. "Affect of Angle of Incidence on Plasmas Generated during Laser Welding". Proc. of ICALEO, Volume 44, 1983, pp28 - 34.
  35. Beyer, E.,Donges, P.,Loosen, P. and Herziger, G. "Optical Feedback during Laser Material Processing". Optoelectronics in Engineering (Proc. of the 6<sup>th</sup> Int. Congress - LASER 83), Germany, 1983, Publ. Springer-Verlag, pp259-253.
  36. Siekmann,J.G and Morijn,R.E. "The Mechanism of Welding with a Sealed off Continous CO<sub>2</sub> Gas Laser.' Philips Research Reports, 23 p367 1968.
  37. Arata, Y. and Miyamoto, I. "Laser welding". Technocrate, Volume 11, No. 5, 1978, p33.
  38. Heiple, C. R. and Burgardt, P. "Effects of SO<sub>2</sub> Shielding Gas Additions on GTA Weld Shape". Welding Research Supplement, June 1985, pp159 - 162.
  39. Arata, Y.,Marou, H.,Miyamoto, I. and Ionoe, Y. "Dynamic Beam Hole Behaviour of Laser Welding". IIW DOC IV/222/77.
  40. Gatzweiler, w. Maischner, F. faber, F. J.,Derichs, C., Beyer, E. "Model of Dynamic Behaviour in Laser Beam Welding". Proc. SPIE Volume 1132 High power Lasers and Laser Machining Technology, 1989, pp157 - 164.
  41. Duley, W . W. and Mueller, R . E. "Laser Penetration Welding in low Gravity Environment". Proc. XXII ICHMT Int. Conf. on Manf. and Mat. Proc. August 1990.
  42. Workmann, G. L. and Kaukler, W. F. "Laser Welding in Reduced Gravity". Proc. of ICALEO, 1990, pp430 - 440,.
  43. Foley, J .S. and Banas, C. M. "Laser Welding stability limits". Proc of ICALEO, 1984, pp47-53.
  44. Hawkes, I. C., Lamb,M., Steen,W.M, West,D. R. F. "Surface Topography and Fluid Flow in Laser surface Melting' 3rd Int. Coll. on welding and melting by

electrons and laserbeam Semtember 1983. (references therein)

45. Ishizaki, K. "A New Approach to the Mechanism of Penetration". Proc. Conf. Arc Physics and Weld pool Behaviour, Welding institute 1980.
46. Cline, H. E and Anthony, T. R. "Heat Treating and Melting Material with a Scanning Laser or Electron Beam". Journal of Applied Physics, Vol. 48, No.9, 1977, pp3895-3900.
47. Albright, C. E and Chaing, S. "High Speed Laser Welding Discontinuities". Journal of Laser Applications Fall 1988.
48. Gratzke, U., Kroos, J. and Simon, J. "Humping Effect in Welding". Verlandl. DPG (VI), 27 (Frujahrstagung Hannover 1992), K 6.4, Weinheim, Springer-Verlag, 1992.
49. Bradstreet, B. J. Welding journal Research Supplement, 1968, p314.
50. Steen, W. M. "Laser Materials Processing". Published Springer-Verlag, 1991.
51. Akhter, R. "Laser Welding of Zinc Coated Steel". PhD Thesis, London University, 1990.

## CHAPTER TWO

### EXPERIMENTAL DESIGN, METHOD AND ANALYSIS

#### 2.1 EXPERIMENTAL STRATEGY

Project objectives -

- a) **Overall identification of Welding parameters** - Previous work carried out by Van Leer dealing with laser welding was limited therefore initial experimentation aimed to gain a fundamental understanding of the laser welding process of Van Leer 20 gauge drum grade steel, incorporating all relevant parameters to obtain a full and unique process window.
  
- b) **Basic study of weld pool dynamics related to welding performance** - Gaining an understanding of the dynamic welding situation with respect to keyhole and melt pool stability through high speed video equipment and high gating camera particularly in the butt welding of sheared edged interfaces.
  
- c) **Mapping of optimal process region** - Optimisation of the significant welding variables in particular relating to the weld quality - a specific aim of this was to achieve reliable high integrity welds using guillotine sheared interfaces.
  
- d) **Analysis of in-process weld monitoring** - Feasibility study into an in-process weld monitoring system incorporating specific weld fault diagnosis.
  
- e) **Design and develop a pre - production welding jig** - Produce a semi-automated laboratory scaled welding setup.

## **2.2 EXPERIMENTAL DESIGN**

A literature survey revealed nine welding parameters for the processing of 1 mm thick mild steel, listed in detail below and shown in figure 2.1.

### **The nine variables**

MODE : Power distribution within the beam.

SIDE ANGLE : Angle of incidence perpendicular to the weld direction.

FOCUS : Position of the minimum spot size relative to the workpiece surface.

SPEED : Velocity of workpiece relative to beam.

POWER : Beam power.

LENS : Focal length of focussing optic.

POLARISATION : Orientation of electromagnetic fields of the radiation relative to the welding direction

NORMAL ANGLE : Angle of incidence parallel to the welding direction maintaining the position of focus.

WELD GEOMETRY : Profile of the edges to be welded.

If one considers the experimental implications with regard to the number of welds that must be performed in order to gain the desired knowledge it represents a problem. A simple change one level of one variable at a time system would require a phenomenal amount of time and money !, so, after consulting with Van Leer R & D Division a statistical programme was believed to be the answer. Stat-Ease™ (Appendix A) was the package utilised in the selection of the statistical method, the specific experimental matrix to be used and analysis of the results.

The initial selection procedure involved a second package, Expert Design™ (Appendix A), which asked a series of 50 questions ranging from what experimental facilities were available to the possibility of interactions occurring between the

phase contained a major investigation into the quality of welds produced from different edge preparations.

During the course of the main programmes a few small satellite experiments were performed namely on method of gas delivery, effect of different gases and gas combinations. The specific procedures are detailed in the results section.

The results required for the in-process weld monitoring system and high speed camera work were accomplished in conjunction with the other programmes.

## **2.3 EXPERIMENTAL ARRANGEMENT**

### **2.3.1 Processing Lasers**

The lasers specifically use were the Laser Ecosse AF5, Electrox M1500 and BOC Control laser. The main experimentation being carried out on the AF5, as this offered 5 kW total power required for high speed welding. A further advantage of this laser is the dual mode capability providing both  $TEM_{00}$  and  $TEM_{01}$  by deformation of the cavity mirrors. The characteristics of the individual lasers are given in Table 4.

### **2.3.2 Beam Delivery System**

The raw beam exiting the laser needs to be delivered to the processing area, this was achieved using 75 mm plane gold plated copper mirrors suitably angled - the beam path being encased within aluminium tubes. The integrity of the mirrors reflective surface must be maintained through regular cleaning along with rear water cooling in order to transport away any absorbed heat that may cause thermal distortion. Thus the beam quality and delivery direction remains constant over the length of the total beam path.

The focusing system incorporated a plano convex KCl lens designed to allow fine adjustments to be made in the vertical plane providing precise control of the



position of focus. The focusing beam then passed through a welding nozzle, together with a coaxial shielding gas to the workpiece. In later experimental trials a metal optics system was designed, consisting of a plane 45 degree mirror in conjunction with a 45 degree off axis parabolic, seen in figure 2.3.

### **2.3.3 Sample Clamping and Movement relative to the Beam**

The pieces to be welded must be secured firmly during the welding process as vibrations caused through the movement or thermal distortion of the samples may result in mis-tracking of the beam from the welding line. The clamping arrangement is shown in figure 2.4, the two clamps were positioned as close as possible to prevent any vertical misalignment of the sheets - the clamps are mounted on springs to allow convenient replacement of samples. To allow the welding nozzle and peripherally mounted equipment to move freely along the weld length the clamps are angled towards the welding area. The square groove underneath the welding area served two purposes; to be of large enough dimensions such that an underside shielding shroud could be fitted and to prevent the focussed beam from buckling the jig. The jig itself was secured to a CNC table by clamps screwed into T pieces. The pre-production jig was utilised in the final trials and is discussed later in Chapter 5.

The traversing of the beam across the workpiece was achieved using a CNC workstation, the X-Y table being driven by DC servo motors linked to screw threads giving smooth movement of the workpiece upto 300 mm/s.

### **2.3.4 Shielding Gas Delivery**

Gas delivery relates to the method and type of gas used. During the experimentation the gas was delivered to the welding area on the workpiece both coaxially, by 45 degree jet and by a combination of these. In addition an underside shielding shroud of

7 l/min was provided. The standardised factors of importance are the gas flow rate, gas outlet diameter and the distance of the gas outlet from the weld pool. The values of these were 15 l/min., 3 mm and 2 mm (vertical and horizontal) respectively.

Helium, argon, carbon dioxide, nitrogen and combinations of these were investigated as shielding gases, with one experiment involving the effect of adding oxygen to the main processing gas.

### **2.3.5 Establishing the focal position**

This is vital to the welding operation and there are several methods employed, earlier experimentation used the “blue flash” test - in which argon gas is flooded into the welding area, when the focus is reached a characteristic blue plasma is produced, as the flash technique occurred over the depth of focus, the method later adopted was the use of angled perspex sweeps across the welding nozzle clearly showing the point of minimum spot size. Once the distance from the top of the perspex to the focus is measured and related to a datum, the position of focus is accurately known whilst information regarding depth of focus is also given.

### **2.3.6 Alignment of the processing beam**

The alignment of the invisible CO<sub>2</sub> laser beam through the delivery and focusing optics is possible with the use of a visible HeNe beam mounted on the laser close to the output window. In order for the HeNe beam to accurately represent the position of the processing beam it must be aligned such that it is central and coaxial with the main beam. The main beam must propagate centrally along the delivery and focussing optics, welding nozzle and then to the weld area. This is straight forward task once the processing laser is aligned with the visible HeNe laser, any adjustments to the set up were made relative to the position of the visible beam. The HeNe was removed from the main beam path on firing as the mirror reflecting it

down the beam path was located on the rear of the shutter.

### **2.3.7 Mode selection, tuning and quality**

The requirements of the experimental programme necessitated using two different processing modes, TEM<sub>00</sub> and TEM<sub>01</sub>, interchanging between these and maintaining a quality beam structure was achieved through adjustments in the mirrors located within the laser cavity. The Laser Ecosse AF5 was altered from one mode to another by deformation of the cavity mirrors changing the radius of curvature from 50 m to 60 m, Gaussian being the former. Once the type of mode had been selected fine tuning of the mirrors was needed to optimise cavity alignment for that particular arrangement, this involved micrometer adjustments of the output window and occasionally the rear mirror to produce the highest quality mode shape. Monitoring of the mode shape is achieved with a Laser Beam Analyser which provides a direct measure of the mode shape in both x and y planes, adjustments being made according to these orthogonal mode profiles.

The quality is measured as defined by the M<sup>2</sup> factor (Section 1.2.3), the working beams divergence is assessed by measuring the beam size at two points along the path -

$$\theta_w = D_2^2 - D_1^2 / Z_2^2 - Z_1^2 \quad (2.1)$$

where D = beam diameter, 1/e<sup>2</sup> (m).

Z = distance from centre of resonator (m).

A more accurate value is gained if the distance between the two points is a maximum. The Gaussian divergence is given as -

$$\theta_g = 2\lambda / \pi w_0 \quad (2.2)$$

where  $\lambda$  = wavelength of laser radiation (m).

$w_0$  = minimum beam waist in the resonator (m).

### **2.3.8 High speed video set-up**

The The Kodak Ektapro 1000 high speed video was utilised through out experimentation, the general set-up is shown in figure 2.5. The Ektapro system is capable of 1000 frames per second, providing analysis of the pictures using frame stepping function, cross hair graticules (resolution to a pixel) and control of the contrast and brightness of the recorded images. Hard copies of frames can be obtained and the high speed video can be transfered to normal VHS format video. The specific set-ups are described when they arise.

### **2.3.9 Weld monitoring set-up**

The arrangement of the weld monitors was integrated into the existing clamping jig, as shown in figure 2.6. In the dual wavelength optical sensor set-up the Ultra-violet and Infra-red sensors receive the weld spectral emission through a fibre-optic, the signal is amplified and relayed to a *Philips PM322 digital oscilloscope*. The acoustic nozzle comprises of a piezoelectric transducer attached to a metal sheet using vacuum grease to ensure a good acoustic contact. The metal sheet has plastic sheet covering the metal from heating effects due to the welding, which would interfere with the signal. The signal is relayed, via a pre-amplifier, to the digital oscilloscope and a Marconi spectrum analyser. The plasma charge monitor consists of an electrically isolated welding nozzle. The potential difference between the nozzle and the workpiece (earth) is recorded on the digital oscilloscope, for ease of analysis a smoothing circuit is used.

## **2.4 EVALUATION and TESTING**

### **2.4.1 Metallurgy**

The metallurgical aspect of the analysis was confined to an inspection of the cross-sectional and longitudinal weld profiles, with the majority of butt welds and selected bead on plate welds being sectioned . The specimens were cut using a special metal cut-off machine as opposed to a guillotine which distorts the crystal solidification structure. The samples were mounted in conductive bakerlite by a mounting press machine, therefore allowing any of the samples to be inspected by the Scanning Electron Microscope. Each of the specimens were ground on emery paper graded from 120 to 1200 in four graduated stages then systematically polished on the 6 and 1 micron diamond polishing wheels. To begin with this whole operation was completed manually however later a Struers Prepmatic automatic polisher was used which could produce high quality polished samples from the untouched mounted sample.

The polished specimens were etched in 2% Nital solution in order to examine the fusion zone, heat affected zone and the base metal

### **2.4.2 Optical Microscopy**

The Canon projection microscope was used to observe the detail of the parent metal, HAZ and fusion zone crystal structures. The cross-section, longitudinal section and surface topology of the welds were studied. Photographs of these various sections were taken, all weld dimensions were taken from the projection microscope using a graticule.

### **2.4.3 Joining Efficiency**

The joining efficiency is a simple form of beam/workpiece coupling efficiency which

shows how much of the laser energy has been solely used in the joining process. This quantity is directly related to the penetration of the weld, giving a better measure of true welding efficiency than the melting efficiency. Defined as

$$N_j = Vd / P \quad (2.3)$$

Where  $V$  = welding speed (m/s).

$d$  = penetration depth (m).

$P$  = laser power at the workpiece (kW).

The joining efficiency was calculated for each specimen.

#### 2.4.4 Melting Efficiency

The Melting efficiency is defined as the ratio of melted material to the energy input into the workpiece -

$$\eta = \frac{\rho VA (C_p T_m + L_m)}{P} .100 \quad (2.4)$$

Where  $P$  = laser power delivered to the workpiece (kW)

$\eta$  = melting efficiency

$\rho$  = material density (kg/m<sup>3</sup>)

$C_p$  = specific heat capacity (kJ/kg °C)

$T_m$  = material melting temperature (°K)

$L_m$  = latent heat of melting (kJ/kg)

$A$  = cross-section of fusion zone (m<sup>2</sup>)

The value was calculated for each weld. This provides a more overall picture of the laser-material interaction efficiency.

#### **2.4.5 Specific Energy**

This is a commonly used term in welding for data correlation, it is related to the energy deposited per unit area of the workpiece.

$$\text{Specific Energy} = P / DV \quad (2.5)$$

Where  $D$  = diameter of beam on the workpiece (m).

Relating equation 2.5 with 2.4 assuming the fusion zone to be cylindrical and of similar dimensions as the beam diameter -

$$\text{Specific Energy} = \frac{P}{DV} = \frac{\rho d (C_p T_m + L_m)}{\eta} \quad (2.6)$$

When  $P$  and  $D$  are also constant then -

$$1 / V \propto d \quad (2.7)$$

where  $d$  = the penetration depth (m).

#### **2.4.6 Measurement of the Fusion Zone Area**

This was measured from developed photographs of the welds taken using the projection microscope, the area being divided into appropriate shapes to enable an accurate measurement. The dimensions of these shapes were established using a rule and scaled to graticule photographed and developed under the same conditions as the profile.

#### **2.4.7 Tensile Testing**

Some specimens were selected to compare the tensile strength of the parent metal to

the weld metal. The testing was carried out in Van Leers Research and Development centre in The Netherlands.

An Instron TT machine was used which provided information on the yield strength, percentage elongation and the ultimate tensile strength of failed pieces.

#### **2.4.8 Erichsen Test**

The Erichsen test or cup test is a relatively unknown weld evaluation technique which involves the sample being rigidly clamped while a ball is forced onto the weld eventually resulting in failure. The position of the failure together with the displacement of the ball required to induce failure indicate the integrity of the weld. This test again was performed at Van Leer's R & D centre in The Netherlands.

#### **2.4.9 Weld Quality**

Defining the quality of a specific weld is a difficult and subjective process, there are several associated standards which provide criteria to assess the weld quality or alternatively a measure of acceptability eg; BS, ASME, ISO and proposed CEN standards. More removed from this is defining the quality of the welding operation which, to a large degree, would control the actual weld quality. The standard currently used for the electrical resistance welds for Van Leer are the DIN 50120 Part 1 for tensile tests and DIN 50101 for the Erichsen tests. Also, in this instance the BS4515:1984 standard applying to the fusion welding process is used for the porosity and inclusion levels.

#### **2.4.10 Microhardness Measurement**

The Lietz microhardness tester was used to investigate the hardness of the fusion zone, heat affected zone and the base metal. All butt welds were tested with the



variation of the hardness across and longitudinal to the direction of welding also measured. In order to produce an adequate sized impression of the diamond tip a load of 200 g was required.

#### **2.4.11 Corrosion Testing**

The testing of the corrosive properties of the weld metal against the base metal involved the long term exposure of the samples to atmospheric conditions. The samples were simply placed in an undisturbed position in the laboratory, the test ran for two years.

Experimental design	Desirability (%)	
	Exp. 1	Exp. 2
<b>Full Factorial</b>	<b>93</b>	<b>87</b>
Taguchi	86	82
<b>Fractional Factorial</b>	<b>87</b>	<b>78</b>
Randomised Block	84	71
Completely Randomised	82	83
Paired Comparisons	77	38
Simple Mixture	75	80
Comparison of Means	71	56
Variable-Size Simplex	55	73
Plackett-Burman	54	22
Saturated Fractional Factorial	53	24
Fixed-Size Simplex	53	73
Calibration	53	31
Central Composite	42	45
Box-Behnken	41	40
"Latin Square"	1	45
Hierarchical	0	0

**Table 1** Desirability list for the possible experimental designs, the designs in bold indicate those considered and the designs shaded indicate those selected.

Treatments	Assign	Values
Incident Beam Power (kW)	E	1.5, (2.5), 3.5
Focal Length (mm)	F	100, (125), 150
Traverse Speed (mm/s)	D	40, (100), 140
Focal Position	C	+1.0, (0), -1.0
Weld Geometry	-	Bead on plate, Milled
Mode Structure	A	TEM00, TEM01
Side Angle (Degrees)	B	0, (5), 10
Normal Angle (Degrees)	H	0, (5), 10
Polarisation	G	Circular, Linear

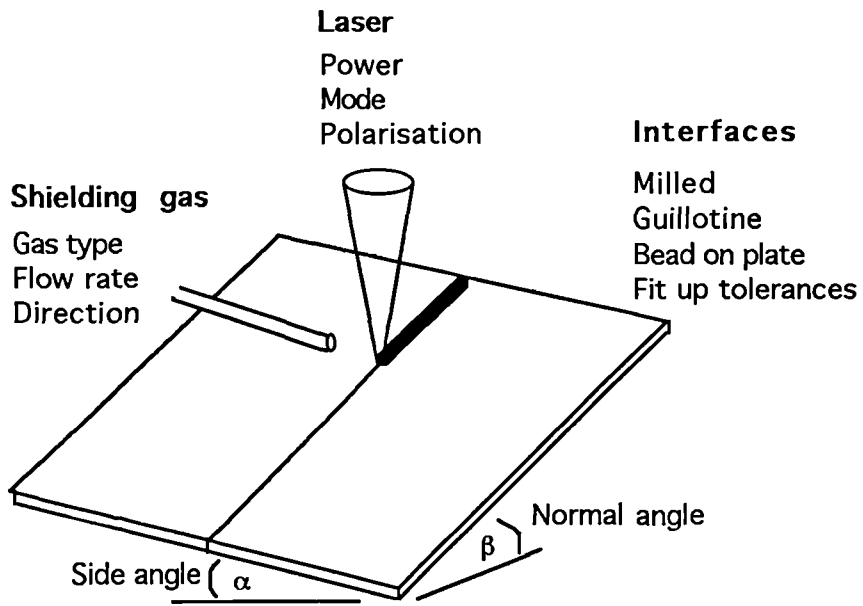
**Table 2** The identified parameters with experimental values, and assigned design matrix position.

	Parameter Levels	
Parameters	Milled edges	Guillotine edges
Normal Angle (degrees)	0, 10, 15, 20, 25	0
Side Angle (degrees)	0	0,10, 15, 20, 25, 30
Interface Side Angle (degrees)	0, 10, 20	0
Focal position	At the workpiece, 1mm above	
Speed (mm/s)	140, 170, 200, 230, 260	
Beam Offset (mm)	0	0, 0.2
Total Experiments	150	120

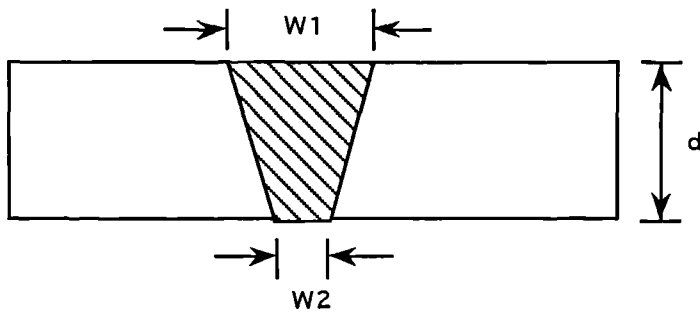
**Table 3** Parameter levels for the second part of experimentation

Parameter	Laser Ecosse AF5	Electrox M1500	BOC Control laser
Mode	TEM00, TEM01	TEM00	TEM01*
Polarisation	Linear	Circular	Unpolarised
Maximum Power (kW)	3.5 and 5	1.5	2
Beam Divergence (mrads)	3	2	2
Raw Beam Size (mm)	20	18	25

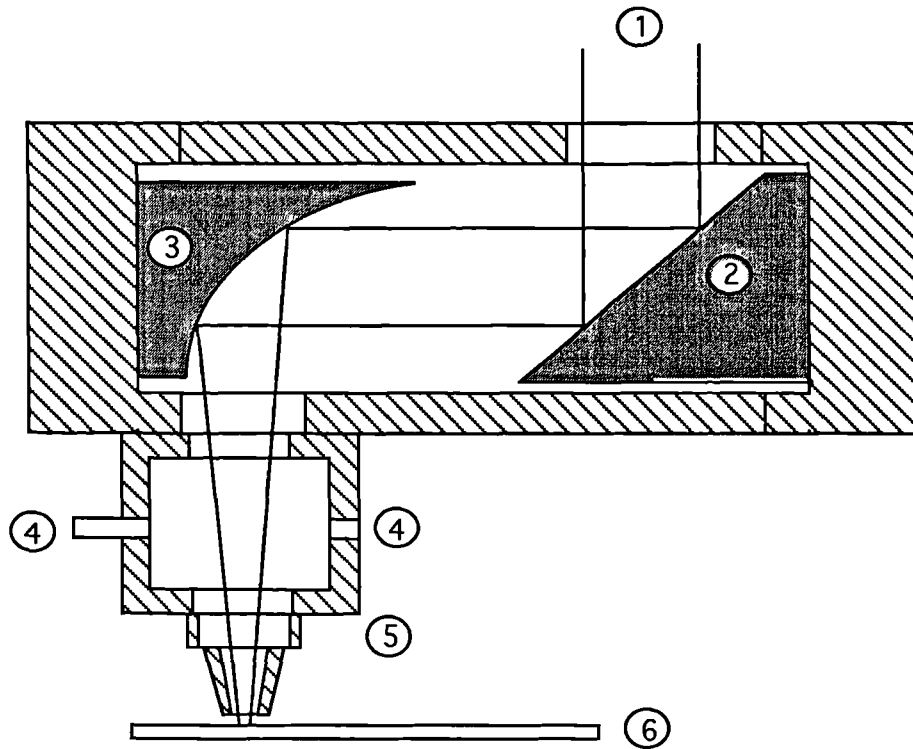
Table 4 Summary of beam characteristics for the three laser used in processing



**Figure 2.1** Schematic representation of the independent welding variables



**Figure 2.2** The weld dimensions chosen as a main response to the experimentation.



Item	Description
1	Incident laser beam
2	45' Plane mirror
3	45' Parabolic mirror
4	Gas inlet/outlet
5	Nozzle assemble
6	Workpiece

Figure 2.3 Schematic arrangement of the metal optics system.

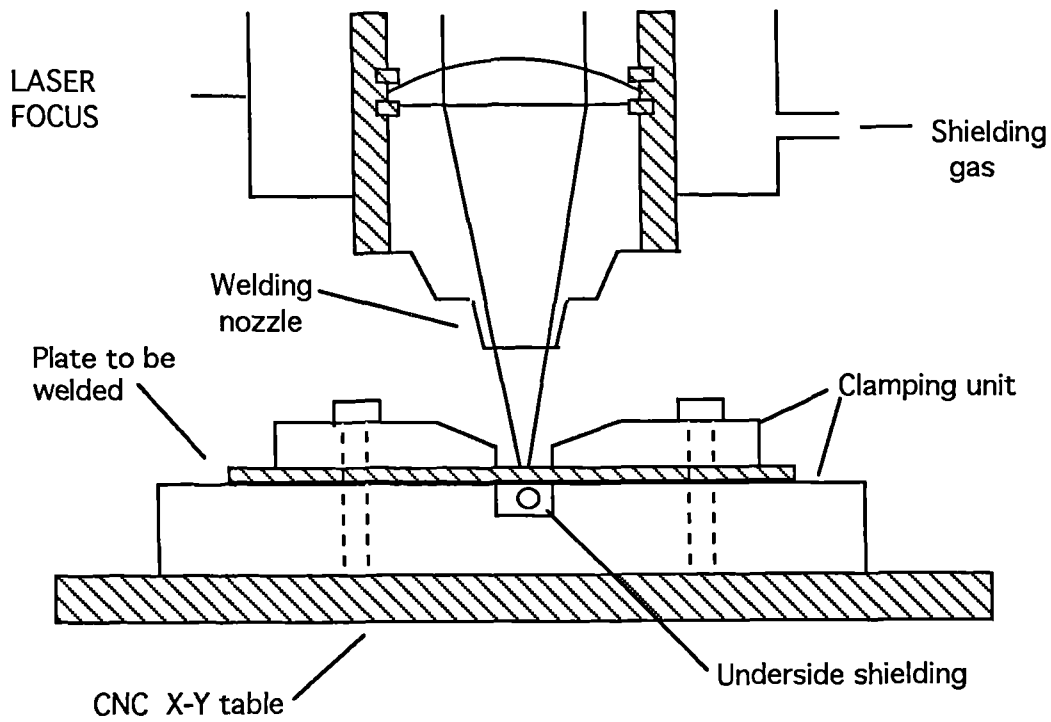


Figure 2.4 Experimental set up used in the initial and secondary programmes.

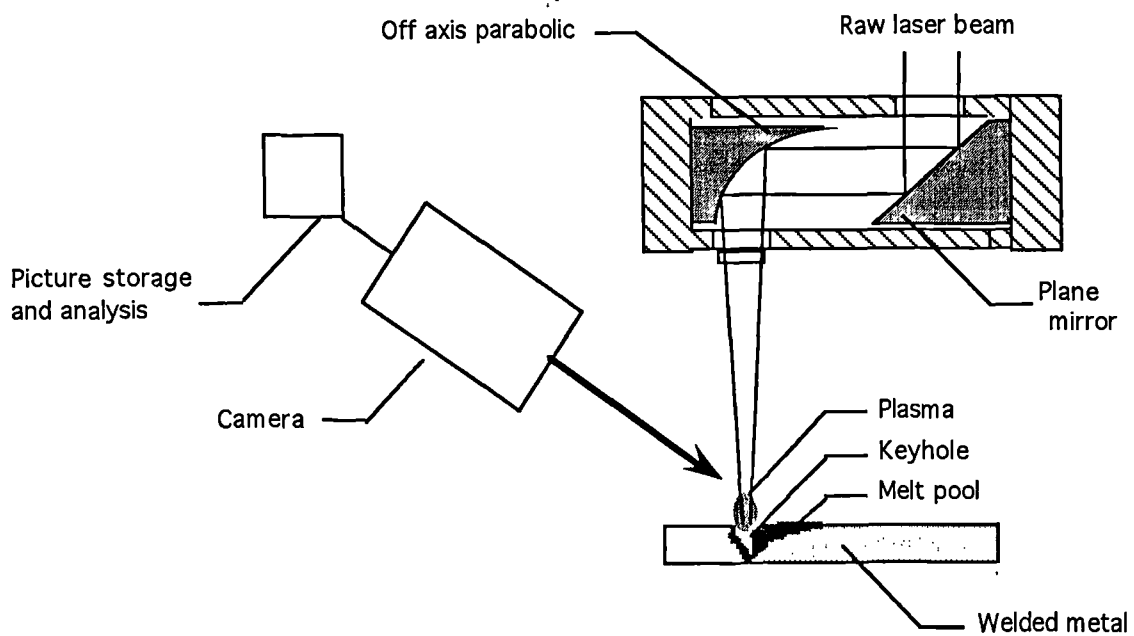
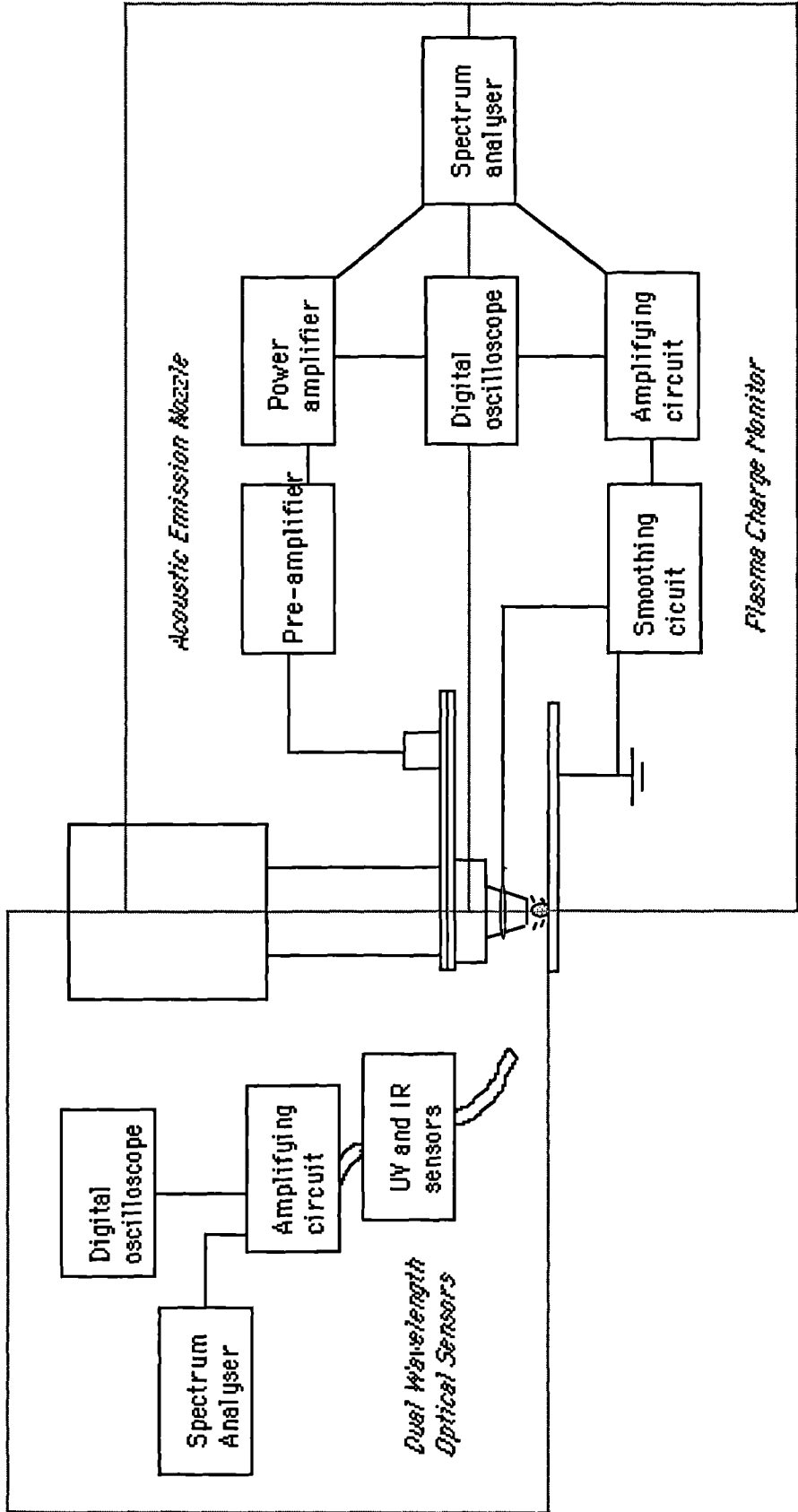


Figure 2.5 Experimental setup for the high speed camera trials.





**Figure 2.6** Schematic arrangement of the sensing systems

## CHAPTER THREE

### PROCESSING - RESULTS AND DISCUSSION

#### 3.1 INTRODUCTION

The Stat-Ease™ statistical package which aided the choice and design of the experimental programmes also has the facility to analyse the results, assessing the effect of a particular parameter to a measured or calculated response and providing information on any interactions between the variables. In weighting each parameter with significance for a particular response a ranking system is provided, however one must be careful in placing any emphasis on this list as the ranges of the individual variables will not be equivalent. This list comprises of “main effects” [1] which show the effect of a single variable on a response, and, interactions which as the name suggests shows the effect of a number of grouped variables.

Basically all the computations within the package revolve around the use of Analysis of Variance (ANOVA) [2] and multiple regression, details of which are given in Appendix B. The interpretation of the graphical information in the first part of the results section is simply related to the gradient of fitted line; increasing gradient means an increasing level of significance, shown in figure 3.1. It should be pointed out that numerical relationships between variable and response cannot be made from the graphical data, as the line only indicates a level of significance not absolute values. The criteria underlying the decision if this level of significance is decided from the use the ANOVA calculation technique. The presence of interactions is assessed by plotting the data on a single graph, again shown in figure 3.1, a significant interaction is represented by a crossing of the lines.

Subsequent experimental results associated with the optimisation of parameters were examined under the criteria used in conventional laser welding.

## **3.2 RESULTS and DISCUSSION - PART 1**

### **3.2.1 Identification of Statistically Significant Welding Variables**

All graphical information regarding the significance of each individual parameter to the various responses are found from figures 3.2 to 3.4. To expand somewhat on the method employed through the ANOVA analysis [1], the level of significance, or, more precisely the significant probabilities [2] represent the probability of an F distribution exceeding the value of the calculated statistic, when the null hypothesis of a non-significant effect is true. Which basically means if the parameter is important when considering a certain response the significant probability (SP) of such an event occurring is low ( $< 0.05$ ) indicating it is unlikely to have occurred by chance and hence is most probably a definite effect. The magnitude of a specified response at the high/low levels of a parameter is averaged over the whole experimental matrix and is independent of any other parameter level. Furthermore the values on the graphs, say between power and lens, cannot be said to have been achieved at, for example 40 or 140 mm/s, as the values would have been used from both speeds. If speed was a factor between the power and lens the set up of the experimental matrix and associated statistical analysis would have highlighted it.

This is the same for main effects and interactions alike, which are described below, for a more precise evaluation all relevant significant probabilities are detailed in Table 1.

#### ***3.2.1.1 Speed and Power***

These two parameters describe the energy input per unit length of the weld and hence are grouped together in this section. The statistical analysis shows them to be significant in affecting the weld dimensions (S.P = 0.001) and to a lesser extent the weld mechanical properties.

This is as expected, from the work of others such as Baarsden (1978)[4],

Locke and Hella (1977)[5] and Watson and Dawes (1983)[6]. Their findings show that the weld dimensions were inversely proportional to the speed but proportional to the power. This is predicted from the theoretical model of Swifhook and Gick (1973)[7] for a moving line source. The relatively fast speeds used in the welding of the sheets would be expected to conform to the high speed solution ( $v > 1 \text{ cm/s}$ ) -  $Y = 0.483X$ , more fully described as

$$P\eta = 0.483vwt (\rho C_p T_m) \quad (3.1)$$

where  $P$  = power at the workpiece (kW)

$\eta$  = coupling efficiency (absorptivity)

$v$  = welding speed (cm/s)

$w$  = average weld width (cm)

$t$  = thickness/depth of penetration (cm)

$\rho$  = density (kg/cm<sup>3</sup>)

$C_p$  = specific heat capacity (KJ/kg °C)

$T_m$  = melting point (°C)

and for the application of this model to the welding of mild steel is simplified to -

$$P / d = 14.9 vw \quad (3.2)$$

From this model, which accommodates latent heat affects in the  $\eta$  term, the observed effects of speed and power are available. In fact a theoretical plot using this relationship is shown on figure 3.5. In this case it is most relevant to plot weld width against speed, and the averaged experimental results although slightly smaller follow the shape of the calculated values. If the constant in equation (3.2) is adjusted to 30 rather than 14.9 there is an almost perfect match, this corresponds to an average experimental coupling efficiency of 50 %. A value recently confirmed by Mannik and Brown (1990)[8] and Kim *et al* (1990)[9]. This coupling efficiency figure is to be used as a baseline to compare significant parameters.

A simple relationship describing the maximum achievable penetration depth for a given speed and power is forwarded by Westinghouse (1985 & 1988)[10], and confirmed by the results presented here is  $d_{\max} = 0.75P/v$ . This can be used as a guide, or a general “rule of thumb” for experimental comparisons for sheet welding under 3 mm thick.

The interaction between power and focal length (power/lens) with the penetration response figure 3.2 shows the 150 mm focal length lens is nearly twice as sensitive to variations in the power as the 100 mm focal length. This is described in section 3.2.1.2.

### 3.2.1.2 Focal Length

The principal effect of the focal length variations will be in the focussed spot size and depth of focus. The minimum spot size and focal length being given by the equations -

$$d_{\min} = 2.44f\lambda(M^2) / D \quad (3.3)$$

$$Z \approx 1.48F\lambda \quad (3.4)$$

where  $d_{\min}$  = minimum spot size (mm)

$f$  = focal length of optics (mm)

$D$  = unfocussed beam diameter ( $1/e^2$ ) (mm)

$F$  = F-number (focal length/raw beam size)

$\lambda$  = radiation wavelength (mm)

$M^2$  = beam quality factor.

From these equations the following can be calculated -

Quantity	100mm FL	150mm FL
Spot size $f$ (mm)	0.32	0.47
Depth of Focus (mm)	1.5	2.25
Power Density (W/cm <sup>2</sup> )	$4.3 * 10^6$	$2 * 10^6$

As can be seen from these values altering the focal length from 150 to 100 mm changes the spot size by the ratio (100/150) which is 0.68 for the same laser welding conditions;  $D$ ,  $\lambda$  and  $M^2$  (19,  $10.6 \cdot 10^3$  and 5). These calculated results are mirrored in the experimental results for weld dimensions, as shown in figures 3.2 and 3.3. The observed penetration is greatest for the shorter focal length, with correspondingly the narrower width weld. This is in line with Herziger (1984)[11] describing the penetration depth to be a function of power density, as shown in Chapter 1, figure 1.11a. The effectively more localised surface heating source explains the narrow fusion width, though is not as accentuated as the penetration differences due to width-beam radius relationship as opposed to the penetration-(beam radius)<sup>2</sup>.

The coupling of the power/focal length interaction from figure 3.2, implies that the penetration depends on the power density at depth. From equation (3.3) we can see that the depth of focus is 2.25 times longer for the 150 mm lens than the 100 mm lens. The power density at the penetration depth is difficult to calculate since it is part direct radiation, part waveguided and part reflected by the weld plasma and keyhole walls. However it must be proportional to the power, with the direct radiation component being related to the depth of focus. This would account for the greater sensitivity of penetration to the power variation for longer focal lengths. Experimentally this is confirmed, as there is no significant differences observed over the test matrix between the underside weld widths of the two focal lengths, suggesting this is the approximate depth at which the equilibrium point of the higher beam intensity against greater depth of focus conundrum.

The coupling efficiency of this parameter, using the 100 mm focal length lens is 60 %.

### 3.2.1.3 *Position of Focus*

The size of the focussed beam on the workpiece surface and the intensity distribution through the material thickness is dependent on the location of the focus. Its effect is

in direct relation to equation (3.2), with a slight modification -

$$d_w = d_{\min} + (hD/f) \quad (3.4)$$

where  $d_w$  = spot size at the surface (mm)

$d_{\min}$  = minimum spot size (mm)

$h$  = distance of surface from  $d_{\min}$  (mm)

$D$  = unfocussed beam diameter ( $1/e^2$ ) (mm)

$f$  = focal length (mm)

In the case of the programme  $h = 0, 1$  (above and below the surface), therefore  $d_w \approx 0.32 + 0.2 (=0.52 \text{ mm})$  for the 100 mm focal length, and,  $d_w \approx 0.47 + 0.13 (=0.6 \text{ mm})$  for the 150 mm focal length. This result would seem to diminish the effect of equation (3.2). The experimental responses indicate the above workpiece and below workpiece focus position act similarly as responses to the 100 mm and 150 mm focal length lens' respectively. We have so far only considered the surface spot size, the explanation must lie within the affect of the depth of focus. This is subject to two factors; the angle of the beam on incidence at the surface and the interaction of the beam in the plasma region.

The beam/workpiece interaction angle is itself a function of the propagation of the beam through the plasma. This can be examined in terms of the absorptivity and the beam diffraction characteristics of the plasma. The absorption of the plasma is strongly related to the electron density and therefore the intensity as described -

$$\alpha = 2.21 \cdot 10^{-29} N_e^2 / T^{3/2} \quad (3.5)$$

where  $\alpha$  = absorption coefficient of plasma (1/cm)

$N_e$  = electron density as a function of intensity ( $\text{cm}^3$ )

$T$  = temperature of plasma (K)

Previous explanations of the role of the plasma in the welding mechanism

suggested the plasma to be advantageous in terms of beam coupling, recently Miyamoto *et al* (1992)[12] experimentally showed the absorption, for similar conditions as those here, to be 0.35 and 1.4 cm<sup>-1</sup> (distance of 1/e<sup>2</sup> beam power to be absorbed) for negative and positive focusing respectively (related to beam intensity above the workpiece). Applying this to the two different focusing conditions under discussion, from [12]

$$W_{\text{loss}} / W = 1 - \exp \left[ - \int_0^h \alpha(z) dz \right] \quad (3.6)$$

where  $W_{\text{loss}}$  = absorbed laser power (W)

$W$  = incident laser power (W)

$h$  = height of the plasma - from high speed video (cm)

$K_p(z)$  = the absorption coefficient at height  $z$  (cm<sup>-1</sup>)

this represents a loss difference of around 300 W in favour of the negative focusing, and therefore does not represent a significant value. Thus the question remains of the beam diffraction in the plasma and the resulting angle of incidence and spot size of the beam at the surface.

The refractive index of the plasma is related to local electron density gradients. With the focus above the surface more severe gradients are resultant due to the higher power density. These gradients are controlled by beam intensity with convective effects tending to obliterate such gradients. The gradients are induced radially and vertically, though from previous experiments the vertical are dominant [12], and therefore will only be considered. The proposed mechanism involves collimation of the beam through the workpiece under the action refractive index changes indicated in figure 3.6, described by [13]-

$$n_e - 1 = -4.46 \cdot 10^{-14} \lambda^2 N_e \quad (3.7)$$



where  $n_e$  = electronic refractive index

Thus the benefits of a short focal length spot size and long focal length depth of focus are combined. The natural divergence/convergence of the beam working with and against the refractive tendencies induced in the plasma. The optimal position of the focus in the plasma maybe slightly closer to the workpiece than 1 mm. Miyamoto *et al* (1992)[12] has recorded refraction angles of 0.5 degree with a 2 kW laser. The 3.5 kW laser used here and faster welding speeds will accentuate this affect, but it is difficult to say to what degree and the extent of the dynamic equilibrium required to maintain this effect during the welding process.

The angle of beam incidence obvious relates to the above discussion. However, from figure 3.6, the difference becomes more apparent when the keyhole is considered. The -1 mm focus converges into the keyhole and the +1mm is collimated into the keyhole - so what ?. Well, firstly the beam absorption at the cavity wall is enhanced with the collimated beam and secondly the reflected part of the beam is more likely to interact with the base of the keyhole. This fact is seen clearly in many welds as a hour glass shaped profile.

The coupling efficiency with positive focusing is 57 %.

#### **3.2.1.4 Mode Structure**

The mode structure from equation (3.2) is directly related to the power density for a given focal length and position of focus. The results in figure 3.2 show the comparison of two different modes, the  $TEM_{00}$  and  $TEM_{01+}$ , clearly identifying the lower order mode ( $TEM_{00}$ ) in providing greater penetration depth becoming more apparent with increasing processing speeds. This is no great surprise, as from optical theory [15] the Gaussian mode offers the minimum focussed spot size diameter and therefore the greatest power density, thus confirming previous work carried out by Beyer (1986)[15]. Another factor here is also the divergence of the beam around the focussing area, the Gaussian mode retaining higher power density

through the workpiece.

This would be the end of the discussion if modes were “black and white”, however a mode is not exact (in fact, made up of mixtures of modes), due to its qualitative description, the labelling of a beam becomes misleading when that beam falls into the grey area that lies in between two modes, or in fact anywhere from the perfect TEM that the labelling implies. This was found to be the case, as when working with a “good quality” lower order mode, which was always ensured during the experimentation, as opposed to a mode of questionable quality, the former always out performed the higher mode however with the latter no advantage was observed. When processing is at the focal point the difference between modes is at a minimum.. At this point we must cast our minds back to Chapter.1, section 1.2.3 in which a more exact classification of the mode structure was defined - the  $M^2$  factor. Measurement of this factor is outlined in Chapter 2, section 2.3.7 and specifically equation (2.1). The following calculations were completed for the Laser Ecosse AF5L and the Electrox M1500 lasers, the results being in Table 2. From the table the importance of a quality factor, in this instance the  $M^2$  factor, becomes clear. Looking at the first three columns describing a “good” and “bad”  $TEM_{00}$  mode and a  $TEM_{01+}$  there exists a limit where the lower order mode is preferable over the higher modes. From the measurements taken this is around an  $M^2$  factor of 7 for the lower mode, confirmed through processing data comparing the two levels of mode quality. With the higher mode quality welds giving joining efficiencies averaging 77,  $M^2 = 5$ , compared to 37 for the samples welded at an  $M^2$  value of 7. Or more to the point can weld the same thickness of material at twice the speed. The power density is a function of  $M^4$ , therefore maximum penetration is largely dictated by the quality of the mode.

Also included in Table 2 is the Electrox laser, which generates a mode of higher quality than the AF5 (2.7 as opposed to 5), which when viewing the figures for the maximum achievable power densities shows that a lower power laser can

compete at the higher processing regimes, at a third the cost ! Although the measured power density is not as flattering to the ElectroX as the calculated, it still highlights the fact that a laser of a third the power can achieve densities of nearly twice that when compared to a higher power beam of lower quality.

Until there comes a time when all lasers generate near perfect standardised mode structures, the inclusion of this quality factor is a vital part of processing information.

The coupling efficiency with a quality TEM<sub>00</sub> is 65 %.

### 3.2.1.5 *Polarisation*

The orientation of the electric and magnetic wave components within the propagating laser beam is not a “primary” welding parameter. As a significant variable it is dependent on the value of other parameters, exhibiting several interactions. Most noticeable with speed especially when related to the joining efficiency. The advantage of the parallel polarisation only occurs at increasing speeds, confirming Beyer *et al* (1986)[15]. His finding showed that the absorption of the incident radiation transfers from the keyhole to the front cavity wall where the absorption mechanism favours linear parallel polarisation relative to the welding direction - the results showed a transition point where the shift in absorption mechanism occurs at a speed of 5 m/min. (83 mm/s). Although the transition speed was not established, the difference in welding depth was - a sample was welded at 250 mm/s (15 m/min.) in the parallel direction and then rotated through 90 degrees to be welded in the perpendicular direction. The parallel polarisation sample achieved about 75 % penetration, in comparison with the perpendicular polarisation which achieved just under 50 % thickness. On inspection of the weld surface occasional pitting and excess splattering towards the edges of the weld were observed due to the non-symmetrical absorption around the keyhole, with the majority occurring at the keyhole front and substantially less at the sides. The extent of the theoretical absorption advantage is described by the Fresnel equations [16]

$$R_s = \frac{1 + (1 - \epsilon \cos \theta)^2}{1 + (1 + \epsilon \cos \theta)^2}, \quad R_p = \frac{\epsilon^2 - 2\epsilon \cos \theta + 2\cos^2 \theta}{\epsilon^2 + 2\epsilon \cos \theta + 2\cos^2 \theta} \quad (3.8)$$

where  $R_s$  = reflection coefficient for s-polarised light

$R_p$  = reflection coefficient for p-polarised light

$\theta$  = angle of reflection light makes with normal to the surface

$\epsilon$  = material-dependent quality given by -

$$\epsilon^2 = 2\epsilon_2 / [\epsilon_1 + (\epsilon_1^2 + \Sigma^2)^{-1/2}] \quad \text{where } \Sigma = \sigma_{st} / \omega\epsilon_0 \quad (3.9)$$

given that  $\omega$  denotes the angular frequency of the light ( $4.504 \cdot 10^{12} \text{ s}^{-1}$  for  $10.6 \text{ } \mu\text{m}$  radiation),  $\epsilon_0$  is the permittivity of free space ( $8.85 \cdot 10^{-12} \text{ Fm}^{-1}$ ),  $\epsilon_1$  and  $\epsilon_2$  are the real parts of the dielectric constants of the metal (both = 1) and  $\sigma_{st}$  is an electrical conductance per unit length ( $4 \cdot 10^4 \text{ } \Omega^{-1}\text{m}^{-1}$ )

Which when calculated gives the absorption for a weld with keyhole angling of 80 degrees of  $R_s=0.98$  ( $A=0.02$ ) and  $R_p=0.95$  ( $A=0.05$ ) for mild steel. The question is, does the extra 3 % absorption provide the 25 % increase in the penetration depth ? These figures highlight the theoretical absorption at the front cavity wall, subsequent keyhole multi reflection/absorption will accentuate this by two or three fold.

The coupling efficiency for parallel polarisation was 59 %. In comparison the coupling for the perpendicular polarisation was 40 %.

### 3.2.1.6 Side angle weld orientation

The angling of the sample perpendicular to the direction of welding showed an improvement in the weld dimensions, shown in figures 3.2 - 3.4. The theory behind these results has been previously investigated by Dixon and Lewis (1984)[17] - who discussed the generation of the plasma and the Laser Supported Combustion (LSC) wave in separate terms. By monitoring the transmitted and reflected portions

of the laser beam along with high speed video of the plasma, the Laser Supported Combustion waves were shown to propagate along the optical beam path while the plasma is generated perpendicular to the surface. Therefore, a larger percentage of the beam is unaffected by the plasma allowing higher surface power densities and deeper welds. Dixon and Lewis' results were achieved using a pulsed YAG laser on aluminium targets achieving power densities of  $10^9$  W/cm<sup>2</sup> which is readily applicable to the processing of steel with a high power CO<sub>2</sub> laser as the welding mechanism is identical apart from reduced power densities. Although this is an observed effect the absorptivity of the plasma as discussed in section 3.2.1.3 is such that the decrease in path length through the plasma is not of sufficient magnitude as to explain the results.

An alternative reason why angling the sample offers preferential processing became apparent when the samples were sectioned, all the weld profiles were perpendicular to the surface along the weld interface as opposed to being in line with the beam incident angle. The explanation for this is that some form of wave guiding along the weld interfaces is occurring. The angling of the joint was such that the keyhole is formed along the interface and not directly through the workpiece. An optimal side angle can be calculated using the data required to initiate the keyhole which has been estimated by Duley (1987)[18] at  $9 \cdot 10^5$  W/cm<sup>2</sup>, the conditions of processing here give a maximum intensity  $I_0 = 4 \cdot 10^6$  W/cm<sup>2</sup>. In addition what must be considered is the effect of welding speed. We are attempting to establish the angle at which melting/vaporisation occurs at the initial beam interaction point to a specified depth, thus the remaining portion is reflected along the interface as shown in figure 3.7, thus optimising use of the beam energy. Considering the central part of the beam and assuming an average intensity  $I_0$ , after penetrating a small thickness, the beam is incident on the interface. Thus the angle selection to optimise processing is as follows. Firstly, from Chande and Mazumder (1983)[20], the intensity loss penetrating the initial small thickness is determined from the Beer

Lambert Law -

$$I_{\text{depth}} = I_0 \exp(-\beta z) \quad (3.10)$$

where  $I_0$  = intensity at surface of workpiece (W/cm<sup>2</sup>).

$I_{\text{depth}}$  = intensity at depth  $z$  (W/cm<sup>2</sup>).

$\beta$  = beam attenuation through material (m<sup>-1</sup>)

$z$  = depth (m).

In this case  $\beta$ , is evaluated through experimentation, and was found to be equal to 2000 m<sup>-1</sup>.

Thus, the beam initially penetrates through a nominal material thickness, say 0.1 mm, therefore from equation (3.10) and using  $\beta = 2000$ ,  $I_{\text{depth}} = 0.8I_0$ . The maximum energy that can be absorbed at the angled interface is  $9 \times 10^5$  W/cm<sup>2</sup>, the keyhole threshold intensity ( $I_k$ ). Therefore by rearranging Fresnel absorption equation (3.8) for p-polarisation and incorporating the  $I_k / I_{\text{depth}}$  ratio as the required reflected beam energy, the optimal angle can be calculated for, in this case, mild steel -

$$0.09a \cos^2 \theta - 0.16a \cos \theta + 0.002a = 0 \quad \text{where } a = 9 \times 10^5 / I_{\text{depth}}$$

This can be solved for  $\theta$  using the quadratic root formula, here,  $\theta = 85$  or  $76$  degrees.  $\theta$  is the angle to the normal, which corresponds as  $(90 - \theta)$  for the side angle ( $\phi$ )(see figure 3.7). As 10 degrees as already been attempted 14 is the applicable answer which is confirmed through experimentation (see section 3.3.3).

This simple operation optimises the angle of incination for a particular set of welding parameters.

The coupling efficiency for the side angle orientation of 10 degrees is 63 % compared with the coupling effeciency of 70 % for the 14 degree case.

### **3.2.1.7 Normal angle weld orientation**

Inclining the workpiece in the direction of welding improved the penetration depth and, can be explained in terms of the keyhole shape relative to the tilt angle. In welding, and more specifically at high process speeds the absorption front becomes swept back, shown from experimental work by upto 45 degrees, as shown in figure 3.8. The geometry of the absorption front can be assumed to be an arc of suitable radius, from figure 3.8 length of this arc can be described by a chord with only a 2 % difference in length. By angling the workpiece or beam this keyhole/chord length tends to become normal to the workpiece surface. Using simple geometry optimising the incident angle of the beam gives an increase in depth by 30 %. The fact that only a tilt angle of 5 degrees was investigated, this being relatively small compared to the keyhole angle only a similarly small advantage was realised. Deciding upon the optimal angle is obviously related to the swept back angle and shape of the keyhole which in turn is dependent on the speed and to a lesser extent the input power at which processing is occurring.

This particular mechanism is directional dependent and samples must be welded “uphill” or with the beam tilted in a similar manner. To investigate the extent of the direction, several samples were welded “uphill” and “downhill” at 3, 5 and 11 degree inclination under similar welding conditions. The results were as expected with the uphill samples exhibiting enlarged through thickness fusion zones of around 10 %. The downhill, in contrast, at the 11 degree inclination reached the limit of penetration, plus a slight tendency to produce a humping bead. The profile of the two welds were fundamentally different, the uphill samples exhibiting a nail head shape, with the downhill welds showing a uniformly tapered bead. This, along with high speed video taken of the welding, indicated an insufficient plasma control associated with the uphill samples when using a coaxial gas delivery. This is explained by the observation that the plasma is positioned normal to the surface; in the uphill the plasma tends to radiate in to the beam path, while the downhill the

opposite is true. The consequence of this is that the advantage of the normal angling is only realised above a certain speed in the case of coaxial shielding (around 100 mm/s-7 m/min.), or, a plasma disruption jet must be used to counteract the effect.

### 3.2.2 Weld Profiles

It can be seen from figure 3.9 that five types of weld profile were produced, these characteristically represent the effect of different heat input conditions and more subtly the effect of the other experimental variables. When observing the grain boundaries and structural orientation, the crystal growth follows a direction appropriate between a preferred growth direction  $\langle 100 \rangle$ , governed by the metals crystallography, and that of the steepest local temperature gradient. The individual crystal size and shape are also largely governed by the thermal cycling and cooling rate experienced by the weld metal and surrounding region. The discussion is centred around the specific energy ( $P/vd$ ) input associated with individual profiles and any other outstanding parameter effects.

**Profile 1** : Exhibits a large U shaped fusion zone and heat affected zone (HAZ), the modification of the the micro-structure is minimal with, in some cases, the fusion zone being indefinable from the base metal structure. The formation of large horizontal columnar crystal structure due to the relatively slow cooling rate within a large solidifying molten pool, typically producing a slight drop-out of material in association with concave edges of the top surface and slightly humped middle section. All the above observations are a result of excessive heat input provided by a combination of low speed and high power, typically a specific energy of around 400 kJ/mm<sup>2</sup>.

**Profile 2** : Shows a slightly reduced fusion zone and HAZ with an aspect ratio around unity, the fusion zone being a more exact “wine glass” profile. The bead has



a relatively large surface width compared to the fusion zone beneath, this shape is referred to as a “nailhead” profile. The “nailhead” which results from a radiating plasma in or near the surface creating a larger melt width at the surface. Again, the microstructure shows large crystal growth slightly angled upwards and towards the weld centre line, though with increasing depth as the fusion zone contracts the growth becomes finer and largely equiaxial. A slight hump is evident at the top with in most cases a slight protrusion of the fusion zone at the underside of the weld. The common factor here is again excessive heat input in association with large plasma generation from processing at low speeds without adequate side jet- typically a specific energy of 250 kJ/mm<sup>2</sup>.

**Profile 3 :** This profile is a much neater and more compact, with a small fusion zone being slightly tapered or with parallel sides, in association with a small HAZ. This suggests a more efficient use of the incident radiation, with the microstructure being of finer growth maintaining the basic crystal orientation shown in the first two profiles. The nucleation direction is slightly more inclined towards the centreline showing an increase in this angle with depth upto about half of the full penetration depth, thereafter the angle remains constant. There is an occasional tendency of undercut which is a result of a rapid freezing of the outer weld metal under the fluid dynamic forces associated with the humping. The heat input is lower than the two previous profiles, with a specific energy of 130 kJ/mm<sup>2</sup>. The common factors are high power/high speed or low power/low speed combinations, together with in the majority of cases a 100 mm lens.

**Profile 4 :** The profile in this instance is of an hour glass shape, with the HAZ being parallel through the material thickness. It is interesting to note that this particular profile shape is not only confined to the low thermal input regime, as shown in figure 3.9 but also occurs at conditions similar to those common to profiles 1 and 2, thus indicating the shape governing parameter(s) are independent of the

heat input. In the large fusion zone samples the crystal growth is similar to those seen in profile 1, with large horizontal columnar structures, with the slight difference of having occasional large equi-axial crystal located towards the centre of the fusion zone. The surface and underside of the bead are flat.

The samples exhibiting smaller fusion zones have a finer structure. Also present is a slight protrusion of the fusion zone at the surface and underside in association with occasional undercutting. There seems to be no common factor for the larger welds apart from low speed/high power with a specific energy of 200 kJ/mm<sup>2</sup>. However the other welds all have a specific energy input of 90 kJ/mm<sup>2</sup> plus positive focussing (above the workpiece) and were orientated in some way; either in the normal or side angle. The flaring of the fusion zone near the root of the weld can be directly linked with the position of focus and the workpiece angling, as detailed in sections 3.2.1.3, 3.2.1.6 and 3.2.1.7. These two parameters induce a diverging incident beam, and, keyhole multi-reflections.

Consider positive focusing, the beam is incident to the workpiece at 7° (ignoring plasma diffraction effects). By assuming a suitable keyhole dimensions established from one of the samples, it can be verified that an increased percentage of the reflected beam from the first beam/cavity interaction will be absorbed in the root of the weld. The effect of workpiece orientation is to accentuate this fact.

**Profile 5 :** All these samples were non-penetrating welds, the maximum depth achieved being around 50 % thickness, however the surface weld width was about 0.5 to 0.75 mm, and therefore, on average about twice the depth of the fusion zone. The structure of the fusion zone was comprised of long fine columnar crystals angled towards the top centre of the weld, with very little heat affected zone being visible. Some of the profiles show slight undercut, with the common factors being high speed/low power in association with using a 150 mm lens - giving a very low specific energy input of around 50 kJ/mm<sup>2</sup>.

The dominant mechanism in the generation of profile 5 is the highly

convective outward flow associated with severe thermal gradients within the melt pool. This leads to characteristic large surface widths welds with little penetration, this reflects the findings of Chan *et al* (1987)[20] and Paul and DebRoy (1988)[21].

### 3.2.3 Weld Surface Characterisation

Having described the five weld profiles in the previous section is there some correlation between the surface appearance of these welds and the profile itself ?

The solidification lines that characteristically appear on the surface of a weld, be it laser or otherwise, give an indication of the energy input conditions in terms of speed and power, and the nature of the shielding arrangement. A visible regular surface solidification pattern with a well defined centreline is a good indication of a sound weld. At lower speeds this pattern is periodically and mostly randomly interrupted due to over energised plasma, at high speeds an incomplete pattern is formed due to excessively long melt pool lengths and increasing heat flow restrictions. The colouration of the surface is also important, a sound weld for mild steel appears as a dull grey. A weld of lower integrity appears a blue, silver or gold colour related to interference colours arising from the thin surface oxide covering suggesting a shrouding problem. These factors indicate the quality of weld produced but cannot really give information regarding the profile achieved, another factor is the heat affected zone, used in conjunction can define the profile with the possible exception of assessing the level of penetration. A description of the underside of the weld in is also provided for completeness. Surface and underside weld patterns are shown in figure 3.10.

**Profile1 surface :** This has a characteristically regular surface pattern, the angled solidification lines appear visible and are clearly separated by the weld centreline. Occasional irregularities in the surface pattern are apparent, in terms

of a termination in the pattern for 2-3 mm and a slight loss of weld width though the underside weld pattern remains continuous. This may occur two or three times along the length of the weld otherwise the fusion width remains constant over the length of the weld. The underside is typically half the surface width with solidification lines ridged towards the centre, these being particularly wide and somewhat irregularly positioned with outer lines curving back towards the centre. The heat affected zone is approximately twice the width of the fusion zone, with the outer edges defined by the blue colouration.

**Profile 2 surface :** The regular surface pattern is still visible with a less defined centre line such that the solidification lines which are angled at approximately 45 degrees to welding direction. The weld shows a slight longitudinal width variation of a random nature which is also apparent on the underside, however the underside variation is more regular with a modulation of around 12 Hz.

**Profile 3 surface :** This pattern shows the solidification lines becoming increasingly swept back though still regular, the increasing processing speed having reduced the density of the lines which can be individually identified. Towards the outer edges of the fusion zone dark regions are encountered, these indicate the undercutting where the surface of the weld metal has solidified below the surface of the base metal. The underside has a well defined pattern with a clear centreline and a width that is only marginally smaller than the top surface. The edges of the HAZ are very close to the fused metal.

**Profile 4 surface :** The surface is regular similar to that of the pattern present in profile one, the key is the . This underside centreline is well defined though of a ropery nature, with the edges showing a ragged solidification and spattering of weld metal. If the profile is of high integrity the surface and underside are difficult to distinguish between.

**Profile Surface:** What is immediately apparent, though not from the small section shown, is the periodic nature of the solidification pattern associated with modulation of the fusion width of around 18 Hz which is unusually large and comparable with profiles 2 & 4. In some instances there is a complete failure of the welding action resulting in short thin sections that have only been remelted. A further aspect of the weld is the colouration of the bead surface, which will vary from the acceptable dull grey to blue, silver and gold. It can be stated without inspection of the underside that no through penetration has occurred with occasional signs of the HAZ being visible on the underside. The extent of the HAZ on the top surface is undetectable without the use of microscopy.

If the solidification patterns are sectioned both across and along the length of the weld a distinct saw tooth profile is observed, when viewed under a magnification of around x100. The surface solidification is a result of the periodic oscillation of the solidification front, the mechanism is detailed Chapter 1 by Ishizaki (1980). The ability to identify the weld profile from the surface for profiles 1 and 2 is straight forward due to the size of the fusion and heat affected zones foremost, and the tight grouping of the solidification lines. The subsequent profiles; 3, 4 and 5 can also be matched to the corresponding profile which in turn have common processing conditions as outlined in the results section 3.2.3.

### **3.2.4 Weld fault Categorisation**

#### ***3.2.4.1 Porosity***

Porosity was found in 8 welds (out of 65) which is 12 % of welds studied. Common factors associated with this fault were the use of the longer 150 mm focal length lens and operating at maximum power/low speeds. The observed porosity was largely present at the bottom of the fusion zone in the region of the minimum fusion width

and, usually confined to single large pores as shown in figure 3.11b where it is located to one side of the fusion zone. Occasionally, porosity was found near the surface of the fusion zone.

The source of weld pores has six possibilities; a) frozen vapour bubbles, b) frozen bubbles of gas ejected from the melt, c) a reaction with shielding gases giving a gaseous product, d) gases trapped in the gap between the interfaces, e) gas inclusions as a result of the gas delivery system and finally f) from periodic oscillations in the liquid on the trailing edge of the keyhole. The first mechanism of trapped vapour bubbles may result from excess localised vapor pressure near the root of the keyhole blowing vapour into the weld pool at the rear. These bubbles are frozen near the bead root as originally observed by Arata *et al* (1983)[22].

The absorption of gases or any reactions with reactive gases in the shrouding system would involve the formation of carbon dioxide, as a reaction between carbon in the melt and oxygen contamination of the shroud gas, or water formed between absorbed carbon dioxide and hydrogen in the shroud gas. The gaseous product forms may have a reduced solubility when the melt cools and hence be rejected as a bubble.

The entrapment of gas (d) in between the butt interfaces is a geometric effect. With guillotined edges the orientation of the sample (burr facing upward or downward) may, in the case of the upward position cause localised gas pockets, with the geometry acting as a natural collecting vessel. These gas pockets would be transported around the keyhole and appear as porosity in the solidified weld metal.

Gas inclusions may be caused by the gas delivery system (e), and specifically the use of a plasma disruption jet. Miyamoto *et al* (1984)[24], outlined such a porosity mechanism as shown in figure 3.12. Incorrect positioning or flow rate of the jet may push the melt back into the keyhole, this back flow causes a blockage in the keyhole, thus trapping vapour. The effect is largely concentrated along the line of the keyhole.

Arata (1987)[25] and Tong and Giedt (1970)[26] have observed wavelike

structures in penetration welding, mechanism (f). Duley *et al* (1992)[27] modelled these waves, the model describes the appearance of voids and bubbles under certain flow conditions.

The porosity within the samples only occurred in the butt geometry and not the bead on plate, therefore this eliminates all mechanisms except (d). The porosity was observed in both guillotine and milled samples predominately along the joint line, with more frequency in the former though no individual guillotine configuration being susceptible. Thus, it appears that the porosity may be a combination of several factors; the instability of the keyhole due to the non-uniform guillotined edge, the inclusion of gas pockets again associated with the guillotine edges

#### **3.2.4.2 Cracking/Incomplete Fusion**

Cracking appeared in 9 % of all welds and tended to occur at the higher thermal inputs with angled samples. In all cases the crack propagated along the boundary between the fusion zone and the original joint edge, located at the bottom or middle of the weld.

The causes of cracking are many; a) centreline cracking b) hydrogen cracking c) stress cracking d) misalignment. The only cracking observed in this work were similar to those shown in figure 3.11a. Thus the only observed cause of cracking was misalignment and failure to fully melt one interface.

#### **3.2.4.3 Carbide Formation**

The presence of small dark spherical deposits were found in 15 % of welds, the nucleation sites being confined to grain boundaries, shown in figure 3.11g. On closer examination with an electron microscope, the "dark spot" phase was identified as Iron Carbide.

The formation of the carbides may cause localised hardening and embrittlement, however in low carbon steels this is not usually a problem, since only a small amount is present. The results from the tensile and Erichsen tests show

that this is the case.

#### **3.2.4.4 *Surface Defects***

Surface faults are associated with the morphology of the weld bead surface, figure 3.11 shows the four identified defects. The defects encountered are

a) Upwelling on the top surface under surface tension forces produced by an off centred beam (fig 3.11c). b) Too large a gap between the interfaces for the welding conditions (fig 3.11d). c) Similar to b) however not under so severe welding conditions and subject to excess gas assist pressure (fig 3.11e). d) Vertical misalignment of the sheets resulting in a stepped weld (fig 3.11f).

#### **3.2.5 Comparison between Bead on Plate and Butt Welds**

The experimental programmes involved the use of these two different welding geometries. There is little difference in the shape and nature of the profiles, only that the butt welded geometry has a larger fusion zone and in particular shows greater penetration depth by around 10 %. It is worth noting that the bead on plate welds exhibited no cracks or porosity which were sometimes found with the butt welds (sections 3.2.4.1 & 3.2.4.2).

Since the beginning of research into laser welding the bead on plate weld has provided the experimenter with a convenient short cut that simulates butt welding, but how comparable are they ? This study ran two parallel programmes identical apart from the welding geometries; one bead on plate (bop) the other square milled edges (butt).

In general the bop welds are 25 % smaller in width and and 10 % less in penetration than the equivalent butt welds. This may be due to the gap in the butt weld providing a direct route to the base of the material and the gap aiding absorption. Thus a scaling constant could provide a close enough simulation between the Bop and butt results. It is interesting to note that the weld metallurgy is the



same for both but the bop welds never displayed either cracking or porosity. Thus, both cracking and porosity are effects resulting from a prior gap.

### **3.2.6 Mechanical Testing**

Appendix C shows some of the tensile and Erichsen data made at Van Leer's Research Laboratories in The Netherlands, on the strengths of welds reported here.

#### **3.2.6.1 *Tensile Test***

The tensile tests were performed under DIN 50120 on a selection of the welds ranging from those of a high quality to welds of lesser integrity. The results are compared to the values for the base metal acting as a control. The tensile test data is summarised in Table 3, the values from all the welds tested having been averaged and categorised into the five previously identified weld profiles (section 3.2.2 - 120 samples, around 10 per profile category). Failure usually occurred in the parent material. Thus, the values for yield strength and ultimate tensile test (not tabulated), were around 160 and 310 MPa respectively, similar to that of the base metal. Faulty welds showed similar values, although failure had occurred in the weld metal.

#### **3.2.6.2 *Erichsen Test***

This formability test differs from the tensile in that the cleaving force is applied directly to the weld joint itself, and provides data regarding energy required to fail the sample along with a fault characterisation by the mode of failure, see Appendix C. The values obtained for the base metal control averaged out at  $10.95 \pm 0.5$  mm displacement, again from Table 3, with the failure occurring around the circumference of the ball indenter and therefore indicating a "sound" mode of failure. The majority of the welds tested over profiles 1-4 showed the mode of failure representing that of a sound weld with the displacement values slightly under that of the base metal (10.5 mm), though well within the 80 % required for the DIN

50101 standard. However, the welds in the profile 5 category failed along the seam of the weld, with displacement values around the 3 to 6 mm mark, directly proportional to the depth of penetration.

### **3.2.6.3 *Microhardness Test***

This test assesses the thermal cycle that the weld metal, and surrounding heat affected zone, have experienced, providing information on surface cooling rates and likely grain structure. The value for the base metal was measured at 120 HV. As can be seen from Table 3, the hardness measurements neatly fall into the profile categories, starting at 250 HV rising to 380 HV. From these values there is a clear cut off between three energy input regimes, the transition between profiles 2 & 3 and 4 & 5 shows an increase of 100, unlike the 40/50 changes within each band. The variation of microhardness values with the specific energy input is a result of the different cooling rates experienced by the weld metal.

Three other hardness measurements were taken; a cross-section from the base metal through the fusion zone and again to the base metal, the variation through the depth of the fusion zone and the longitudinal variation along the direction of welding.

The cross-sectional variation in figure 3.13 clearly shows the gradual increase through the heat affected zone until the fusion zone is reached, the hardness value then sharply increases to nearly twice that of the base metal. Across the fusion zone there is some modulation then, as the HAZ is reached a dramatic fall off is once again seen. The longitudinal microhardness variation, which covered about 20 mm of weld length, showed an average value of 270 HV with a modulation of 20 - 30 HV.

The physical testing undertaken in the analysis of the welded samples basically showed that only in faulty welds of profile 5, were the mechanical properties of the weld values affected by the processing conditions, apart from the microhardness. The hardness is determined mainly by the material chemical

composition, in this case a carbon content of 0.06 % plus other trace elements.

Comparing the laser butt welding to the Electrical Resistance Welding (ERW) is not possible since the ERW system increases the joint thickness from 1 mm to 1.7 mm. The strength of the laser welds have been shown to match the base metal therefore the comparison is unnecessary. An interesting difference in the two joining methods arises from the fact that the ERW can weaken the weld through 'burning' due to excessive current, such a weakening does not occur in laser welding. It should also be noted that the laser can butt weld whereas resistance welding needs a lap and therefore more material. If the weld has penetrated and passes on surface inspection the weld will usually be mechanically sound. A further advantage of the laser process is the zero increase in thickness, the thickness increase in ERW makes not only testing difficult but presents post welding manufacturing problems outlined in the introduction.

Laser welding standards have yet to be issued. Current standards for laser welding has centred around the DIN 50120/50101 for mash seams and the BS 4515 for fusion welding. In the intervening time new standards specifically for laser welding need to be devised based on experimental studies such as this one.

#### **3.2.6.4 *Corrosion resistance***

The long term results indicated no positive or detrimental effect of laser welding on the corrosion resistance.

#### **3.2.7 Weld quality assessment**

The required weld qualities on a drum are strength and formability. From the mechanical testing it is evident that these are guaranteed over a wide range of processing conditions. The categorised weld faults are therefore the key to establishing weld quality assessment. This assessment can be achieved by visual inspection alone (sections 3.2.3). One looks for weld width, surface discontinuities

(excess splatter, weld interruptions, solidification pattern, weld colouration, bead morphology) and misalignments. Therefore, with minimal instruction the quality of a laser weld in drum steel can be established.

### 3.2.8 Statistical Modelling

From the data entered into the statistical package a model can be formulated based on the responses, for the penetration depth and weld widths. These are listed below -

#### Penetration depth

$$|\text{Depth}| = 0.11\text{Power} + 0.043\text{Speed}.\text{Power} - 0.15\text{Speed} - 0.05\text{Lens} - 0.039\text{Side Angle}.\text{Focus}.\text{Lens} + 0.85 \quad (3.11)$$

#### Weld width at the surface

$$|W1| = 0.11\text{Power} - 0.26\text{Speed} - 0.046\text{Mode}.\text{Lens} - 0.043\text{Side Angle}.\text{Focus}.\text{Lens} + 0.92 \quad (3.12)$$

#### Weld width at base

$$|W2| = 0.15\text{Power} + 0.03\text{Focus} - 0.22\text{Speed} - 0.03\text{Side Angle} - 0.042\text{Power}.\text{Normal Angle} - 0.042\text{Power}.\text{Normal Angle} + 0.42 \quad (3.13)$$

where Power is in kilowatts.

Speed is in millimetres/second.

Lens focal length is in millimetres for plano-convex lens.

Side and Normal Angle are in degrees from the normal.

Mode is the M<sup>2</sup> factor.

Focus is either +1 or -1mm.

The accuracy of these equations as a predictive tool for the welding depth or width is open to debate since it is essentially a best fit to the experimental data.

Thus, the application of these simple equations to any general welding situation is of course not possible unless the conditions under which the welds have been performed match that from which the data originally came, for example no variation in the plane of polarisation was made and so the equations only apply to parallel polarisation (in the direction of welding). However let us see how the set compare to other thin section welding data, using data compiled from Laser Ecosse and the Industrial Laser Handbook for full penetrating butt welds. From the penetration equation (3.11), and including only the first four terms the comparison is as follows

-

Speed (mm/s)	Power (kW)	Lens (mm)	DEPTH (mm)		
			L. E.	I. L. H	Model
140	5.0	150	1.0	2	3.0
70	1.1	100	0.5	0.7	0.7
85	1.5	100	1.0	1.2	1.5
33	1.5	75	2.5	4.5	5.0
30	4	150		6.5	5.5
20	6	200		10	6.2
10	8	300		14	11

From the comparison it is evident the model has limits, these being the low to moderate power ranges (1.5 - 5 kW) in combination with moderate to high speed (40 - 140+ mm/s), as shown in figure 1.14. The difference in the Laser Ecosse and Industrial Laser handbook data may be that the former was limited by full penetration, whereas the latter and that of the model is the maximum penetration. The accuracy of the model is around 30 %, thus, the set of statistical equations can be used as a guide to weld dimensions.

### 3.3 RESULTS -part two

The statistical survey of the effects of the principal operating variables on the main weld quality parameters shown in Table 4 illustrate the optimal conditions when welding thin mild steel sheet, as well as highlighting those areas requiring further investigation.

Secondary and further optimisation studies are concentrated on the following:

- a) Weld assist gas - composition, direction and velocity.
- b) Angle of incidence of the beam on the workpiece.
  - i) angle from the normal to the weld in the welding direction "Normal".
  - ii) angle from the normal at right angles to the weld direction "Side".
- c) Position of focus.
- d) Effect of edge preparation and fit-up.

#### 3.3.1 Weld Assist Gas

The gas jet was positioned behind the welding front and pointing in the direction of welding. Two experiments were made, the first was to assess the effect of the addition of a gas jet and its position relative to the keyhole in terms of the angle, stand-off distance and interaction with the existing coaxial jet. The second experiment involved investigating the effects of using different gases; nitrogen, carbon dioxide, helium, argon, oxygen additions and various combinations of these gases. The experimentation was accomplished at high speed with moderate power allowing the penetration depth and weld width to be assessed for the different gases and flow rates. The weld quality was also assessed.

Varying the jet angle showed no improvement in penetration, however figure 3.15 shows an observed increase in weld width, reaching a maximum at 45 degrees. However, it was noted that the welds at zero jet angle were of higher quality in

relation to smoothness of the bead profile. The stand-off trials are shown in figure 3.16, as a function of flow rate at various distances (3, 7, 10 mm). The findings show the 3 mm standoff produced the maximum welding depth at 20 l/min. At greater stand-off distances the penetration decreased, however the flow rate at which maximum penetration was achieved for each standoff distance remains constant. At 10 mm there is a 50 % loss of penetration, as the welding depth tends to the value at zero flow rate.

The quality of the weld deteriorated in terms of excess weld spatter at distances closer than 3 mm and more generally at flow rates above 25 l/min. The combination of the coaxial and 45 degree jet involved extensive investigation into the effect of different flow rates. The welds indicated that coaxial only and jet only gave similar results, and the optimal combination of the two was at 2 mm stand-off/ 10 l/min. and 3 mm stand-off/ 10 l/min. respectively.

The effect of the different gas species on depth and width are given in figure 3.17, in terms of the gases individual volume flow rate and that of a normalised mass flow rate (to air - individual gas flow rate/relative density to air). The lack of performance of helium at the high speeds is noticeable, showing about 30 % less penetration with He compared to all the other gases. It is interesting to note the maximum penetration for the individual gases does not occur at the same flow rate, the following listed in order of effectiveness; 0.6 mm penetration at 15 l/min. for argon, 0.55 at 20 l/min. for nitrogen, 0.5 at 7 l/min. for carbon dioxide, 0.4 at 3 l/min. for helium. The absolute values of the measured weld width show an intermingled range of values for the various gases and a common trend, an initial minimum followed by rising width with increasing flow rate. This is most clearly seen on the normalised plot.

As mentioned above combinations of gases were tried e.g. Ar/He, N<sub>2</sub>/Ar, CO<sub>2</sub>/He etc. None of these showed any significant improvement in welding depth, and in most cases reduced the overall penetration - most notable the addition of small

amounts of oxygen to the main gas.

The appearance of the welds from a visual inspection showed that only in the case of helium had any weld oxidation occurred suggesting insufficient shrouding. The bead profiles showed very subtle variation, the nitrogen welds had a well defined chevron pattern with a flat surface. The carbon dioxide, argon and helium welds had a more semicircular pattern with slightly convex surfaces.

### **3.3.2 Normal Angle Orientation**

The difficult aspect in fixing of this particular parameter was maintaining a constant position of focus on the workpiece surface. The solution to make bead on plate welds on rotating disc samples, as shown in figure 3.19. As outlined in Chapter 2 the angle of the workpiece was increased in 5 degree increments up to 35 degrees.

Variations in beam incidence in the plane of welding are shown in figure 3.18, the response shows a general decrease in fusion area with increasing inclination. On closer inspection the graph describes a reverse S shape with the rate of decrease following an initial positive then negative exponential fall off, the change occurring at the 20 degree mark - with the welding action completely terminated at 35 degrees.

### **3.3.3 Side angle orientation**

The side angle inclination of the workpiece was investigated for guillotine edge samples at 0, 10, 15 and 20 degrees, with the burr facing downward. The control was established by using samples with edges milled to 0, 10 and 20 degrees.

The governing response was the weld quality in the form of surface inspection and assessment of the weld profile. The results are is shown in figure 3.20, with around 14 degrees being the optimal angle of inclination. However, in these results the problem of porosity was evident, figure 3.21 shows several typical



high speed welds for both the guillotine and milled edged samples. Statistical analysis of the results for the porosity response proved inconclusive, with the angle, position of focus, speed, guillotine edge, vertical misalignment and gap width being tested.

A comparison of the repeatability figures for guillotined and milled samples are given in the form of bar graphs shown in figure 3.22. The milled edges show a near 100 % reliability across the band, whereas the guillotine edges typically average around 50 %- with the occasional variances notable the +1 and 10 degree weld showing an 80 % value.

From this, the following inference is made, that the welding of uncontrolled guillotine edges is only reliable with normal or 10 degree incidence at speeds upto 140 mm/s (8.5 m/min.).

#### **3.3.4 Position of focus**

The variation of fusion area with the position of focus is shown in figure 3.23. A maximum area is seen to occur when the focus is between 0.5 -1.0 mm above the surface. This is reflected in the profile shape; initially showing a parallel bead then a larger distinctive hourglass shape. The recommended distance for the focal position is 0.75 mm above the workpiece. If for any reason the vertical position of the workpiece cannot be kept within  $\pm 0.25$  mm then due to the rapid falloff in penetration above 1mm, a more cautious +0.5 mm is advised.

#### **3.3.5 Edge preparation and fit-up**

The sheared edge has three possible welding configurations as shown in figure 3.24, along with the charactersitic weld profiles (burr downwards). At welding speeds up to 140 mm/s, there is no particular difference at the welding conditions used. Above this speed the (1) and (2) configurations are preferred, with (3) failing on lack of

penetration. However, a further increase in speed to 200 mm/s causes reduced penetration in all three, although configurations (2) and (3) show the “humping” defect. This is illustrated in figure 3.28, and is discussed in detail in section 3.4.5

Vertical, horizontal (gap width) and beam misalignment were investigated for the configuration 1 arrangement and milled edged samples, as shown in figure 3.25. All welds were completed at 3.5 kW, 200 mm/s and a 100 mm focal length lens focused at +0.75 above the workpiece surface. From figure 3.25a the guillotine configuration is particularly sensitive to vertical and horizontal, only  $\pm 0.15$  mm and  $\pm 0.1$  mm respectively. The milled samples nearly doubled these values but showed a reduction in the tolerated beam misalignment ( $\pm 0.15$ ), when in comparison with the guillotine samples ( $\pm 0.2$ )

### 3.4 DISCUSSION - part two

#### 3.4.1 Weld assist gas

There appears to be no significant difference between the coaxial nozzle and the “plasma disruption” jet delivery. On the one hand the jet offers a slightly enlarged fusion width (20 %), which may prove important when considering joint fit-up tolerances but at the expense of a slight reduction in the weld quality and continuity. The coaxial nozzle arrangement is simplicity itself, with little positional problems and less critical tolerances. The increase in the fusion width is due to the more direct interaction of the angled disruption jet with the molten metal and the plasma plume, as previously detailed by Miyamoto *et al* (1984)[24]. He observed the gas jet to push the melt outwards, perpendicular to the direction of welding, thus increasing the width of the bead. Miyamoto indicated the angle of the jet showed no further advantage past the 30° mark when welding 4 mm thick steel, however Norris (1989)[28] clearly identified the 45° to be optimal for welding 12 mm thick steel. This difference is possibly due to there being more dependence on plasma

effects with the thicker sections

The stand-off of the jet gave no great surprises, increasing distance (3, 7 and 10 mm) leading to decreasing depth to a limit similar to that of an ambient atmosphere of the shielding gas used, in this case nitrogen. The 3 mm jet position providing maximum suppression of the plasma in the path of the laser beam, which will be discussed in detail shortly.

The variation of penetration with gas composition using a side jet showed greater penetration with argon. The results for Ar, N<sub>2</sub>, and CO<sub>2</sub> are largely contained within the error band of the optical microscope measurements ( $\pm 0.05$  mm). Also included in the graphical data are the normalised plots providing a true comparison of the efficiency of each gas. The striking result is that of the low penetration achieved using helium. This can be reasoned from three observations; a) momentum, b) plasma coupling and c) plasma radiation.

The normalised plots are in figure 3.17 highlight this theory, showing Ar, N<sub>2</sub>, and CO<sub>2</sub> gases to have effectively larger volumetric flow rates, which in turn leads to higher force "pushing" against the plasma ( $F = \text{gas pressure} * \text{exit area}$ ). Hence, removing the plasma more efficiently, thus reducing beam absorption in the plasma. However, as described in section 3.2.1.3 the plasma absorption is only of the order of 300 W, also the normalised flow rate of helium does at some points equal that of the other gases but nevertheless still shows reduced penetration.

Alexander (1980)[29] observed a change in the maximum penetration for helium at low speeds to argon at high speeds. She reasoned that the absorption front in the plasma added extra coupling to the Fresnel absorption, if the plasma becomes detached the beam focus and power density are affected leading to a reduction in the penetration depth. In this instance the ionisation potential of the argon must be matched to the temporal behaviour of the plasma absorption front (laser supported combustion wave), keeping it closely coupled to the surface. However there is no reason why this should be different with helium, a plasma cannot be "over

suppressed". Consider the dynamics of the plasma, a recoil force is exerted on the melt pool, the magnitude of the force proportional to the plasma. In the case of argon, this force is the greatest, the resulting depression of the melt pool increases penetration by directing beam absorption toward the keyhole.

Radiation emerging from plasma particles is a result of excitation, recombination and bremsstrahlung. Again, consider the temporal plasma dynamics - collisions occur between photons and electron particles and colliding with other particles resulting from this interaction. The extent of this radiation is a function of the collision cross section and the momentum of the particles. At low speeds the plasma is highly energised and the ionisation potential of the shielding gas is the primary control mechanism to minimise the effect of the plasma on the beam. The ionisation potential for the He is higher than the other gases and hence the plasma with He is cooler and less intense. Ar, N<sub>2</sub>, and CO<sub>2</sub> gases by comparison would simply lead to an over energised plasma and massive beam attenuation or distortion. Conversely, at high speeds the plasma is thinner and closer to the interaction surface. It thus aids the Fresnel absorption process. The more intense plasma with Ar, N<sub>2</sub>, and CO<sub>2</sub> gases helps in this case.

The greater penetration depth observed with Ar, N<sub>2</sub>, and CO<sub>2</sub> gases are thus explained in terms of improved coupling due to the surface plasma.

As mentioned earlier some small additions of oxygen (0.1% - 10%) were made to nitrogen and argon in line with Heiple and Burgardt (1985)[30] - that the inclusion of a Group VI elements, usually sulphur or oxygen, may lead to the reversal of normal convective flow in the melt pool from outward to inward. The results showed no such advantage, within the majority of cases a reduction in weld dimensions resulted. The concentration of the SO<sub>2</sub> gas as used by Heiple and Burgardt was only 0.001% in argon, and although these levels could not be duplicated here, the larger concentrations should have indicated some improvement in penetration

even if the resulting weld was mechanically unsound. The conclusion drawn is that although this reversal of melt flow has been observed by Slinde *et al* (1992)[31] it has only been realised at welding speeds of around 25 mm/s (1.5 m/min.). The reversal of the melt flow appears to be overcome by the larger temperature gradients and reduced melt pool surface area occurring at increasing welding speeds that “drive” the “normal” melt flow conditions.

### 3.4.2 Normal angle orientation

There was a reduction of the fusion width with increasing angle as shown in figure 3.18. There was no variation in penetration up to 35 degrees which showed a 10 % reduction. Above 35 degrees the penetration fell sharply with the loss of the keyhole. Up to this point the reduction in processing efficiency is attributed to the reduced surface power density due to the angling. If the keyhole could be maintained using shorter distance optics or higher power an upturn in the response may be seen after 35 degrees. The calculation performed in a previous section (3.2.1.6), cannot be transposed to this situation as the beam coupling is not assumed (as beam may be reflected, as is the case over 40°) and the geometry of the keyhole front wall cannot be accurately estimated. The lack of improved penetration results from angling may have been overshadowed by an unknown effect emerging from the circular welding mechanism.

The shape of the fusion zone was of interest as all the profiles showed a initial vertically directed bead, however about half way through the thickness it becomes angled outwards - this angling affect is obviously a result of the centrepetal action during the circular welding. A further result of the modified melt pool flow is an increase in welding depth. In normal 1G flat orientation the limit of penetration is about 230 mm/s (12 m/min.) at 3.5 kW, in this configuration 315 mm/s (19 m/min.) is possible at similar power input conditions - and this wasn't the limit of penetration but the limit of the motor speed ! The centrepetal action gave a sideways

force of  $m\omega^2$  in addition to gravity this appears to help stabilise the keyhole and improve penetration. The estimation of this force, for a unit mass, is 1.1 G and 0.6 G for 315 and 230 mm/s respectively. This effect is observed from the profile of the beads, with the fusion zone tapering outwards (around 5 degrees) about a third way through the thickness as shown in figure 3.19. The effect of the centrepetal action in the lower part of the weld relates to a decrease in magnitude of the flow forces with melt pool depth. The outward force becomes significant at around a third of the depth corresponding to a reduction in the melt flow velocity. Arata (1987) observed the presence of a vortex around the rear of the keyhole at half depth, also Schauer and Geidt (1978)[34] identified a similar region. The coincidence of this point with the point at which the effect of the centripetal force is seen highlights two parts of the melt pool, as shown in figure 3.26. This centrepetal force component which acts along the keyhole tends to push the melt downward, thus enhancing the melt pool flow dynamics, resulting in stabilisation and greater penetration.

These spinning results are for bead on plate runs as opposed to butt welds, therefore this finding cannot be applied to the problem of linear butt welding. However considering the problem of an all welded drum the joining of the lid and bottom to the main body could be done by this circular method. The welding of the lid/bottom to the main body would involve a blind lap weld of around 1.5 mm thickness plus the added advantage of doing away with the need of a sealing material - which at present must be injected into the precurled interface area and cured at a raised temperature for 10 minutes. The additional drum strength and no sealant leads to a more reliable seam offering greater protection against leakage of the drum contents and increased longevity of the seal; which firstly ensures very little chance of an environmental disaster and secondly allows the drum to transport "hotter" materials.

### **3.4.3 Side Angle orientation**

The results confirm the calculations from section 3.2.1.6, with the optimal angle of inclination being around 14 degrees. Assessing the quality of the welds showed up two distinct groups, the milled samples and the guillotine samples. The milled samples were of high integrity whilst the guillotine welds exhibited gross porosity, as shown in figures 3.20. The presence of the porosity was tested by statistical means to determine any significant factors, no conclusions could be made from this investigation. However, the overriding consideration is the difference between bop welds (no porosity) and milled samples (little porosity) and the guillotine samples. The answer is a combination of the joint geometry related to edge quality, vertical misalignment and the gap width. No one factor is dominant, but all three contribute to the formation of pores. The conclusion is that the lack of material in the weld during the keyhole/melt pool phase is transformed by solidification to porosity. Specific mechanisms, as outlined in section 3.2.4.1, which can be applied must relate to this instability of the welding mechanism. The keyhole effectively oscillates at random, according to conditions in the weld gap (edge mismatch, surface roughness etc). Smaller porosities are resultant from the entrapment of gas and the vigorous action of the melt flow behind the keyhole. The larger pores arise from the keyhole passing through parts of the joint, the surrounding molten metal rapidly freezes, and the void is formed. It is observed that the large pores are often along the weld centreline, extending sideways to the edges of the joint.

### **3.4.4 Position of focus**

The results of the focusing trials confirmed earlier data, that a slightly positive position of focus is optimal - showing a marked improvement in processing over the conventional "negative" position. This result is discussed in section 3.2.1.3.

### 3.4.5 Edge preparation and fit-up

The type of guillotine edge produced is related to the set-up of the machine, the results indicating that the edge profile of (1) from figure 3.24 is the best choice. The dependence of these tolerances to the specific welding conditions cannot be over emphasised, here, the effect of the various joint configurations and the actual tolerance values are stated though one must remember they will only be valid for similar conditions. The allowable misalignments are related to the speed and power, all else being equal. At relatively low speed and high power (<100 mm/s and >3 kW) large fitup tolerances are permissible - in the region of 0.2 mm for vertical and gap, as identified in figure 3.25 (beam misalignment is somewhat independent of energy input conditions). Although not shown in figure 3.25, increasing welding speed shows a transition point between guillotine and milled interfaces, at around 140 mm/s, with the the milled samples showing less sensitivity to the fitup. Further speed increases up to 200 mm/s (as shown in figure 3.24) start to show differences between the types of guillotine edges themselves. From figure 3.24 edges 1 and 2 can be grouped together in terms of tolerances and weldability, the third, however, due to the geometry of the edge and thickness reduction is very sensitive to fitup. In the latter case a sound weld is only achieved from low speed and high power conditions, with fitup tolerances around half that of the other edges. With speeds over 200 mm/s the first configuration is optimal as the “humping” mechanism becomes dominant (see section 3.4.6). The increased weld volume of the milled samples offer more generous tolerances, however are less tolerant to beam misalignment ( $\pm 0.1$  mm). The guillotine edges due to the V-shaped fit-up can withstand  $\pm 0.15$  mm, which, from the high speed filming can be seen to be due to the waveguiding. This was assumed from the observation of a V (guillotine edge) bounded area of liquid metal/plasma in the joint centreline when the beam was completely offset from the centre.

It is suprising fact that laser welding, being an autogenous process, (with no



addition of filler material) can tolerate any mis-fit, but actually shows an apparent increase in metal volume of the weld area. An explanation for this has been provided by Akhter (1990)[35], that due to thermal stresses in the solidifying weld pool the liquidus metal is squeezed together, described by the following - for the gap to be filled by shrinkage -

$$Aw t_p \beta \Delta T = g t_p \quad \text{from which} \quad g = Aw \beta \Delta T \quad (3.15)$$

where  $\beta$  = coefficient of thermal expansion (m/°C).

$\Delta T$  = temperature change (°C).

$t_p$  = sheet thickness (m).

$g$  = gap thickness (m).

$A$  = constant.

$w$  = fusion width (m)

The fusion width is a function of power and speed. It can be predicted from the Swifhook and Gick model (3.1) -

$$P = 0.483 v w t_p (\rho C_p T_m)$$

where  $P$  is absorbed power (kW),  $v$  is welding speed (cm/s) with other symbols as described in section 3.2.1.1. Thus, substituting for  $w$  in equation (3.15)-

$$g = AP \beta \Delta T / 0.483 v t_p (\rho C_p T_m) \quad (3.16)$$

$$\text{now } \Delta T \approx T_m \text{ so} \quad g = 2A P \beta / v t_p \rho C_p$$

Simplified further to  $g = BP/vt_p$ , where  $B$  is the new constant. The constant  $B$  is calculated by considering a bead on plate weld, determining the maximum possible increase in the weld volume from a weld profile at high power and low speed combination (3.5 kW and 3.5 cm/s). Substituting this value for  $gt$ , the calculation gives  $B = 0.12 * 10^{-6} \text{ m}^3/\text{J}$ , and therefore

$$g = 0.12 * 10^{-6} P / vt_p \quad (3.17)$$

where P is in kW, v is in cm/s,  $t_p$  is in metres and g is in metres.

Thus the gap tolerances as a function of welding speed and power is shown in figure 3.27., along with measured fusion expansion widths (from bop welds - increase in fusion area/material thickness) and a measured tolerance. The fusion expansion widths represent the maximum gap that could be filled based on bop welds where the fusion metal covers a greater area than the original base metal (surface and underside protrusions). The predicted values are similar to the bop fusion width expansion values, however both are considerably lower than the measured tolerance. It appears that the presence of the gap in itself plays a part in the “filling” mechanism. The equation (3.17) is around a 60 % underestimate, however it does not take account of the spot size at the workpiece or joint geometry, other than the gap width.

The surface roughness and straightness of the cut edge are also of great importance. Surface roughness is the most critical and tests showed 60 % passed the specified Ra value of  $\pm 0.05$  mm. These surface roughness values were determined using a Taylor-Hobson Surtronic 3 profiler accurate to 2 % of reading, with over 2 m of edges being evaluated. The straightness of an edge can usually be accommodated in the fitup.

Therefore the cut edge must first be standardised before the welding operation can be commercially implemented.

#### **3.4.6 Investigation of the humping effect**

Another problem encountered at these high speeds is the appearance of a weld fault commonly known as the “humping effect”. This weld defect, first noted by Braadstreet (1968)[36] imposes a physical limit on the maximum welding speed for a given material. This effect causes the formation of a series of humps along the

weld centreline thus producing a longitudinal height modulation as shown in figure 3.28. The generation of these upswellings is a result of the keyhole and melt pool instabilities. In an attempt to understand the formation of this defect a high speed video film was made of weld bead formation during humping..

#### **3.4.6.1 *Experimental procedure to observe weld bead formation***

The experimental procedure is described here as opposed to Chapter 2, due to its specific nature involving the high speed camera. The laser used throughout the experimentation was the Laser Ecosse AF5L operating in the TEM<sub>00</sub> mode, the samples were mild steel welded in the butt configuration, the edges were guillotined (type (1) from figure 3.24) and square milled which acted as a control. The beam was focused using a parabolic mirror, described in Chapter 2 section 2.3.2, with a focal length of 100 mm. The plasma suppression was provided by nitrogen gas supplied at 15 l/min. and delivered by a jet of 2 mm diameter angled at 45 degrees following the weld, thus providing a clear view of the welding. The experimental arrangement is shown in figure 2.5 (chapter 2), with the clamping jig secured to a X-Y CNC servo driven table capable of translational speeds up to 260 mm/s. The welds were completed in the 3.5 kW power range and between speeds of 140 -260 mm/s, the focus was at the workpiece with the angling of the samples being achieved by appropriate wedges under one side of the jig.

Initial investigation was also carried out into the variation of edge fit-up for the guillotine cut samples - as discussed in section 3.4.5. The three possible guillotine joint configurations, as shown in figure 3.29, and milled edged samples were used for the side angle welding. The side angle, being perpendicular to the direction of welding, was increased from 0 to 30 degrees in increments of 5 degrees. There was no further edge preparation after shearing or milling of the edges. The offset of the laser was adjusted from the weld centreline until the weld failed.

The welds were filmed with a Kodak Ektapro high speed video camera. The set-up and specification are described in Chapter 2, section 2.3.8. The camera lens

was a long distance microscope lens which gave a standoff distance of about 60 cm protecting the lens from weld spatter, giving a viewing area an approximately 3 by 7 mm. A ruler was filmed in the vertical position and in the horizontal welding directions to give scaling factors. The lighting of the weld region was totally self-illuminated by the plasma/metal vapour within and above the keyhole, the Ektapro system incorporated picture contrast/brightness manipulation to standardise any lighting variations. For the angled samples the Ektapro was tilted by an identical angle so that a similar shot of the weld is produced for comparison with the flat welds. The pictures were initially recorded onto high speed video on which all the film analysis was performed and then systematically transferred onto VHS video, any hard copies were produced by a screen printer.

#### **3.4.6.2 Results of the Filming**

Shown in figure 3.30 are the characteristic weld profiles and stills of the welding action for the various joint configurations, and the best angle conditions. Immediately apparent is the porosity inclusions and the humping defect in the milled and guillotine 1 and 2 fit-ups. Guillotine 1 sample exhibited regular hump formation across the weld length of approximate 4 mm spacing at 230 mm/s travel speed giving a frequency of roughly 60 Hz. The hump evolved from behind the plasma cloud and therefore close to the keyhole, swelling to size in a matter of milliseconds and solidifying at the point of generation, not being carried along in the wake of the melt pool. The sequence of pictures shown in figure 3.31 highlight the temporal formation of the hump at 2 ms time intervals. The milled and guillotine 2 showed irregular humping, with an observed 33 Hz modulation in the melt pool

The “best” result was obtained with both burrs angled downwards, the melt behind the keyhole is of smaller width with slight hump formations along the weld length. In this case the detection of these defects was only possible by checking the smoothness of the bead surface by touch.

The formation of the hump occurred when there was an upwelling behind the keyhole at the same time that the weld pool was of a critical length. An extreme case of this welding phenomenon was the creation of slotted holes along the bead. The hump forms behind the keyhole in the normal manner then, due to the reduced pressure in the larger radius hump and stream of liquid with a smaller radius will flow into it, this may occasionally cause the remaining liquid metal to break apart to the two separate sides of the weld leaving the gap which solidified into the slot.

The maximum side angle of 30 degree was found to give the greatest weld integrity for the speed of 260 mm/s (15.5 m/min.) at 3.5 kW at the workpiece.. No traces of humping were detected on any of the angled welds over the 10 degree mark. As the maximum speed of the x-y table was 260 mm/s the limit of this angling effect could not be established. The offset of the laser beam with respect to the welding line was investigated and the optimal position found required a 0.15 mm sideways offset of the beam at the 30 degree side angle. Below this value the fusion volume was reduced resulting in occasional porosity problems and over this value humping and incomplete joining occurred.

The "plasma" was seen to be formed perpendicular to the workpiece in the case of the angled samples even though the beam was incident at 30 degrees, with the melt pool largely confined by the joint geometry.

#### **3.4.6.3 Discussion of the high speed videos**

The formation of the humps in laser welding has been previously described by Beck *et al* (1991)[37b] and Gratzke *et al* (1992)[38]. The former identified a high pressure stagnation point at the end of the melt pool with the occurrence of the hump, whilst the latter modelled the melt pool on the instability of a semi bounded cylinder under the action of kinematic forces (surface tension). Beck *et al* have mapped out flow lines in the melt pool, thus identifying the cause. The high speed filming done here agrees with this, the hump being more likely to form under extreme melt pool flow conditions resulting from increasing welding speed. The

Gratzke model is concerned with assessing the limiting conditions under which the hump will occur, having assumed its formation. An instability criterion is forwarded, which simplifies to the ratio of melt pool width/length ( $j$ ). The melt pool is stable (no humping) when  $j > 0.11$ . The  $j$  ratio is included in figure 3.30.

The tendency of the different joint fitups to show the humping defect, and the improvement of the angling/offset method can be explained in terms of weld geometry and the stabilisation criteria.

The humping was alleviated with the “burrs down” guillotine configuration, the filming showed the upwellings were attenuated in the V slot reducing the tendency of hump formation. This was confirmed when a gap of 0.1 mm was introduced between two milled edges - the humping tendency under identical processing conditions were eliminated in the gap sample, and a sound weld was produced. The figures of the estimated  $j$  factors for individual weld geometries confirm the above. The humping phenomenon appears to be accentuated by restrictive melt flow conditions when the joint configuration and/or heat flow restriction induces fluid flow confinement.

The angled sample/offset laser combination increases the critical speed for the onset of humping by stabilising the melt pool. This combination causes the beam to cover a larger surface area tending to create a wider melt pool, reflected in the increased  $j$  factor. The formulation of the model means greater accuracy is achieved when the weld is non-penetrating. A more speculative reason may relate to Beck's observation of the stagnation point. An asymmetric flow system could be produced as a direct result of an imbalance in distribution of material either side of the weld centreline (figure 3.32). This modification of flow conditions may prevent/attenuate the stagnation point and the formation of any “would be” hump.

Observation of humping suggest the two theories, Beck and Gratzke, are both correct. The sequence in figure 3.31, although not well defined, depicts the hump formation as a mass of ballooning melt just behind the keyhole in line with Beck. The

instability theory is also supported (not shown in figure 3.31), particularly in non-penetrating welds, where the hump occurs at the rear of the melt pool.

A further point shown by Hiramoto *et al* (1987)[39] was that only a maximum reduction in welding depth of 20 % was exhibited with the occurrence of the hump. This is confirmed with the lack of penetration being a definite common factor between welds exhibiting humping.

The tolerances of the described angling technique, with regard to optimal angle and offset distance, are very much related to the focal length of the optics, the mode structure, position of focus and to a lesser extent the raw beam diameter - basically those factors which are fundamental in characterising the spot size at the workpiece. Related to the conventional flat welding position the fit-up is more forgiving for any discontinuities of the sheared edges, although no figures are available. It also must be mentioned that the PRC Corporation have already patented a form of weld fit-up for the manufacture of tin cans [40], involving the angling of both edges upwards, this method although it is in a slightly similar vane does not in any way contravene this patent.

#### **3.4.7 The Application of a mathematical model**

It is useful in any process to have the predictive means to assess an outcome **without** having to actually perform the experimentation. This section looks at the implementation, as opposed to the development of a mathematical model of laser welding. In assessing the model most suited to the laser welding of sheet steel the first question is, what is required from the model ? - the penetration, weld and HAZ width, cooling rates, weld profile or dynamic plasma and melt pool behaviour. There are two sides to this question, from the point of view of the manufacturers and the researchers

It has to be said that the modelling of thin gauge material has traditionally been the poor relation of deep penetration welding. Recently though, a shifting of

emphasis has occurred with the realisation that high speed sheet welding is a definite winner for the future. There are three basic forms of modelling; analytical, numerical and statistical, of which the latter two rely on existing experimental data and are more specific in application versatility. The analytical is a fundamental descriptive tool.

The analytical modelling of sheet material is described best by the use of a 2 dimensional line source, which assumes a negligible through thickness temperature gradient as I believe is evident from the profiles already shown. Another major difference between deep penetration model considerations and thin gauge is the "plasma factor", which at high speed becomes increasingly unimportant. Therefore, the inclusion of a plasma absorption/beam diffusion coefficient is not as critical, what is however is consideration of the absorbed laser energy. The assumption that 100 % beam absorption occurs in the black body keyhole does not apply, a loss term must be included for the laser radiation which is lost by simply passing through the keyhole as a function of the welding speed.

The foundation of heat flow modelling today are the papers of Rosenthal (1941,1946)[41], Carslaw and Jaeger (1959)[42] and later Swifhook and Gick (1973)[7]. Assessing the fluid dynamics of the melt pool offers an alternative modelling basis, initially developed by Andrews and Atthey (1976)[43] and Klemens (1978)[43], and in recent years Dowden and Kapadia (1981,1992)[45]. The use of these models may present a more accurate picture by the inclusion of the flow conditions driven by convective, surface tension and viscosity forces subject to the initial beam absorption. At the higher processing speeds and powers the melt pool fluid dynamics become increasingly important in *controlling the welding mechanism*.

The decision then, is the Swifhook and Gick model, although an older model it is still a fundamental paper.

As the model stands, the predicted weld dimensions for a particular set of



energy input conditions are somewhat high, as would be expected as heat losses are ignored. However, the inclusion of a scaling factor, found simply through minimal experimentation allows the universal practical application of the model. In this case the scaling factor was 0.6 to give the adjusted model as -

$$P_{\eta} = 0.3vwt (\rho C_p T_m) \quad (3.18)$$

All symbols as from section 3.2.1.1

All through this chapter the results have been referenced to the Swifthook and Gick model. It has proved to be valid across the processing ranges from laser power of 1 - 3.5kW and welding speeds of 40 - 260 mm/s.

	Depth	Top width (W1)	Underside width (W2)	Hardness	Melting Efficiency	Joining Efficiency
MODE	0.03	0.038	0.06	0.53	0.08	0.028
SIDE ANGLE	0.04	0.025	0.044	0.52	0.1	0.09
POSITION OF FOCUS	0.03	0.03	0.05	0.31	0.07	0.055
SPEED	0.0001	0.0001	0.0001	0.0001	0.0001	0.0001
POWER	0.0001	0.0001	0.0001	0.08	0.0001	0.0001
LENS FOCAL LENGTH	0.0188	0.04	0.055	0.36	0.025	0.025
POLARITY	0.09	0.4	0.023	0.05	0.2	0.2
NORMAL ANGLE	0.035	0.1	0.12	0.91	0.15	0.03
<b>INTERACTIONS</b>						
POWER/ NORMAL	0.03	-	0.029	-	-	-
POWER/ LENS	0.02	0.03	-	-	-	-
SPEED/ LENS	-	-	-	-	0.01	0.03

**Table 1** Summary of the significant probabilities for the welding variables and selected responses, showing both main effects and first order interactions

Parameter	Laser Ecosse AF5			Electrox M1500 TEM01*
	"Good" TEM00	"Bad" TEM00	TEM01*	
Raw beam size (D, mm)	19	22	28	18
Focal length (f, mm)	100	100	100	100
F-Number	5	4.5	3.8	5.6
M2 Factor	5	6	7.5	2.7
Calculated minimum spot size (mm)	0.31	0.34	0.36	0.2
Power at Workpiece (kW)	3.5	3.5	4.5	1.5
Calculated Maximum power density (W/cm <sup>2</sup> 10*6)	4.6	3.8	3.9	4.7
Measured Spot size (mm)	0.38	0.5	0.6	0.32
Measured power density (W/cm <sup>2</sup> 10*6)	3	1.7	1.59	1.8

**Table 2** Comparison between the beam characteristics of the Laser Ecosse AF5 and Electrox lasers plus the effect of the mode quality.

Weld Type	Specific energy (kJ/mm <sup>2</sup> )	Weld Thickness	Tensile (Yield Strength MPa)	Micro - Hardness (HV)	Erichsen (mm)
Base Metal	NA	0.98 ±0.02	182 ±35	120 ±10	10.9 ±0.8
Profile 1	400±100	0.96 ±0.02	167 ±30	240 ±30	10.5 ±0.5
Profile 2	250±75	0.98 ±0.01	166 ±20	290 ±20	10.5 ±0.3
Profile 3	130±50	0.98 ±0.01	165 ±20	370 ±20	10.5 ±0.5
Profile 4	140±60	0.99±0.02	177 ±35	310 ±40	10.3 ±0.6
Profile 5	50±15	0.98 ±0.01	157 ±10	380 ±50	6.93 ±3
Faulty Weld	NA	0.98 ±0.01	157 ±10	400 ±50	6.69 ±0.5

**Table 3** Summary of post weld mechanical properties averaged over a series of testing programmes (10 samples/profile group) with the inclusion of sample variation bands.(see section 3.2.2 for profile definition)

VARIABLE	WELD DIMENSIONS			Bead profile	Weld Strength	Weld faults
	DEPTH	W1	W2			
Mode Structure	TEM <sub>00</sub>	TEM <sub>01</sub>	TEM <sub>00</sub>	TEM <sub>00</sub>	No effect	No effect
Side Angle (Degrees)	No effect	10°	10°	10°	No effect	No effect
Position of Focus (mm)	+1.0	-1.0	+1.0	+1.0	+1.0 Lower hardness	No effect
Focal Length (mm)	100	150	No effect	100 Narrow & deeper	100 Higher hardness	150 Higher Porosity
Normal Angle (Degrees)	5.5°	5.5°	0°	5.5°	No effect	No effect
Power (kW)	3.5	3.5	3.5	3.5	1.5 Higher hardness	3.5 Higher porosity
Speed (mm/s)	40	40	40	40	140 Higher hardness	40 Higher porosity
Laser Polarisation	Parallel	Parallel	Parallel	Parallel Deeper	No effect	No effect
KEY	REQUIRES FURTHER INVESTIGATION					

Table 4 The results from the initial programme for the optimal conditions for welding thin sheet mild steel are presented, highlighting are those requiring further experimentation

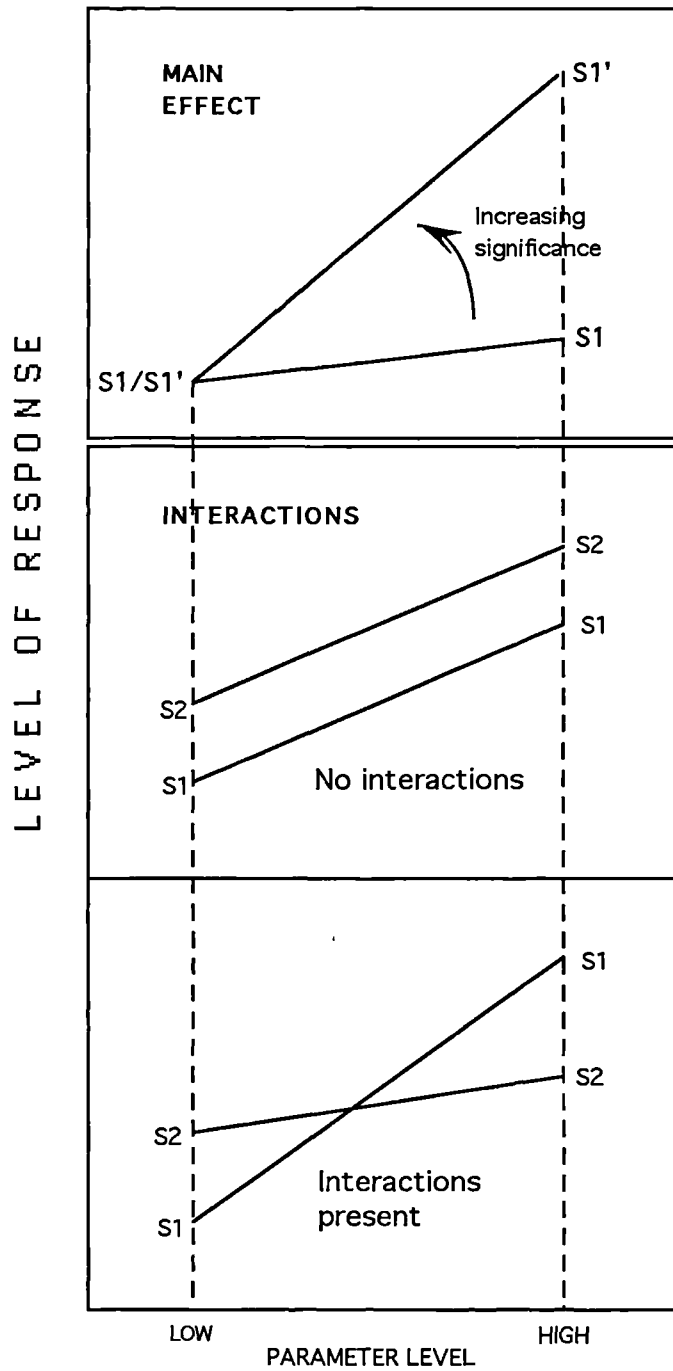


Figure 3.1 Shows the interpretation of the graphical data for one variable on a response and a combination of two variables on a response.

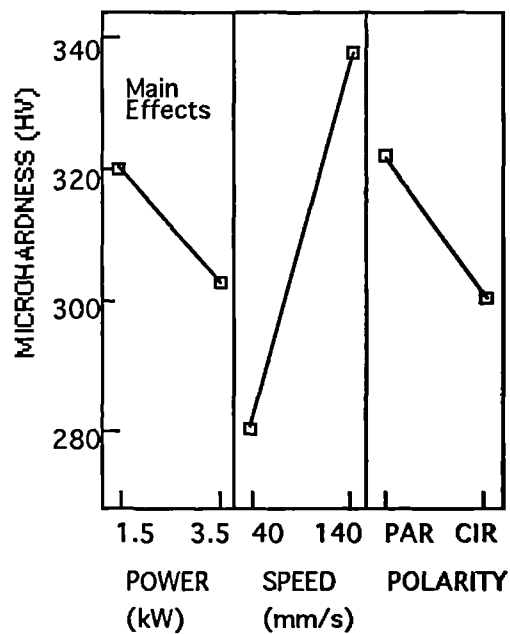
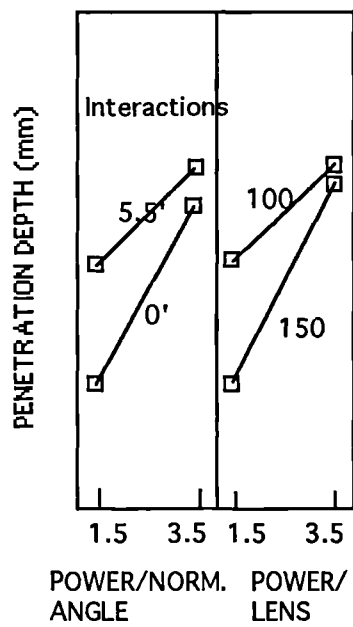
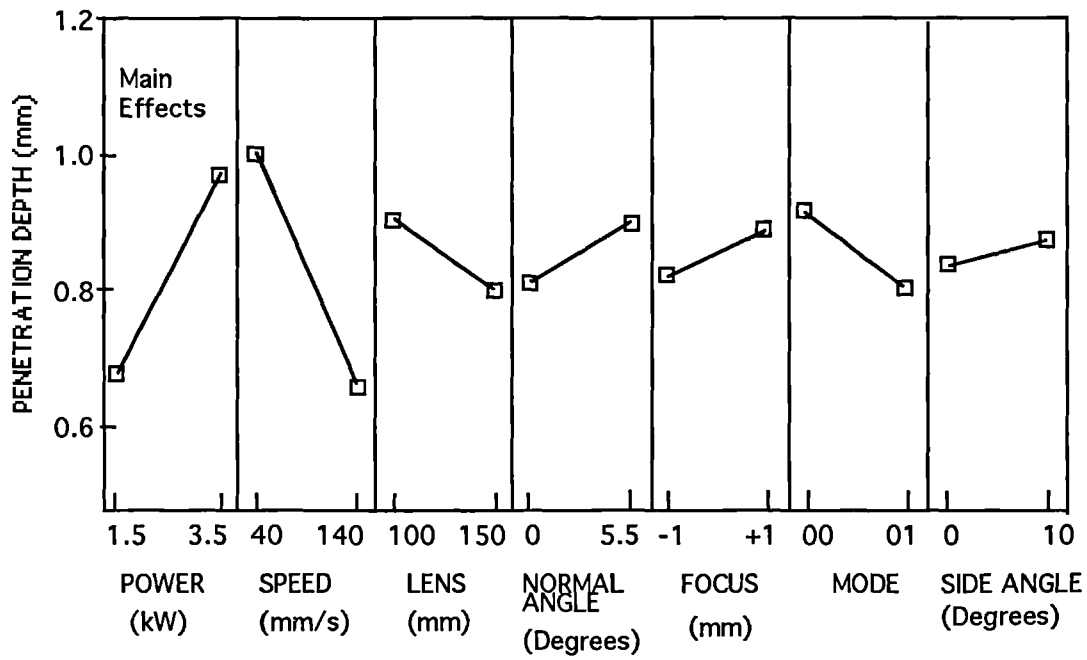


Figure 3.2 Main Effects and interactions for penetration depth and hardness responses.

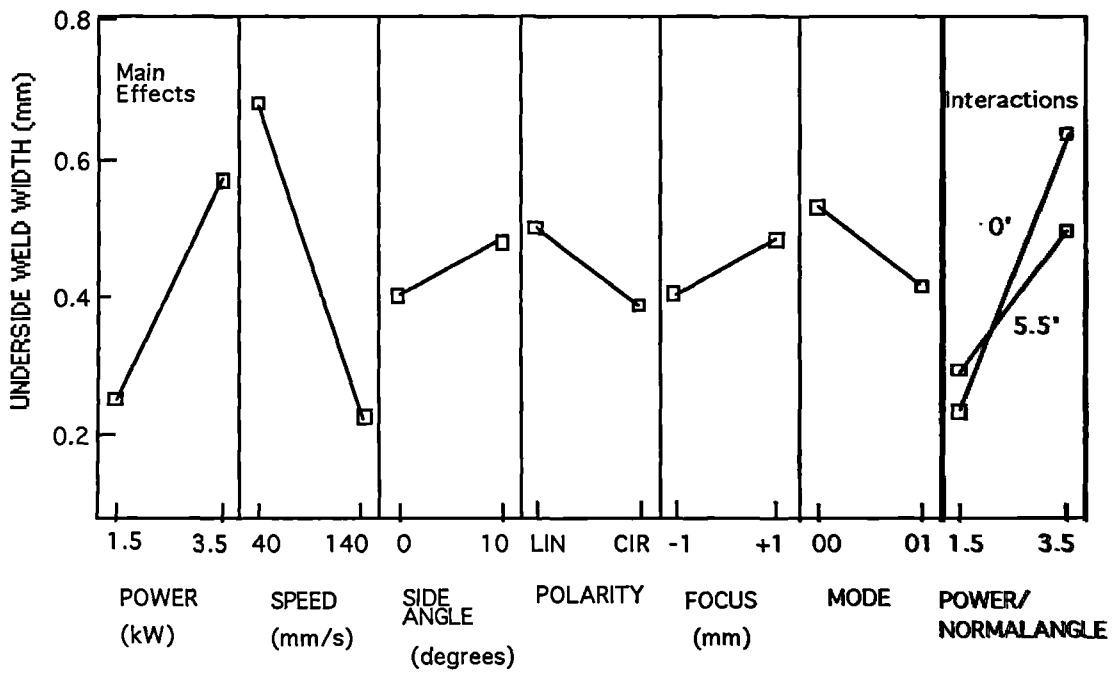
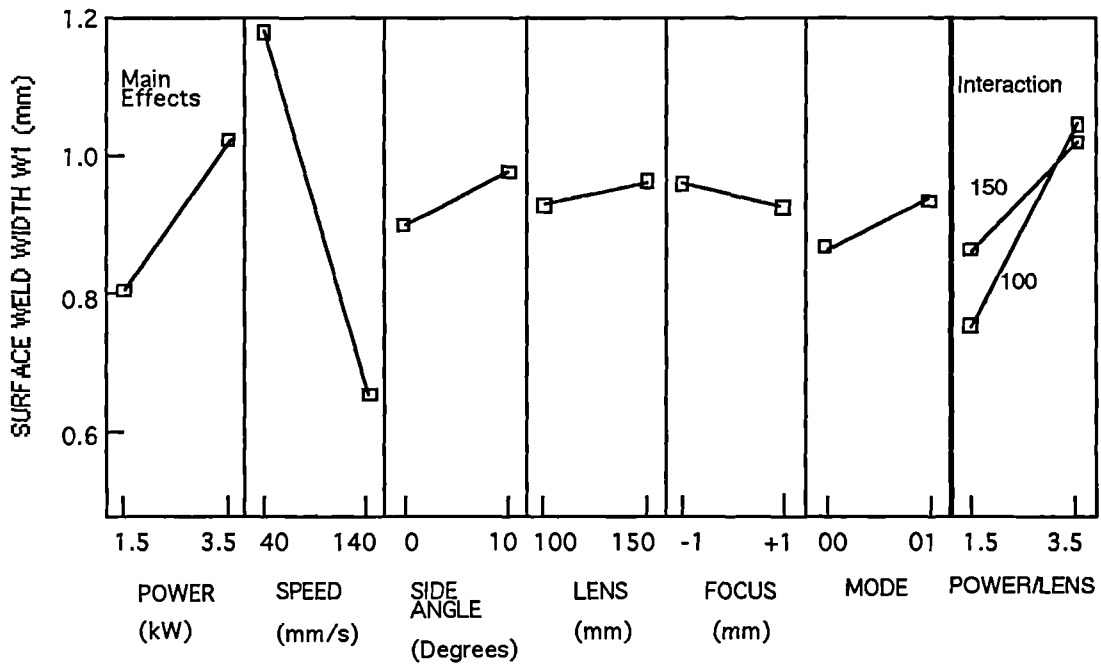


Figure 3.3 Main Effects and Interactions for surface and underside weld width responses, W1 and W2 respectively.



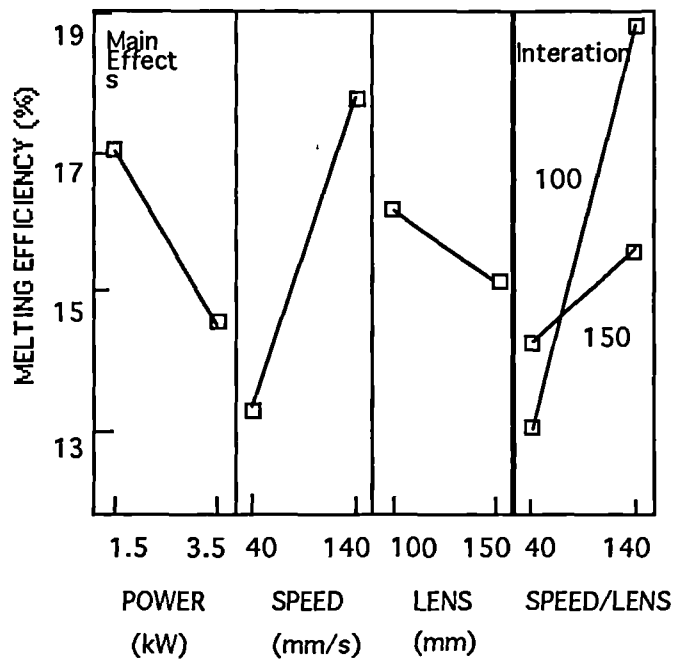
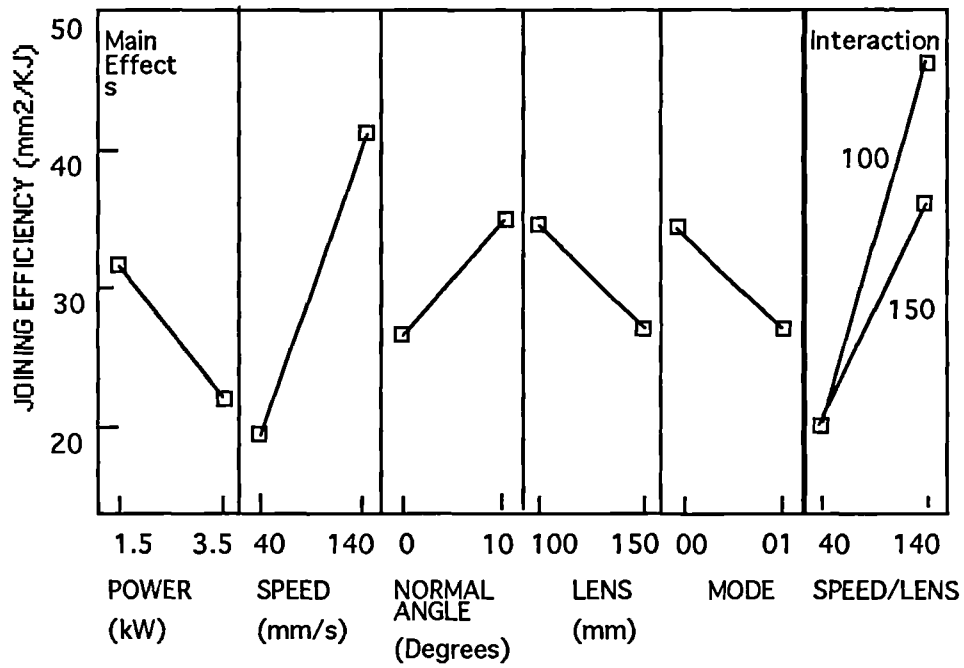


Figure 3.4 Main effects and interactions of Joining and Melting efficiency responses.

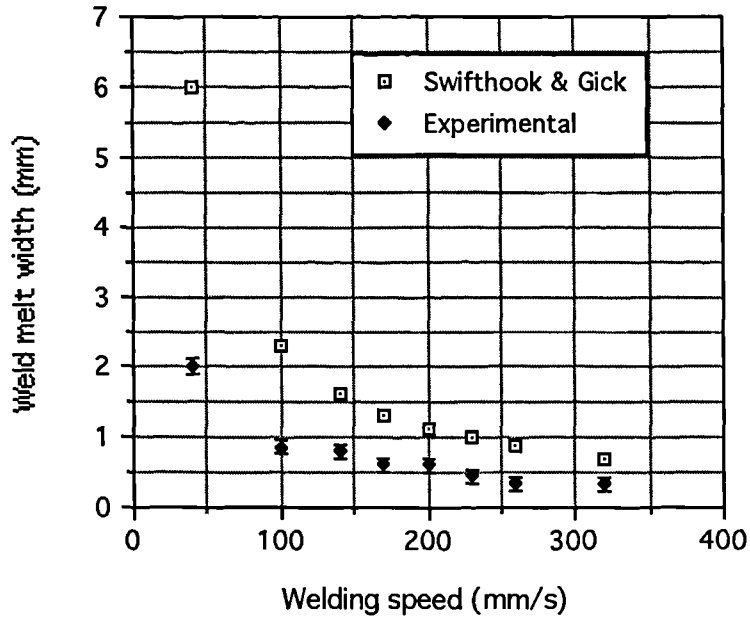


Figure 3.5 A comparison of the Swifthook and Gick model to the experimental results, for 3.5 kW, the experimental values being averaged over all other parameter levels.

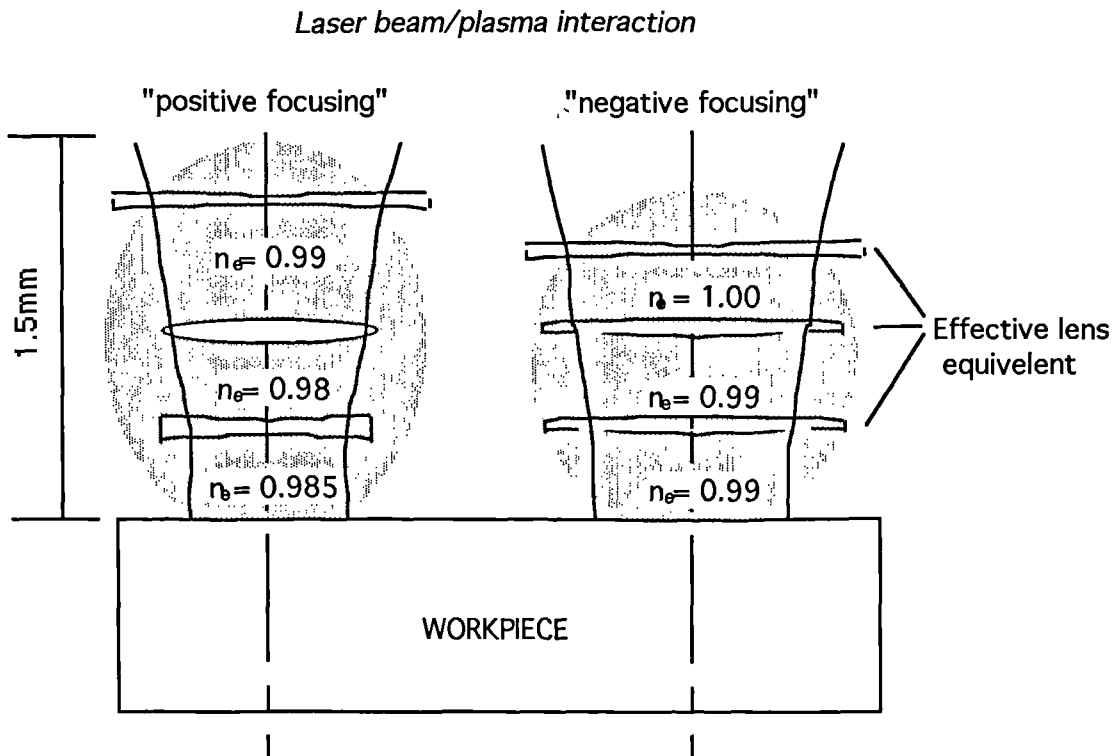
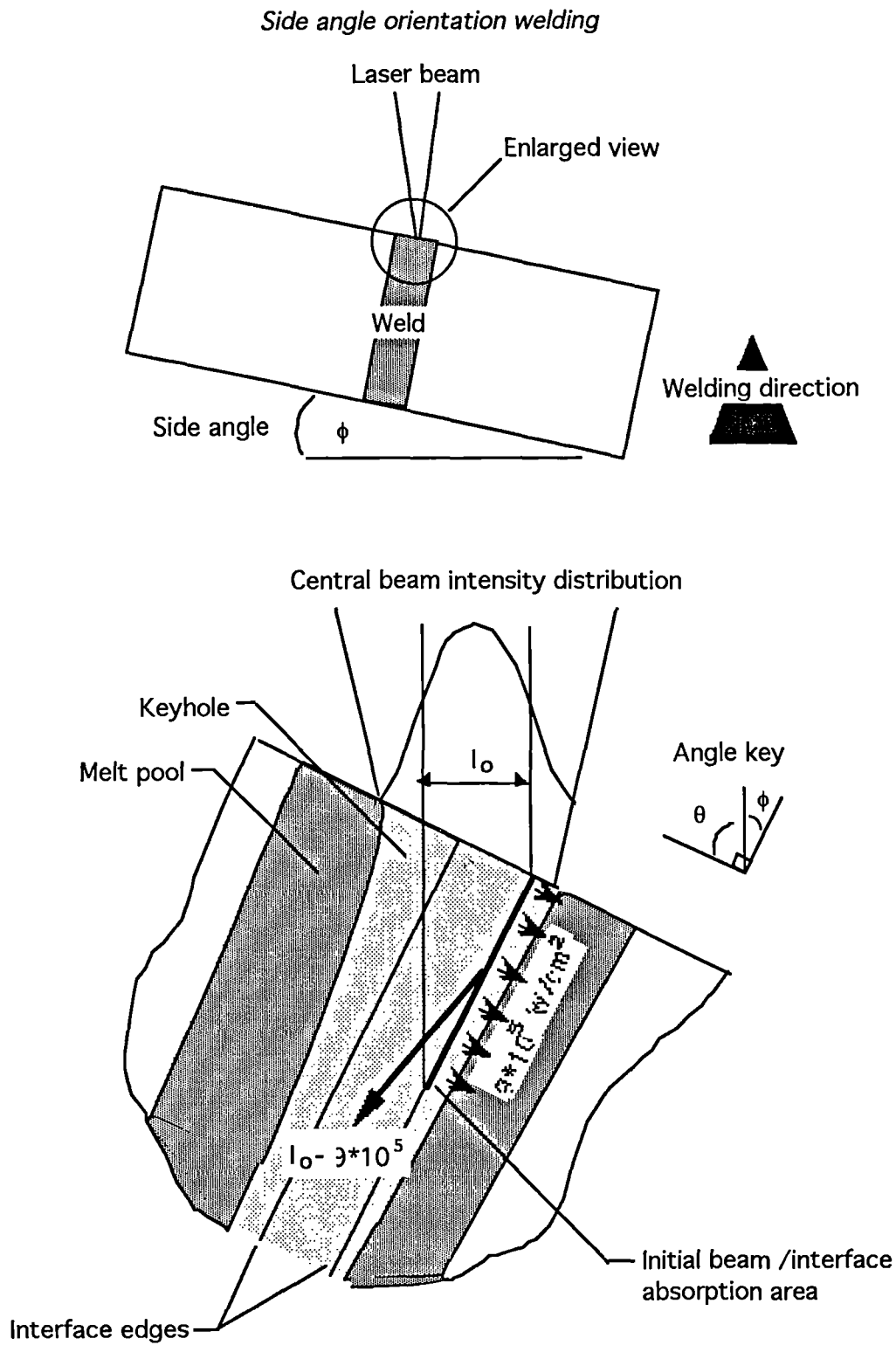
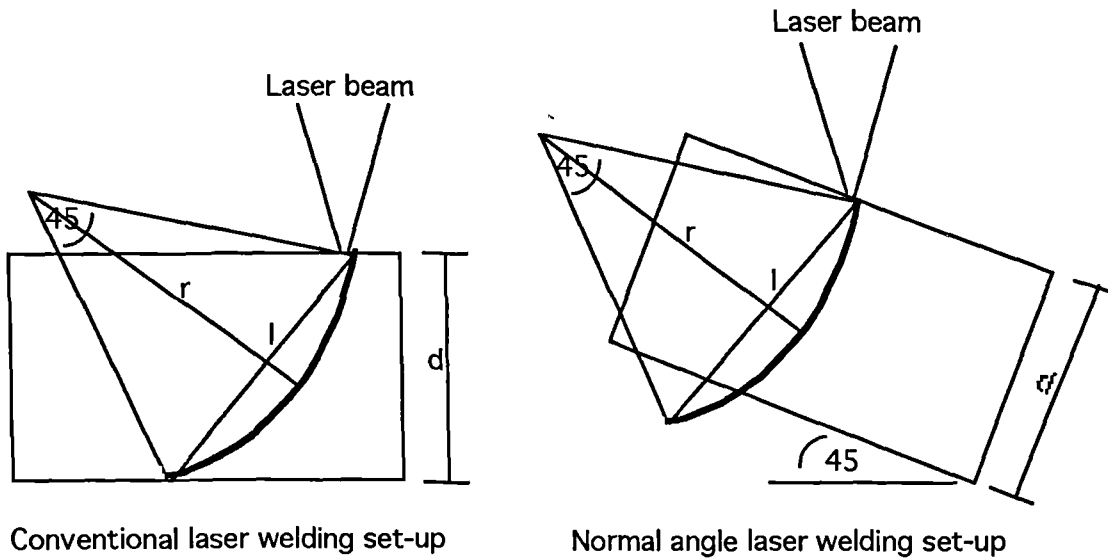
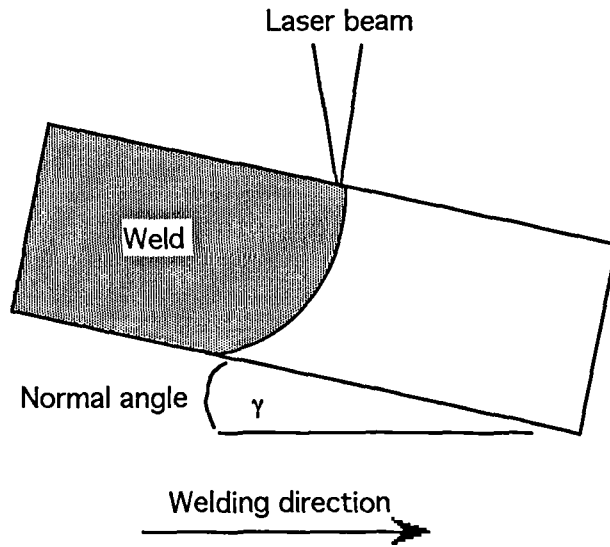


Figure 3.6 Exaggerated beam diffraction in the plasma by localised plasma refraction indices for the two focusing conditions, at 3.5 kW and 140 mm/s, Nitrogen at 20 l/min. coaxial.

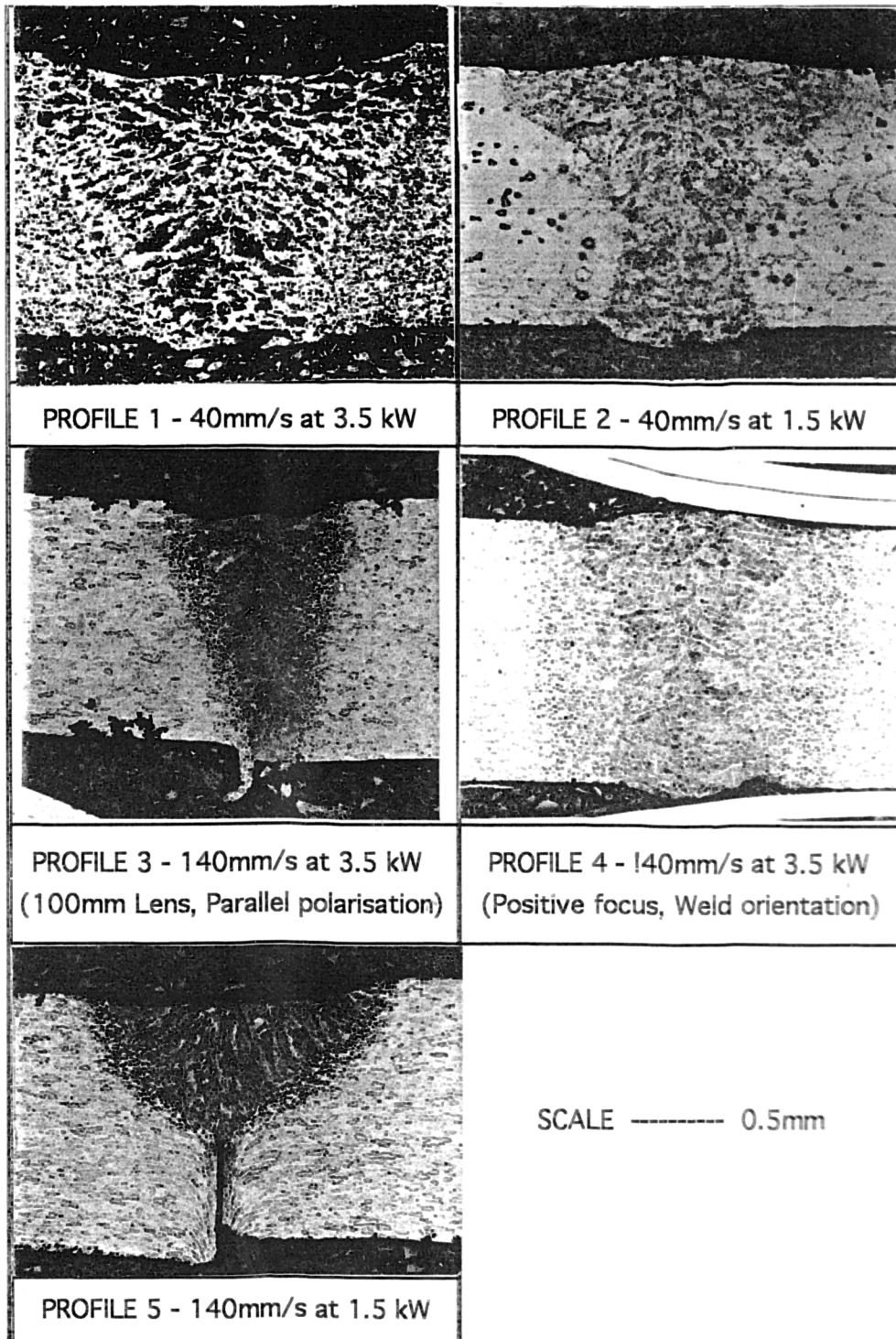


**Figure 3.7** Schematic of side angle orientation depicting the beam/joint interaction, regarding the redistribution of beam density on the interface. With the keyhole and weld following the joint interface line.

*Normal angle orientation welding*



**Figure 3.8** Using simple geomtry the normal angle welding arrangement indicates the increased penetration by optimisation of the keyhole angle with repect to the workpiece.



**Figure 3.9** The five weld profiles characteristic of the welding programme, along with processing conditions and common factors.



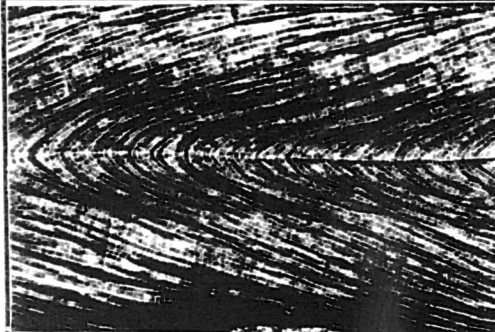
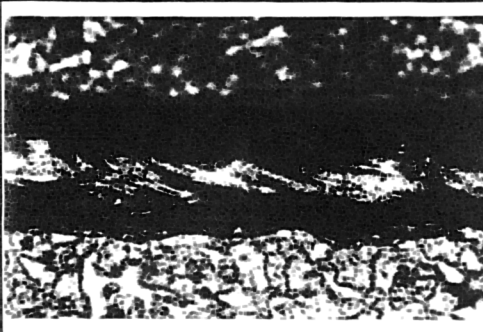
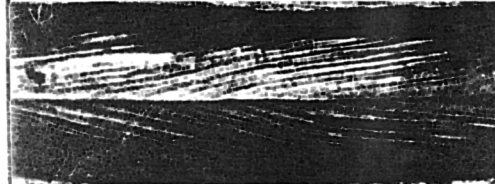
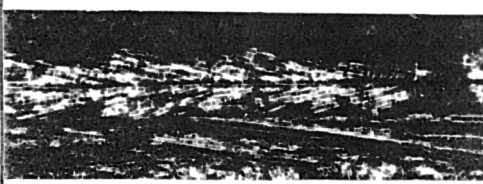
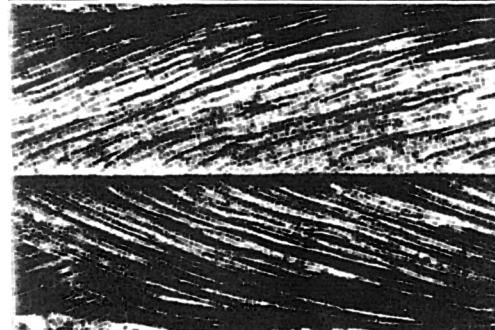
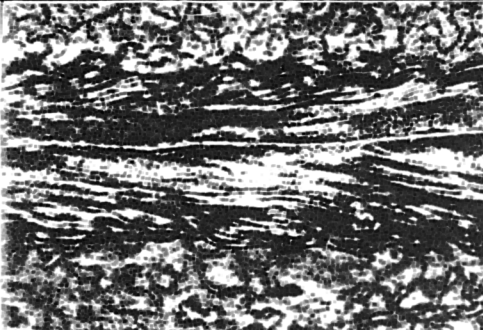
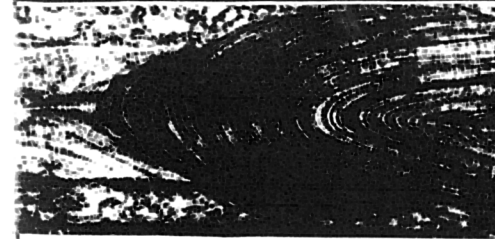
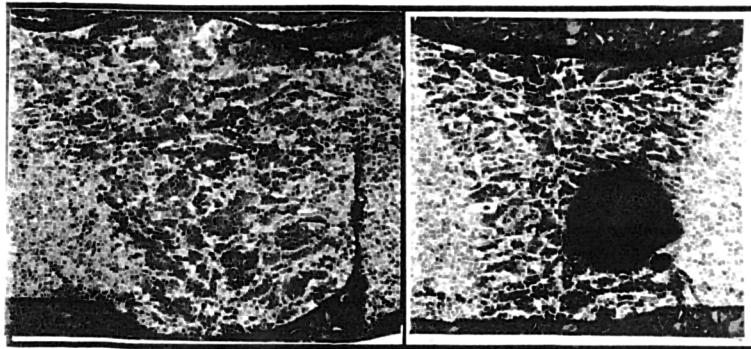
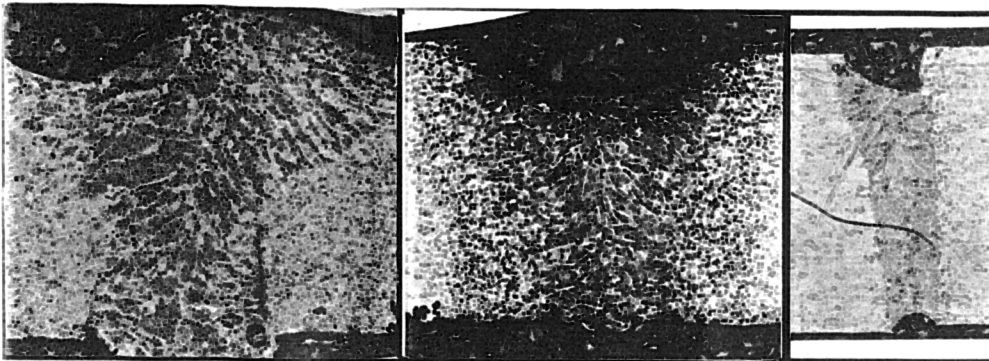
Top surface	Welding level	Underside
	1. 40 mm/s at 3.5 kW.	
	2. 40 mm/s at 1.5 kW.	
	3. 140 mm/s at 3.5 kW.	
	4. 140 mm/s at 3.5 kW.	
	5. 140 mm/s at 1.5 kW.	SCALE ——— 0.3mm

Figure 3.10 The surface and underside weld solidification patterns associated with the five characteristic weld profiles.



(a)  
Cracking - 3.5 kW & 40 mm/s

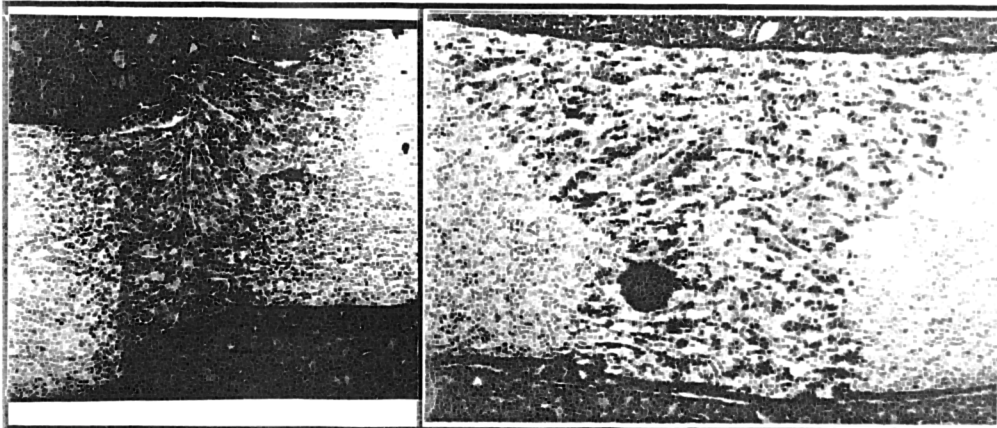
(b)  
Porosity - 1.5 kW & 40 mm/s



(c)  
Uneven weld surface  
3.5 kW & 40 mm/s

(d)  
Depression of weld cap  
1.5 kW & 40 mm/s

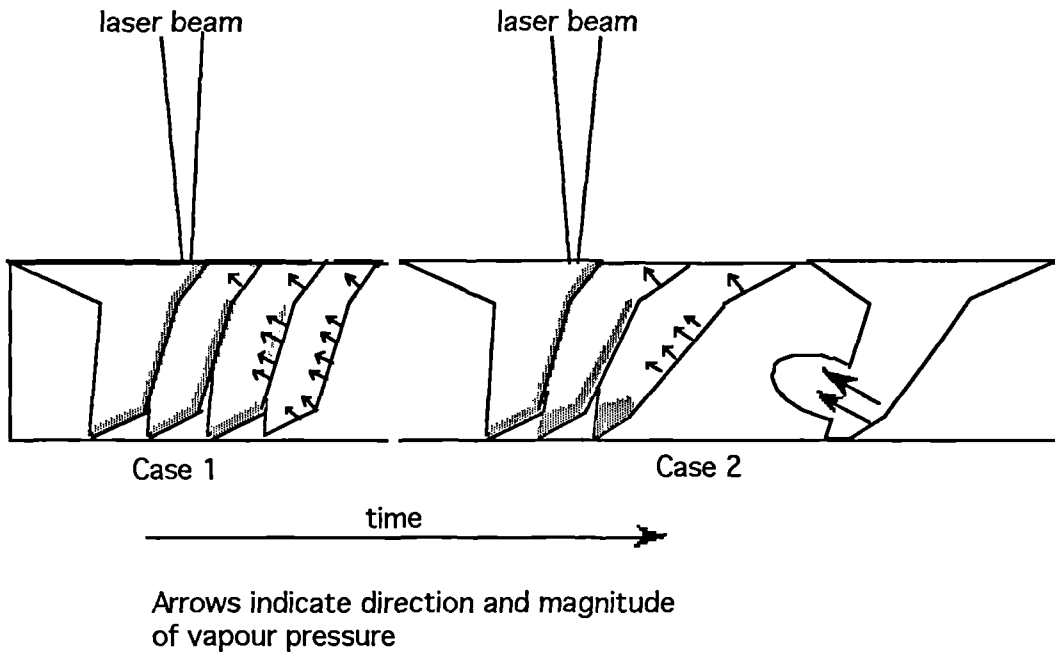
(e)  
Weld underfill  
1.5 & 140



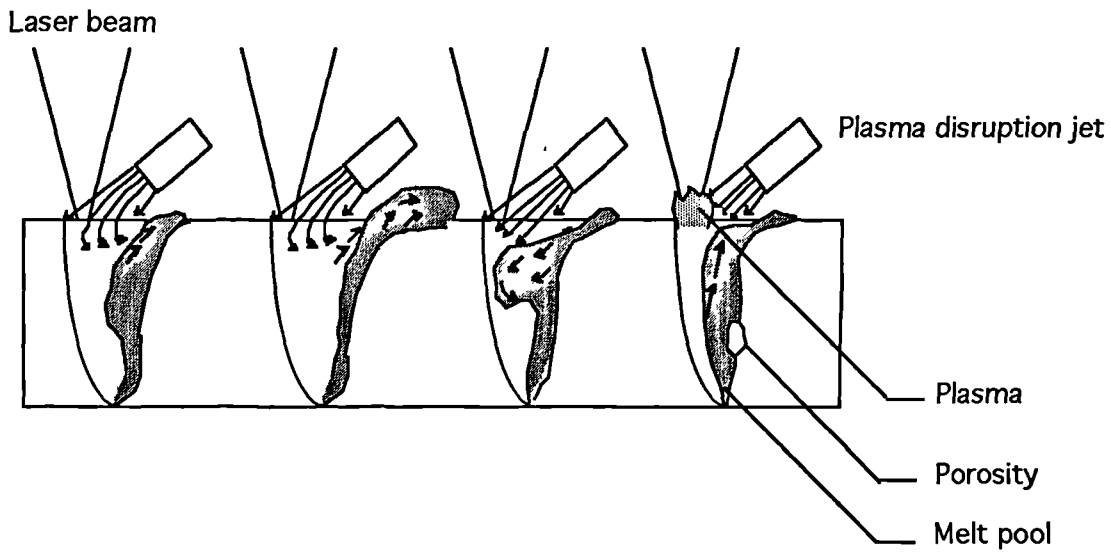
(f)  
Vertical misalignment

(g)  
Carbide deposits

**Figure 3.11** The seven characteristic weld faults identified.



(a)



(b)

**Figure 3.12** Two of the proposed porosity mechanisms **a.** An imbalance of the internal vapor pressure and **b.** The inclusion of gases or inclusions through the compressive forces ahead of the welding action.



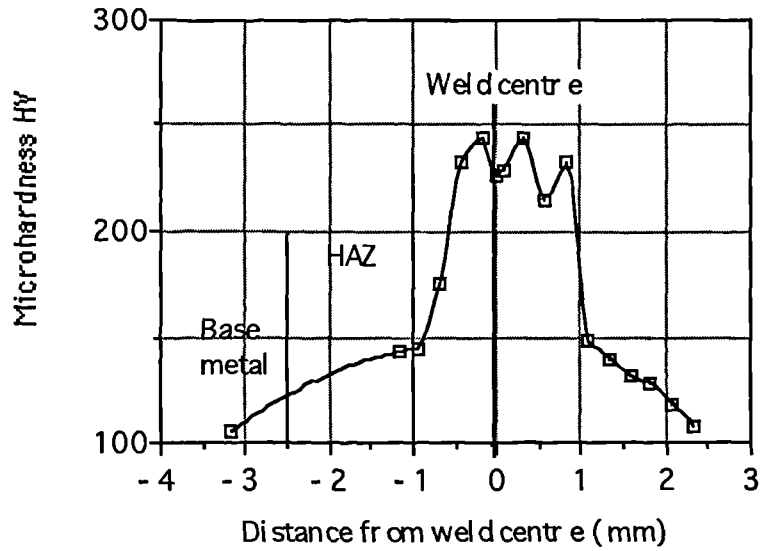


Figure 3.13 The variation of Microhardness across the weld showing the transition between fusion zone/HAZ/Base metal.

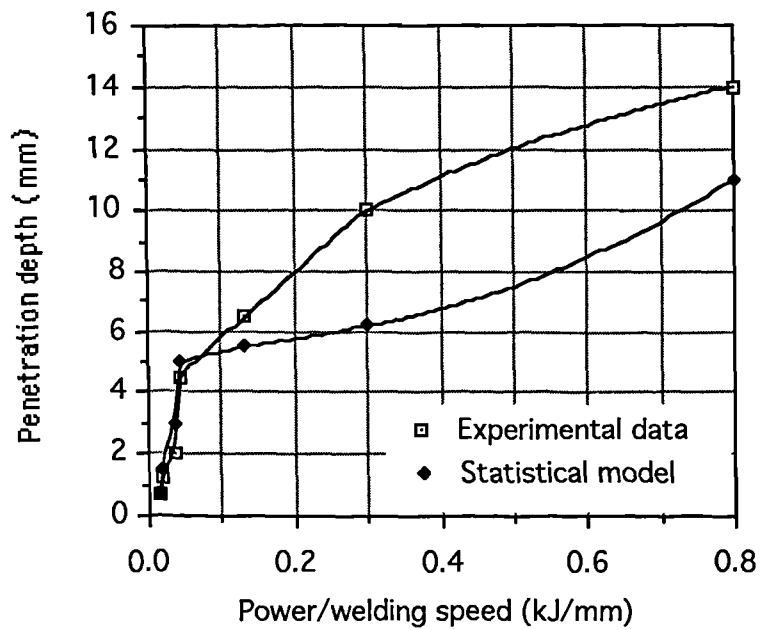
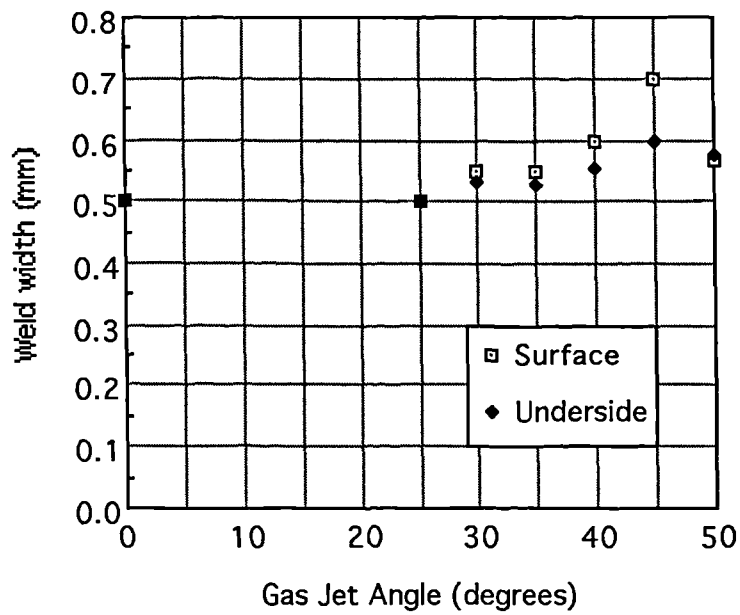
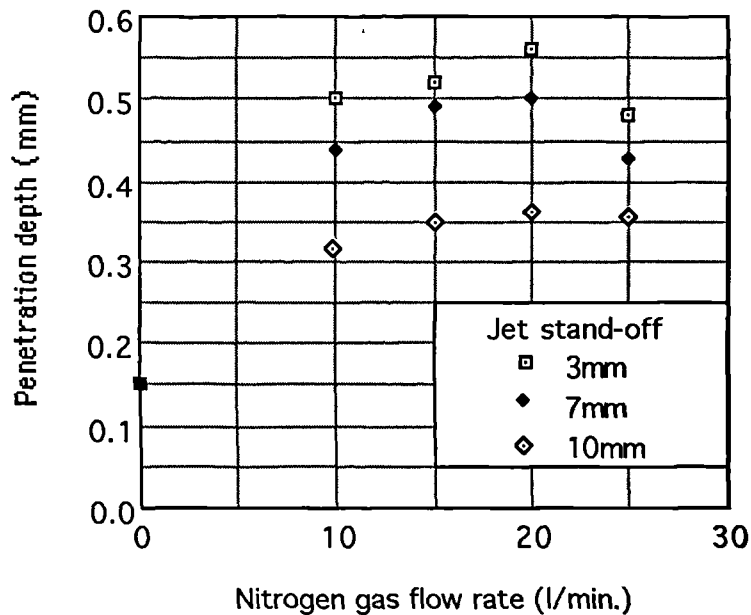


Figure 1.14 The comparison of experimental data and the statistical model, as a function of the energy input.



**Figure 3.15** The effect a of nitrogen disruption jet angle, following the weld, on the fusion zone width. Laser power at 3.5 kW and traverse speed of 140 mm/s, constant gas flow rate of 15 l/min.



**Figure 3.16** The effect of the direct distance between a 45 degree jet and the point of beam/workpiece interaction, as measured by the penetration normalised to the sample thickness.

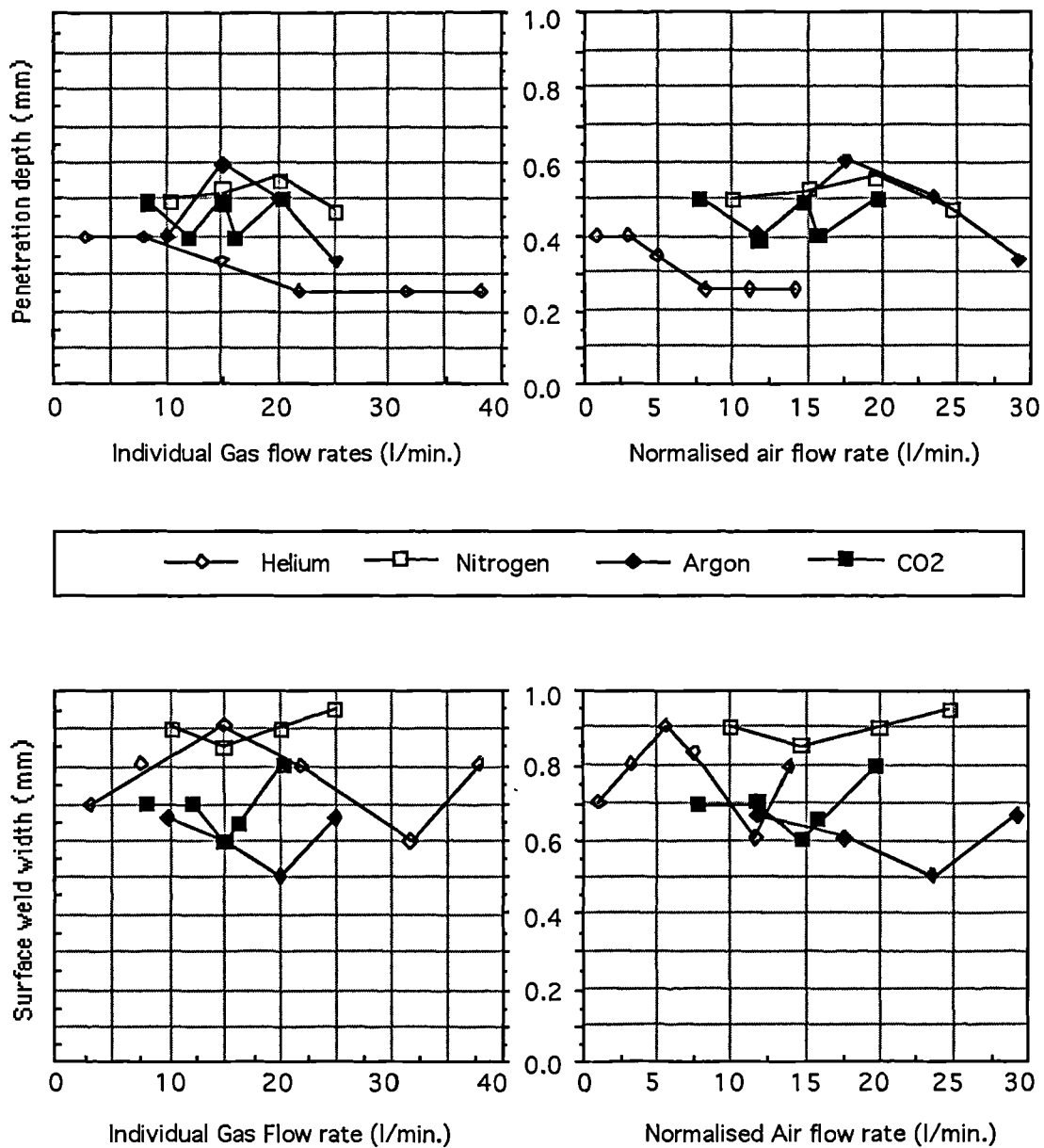
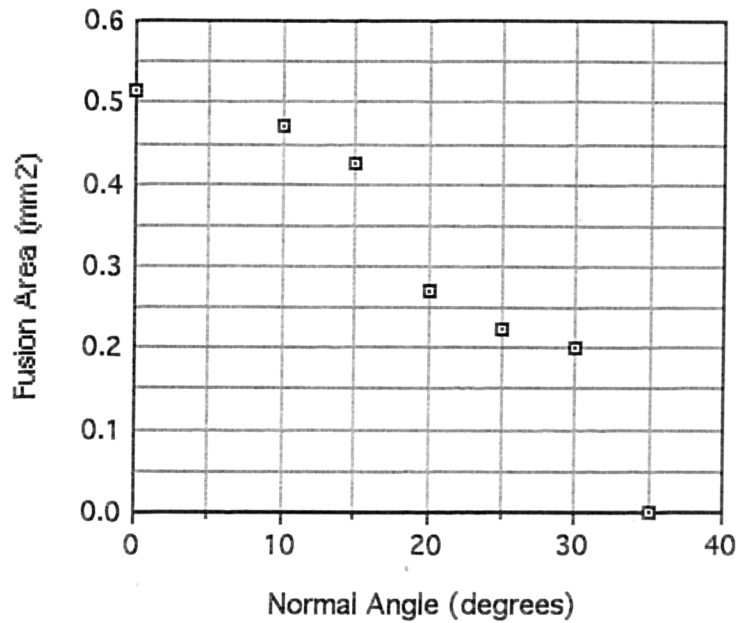
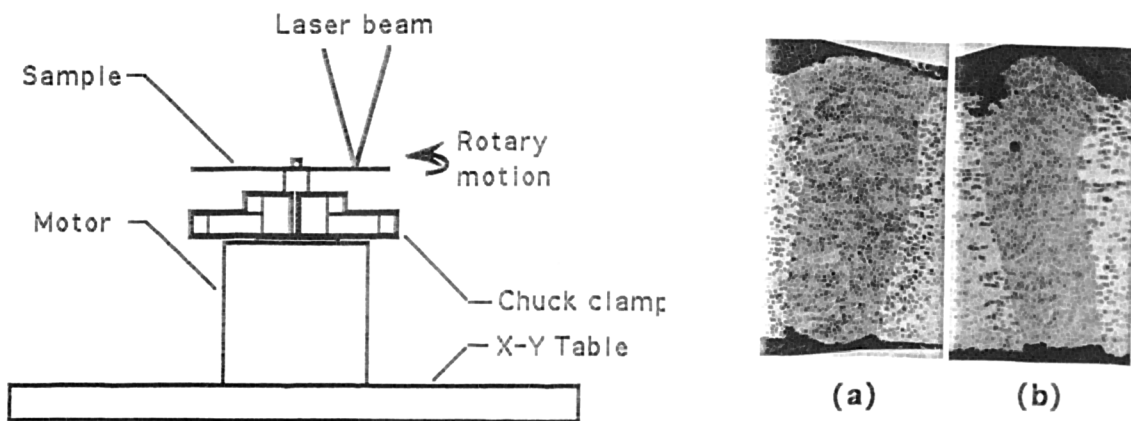


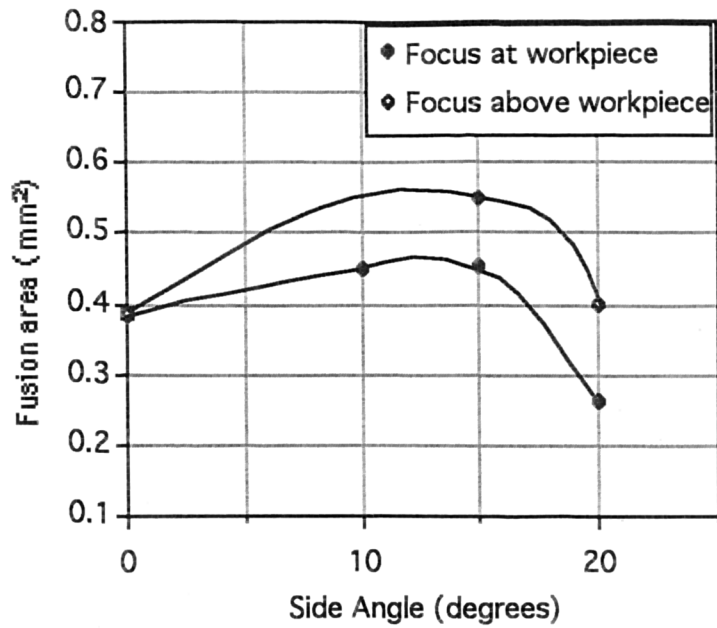
Figure 3.17 Shows the the effects of the four different gases (coaxial delivery) on the weld penetration and width, with comparative flow rates normalised to air. The conditions for the welds were 2 kW at 200 mm/s (12m/min.).



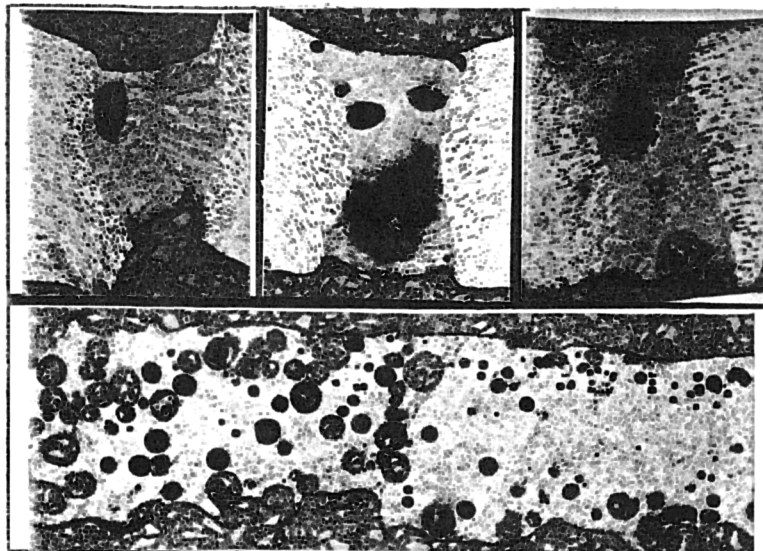
**Figure 3.18** The relationship of focal position against fusion area at 3.5 kW and 200 mm/s, below the affect of the normal angle for similar response and processing conditions.



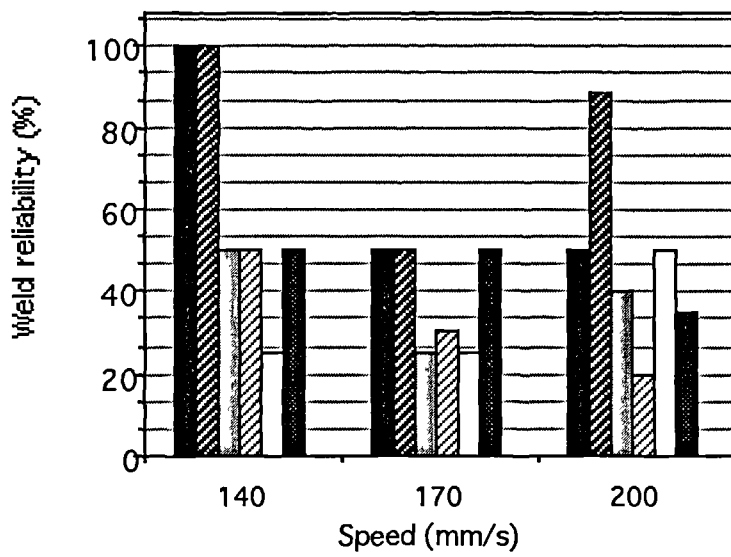
**Figure 3.19** A schematic of circular welding jig and weld profiles obtained using the high speed circular samples at laser power of 3.5 kW welding speed a) 200 mm/s and b) 315 mm/s.



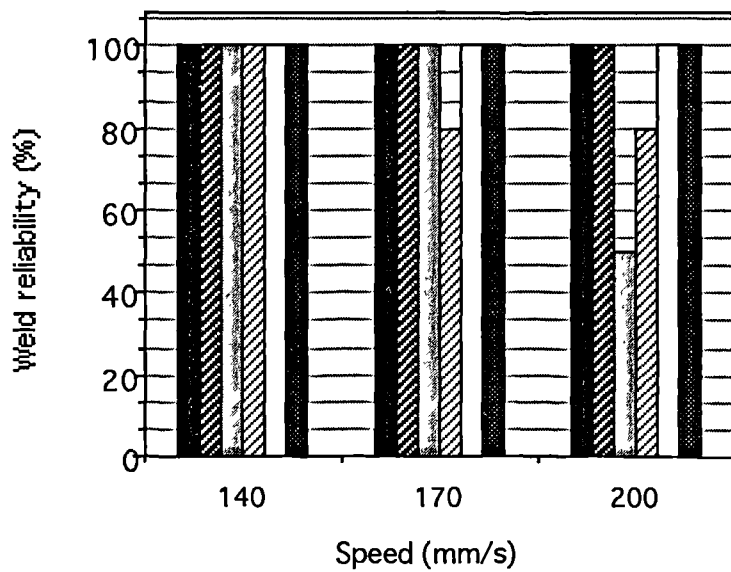
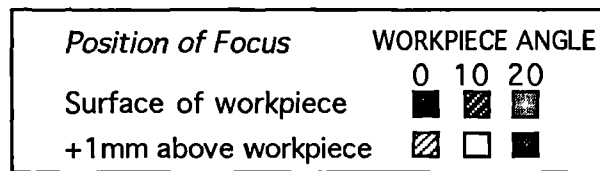
**Figure 3.20** The effect of the side angle of the workpiece on fusion area at different positions of focus for guillotine welded samples. Power is 3.5 kW, and speed was varied over 140, 170 and 200 mm/s.



**Figure 3.21** highlighting the problem of porosity with guillotine and milled edges at 3.5 kW at 200 mm/s (12.5 m/min.), also shown is a longitudinal section

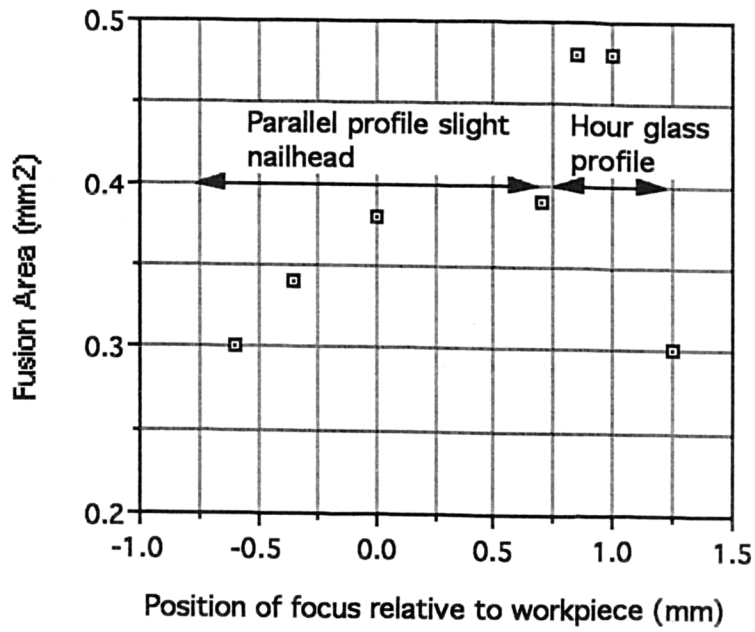


(a)

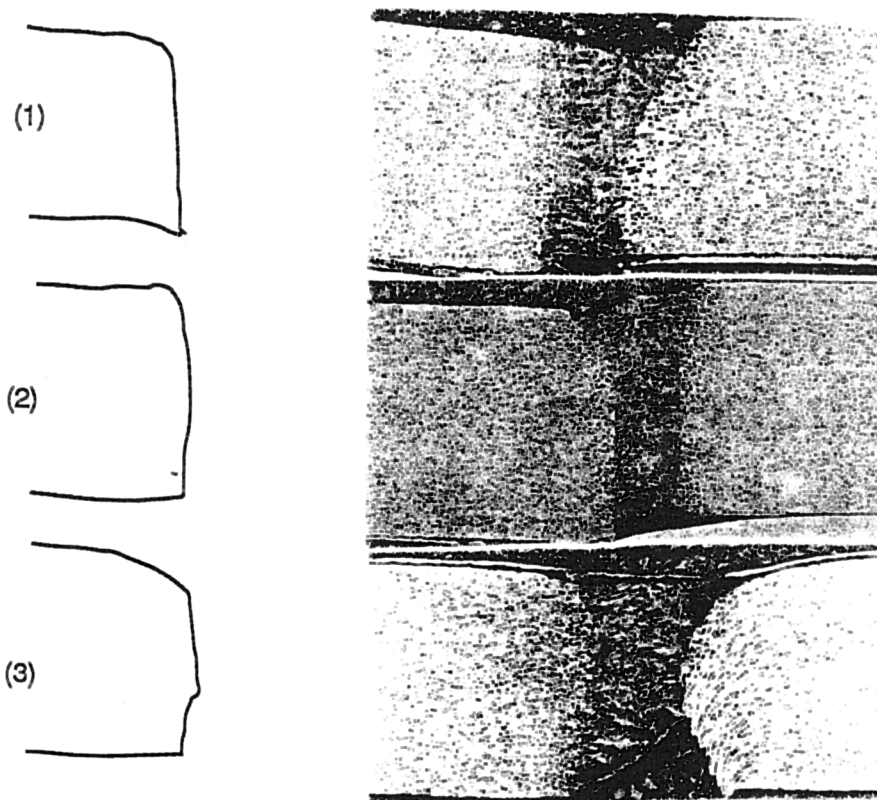


(b)

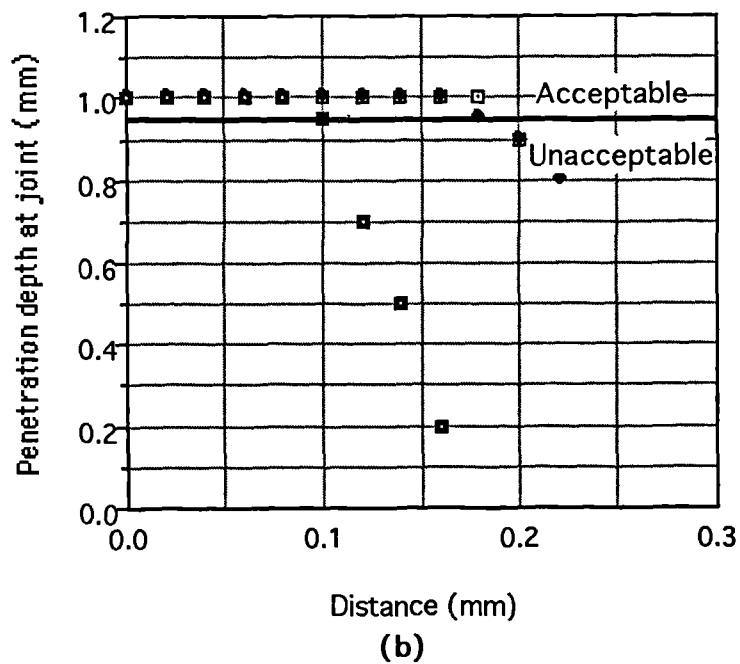
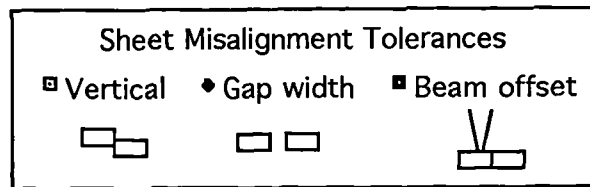
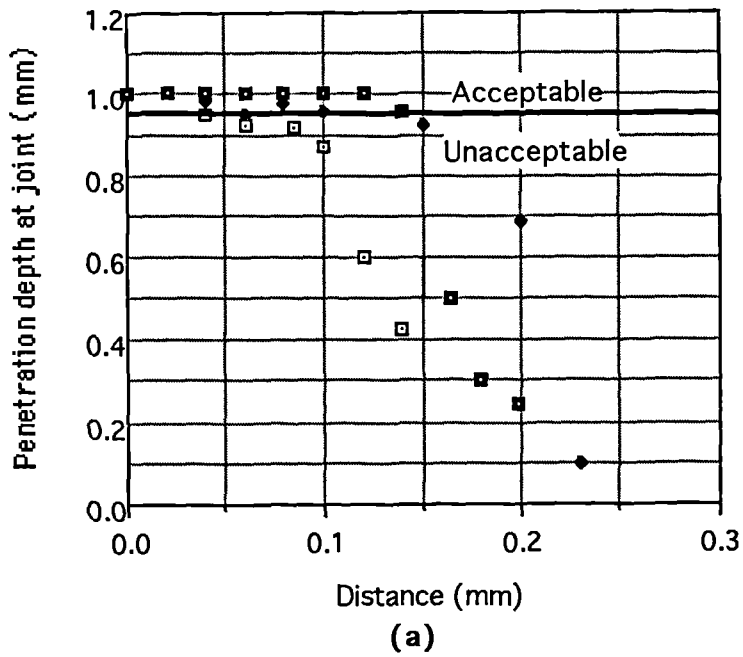
Figure 3.22 Shows the reliability of the welding for (a) guillotine edges and (b) milled edges at different speeds and inclinations corresponding to the centred key.



**Figure 3.23** The relationship of the focal position on bead area and profile at 3.5 kW and 200 mm/s.

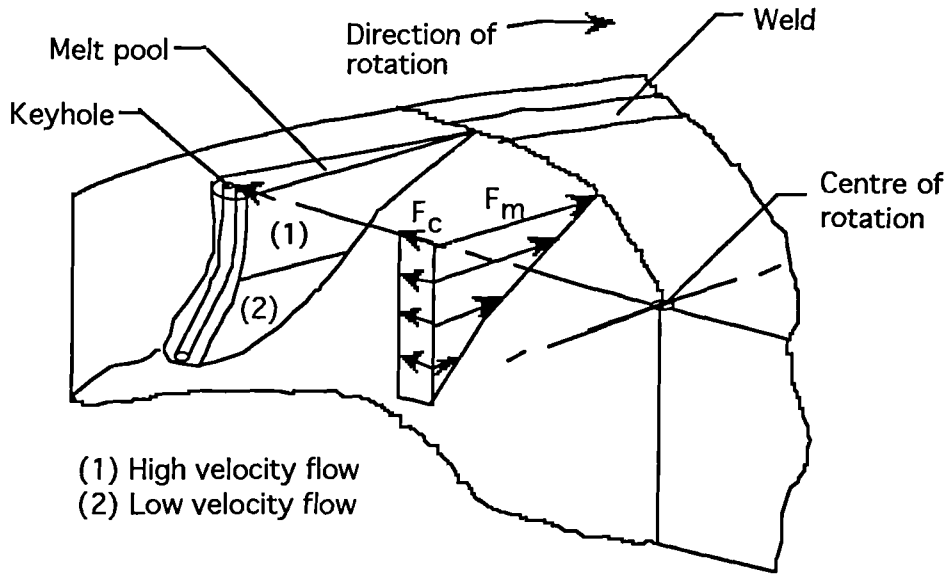


**Figure 3.24** The three types of guillotine edge possible along with the characteristic weld profile.

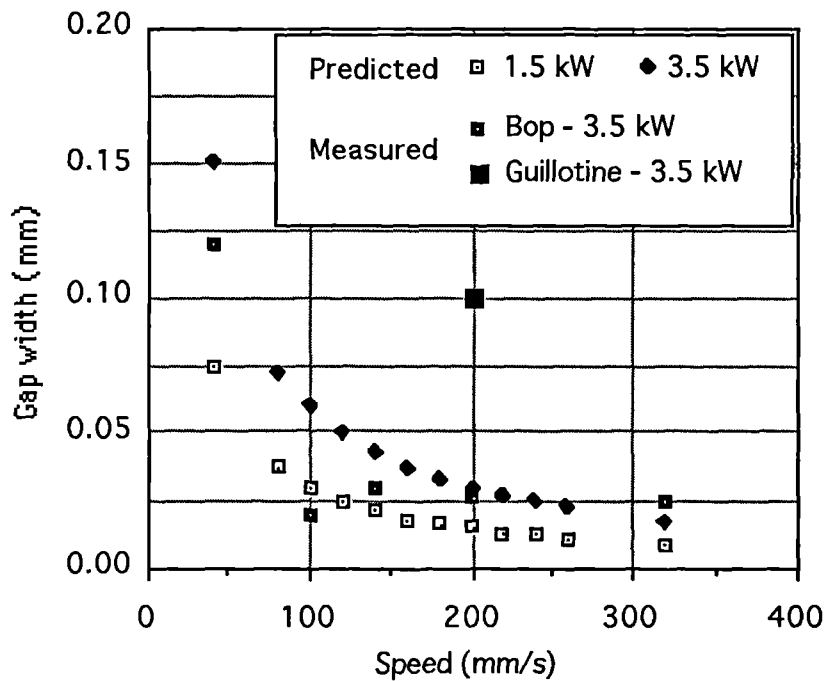


**Figure 3.25** The effect of fit-up tolerances on a) guillotine welding configuration and b) milled edged configuration, for 3.5 kW and 200 mm/s. Included is the level of acceptability.





**Figure 3.26** A representation of the effect of the centrepetal force on the keyhole and melt pool.  $F_m$  denotes the force of the melt ( $F=ma$ ) and  $F_c$  is the force exerted by the spinning motion. The vapour force in the keyhole is also present though not shown.



**Figure 3.27** The predicted permissible gap widths for welding 1 mm mild sheet steel at various welding speeds and different powers. Also shown is the measured increase in fused metal width for bead on plate welds and measured gap width tolerance for a guillotine joint.

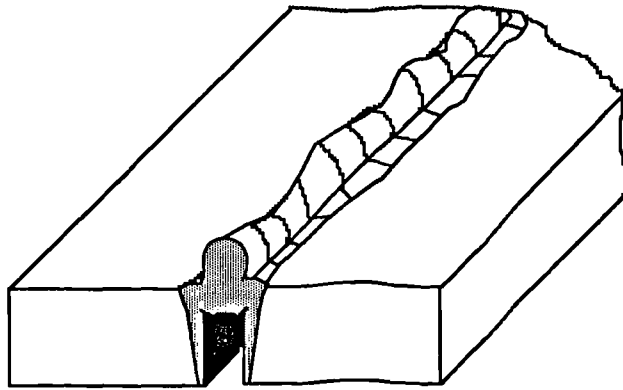


Figure 3.28 A schematic representation of the appearance of a humping weld bead.

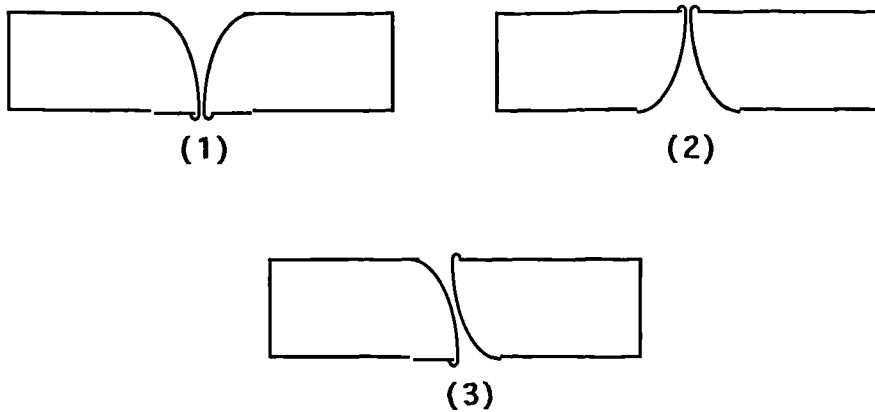
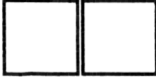

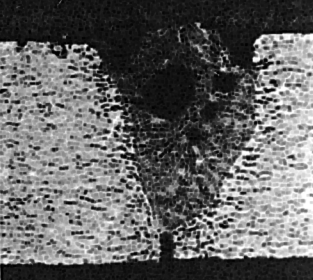


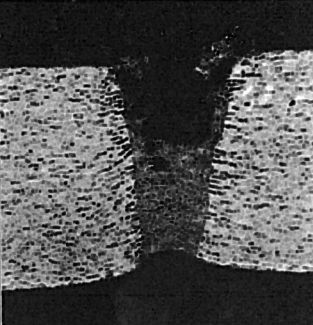


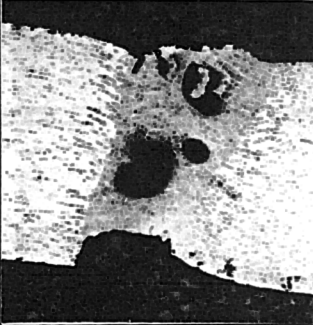


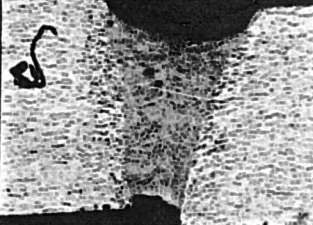
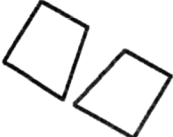


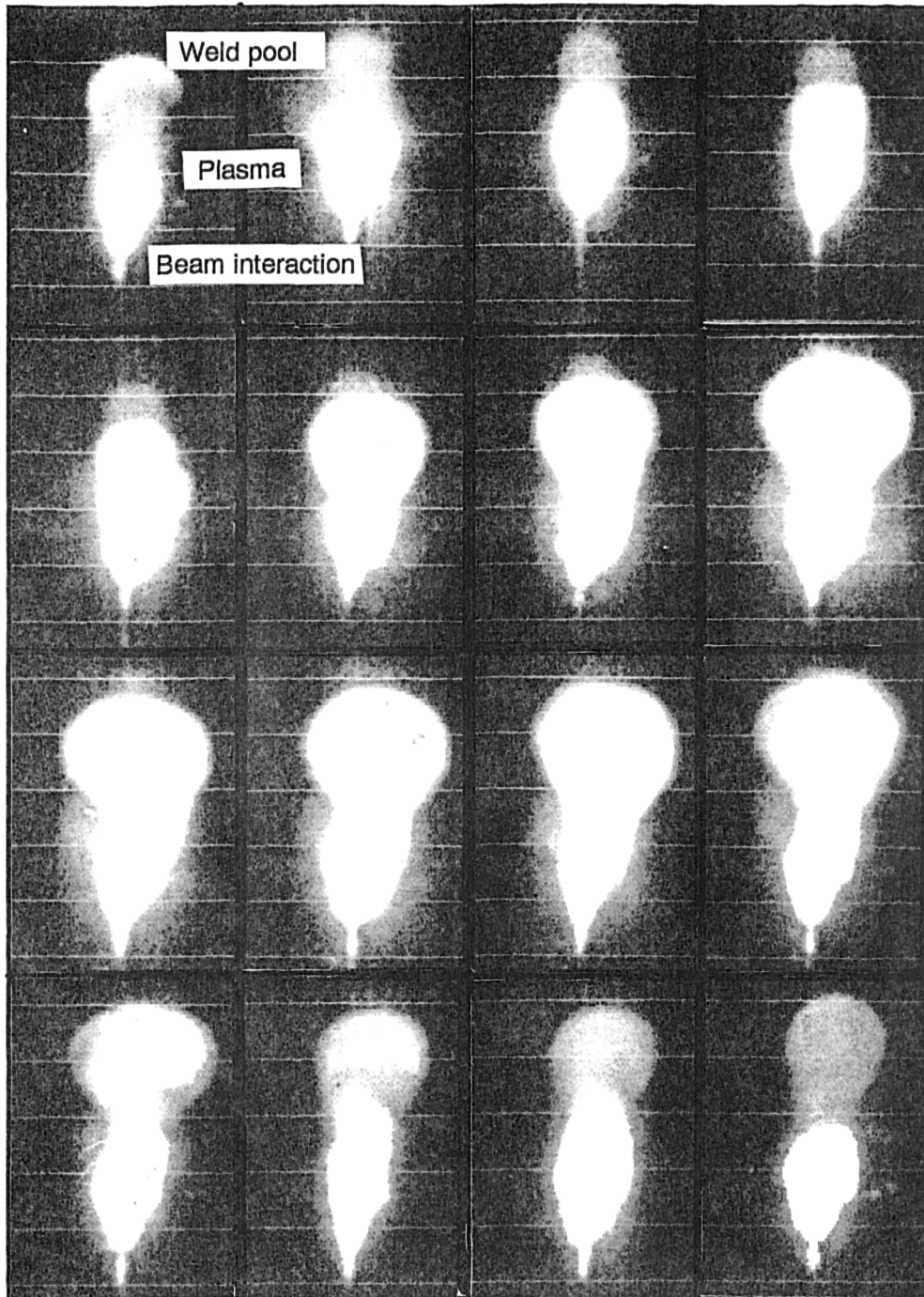


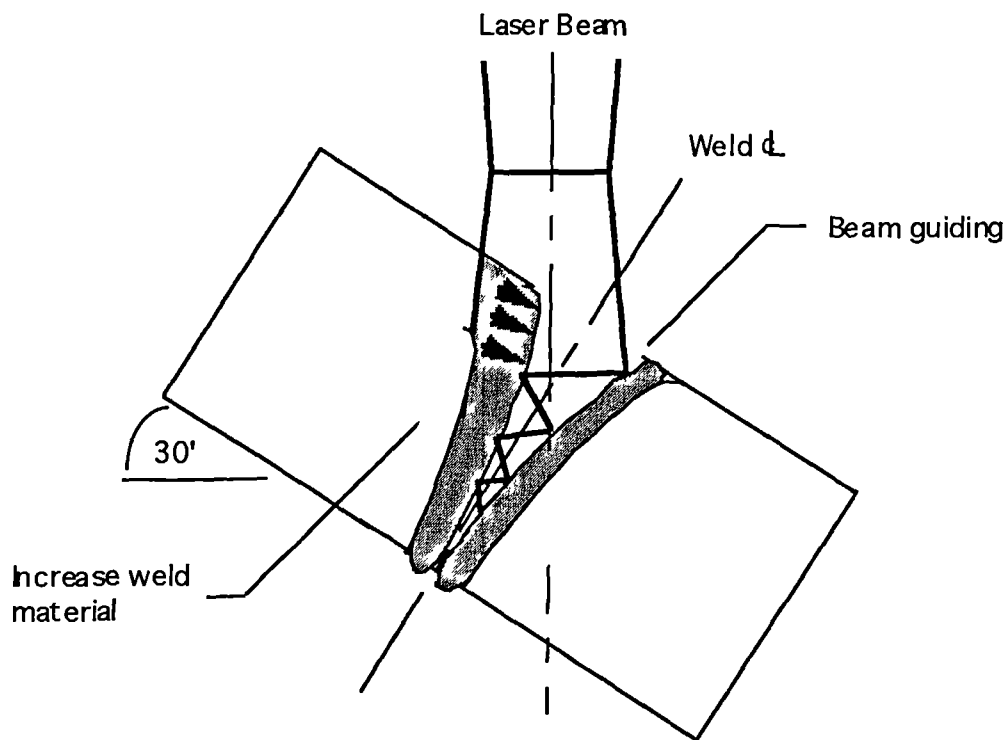
Figure 3.29 The three possible combinations of guillotine edges assessed for weldability.

Joint configuration	Film Snap shot	Weld Profile
<p>Milled</p>  <p><math>J = 0.2</math></p>		
<p>Guillotine 1</p>  <p><math>J = 0.12</math></p>		
<p>Guillotine 2</p>  <p><math>J = 0.14</math></p>		
<p>Guillotine 3</p>  <p><math>J = 0.16</math></p>		
<p>Angled guillotine 3, at 30 degrees.</p>  <p><math>J = 0.2</math></p>		

**Figure 3.30** The welding stills from each configuration along with profile At 3.5 kW and 230 mm/s (14 m/min.) except the angled sample, performed at 260 mm/s.



**Figure 3.31** Shows the formation of the hump from a sequence of high speed video camera, with 2 ms between each still.



**Figure 3.32** Schematic explanation of the advantages using the angled mechanism for enhanced absorption of the incident radiation and increasing available weld material. The resulting melt areas are highlighted.

## REFERENCES

1. Dixon and Massey, Introduction to Statistical Analysis, 2nd edition, McGraw Hill 1969.
2. Draper and Smith, Applied Regression Analysis, Wiley and Sons, 1971.
3. Mehta, P., Cooper, R. and Miller, R. "Laser Welding: A Parametric Study on Inco718". The Laser Institute of America, International Congress on the Application of Lasers and Electro-Optics (ICALEO), Vol. 44, 1984, pp43-52.
4. Baarsden, E. L., Schmatz, D. J. and Bisaro, R. E. "High Speed Welding of Sheet Steel with a CO<sub>2</sub> Laser". Welding Journal, April 1973.
5. Locke, V. E. and Hella, R. A. "Metal Processing with a High Power CO<sub>2</sub> Laser". IEEE Journal of Quantum Electronics, QE-10 No. 2, 1974.
6. Dawes, C. J. and Watson, M. N. "CO<sub>2</sub> Laser Welding of Deep Drawing Sheet Steel and Microalloyed Steel Plates". The Laser Institute of America Vol. 38, ICALEO, 1983, pp73-79.
7. Swifthook, D. T and Gick, A. E. F. "Penetration Welding with Lasers". Welding Journal, November 1973, pp492-499s.
8. Mannik, L and Brown, S. K. "Laser Welding of Steels: Relationship between Laser Power, Penetration depth, Welding speed and Beam Polarisation". Proc of ICALEO, 1990, pp364-372.
- 9 Kim, T. H, Albright, C. E. and Chaing, S. "The Energy Transfer Efficiency in Laser Welding Process". Journal of Laser Applications, 2(1), 1990, pp23-28.
- 10 Gregson, V. Laser welding data. The Industrial Laser Handbook-edited by Belforte and Levitt, Publ. PennWell Pub Co., 1988, pp13-15.
11. Herziger, G. "Physics of Laser Material Processing". Proc SPIE 650, High Power Lasers and their Industrial Applications, 1986, pp188-194.
12. Miyamoto, I and Marou, H. "Spatial and Temporal Characteristics of Laser-Induced Plasma in CO<sub>2</sub> Laser Welding". Proceedings of Laser Advanced Materials Processing (LAMP), 1992, pp311-316.
13. Fabbro, R. "Beam-plasma Coupling in Laser Materials Processing". Proc of LAMP, 1992, pp305-310.
13. Marode, E, Bastien, F. and Bakker, G. J. Appl. Phys. Vol. 50, 1979, p740.
14. Weichel, H and Pedrotti, L. S. "A Summary of Useful Laser Equations-An LIA Report". Electro-Optical Systems Design Vol. 8, July 1976, pp22-36.
15. Beyer, E., Behler, K. and Herziger, G. "Influence of Laser Beam Polarisation in Welding". Proc. the Int. Conf. Lasers in Manufacturing, 1986, pp230-240,

- 16 Schultz, W., Simon, G., Urbassek, H. M and Decker, I. "On Laser Fusion Cutting of Metals". J.Phys. D; Appl. Phys. 20, 1987, pp481-488.
17. Dixon, R. D. and Lewis,G. K. 'Affect of Angle of Incidence on Plasmas Generated during Laser Welding". The Laser Institute of America Vol. 44, ICALEO, 1983, pp28-34.
18. Duley, W. W. "A Summary of Beam Material Interactions During Laser Processing". Proc. of LAMP, 1987, pp13-18.
19. Chande, T and Mazumder, J. "Estimating Effects of Processing Conditions and Variable Properties upon Pool Shape, Cooling Rates and Absorption Coefficient in Laser Welding". J. Appl. Phys, 1983.
20. Chan, C. L., Mazumder, J. and Chen,M. M. "Three-Dimensional Axisymmetric Model for Convection in Laser-Melted Pools". Material Science Technology, No. 3, 1987.
21. Paul, A. and DebRoy, T. "Prediction of Marangoni Convection, Heat Transfer and Surface Profiles during Laser Welding". Modelling of Casting and Welding Processes IV, Eds. A. F. Giamen and G. J. Abbaschian, The Minerals, Metals and Materials Society, 1988, pp421-431.
22. Arata, Y. Abe, N. and Oda, T. "Beam Hole Behaviour during Laser Welding". The Laser Institute of America, Vol. 38 ICALEO, 1983, pp59-66.
23. Ahkter, R. "Laser Welding of Zinc Coated Sheet Steel". PhD thesis Imperial College of the Royal School of Mines, 1990.
24. Miyamoto, I. Marou, H. and Arata, Y. "The Role of Assist Gas in CO<sub>2</sub> Laser Welding". Proc. of ICALEO, Vol. 44, 1984, pp68-75.
25. Arata, Y. "Challenge to Advanced Laser Materials Processing". Proc. of LAMP, 1987, pp3-12.
26. Tong, H and Giedt, W. H. "A Dynamic Interpretation of Electron Beam Welding". Welding Journal, 49, 1970, pp2595-2665.
27. Duley, W. W, Olfert, M., Bridger, P., Bird, J. and Mueller, R. E. "Basic Physical Phenomena During Laser Processing of Materials". Proc. of LAMP, 1992, pp261-268.
28. Norris, I. "Current Status of Structural Steel Welding". Advances in joining and Cutting Processes, Harrogate, UK, Vol 1 Abingdon Publishing, 1989, pp196-218.
- 29 Alexander, J and Steen, W. M. "Penetration Studies On Arc Augmented Laser Welding" Proc. Int. Conf. on Welding Research, Osaka Japan, 198, Papar A-21, 1983, pp121-125.
30. Heiple, C. R. and Burgardt, P. "Effects of SO<sub>2</sub> Shielding Gas additions on GTA

- Weld Shapes". Welding Research Supplement, No. 64, 1985, pp159-162.
31. Slinde, H., Gabzdyl, J. T., West, D. R. F. and Reed, R. C. "The Influence of Assist Gas during Laser Welding of Low Alloy Steel". Proc. of Laser Advanced Material Processing (LAMP), 1992, pp469-475.
  32. Uman, M. A. Introduction to Plasma Physics. Published by McGraw Hill, 1964.
  33. Schauer, D. A and Geidt, W. A. "Prediction of Electron Beam Welding Spiking Tendency". Welding Journal, Research Supplement, July 1978, pp189-195.
  34. Bradstreet, R. J. "Effect of Surface Tension and Metal Flow on Weld Bead Formation". Welding Journal, Vol 47, No. 7, 1968, pp314s-322s.
  35. Beck, M and Dausinger, F. "Modelling of Laser Deep Welding Processes". European Scientific Laser Workshop on Mathematical Simulation, Sprechaal Publishing Group, Lisbon. 1989
  36. Beck, M. Numerical Simulation of Deep Penetrating Welding within the Framework of EU194. Proceedings of Modelling of Laser Material Processing, Eurolase EU194 Working Group, Mathematical Modelling, 1992.
  37. Gratzke, U.,Kapadia, Dowden, J, Kroos, S. and Simon, G. "Theoretical Approach to the Humping Phenomenon in Welding Process." to be published.
  38. Hiramoto, S., Ohmine, M., Okuda, T and Shinmi, A. "Deep Penetration Welding with High Power CO<sub>2</sub> Laser". Proc of LAMP, 1987, pp157-162.
  39. Sharp, M. C. Method of Laser Butt Welding US Patent No. 4 577 088.
  40. Rosenthal, D. "Mathematical Theory of Heat Distribution During Welding and Cutting". Welding Research Supplement, May 1941, pp220-236 & "The Theory of Moving Sources of Heat and Its Application to Metal Treatments". Transactions of American Society of Mechanical Engineering, 1946, pp849-863.
  41. Carslaw, H. C and Jaeger, J. C. Heat Conduction in Solids. Oxford Press, London 1957
  42. Andrews, J. G and Atthey, D. R. "A Hydrodynamic Limit to Penetration of a Material by a High-Power Beam". J. Phys. D: Appl. Phys., Vol 9, 1976, pp2181-2194.
  43. Klemens, P. G. "Heat Balance and Flow Conditions for Electron Beam and Laser Welding". J. Appl. Phys. Vol 47, pp2165-2174.
  44. Kapadia, P, Dowden, J and Ducharme, "A Mathematical Model of the defocusing of Laser Light Above a Workpiece in Laser Materials Processing" Proc of ICALAO, Orlando, 1992, pp187-197(Kapadia et al and Ducharme et al references therein).



## CHAPTER 4

### IN-PROCESS WELD MONITORING

#### 4.1 INTRODUCTION

Once the welding process has been fully investigated and on the way to becoming optimised for a specific application, an important consideration particularly in a manufacturing process is the need for quality assurance. This can be enforced in several ways ranging from manual inspection to a fully automated system. Over the last five years the increasing implementation of laser welding production facilities and, an emphasis on product quality a fully automated system has been sought after. In line with this demand the development of such monitoring devices has been on going. There are two options in the implementation of a monitoring system; information is provided to the operator during the welding process indicating dynamic weld quality, any sub standard weld is identified and suitable action is taken by the operator - the in-process signals are used to control the process. Secondly, the closed loop system and this is where most current research is targeted, is the idea of closed loop feedback systems. The weld fault is identified and categorised leading to an automatic adjustment of the controlling processing parameters for that specific defect.

A further progression from this, is not only to react to the occurrence of a weld defect but to anticipate the behaviour of the welding mechanism and affect the appropriate changes before it has had a chance to occur. Now we are talking about a predictive system, and big money ! There are several methods through which a weld may be “monitored”, to clarify this point the following gives a brief outline of the current sensors available, and those to be used in the experimentation.

## **4.2 WELDING SENSOR SURVEY**

In the welding action there are several components that can be identified; the laser beam, the melt pool, the keyhole and “plasma”, all of which are evident on both sides of the workpiece assuming full penetration conditions. Correspondingly, any monitoring device must assess either or all of the following; some quantitative beam measurement sensitive to the welding action, the temporal behaviour of the melt pool in terms of fluid dynamics or temperature, the temporal and spatial behaviour of the keyhole and similarly for the “plasma”. At the present it is possible to produce measurable quantitative results for all except the behaviour of the keyhole.

### **4.2.1 Laser beam monitoring**

During the welding action, or in fact any laser processing technique, some of the laser radiation incident on the workpiece is reflected back down the optical axis. This reflected radiation enters the laser cavity, causing instability in the quality of the laser, as described by the  $M^2$  factor, and fluctuations in the output power. Finding a link between the back reflected radiation and process monitoring forms the basis a system outlined by Olsen *et al* (1992)[1]. The beam is sampled enroute to the welding area, and the back reflections are also measured, by comparison these would indicate any arising faults. Unfortunately, this method is a quite complex arrangement and the actual effectiveness is open to question, given that increasing powers tend to damp out any signal [2]. Also any back reflection is dependent on the surface conditions and plasma behaviour - which are certainly not constant and very difficult to predict. This method works best with metals of high reflectivity (aluminium and copper - 98 %), however the reflectivity of the drum quality mild steel is 90 % [2] even for a well polished surface. If perfected, this system gives information at the speed of light and that is fast feedback.

A slight variation on a similar theme is described by Steen and Weerasinghe (1986)[3]. Discovering that a pressure wave is generated in a solid when the beam is deflected by the surface of that solid, the system comprises a piezoelectric sensor mounted at the rear of one of the guidance mirrors - the idea being that the back reflected radiation as a function of the weld quality will be sampled providing the information for weld assessment. The system monitors changes in the signals thus relying on the stability of the original laser source, this being modified by sampling the original beam. The experimental results have been promising though not conclusive.

A system which measures the extent of the beam emerging from the underside of the weld is suggested by Maischner *et al* (1992)[4], the results did not define any specific faults merely when full penetration had occurred.

#### **4.2.2 Melt pool monitoring**

As mentioned above the fluid dynamics or temperature are the relevant melt pool quantities that can be visualised or measured. Observation of melt pool dynamics has been achieved by Arata (1987)[5] and Voelkel and Mazumder (1990)[6]. The latter only observing conduction limited welds. Williams and Steen (1992)[7] recorded keyhole welding and the ripple patterns on the surface of the melt pool but primarily viewed spot welds. Beyer *et al* (1987)[8] investigated the solidified weld pattern by observation of the ripples on the melt pool surface with involving an argon laser diagnostic system. These visualisation arrangements, however, are largely qualitative with the emphasis on understanding as opposed to diagnostic treatments. In reality, the melt pool temperature/spectral emission can be measured relatively simply (provided it is not obscured by plasma emissions) using a fully calibrated device or more simply a photodiode of suitable spectral response. The advantage of this system is that the relative signal (to a good weld) not absolute is required and therefore, can be applied to any material or welding configuration.

### 4.2.3 Plasma monitoring

The presence of plasma above the workpiece is suppressed using shielding gas, however, the shielding gas only suppresses the plasma and does not eliminate it. The behaviour of the plasma directly relates to the absorption mechanism inside the keyhole and therefore reflects what is happening during welding. Plasma generation may even preempt the melt solidification outcome, good or bad, due to different conditions in the keyhole/melt pool.

Observation and monitoring of the temporal behaviour of the plasma can be achieved by four methods; from ultra-violet light emissions [10], acoustic emissions [11, 12], plasma charge separation [13] and sensing the nature of the plasma with regard to the size, density etc [14].

Chen *et al* (1991)[9] and Maischner *et al* (1990)[4] used of a photodiode to monitor the emission of the ultra violet spectra. The results of which, particularly in the latter case suggests clear identification of specific welding faults.

The acoustic emission from the plasma can be measured using an external microphone [11] and later by an acoustic nozzle, which simply comprises of a piezoelectric pressure sensor placed near the interaction point [12]. The theory behind the use of the sonic microphones is encompassed in Chapter 1, section 1.4.6 - due to the extreme surface heating of the workpiece shock waves are generated which radiate from the workpiece. The added advantage of the acoustic sensor is that it can be used as a monitoring device even when plasma is not generated.

The plasma charge sensor, first applied by Li *et al* (1990)[12], monitors the difference in charge between the plasma and the workpiece, the reported results are promising with similar fault differentiation characteristics as the above mentioned photodiode. It has the advantages of being very simple to implement, inexpensive and robust, and is omnidirectional.

Sensing the nature of the plasma is achieved with the use of a diagnostic

laser, usually a HeNe or CO<sub>2</sub>. The HeNe/CO<sub>2</sub> laser is projected through the plasma using interferometry analysis techniques to provide data on the plasma. The CO<sub>2</sub> laser gives information regarding plasma absorption and beam diffraction. Both of the described methods have been previously implemented with success [14]. The latest diagnostic equipment in this area is using laser micro analysis techniques, whereby the composition of the plasma is examined.

### **4.3 SELECTION OF IN-PROCESS WELD MONITORS**

The sensory techniques shortlisted are the photodiode for infrared and ultra violet sensing, the acoustic nozzle and the plasma charge monitor. One of the main reasons for these choices, apart from their suitability, is that some work has already been performed in all these areas in the same research laboratory. Therefore, the work of developing these sensors is for the benefit of the project, of course!, and that of increasing the data and usage of the sensor arrangement itself.

The arrangement of the selected sensors was such that all four could be set up and used simultaneously, figure 2.6 (Chapter 2) shows how they fitted together within the welding set-up

#### **4.3.1 Dual wavelength optical sensors (DWOS)**

The photodiode arrangement of the infrared (IR) and ultra-violet (u/v) sensor comes in this system as a single package, the two diodes are connected to fibre optic cable, which is positioned near the welding process. The output from the sensors is relayed to an oscilloscope through an amplifying circuit.

The underlying theory that explains why these particular sensors can be used is related to Planck's Law, which describes the radiant power from a black/grey body over all wavelengths by -

$$W_{bh} d\lambda = \frac{c_1}{\lambda^5 [ e^{\frac{c_2}{\lambda T}} - 1 ]} d\lambda \quad (4.1)$$

where  $W_{bh} d\lambda$  = an emission of unpolarised radiation/unit area in the wavelength range  $d\lambda$ . (W/m<sup>3</sup>)

$c_1, c_2$  = constants (3.74 \* 10<sup>-16</sup> Wm<sup>2</sup> and 1.439 mK)

$\lambda$  = wavelength (m)

$T$  = absolute temperature ('K)

Thus, for a given temperature there exists a distribution curve of the energy emission spectrum. Within this spectrum a maximum in emission occurs, inversely proportional to the temperature. This maximum occurs at a wavelength determined from Wein's Law, such that

$$\lambda_{max} = 2891/T \text{ (microns)} \quad (4.2)$$

From this an approximation of the plasma and melt pool temperature can be estimated and therefore the required spectral response of the sensors. For the melt pool (IR) this value is around 1 micron, for the plasma (u/v) it is around 400 nanometres. The signal strength recorded by each sensor is described by -

$$S_\lambda = \int_{\lambda_1}^{\lambda_2} W (1 - L) s_d d\lambda \quad (4.3)$$

where  $S_\lambda$  = signal strength (V)

$W$  = total emission of light for a wavelength (W).

$L$  = Total losses in optical delivery system (absorptivity, coupling, reflection) (%).

$s_d$  = sensitivity of detector (A/W)

This seems fine, but why does the value and variation of the signal in terms of UV and

IR tell us about the welding process ? Any fluctuations in plasma temperature gives a large change in the u/v signal compared to the IR. This is discussed further in section 4.4.1

The magnitude of the signal and the modulation of the UV signal are both needed to define the weld quality. The magnitude indicates the extent of the plasma - low, medium and high. The modulation of the signal falls into the low and high categories. The interpretation and explanation of these different signals are discussed later, in section 4.4.

#### 4.3.2 Acoustic emission nozzle (AEN)

The acoustic emission nozzle relies on the theory outlined in Chapter 1, section 1.4.2.3, that the rapid rise in surface temperature and resulting explosive expansion of vaporised material creates airborne pressure waves, and due to the recoil forces exerted by the vaporising metal, in the workpiece as well. In this case of weld monitoring it is the airborne waves that are of most interest, as those propagating within the solid will be subject to interference and damping by the driving x-y table and clamping arrangement.

The dependence of the acoustic signal on the welding process is given in terms of the vapour generation [12] -

$$n_m(t) = \text{const.} \left[ A I - \frac{\sqrt{2\pi} T_v K / r_f}{\tan^{-1} \frac{\sqrt{8Kt}}{r_f}} \right] \quad (4.4)$$

- where
- $n_m(t)$  = vapour density ( $1/m^3$ ).
  - $A$  = absorptivity ( $1/m$ )
  - $I$  = laser intensity ( $w/cm^2$ )
  - $T_v$  = vaporisation temperature (K)
  - $K$  = thermal diffusivity ( $m^2/s$ )

- K = thermal conductivity (W/mK)
- t = beam/material interaction time (s)
- $r_f$  = focus beam radius (m)

The form of the equation highlights the fact that the generation of the pressure waves does not require the formation of a plasma, but is simply a heating effect. This means that this type of device could be applied to conventional welding techniques and other forms of processing where a plasma is not formed. The set-up of this sensor is mounted on a metal plate attached to the welding nozzle, the underside of the plate is protected by a plastic cover to prevent heating of the metal plate, and a possible interference in the signal. The signal can be analysed by temporal variation of signal amplitude and also by fast Fourier transformations providing the acoustic spectrum.

#### 4.3.3 Plasma charge sensor (PCS)

This device detects an electric field which is present during the welding operation between the plasma and workpiece. This field is a result of a charge separation occurring in the plasma due to the relative difference in velocities of electrons and positive ions. The field behaviour is dependent on the production of free electrons and the nature of the charge separation. The sources of free electrons in the welding area result from the heating process (thermionic) and the absorption of laser radiation by the plasma (inverse bremsstrahlung).

Thermionic electrons are liberated from the workpiece, their numbers are related to the temperature rise experienced by the solid workpiece. The rate of generation is described by Richardson's equation [12] -

$$j = BT^2 \exp(-f / kT_s) \quad (4.5a)$$

where  $j$  = current density (A/cm<sup>2</sup>)



B = constant equal to 60.2 A/cm<sup>2</sup>deg<sup>2</sup>.

T = maximum temperature (C)

f = a work function of the workpiece (eV).

k = stefan-boltzmann constant (1.3804 \* 10<sup>23</sup> J/deg)

T<sub>s</sub> = temperature of the workpiece surface (C)

The stripping of electrons from the plasma by laser radiation is by inverse Bremsstrahlung, where the bound electrons absorb energy through collision with laser photons. The factors governing the production of electrons in this manner is more complex than the thermionic process and has been derived by Lampiur and Saha [12] -

$$N_+ / N_o = \exp [ (f - I_p) / kT ] \quad (4.5b)$$

where N<sub>+</sub> = number of positive ions.

N<sub>o</sub> = number of atoms.

e = electron charge (1.6021 \* 10<sup>-19</sup> C)

f = a work function of the surface.

I<sub>p</sub> = ionisation potential of the material (eV).

k = stefan-boltzmann constant (1.3804 \* 10<sup>23</sup> J/deg)

T = vapour temperature (°K)

For this process to occur the plasma must be of high temperature (10000K), which is achieved through absorption of the incident radiation by inverse bremsstrahlung at a rate given by -

$$\frac{de}{dt} = \frac{e}{m} \frac{E^2}{v_c (1 + \omega^2 / v_c^2)} \quad (4.6)$$

where de/dt = electron gain rate.(eV/s)

- e = electron energy (eV)
- m = electron mass (kg)
- E = root mean square of electric field (eV)
- w = plasma frequency (Hz)
- $\nu_c$  = electron-atom collision frequency (Hz)

#### 4.4 RESULTS and DISCUSSION

The responses of the selected monitors to 5 different categorised weld energy input conditions and the more common weld faults are presented. The experimental arrangement is described in Chapter 2, section 2.3.9. The grouping of the sensors into pairs in line with Chen *et al* (1990)[9] and Li *et al* (1992)[11]. A characteristic trace of each of the sensors for a sound weld is shown in figure 4.1.

##### 4.4.1 Dual wavelength optical sensors

The ultra-violet and the infrared sensor results are shown in figure 4.2, in terms of absolute signal level and signal modulation. The increasing signal response of both sensors with higher energy input, shown in figure 4.2a, fits into the five weld energy regions (P/v). This predicted is by equation (4.3) until the welding action tends towards hole formation and cutting. The onset of cutting causes the processing zone to become more exothermic, whilst the plasma is blown through the cut by the assist gas. This is reflected in the with very low u/v and high IR value. The percentage modulation of the signal, in figure 4.2b, shows a reversal in signal stability with the IR being larger in the good and partial penetration regions, and smaller in all others. This indicates the dynamic equilibrium of the plasma in regions (a) and (b). From equation (4.6) this stabilisation occurs when the recombination rate (electron-ion) is equivalent to the free electron generation rate.

The fault recognition/differentiation is shown in figure 4.4, it is evident that the magnitude and modulation for the UV and IR values are specific to a certain weld fault. Which, more importantly, conforms with the theory.

#### 4.4.2 Plasma charge monitor and Acoustic emission nozzle

The responses of these sensors to energy input in figure 4.3, can be categorised into the distinct energy input regions. For this specific welding arrangement the sound weld corresponds to similar signal levels of the sensors. Again a fall off in the signal level of the PCM and AEN is observed in the hole formation/cutting region, however the signal modulation is almost 100 %. The detection of a signal with the presence of little or no plasma, agrees with equation (4.4) for the AEN. The plasma charge monitor signal is explained by presence of thermionic electrons, providing a low and highly variable signal. This fact means that these sensors may also be utilised in cut monitoring. Generally the signal modulation, from figure 4.3b, shows a reversing effect. The PCM is lower with a controlled plasma, then on increasing energy input becomes the larger as the plasma is over energised. The AEN modulation decreases, as the acoustic emission becomes saturated.

The fault assessment, shown in figure 4.4b, clearly shows failure to distinguish between defects or in fact register the defect has occurred at all. The PCM can only indicate a fault by a collapse of the plasma, as is the case for the gap and hole, there is no gradation in the signal. The AEN, considering the modulation, did not detect any of the faults. As the AEN only responds to a reaction of the workpiece to the heating effect, this effect will always be present regardless of the fault.

In the region of sound (c) and over power (d) the PCM signal was not consistent. The signal occasionally reversed polarity and in some cases no signal was detected. This changeable signal is a result of the charge separation, as shown in figure 4.5a - with the through penetration case there are three possible charge distributions shown in figure 4.5b. Cases (1) and (2) exhibiting polarity change

whereas the third shows little or no signal, due to an equal distribution of charge. During the course of a weld all three probably occur corresponding to the absorption conditions in the keyhole, however one is normally dominant. Ensuring that one type of charge distribution is always dominant is not possible, therefore the signal will be subject to an intrinsic unreliability.

#### 4.4.3 Reliability and Ease of implementation

Throughout the trials Dual Wavelength Optical Sensors results showed universal agreement. This being subject to a consistent set-up, with regard to distance and inclination of the fibre relative to the welding action. Ensuring a small inclination to the normal of the workpiece gives the arrangement an omnidirectional ability. This only becomes a problem when the welding nozzle is close to the workpiece and obscures the plasma/melt pool, other set-ups overcome this [9] alternatively an assist jet can be used. The interference of ambient lighting conditions only becomes a factor when the signals are very small, in this instance no effect was observed with a stand-off distance of up to 20 cm. The important requirement is that the lighting conditions are consistent.

The Plasma Charge Monitor and Acoustic Emission Nozzle were not as reliable or user friendly as the DWOS arrangement. The PCM has the advantage of being omnidirectional and robust, unfortunately care has to be taken in isolating the nozzle and earthing the workpiece. This on several occasions proved difficult, also the correct load resistor and smoothing capacitor must be selected for the specific welding operation. There was a tendency for the PCM reading to change polarity, to overcome this an applied dc voltage is recommended [12]. This does not eliminate the problem as the measured signal increases with the applied voltage, and therefore large modulation and signal failure are still present.

The acoustic nozzle was easy to set-up ensuring a sound contact of the piezoelectric sensor. The sensitivity of the piezoelectric device caused vibrations

and ambient radio waves to interfere with the signal. This was accentuated when using the Laser Ecosse AF5 fast flow laser due to the vicinity of the mechanical blowers. To differentiate these various interferences an attempt was made to analyse the frequency components of the signal. The laser welding signal was around 100 kHz which could be picked out, but no diagnostic information could be interpreted regarding a shift in the frequency or amplitude changes. Though a sensitive diagnostic device the acoustic nozzle readings were subject to the multi-pressure wave generation and interference environment of the plasma, which could not be consistent or reliable for different weld faults.

#### **4.4.4 Weld sensor recommendation**

Although Keren *et al* (1992)[14] have based a real time laser weld diagnostic system on the plasma charge and acoustic emission sensors, they are not suitable in this instance and, are out performed by the optical sensors for reliable weld fault identification. The plasma charge monitor is a useful detector in its own right particularly as a plasma diagnostic instrument, the acoustic sensor appears unsuited for the welding process and may prove more applicable to the cutting and surface treatment operations. Thus the DWOS arrangement is the choice.

### **4.5 FURTHER CHARACTERISATION OF OPTICAL SENSORS**

The sensors have proven fault detection, the next step is to establish the “real time” and possible the predictive nature of the DWOS arrangement.

#### **4.5.1 Real time weld diagnostic system**

This was established using high speed video equipment, the set-up with the Kodak Ektapro similar to that in Chapter 3, section 3.5.5. The sensor traces were triggering by initiation of the welding action , the video was simply kept running.

The high speed video could be rewound to the start, the millisecond frame stepping enabling the welding initiation point to be found. A graphical representation of a trace and video were compared, as shown in figure 4.6, noting the u/v trace is shown - the IR being identical. The maximum and minimum plasma size from the video compares almost perfectly with a trace of the same weld, it is worth noting the plasma ignition time is 10ms. Also that after the transient period (0-40ms), the modulation of the UV signal is around 80 Hz.

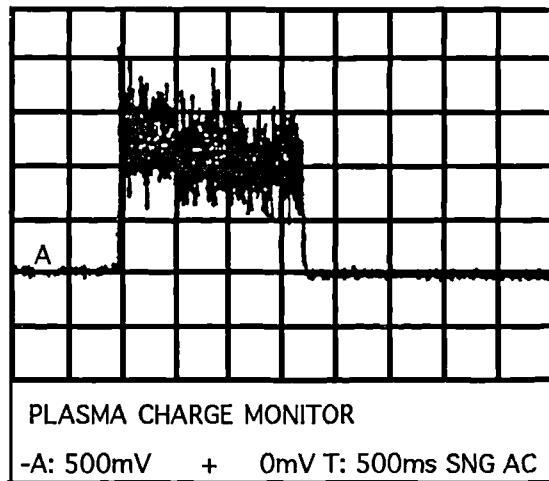
#### 4.5.2 Predictive nature of the sensors

Chen *et al* (1991)[9] reasoned that the u/v sensor should present the possibility of a predictive weld monitoring mechanism as the plasma effectively “leads” the melt pool and therefore is a precursor to its behaviour. The evidence presented is the extinction times of the u/v (plasma) and IR (melt pool) signals measured on termination of the beam. The results show the u/v signal to fall to zero in 10ms as opposed to 35ms for the IR, therefore the change in u/v signal can be acted upon before the change occurs in the IR, hence any immanent weld defects are avoided.

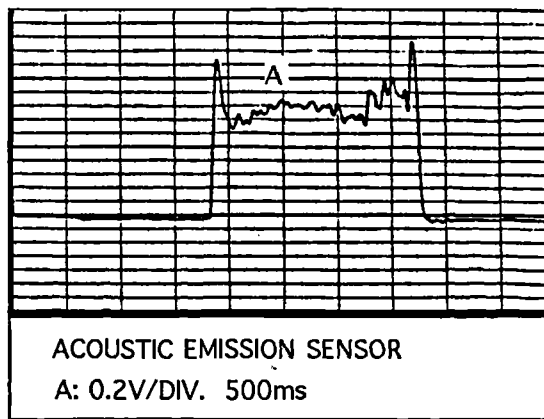
The question of whether the plasma “leads” the melt pool or vice versa is shown in figure 4.7. The signals exhibit identical temporal variation. The signal from both sensors are in phase after the initial heating up and keyhole formation. To confirm that the response of the individual sensors are also similar the rise and decay of both sensors to a periodic step input are shown in figure 4.8. The rise time (10-90%) of both sensors are around 1ms, while the IR has the greater decay time of 5ms. As the normal welding signal is constantly modulating this 5ms delay is never realised, and so can be ignored. Although the plasma and melt pool appear to be simultaneous (at the ms timescale), Kapadia *et al* (1992)[15] have predicted that both the IR and u/v signal are predominately emitted by the plasma. Therefore, the near perfect fit of the graph in figure 4.7 may be so because the signals are from the same source. Thus the melt pool signal is effectively blocked out. The possibility of

some form of predictive nature may arise from the rate of change of the signal gradients.

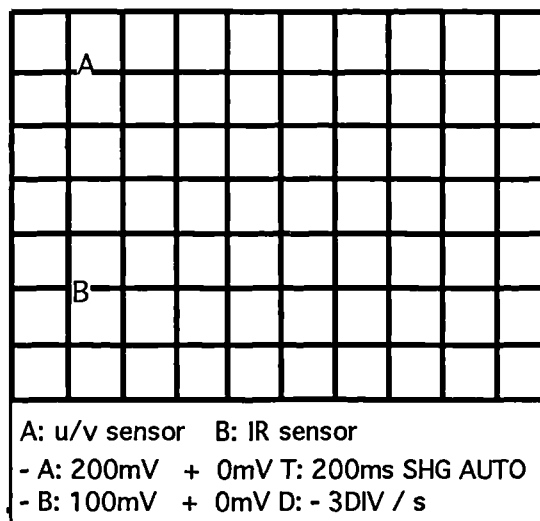
The signal from a good weld has a degree of modulation, if a fault occurs the signal rises or falls out of the normal range of modulation. The rate of change of the signal may vary for that of the "normal" as opposed to fault signal. This being true the signal could be sampled, say every millisecond (in the case of high speed welding), any sign of a fault can then be acted on.



(a)



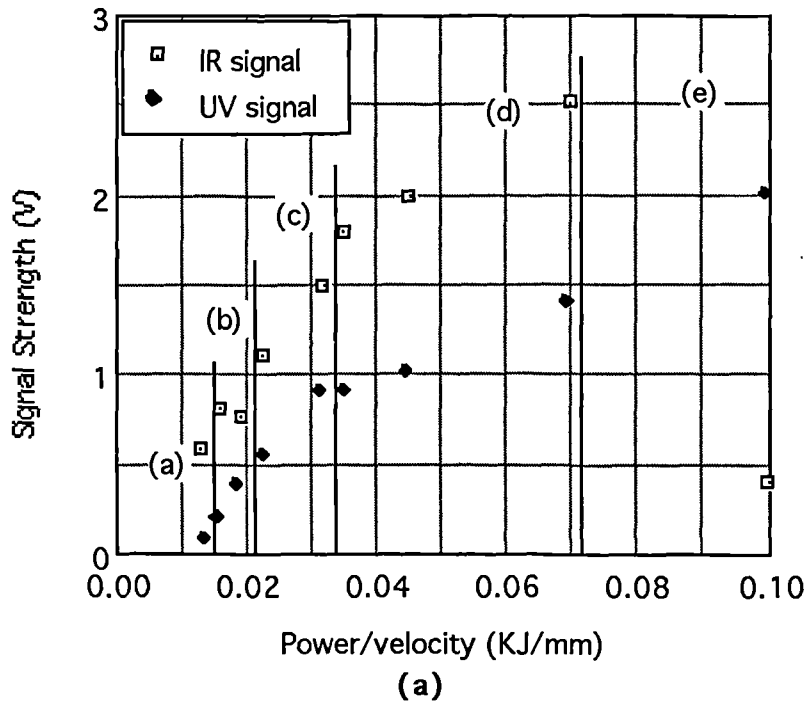
(b)



(c)

Figure 4.1 Typical signals obtained a)PCM b) AEN and c) IR and u/v





(a) Ropey/humping bead	(d) Over power
(b) Partial penetration	(e) Hole formation/cutting
(c) Sound weld	

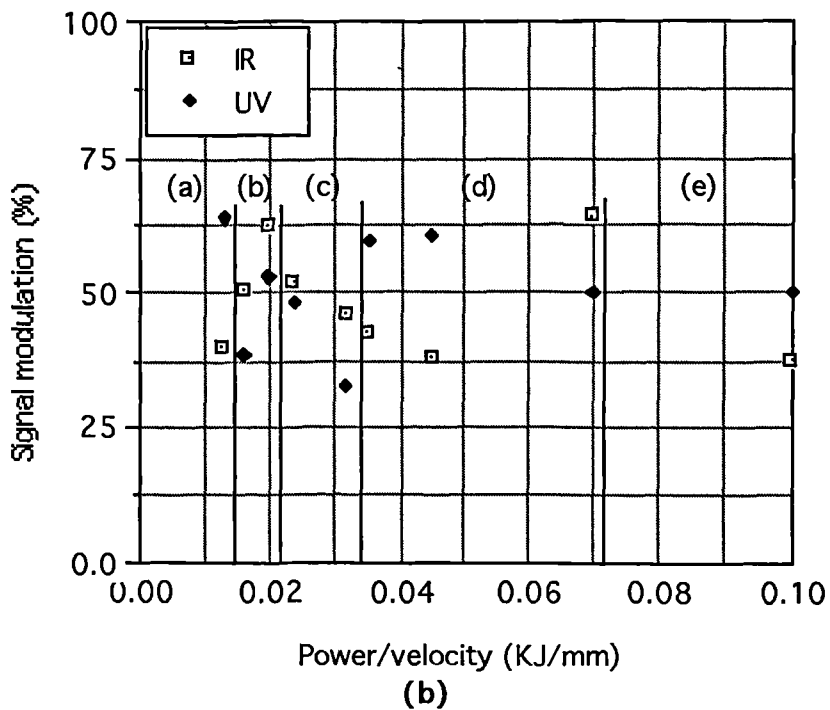
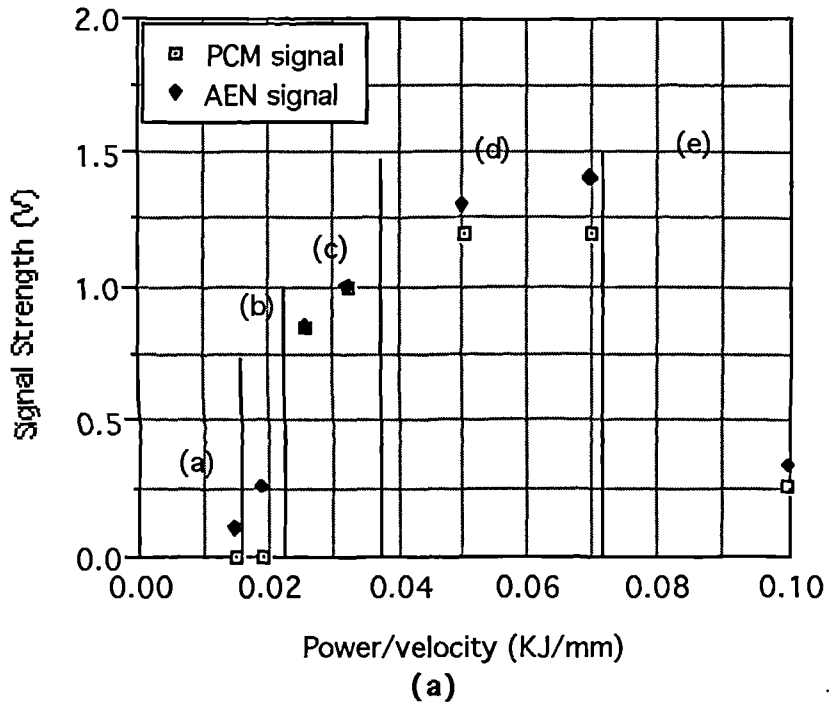


Figure 4.2 Response of u/v and IR for different energy input conditions, for signal strength and signal modulation. At 1.5-3.5KW, 40-230mm/s & 100mm lens.



(a) Ropey/humping bead	(d) Over power
(b) Partial penetration	(e) Hole formation/cutting
(c) Sound weld	

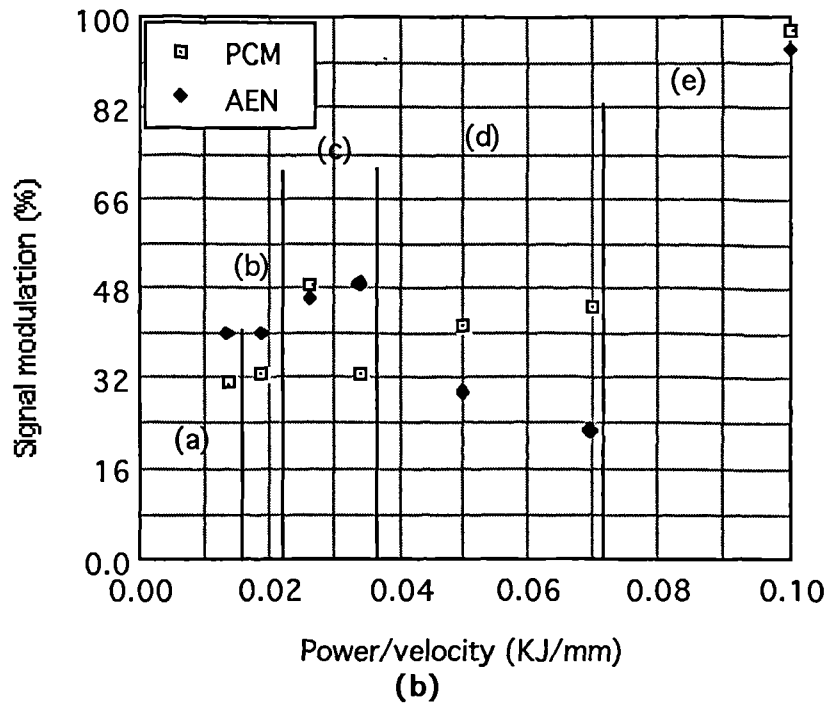
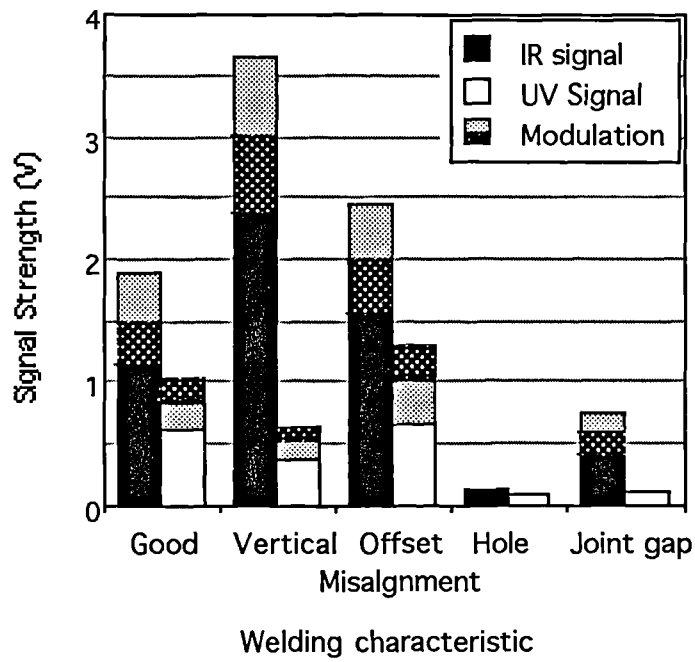
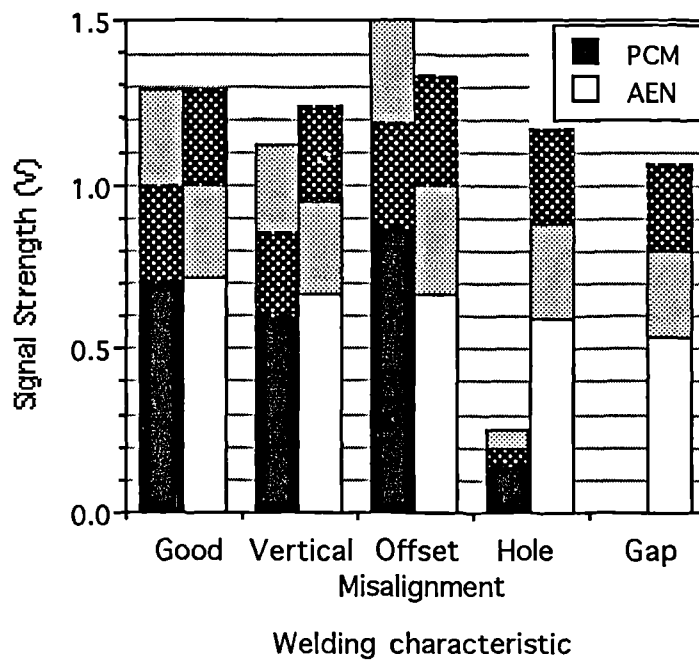


Figure 4.3 Response of signal and modulation of the PCM and AEN for varying energy input conditions. At 1.5-3.5KW, 40-230mm/s and 100mm lens.

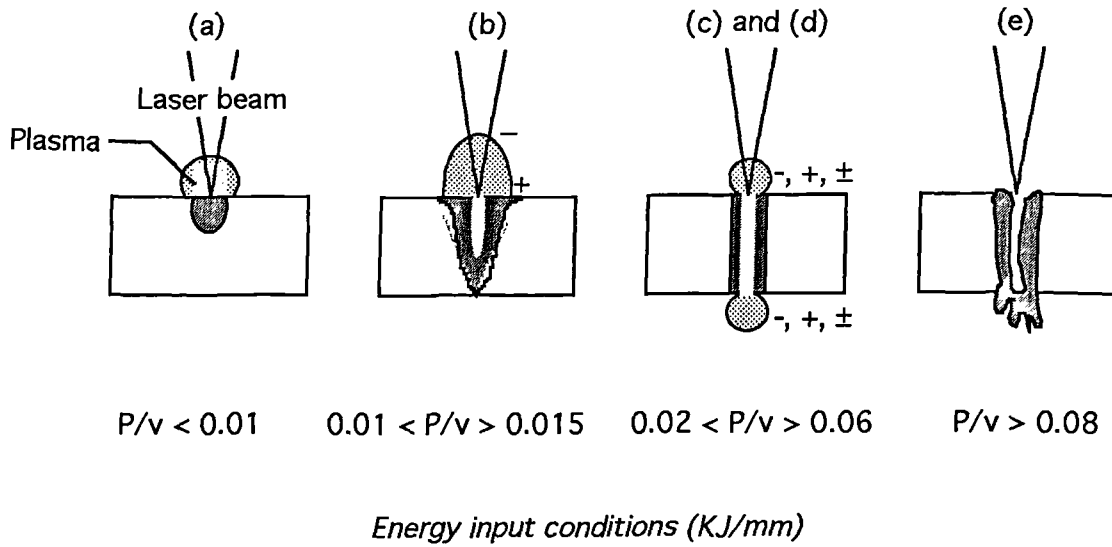


(a)

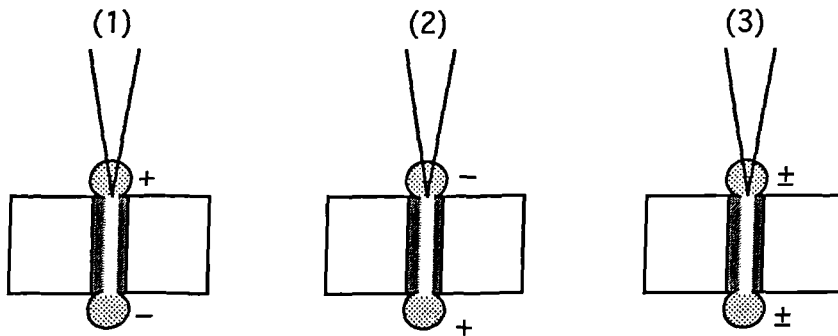


(b)

Figure 4.4 Comparison of “faulty” signals against a good weld for (a) Ultra-violet and Infra-red and (b) Plasma charge monitor and Acoustic emission nozzle.



(a)



*Three charge separation possibilities*

(b)

**Figure 4.5a** Schematically shows the charge distribution for the categorised energy inputs and **b** The three different signal that the PCM measures from the through thickness penetration welding. Welds at 3.5kW and speeds 40-230mm/s.

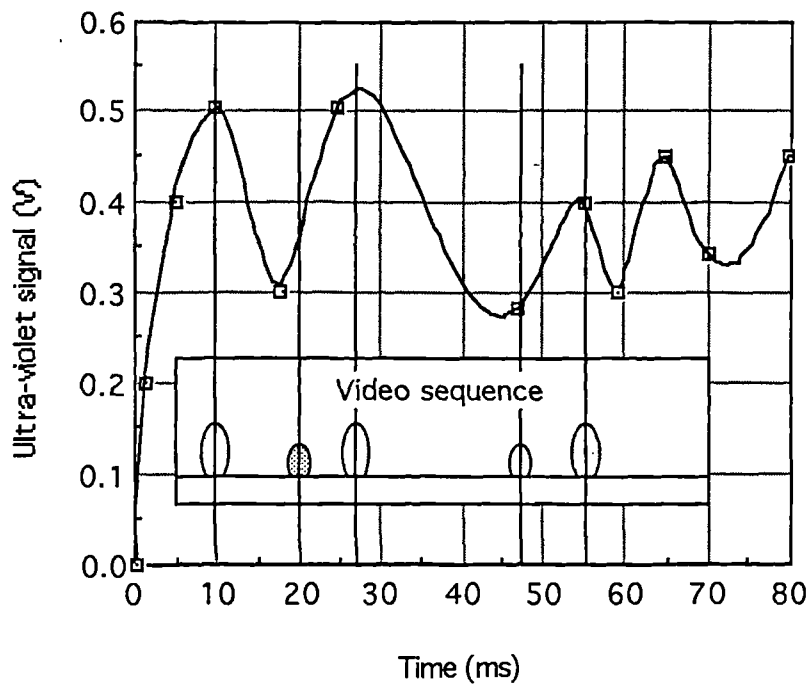


Figure 4.6 The comparison of signal response to the maxima and minima of plasma observed from the high speed video, welding at 3.5KW and 200mm/s with 100mm focal length.

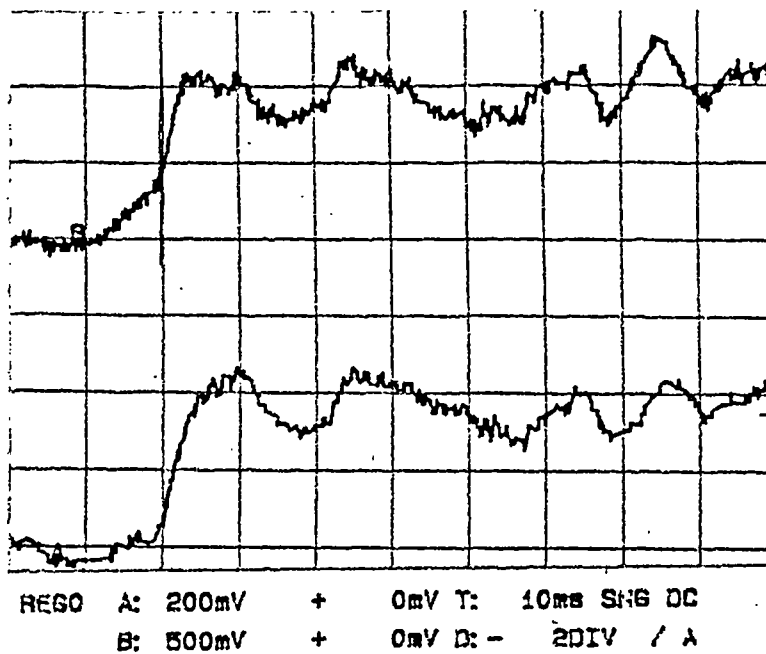
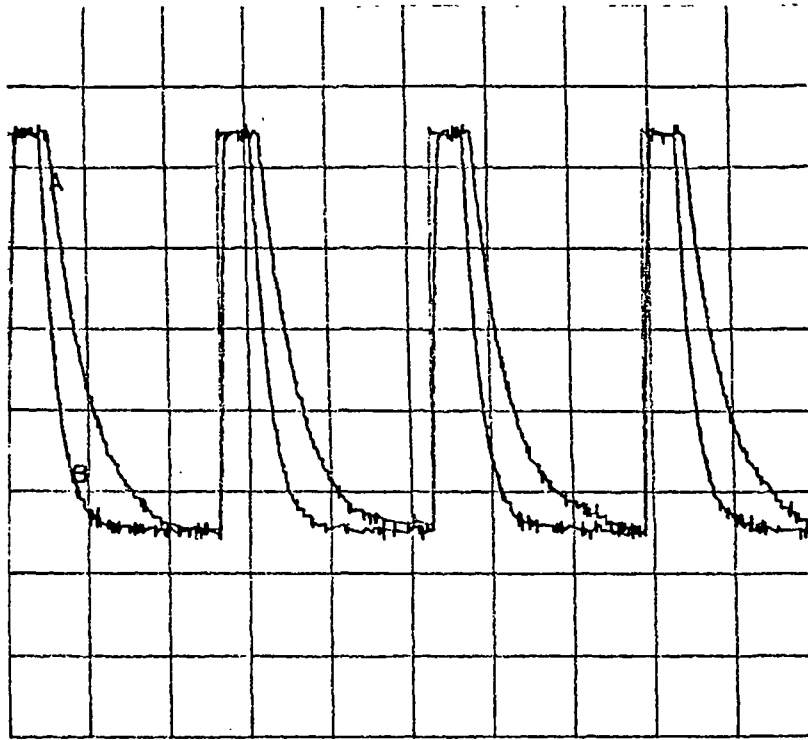


Figure 4.7 Shows the temporal response of the u/v and IR signal to an instantaneous weld signal.



.REG0 A~ 534mV + 0mV T: 10ms SNG DC  
 . B~ 510mV + 0mV D: + 0DIV / B

Figure 4.8 Compares the response times of the u/v and IR detectors to a step input.

## REFERENCES

1. Olsen, O., Jorgensen, H., Bagger, C., Kristensen, T. and Gregersen, O. "Recent Investigations in Sensorics for Adaptive Control of Laser Cutting and Welding". Proc. of Laser Advanced Materials Processing (LAMP), Osaka, 1992, pp405-413
2. Beyer, E., Donges, A., Loosen, P. and Herziger, G. "Optical Feedback During Laser Materials Processing". Optoelectronics in Engineering (Proc. of the 6<sup>th</sup> Int. Congress - LASER 83), Germany, 1983, Publ. Springer-Verlag, pp259-253.
3. Steen, W. M and Weerasinghe, V. M. "Monitoring of Materials Processes". Conf of SPIE. Innsbruck, 1986.
4. Maischner, D., Drenker, D., Seidel, B., Abels, P and Beyer, E. "Process Copntrol During Laser Beam Welding". Proc of International Congress on the Applications of Lasers and Electro-Optics (ICALEO), 1990.
5. Arata, Y. "Challenge to Laser Advanced Materials Processing". Proc. of Laser Advanced Material Processing (LAMP), May 1987, pp3-12.
6. Voelkel, D. D. and Mazumder, J. "Visualisation and Dimensional Measurement of the Laser Melt Pool". Proc of ICALEO, 1990, pp422-428.
7. Williams, K. and Steen, W. M. "Melt-pool and Keyhole Dynamics during Thin Plate Welding of Steel". Gas and Dynamics Laser Symposium, SPIE, Elouadra, Crete, 1992.
8. Beyer, E., Gasser, A., Gatzweiler, W. and Sokolowski, W. "PLasma Fluctuations in Laser Welding with CW-CO<sub>2</sub> Lasers". Proc of ICALEO, San Diego 1987, pp17-23.
9. Chen, H. B., Li, L., Brookfield, D., Williams, K. and Steen, W. M. "Laser Processing with Dual Wavelength Optical Sensors". Proc of ICALEO 1991.
10. Dixon, R. D. and Lewis, G. K. "The Influence of a Plasma During Laser Welding". Proc of ICALEO, 1983, pp44-49.
11. Li, L., Steen, W. M., Shi, K. and Brookfield, D. "Sensor Development for In-process Quality Inspection and Optimisation of High Speed Laser Can Welding Process". Proc of LAMP, Osaka, 1992.
12. Li, L., Qi, N., Brookfield, D and Steen, W. M. "On-line Laser Weld Sensing For Quality Control". Proc of ICALEO, 1990, pp411-421
13. Miyamoto, I. and Marou, H. "Spatial and Temporal Characteristics of Laser-Induced Plasma in CO<sub>2</sub> Laser Welding". Proc. of LAMP, 1992, pp311-316.
14. Shi, K., Li, L., Steen, W. M. and Brookfield, D. "Real Time Expert System for

Laser Can Weld Diagnosis". Proc of LAMP, 1992.

15. Ducharme, R., Kapadia, P. and Dowden, J. "A Mathematical Model of the Defocusing of Laser Light Above a Workpiece in Laser Materials Processing". Proc. of ICALEO, Orlando, 1992, pp187-197.



## CHAPTER FIVE

### LASER WELDING SYSTEM

#### **5.1 INTRODUCTION**

The laser welding of drum quality mild steel has been thoroughly investigated in the previous chapters. Consideration is now made for the transposing of the basic laboratory set-up into a semi-automated prototype manufacturing jig and a fully automated production system. The handling and welding procedures of the current Electrical Resistance Welding system would have to be largely replaced, with shift in emphasis to edge fit-up and laser beam/joint alignment. The general requirement of any laser system is that there is no substantial loss in production rates, line integration is made easy and suitably educated operators are available. The advantages intrinsic to a laser system is its flexibility; drums of varying shapes, sizes and thicknesses must be accommodated, laser "on" time can be maximised by time sharing the beam between several workstations, operators require minimal technical ability and a high degree of quality assurance is possible.

The specification from the welding research in the previous chapters are given in Table 1.

#### **5.2 SEMI-AUTOMATED LABORATORY WELDING SYSTEM**

The design and manufacture of the prototype pre-production welding jig was carried out between the University of Liverpool, Van Leer UK and Van Leer R & D laboratories in the Netherlands. The goals of the jig design were that it should be a realistic step toward the final production model, weld greater length test pieces and

incorporate some form of weld quality assurance device. The design underwent several evolutionary stages of development, the final design is shown in figure 5.1. The welding system followed the sequence shown in figure 5.2 and summarised below-

- (1) Datum bar up.
- (2) Insert test pieces.
- (3) Clamp test piece against the datum edge.
- (4) Remove datum bar.
- (5) Test pieces snap together under spring loaded lateral clamp.
- (6) Clamp second test piece.
- (7) Initiate welding action.

A picture of the welding jig in action is shown in figure 5.3, showing the integration of the focusing optics and the clamping sequence controller. A number of the critical areas of the design and sequencing are now discussed.

### **5.2.1 Fit-up and joint positioning**

From the specification of the system the laser spot size at the workpiece surface is 0.45 mm, which from previous testing allows the following tolerances; beam misalignment of  $\pm 0.2$  mm, gap width of  $< 0.15$  mm and vertical misalignment of  $< 0.15$  mm. In this instance the target was  $\pm 0.1$  mm thus incorporating any non-uniformity of edge straightness. To achieve this, a repeatable datum position was provided by a machined edge running the length of the weld. One of the pieces was held against this datum edge then clamped, the datum edge dropped away allowing the other piece to be clamped against the first. Correct positioning of the joint line was obviously pre-empted by aligning the beam with the datum edge using the visible He Ne guidance laser.

The gap width between the two test pieces was effectively eliminated by the

“snap” force created by the lateral spring loaded clamp. The action of the initial impact force reduced the extent of any minor surface protrusions, the constant clamping force allowed this force to be maintained through the welding procedure.

The vertical misalignment of the sheets was overcome by the proximity and force of the clamps to flatten out any sheet discontinuities. This was enhanced by minimising the width (to 6 mm) directly below the weld area between the underside surfaces that the samples are clamped against.

### **5.2.2 Focusing optics**

A set of metal optics were chosen in preference to a lens system for reasons of durability and performance. The mirrors are obviously more robust and can be cleaned. The 100 mm focal length specification, required that the optics would stand clear of the clamps yet be as near as possible, as highlighted in figure 5.3. The focusing system shown comprises of two 50 mm diameter 45 degree mirrors; the first a plane and the second an off axis parabolic, the design was shown in Chapter 2, figure 2.5. Although the off axis parabolic mirror is recommended it should be appreciated that the alignment tolerances of such a system are around  $\pm 0.002$  mm.

The mirror construction must include water cooling of the copper base with the reflective coating being a nickel/gold combination. A low flow rate of gas must also be maintained through the optics preventing airborne dust particles from settling on the optics. Protection of the mirrors from weld spatter is vital and was achieved using a high pressure coaxial shielding gas of around 20 l/min. through a 3 mm diameter nozzle (gas velocity of 50 m/s). This was still at a sufficiently low enough level whereby the weld was not “blown away”. The use of a cross flow “air knife” in front of the mirror was unable to adequately protect the mirror from spatter, and tended to contaminate the coaxial assist gas. The option of a sacrificial KCl window ahead of the optics did not overcome the problem but merely caused others (inspection requirements and window changing etc).

### **5.2.3 Gas delivery system**

From the specification option of coaxial or side jet gas delivery, the coaxial welding nozzle was selected. The reason for the choice was a combination of convenience and practicality, the nozzle does not suffer the positional tolerances of a side jet system and as described in the above section 5.2.2 protects the optics. The design of the copper welding nozzle is a long conical section fitting into the V shape of the clamping units. The gas nozzle primarily suppresses the plasma and protects the optics, however the weld must also be protected from oxidation. Normally some form of welding “shoe” is used with diffused gas delivery over the cooling weld, here, due to the proximity and depth of the side clamps and the focusing optics a the gas shroud naturally flows over the weld preventing weld oxidation, even in the cooling zone.

### **5.2.4 Clamping units and datum bar**

The whole welding jig system is operated by compressed air, in total there are five Festo air cylinders (AV-50-10-C) as part of the clamping and datum bar mechanism. Each sample is clamped by two of these air cylinders acting on a single clamping bar, the design is such that maximum clamping force is provided from the leverage on the bar. If required the applied clamping force can be altered by an air inlet valve which regulates the air pressure to the cylinders. The clearance of the “at rest” clamps from the sheets is around 0.4 mm, so when the test pieces snap together they do not override. Also this allows 1.4 mm sheets to be welded which is the maximum thickness currently used by Van Leer in drum manufacture.

The datum bar was the entire length of the weld and is positioned using a cam leverage system. Its movement describes a circle which at the weld area is moving directly up or down. It is noted that the other side of the datum edge is tapered. Thus, on removing the bar, the unclamped sample it is gradually brought toward the already clamped sample, avoiding an excessive knock. The datum bar is pulled back

from the weld underside so that it is completely out of the beam path which otherwise might cause thermal distortion of the datum edge.

#### **5.2.5 Welding system control unit**

After insertion of both test pieces clamp pair A was manually activated at the control cabinet shown in figure 5.3. Similarly for the datum bar removal and clamp pair B activation. Throughout this sequence an array of lights confirmed the level of the sequence, the welding go-ahead given only when all three were lit. The control and timing of the shutter, gas and movement was pre-programmed into the Trio table controller via the PC - initiating the table movement, assist gas and laser "on and off".

#### **5.2.6 Edge preparation and fit-up**

As described in previous chapters the edge preparation and fit-up is the key to reliable welding. A survey of the Van Leer and in-house guillotine sheared edges were not of high enough quality or repeatability for use in laser butt welding. In tests on multiple guillotine cuts over 2 m, only 60 % passed the surface roughness tolerances ( $\pm 0.1$  mm variance), with the required edge profile. However the set up of these guillotines were not optimised. The straightness of the edge is important but not as critical. A brief investigation into the limits of a guillotine setup and discussions with Pullman and Edwards Pearson showed that a consistent edge quality could be produced with  $\pm 0.15$  mm straightness tolerance over 1 m length. This is on the borderline for acceptability and requires further investigation with regard to other suppliers and improved shearing techniques. Alternatively, as laser technology would already be available laser cutting, which has a high quality, should be considered as an integral part of the welder or as a separate machine.

The laser cutting mechanism uses an oxygen assist gas which provides around

50% of the cutting energy, therefore only 1 kW of laser power would be needed to maintain the line speed [1]. This could be provided by a separate laser, or, a portion of the main welding laser could be diverted to the cutting workstation.

### **5.2.7 Weld quality assurance**

As discussed in Chapter 4, the Dual Wavelength Optical Sensor arrangement is recommended as a weld monitoring system. Before the development of this sensor arrangement was proven [2] a more simplistic method was suggested. Two quadrant diode sensors were positioned in line with the datum bar just below the focus point, at opposite ends of the welding area, corresponding to the beginning and completion of welding as shown in figure 5.4a. The diodes are sensitive to the misalignment of the HeNe laser beam which was arranged to be coaxial with the main processing beam. Misalignment of the HeNe beam would signal misalignment of the main beam with the butt joint. The four sections of the diode were paired, effectively into halves (a 2 section diode was unobtainable). The two signals are compared - therefore, if both signals were null (beam centred) the beam will follow the joint correctly. This rudimentary method assumes that a central position automatically indicates a good weld. In production the weld interfaces should be of a specified standard thus ensuring the assumption is correct. The signal analysis gives a simple "good" or "bad" result. The results of the diode response to a focussed HeNe shown in figure 5.4b, show misalignment can be signalled. The sensitivity of the diode response can be tailored to the specific welding operation. The circuit which was constructed and the diode specifications are given in Appendix E.

### **5.2.8 Experimental trials**

The performance of the welding system was tested for ease of operation and weld quality. The test pieces were 300 mm by 100 mm with a guillotine edge positioned with the burr downwards configuration. The experimentation involved simple speed

and power combinations ranging from 140-230 mm/s and 2-3.5 kW. The analysis was based on a visually sound, full penetration weld along the length of the weld.

The results are presented in the form of reliability histograms, indicating the percentage of the welds which were sound along the entire length of the weld. The comparison of the weld reliability with the old and new jig are shown in figure 5.5. The advantage of the improved clamping arrangement can be seen, extending the range of 100 % reliability to higher speeds. The cut off speed for a 100 % reliable weld is 170 mm/s, as opposed to the existing jig of 140 mm/s.

### **5.3 PRODUCTION SYSTEM RECOMENDATIONS**

From the results of this thesis it has been shown that welding of the required quality and reliability can be done at the required production speeds of 800 drums/hr. Thus the design and economic feasibility of this process in production was considered with particular interest in the possibility of adapting welding equipment. These considerations are discussed here.

#### **5.3.1 Discussion of the production system**

A production system would have to be able to match the current line speed of 800 drums/hr. The length of a drum is 905 mm, and the required production rate is 800 drums/hr which translates to a continuous welding speed of 200 mm/s. The welding speed in this work and using good clamping and edge preparation techniques could achieve these speeds. However as discussed in the previous section 5.2.7, 170 mm/s would be expected to be more reliable when using a 3.5 kW laser.

To fulfill the line production speeds the welding cycle must be completed in 4.5 seconds. Assuming a loading and unloading time of 1 second, the weld must be

achieved in 3.5 seconds. This requires a welding speed of 260 mm/s which is near the limit for 3.5 kW of laser power as seen in figure 5.5.

It has been shown in equation 3.14 that  $P = 0.3vwt(\rho C_p T_m)$  fitted the results well. Thus the extra speed could be obtained using a 5.2 kW laser (6 kW). This would require a larger and more expensive laser and the TEM<sub>00</sub> mode would not be available.

Alternatively, a twin workstation system could be used, as illustrated in figure 5.6 with the 3.5 kW beam switched between them. This allows a more realistic 9 second load/unload cycle time with a weld time of 4.5 seconds.

If a cutting module is added cutting speeds of 250 mm/s could be achieved using a 1 kW laser on 1mm mild steel with an oxygen assist gas at 2 bar [3]. For this cutting process to supply both workstations a total cycle time of 4 seconds is required.

The method of ensuring the fit-up and weld area clamping can be based on the semi-automatic welding jig. The manipulation and supporting of the drum body during welding must be devised, and can be achieved by a variety of methods. Consideration must also be made regarding the loading and unloading mechanism of the body. In the development of such a design care must be noted not to infringe the PRC Corporation patent on tin can welding system [3] or to pay the appropriate licence fee.

Once the drum body is positioned, traversing the beam along the joint favours flying optics, particularly as only a relatively short linear movement is required. The weight and inertia of traversing the drum clamping system at the necessary welding speed would be considerable, requiring substantial and bulky equipment.

The tolerance requirements regarding joint alignment ( $\pm 0.1$  mm) would be comfortably met by a single axis flying optics system capable of both cutting and welding. The value of seam tracking devices with an efficient clamping arrangement and a weld distance of 1m becomes irrelevant.



### 5.3.2 Economic feasibility

The “selling” feature of a laser welding system would include the improved cosmetic appearance, quality assurance on line and improvements in the factory environment. When considering Van Leer has a substantial commitment to the ISO 9000 standards programme, the value of this quality assurance element cannot be overstated.

The first consideration is the capital cost of buying the laser. This, although steadily declining, represents a significant sum and in the present market a 5 kW Laser Ecosse AF5L is around £110,000, which still compares favorably to an electrical resistance welding (ERW) equipment (£100,000). It would be hoped that an amount of the existing workpiece manipulation equipment could be modified (retrofitting), with the need for a new clamping arrangement and flying optics system as described in section 5.3.1.

A comparison of the two systems is given in Table 2, the figures are based on 8000 hrs/year operation. The capital depreciation has been taken over five years and subject to 10 % compound interest. All other information was supplied by Van Leer B.V. Note the material saving of 0.3 % when the butt welding configuration is used.

From Table 2 a 25 % saving in welding costs per drum might be expected at 800 drums/hr, giving a total saving of (4 p/drum) £262400/year. This is sufficient to warrant a serious analysis by Van Leer since the equipment is paid for in 1 year.

Welding Parameter	Specification
Power	3.5 kW
Mode	TEMoo
M2 factor	< 2.5
Focusing optics	Off-axis parabolic mirror
Focal length	100mm
Position of focus	+ 0.75mm
Gas delivery	coaxial
Gas type	Argon
Flow rate	10l/min.
Welding nozzle diameter	3mm
Nozzle stand-off	2mm
Welding speed	
Uncontrolled guillotine	140mm/s (8.4m/min.)
Controlled guillotine	170mm/s (10m/min.)
Angled controlled guillotine	200mm/s (12m/min.)

**Table 1** Summarises the specification for the welding system

ITEM	Cost / drum (£)	
	LASER	ERW
Capital depreciation for 1m weld	0.0117	0.009
Labour	same	same
Electricity (@ 6p/unit)	0.01	0.052
Water	same	same
Gas (@ £4/hour)	0.005	N/A
Maintenance	0.005	0.01
Raw materials (@ £200/ton)	0.097	0.1
TOTAL	0.129	0.17

Table 2 Shows the relative costing of the laser welding system as compared with the present ERW system per drum.



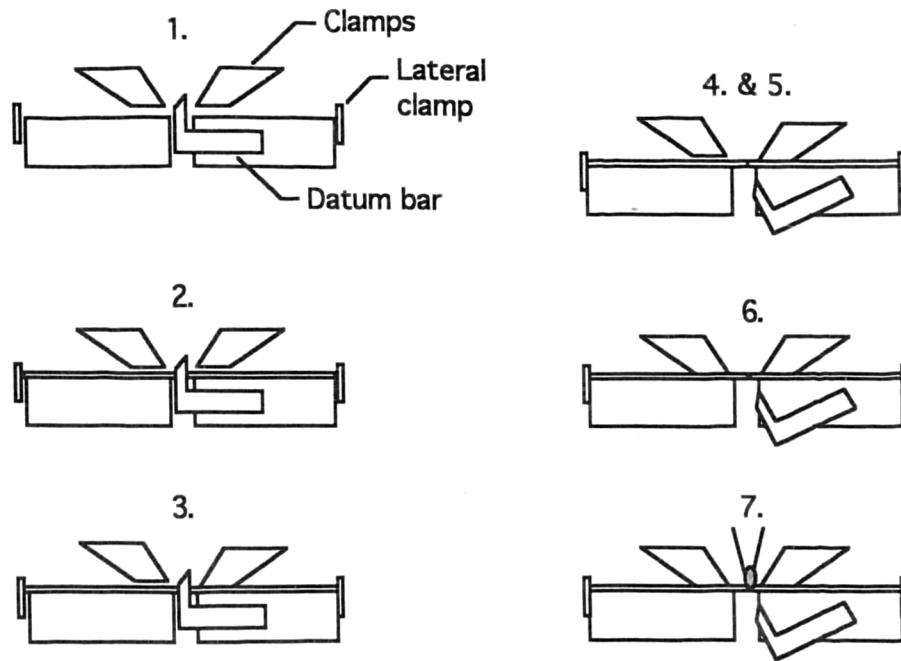


Figure 5.2 Graphical depiction of the weld clamp sequence and weld initiation.

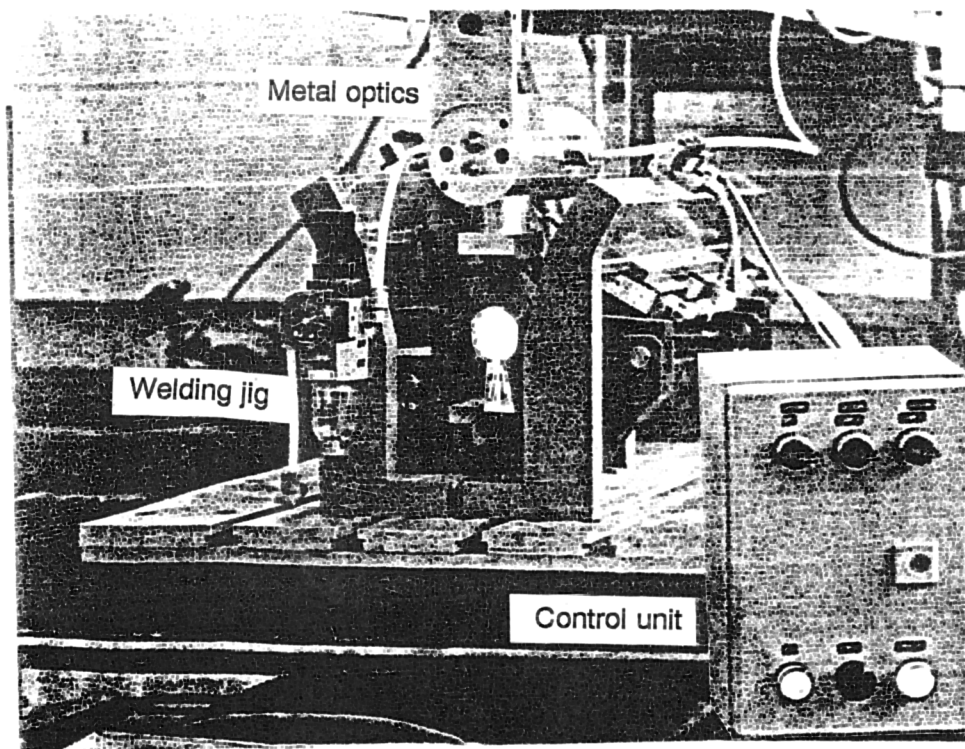
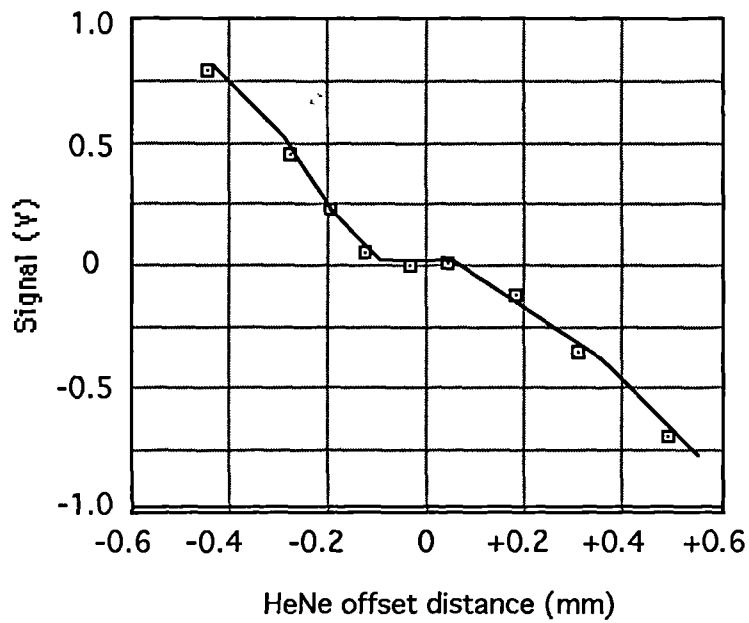
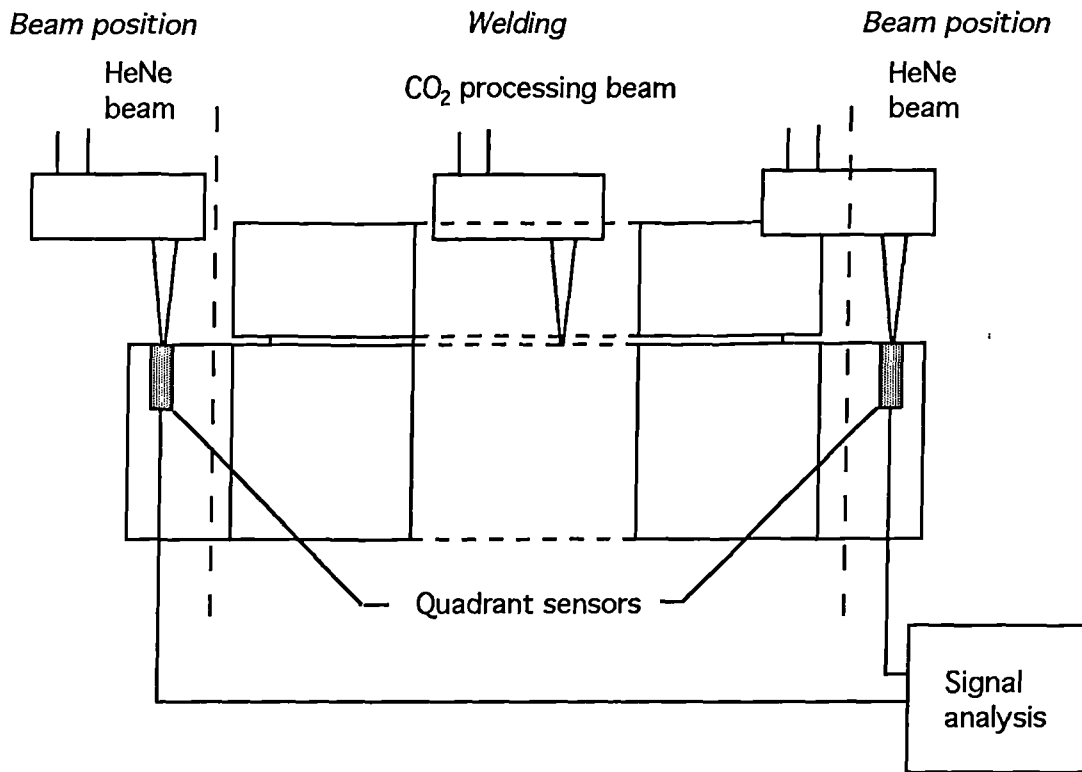
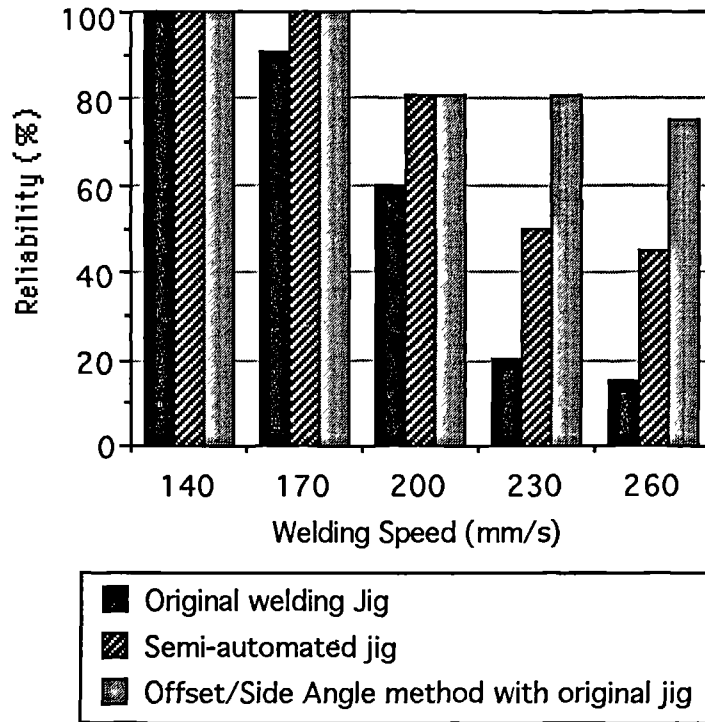


Figure 5.3 Shows the welding jig in action, integrated with the metal optics. To the right is the clamping control unit.



**Figure 5.4** a) Indicates the diode alignment method and b) Results of traversing a focussed HeNe beam across the sensor, note the null position at the centre.



**Figure 5.5** Reliability comparison of the two welding jigs and the proposed offset/side angle welding method. Figures relate to percentage length of a weld.

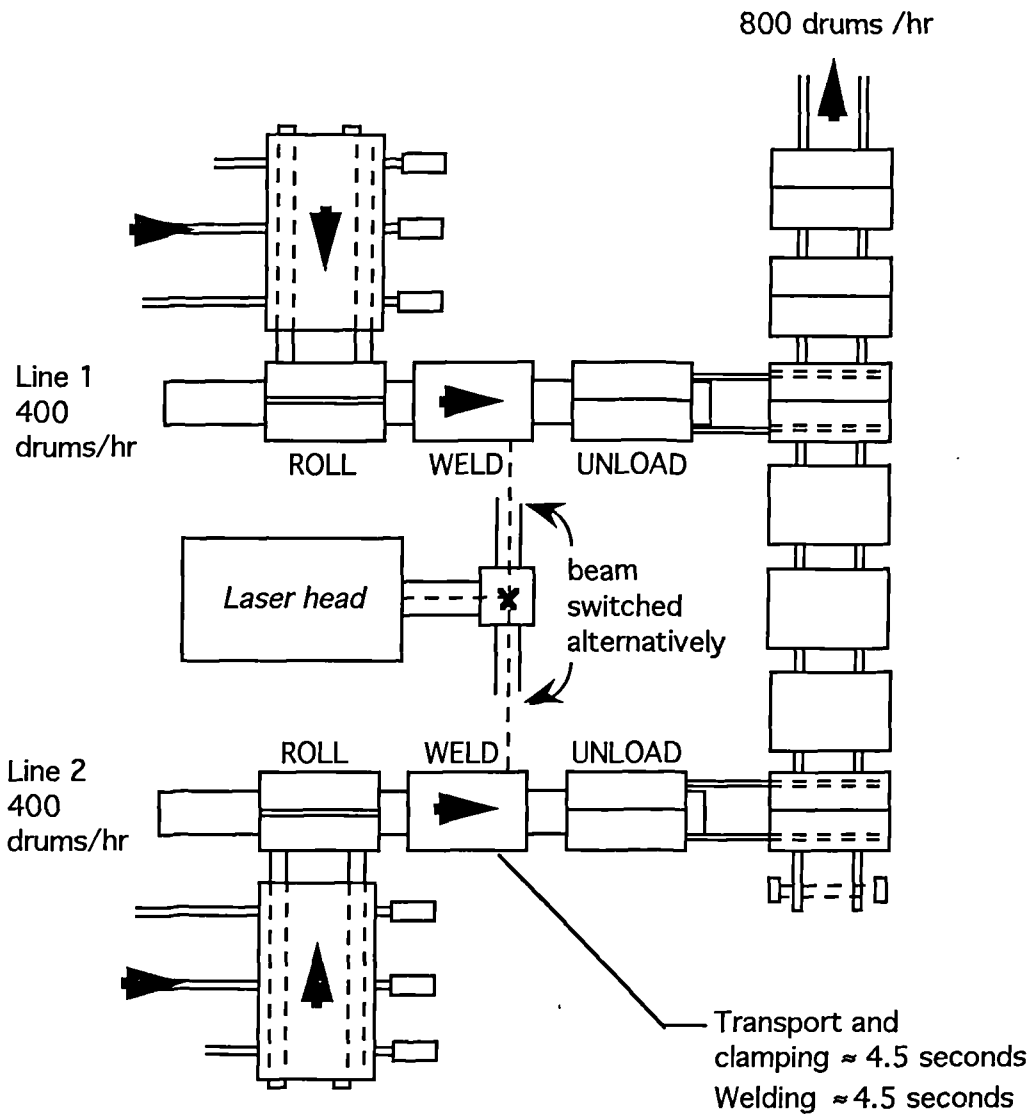


Figure 5.6 A plan view of the schematic arrangement of a dual workstation system



## REFERENCES

1. Industrial Laser Handbook, edited by M .Belforte, Tulsa, 1990.
2. Chen, H. B., Li, L., Brookfield, D., Williams, K. and Steen, W. M. "Laser Processing with Dual Wavelength Optical Sensors". Proc of ICALEO 1991.
3. Sharp, M. C. Method of Laser Butt Welding US Patent No. 4 577 088.

## CHAPTER SIX

### CONCLUSION

A unique and extensive research project has been carried out in the area of thin sheet laser welding. Through the three years of this study a sound and effective working relationship has built up between the University of Liverpool and Van Leer B.V., which has benefited both the project and those involved. From all the work presented there are several aspects which are significant -

The implementation of the statistically designed experimentation vastly increased the initial coverage of the research work, leading to the formation of a comprehensive base of welding knowledge and a statistical model which proved valid within the defined operating region. From this, a further investigation into the critical areas was possible resulting in the specification for an optimised welding set-up.

The main achievements were:-

1. The design, manufacture and testing of a pre-production welding system.
2. The development of improved laser welding methods:
  - a) Angling of the workpiece perpendicular the direction of welding and offsetting the beam. This achieved more reliable welds at increased speeds and alleviated the problem of humping.
  - b) The circumferential welding using spinning samples increased the welding speed for a certain depth by over 30 %.
  - c) Angling the workpiece parallel to the direction of welding. Preliminary results point towards increased penetration.
  - d) The adoption of positive focusing.

3. An in depth investigation into the welding of guillotine sheared edges. Assessing the types and weldability of edges, associated welding tolerances and the particular implications for a production system.
4. The assessment of several in-process weld monitoring systems, with the recommendation of the Dual Wavelength Optical Sensors arrangement.
5. The use of a high speed video camera in providing valuable general qualitative information of the temporal behaviour of the melt pool and plasma, and specifically in the investigation of the humping phenomena.
6. The results show that the process is a feasible production alternative. The financial discussion suggests it was a profitable alternative

## FUTURE WORK

The direction of any further work can take two forms; development of the overall welding system or the generic research of the laser welding process. The following suggestions are a combination of the two -

- a) Development of the pre-production jig to a full size test jig
- b) Investigation into the welding of painted and coated drums.
- c) Development of the laser welding of guillotine edges, incorporating
  - i) Further work into the suggested angling mechanisms.
  - ii) Use of wire feed systems.
  - iii) In depth study into edge cutting methods.
- d) Development of the Dual Wavelength Optical Sensor arrangement to an automatic fault diagnosis in-process system.
- e) Assessing the feasibility of an all laser welded drum.

## APPENDIX A

Stat-Ease Statistical software and Design matrix report

# DESIGN-EASE™

Software by STAT-EASE, Inc.

DESIGN-EASE is an easy-to-use program enabling scientists and engineers to design and analyze their own experiments. The program guides you to the proper choice of an experimental design. Analysis is provided by easily understood graphical procedures for interpreting and communicating experimental results. DESIGN-EASE offers a full range of two-level factorial, fractional factorial and Plackett-Burman designs. These designs are the basic building blocks for the successful application of statistical experiment design in industrial and research environments. DESIGN-EASE is an excellent program for the non-statistician to use when designing experiments.

## HIGHLIGHTS:

DESIGN-EASE software combines ease of use with powerful two-level factorial design. Pop-up menus make the program easy to learn and fast to use. No knowledge of computers is required to use the package and there are no commands to learn.

The documentation includes a complete tutorial using data from the text STATISTICS FOR EXPERIMENTERS, by Box, Hunter and Hunter, available from John Wiley & Sons, Inc., New York. This tutorial will lead you through choosing, setting up and analyzing a factorial design.

Experimental designs are selected from easy-to-understand menus. To aid you in your choice, the alias structure for each fractional factorial design is given. DESIGN-EASE handles the details that in the past were barriers to using statistical experiment design. Center points can be added to the full and fractional factorial designs. Designs containing more than eight experiments can be run completely randomized or in blocks.

Key	Program Option
F1	First Time Help
F2	Factorial Design Menu
F3	Plackett-Burman Designs
F4	Data File Selection
F5	Enter / Edit Variables
F6	Enter / Edit Responses
F7	Data Analysis
F8	Create Reports
F9	File / Print Utility
F10	Design Status

### FACTORIAL DESIGNS

		Number of Variables									
		3	4	5	6	7	8	9	10	11	
EXPERIMENTS	8	Full	$\frac{1}{2}$ Rep	$\frac{1}{4}$ Rep	$\frac{1}{8}$ Rep	$\frac{1}{16}$ Rep					
	16	2 Rep	Full	$\frac{1}{2}$ Rep	$\frac{1}{4}$ Rep	$\frac{1}{8}$ Rep	$\frac{1}{16}$ Rep	$\frac{1}{32}$ Rep	$\frac{1}{64}$ Rep	$\frac{1}{128}$ Rep	
	32	4 Rep	2 Rep	Full	$\frac{1}{2}$ Rep	$\frac{1}{4}$ Rep	$\frac{1}{8}$ Rep	$\frac{1}{16}$ Rep	$\frac{1}{32}$ Rep	$\frac{1}{64}$ Rep	
	64	8 Rep	4 Rep	2 Rep	Full	$\frac{1}{2}$ Rep	$\frac{1}{4}$ Rep	$\frac{1}{8}$ Rep	$\frac{1}{16}$ Rep	$\frac{1}{32}$ Rep	

### PLACKETT & BURMAN DESIGNS

Key	Variables	Experiments
1	— 7 or less	8
2	— 11 or less	12
3	— 15 or less	16
4	— 19 or less	20
5	— 23 or less	24
6	— 31 or less	32
Esc	— Return	

# DESIGN-EASE SOFTWARE

Once you select the design, enter the names and levels of the variables to be studied and the responses to be measured. DESIGN-EASE will produce data sheets with the actual experiments that need to be run. The program will randomize the run order for you.

Data analysis is presented in an easy-to-understand format. Results are reviewed in a scroll back buffer and an appropriate model is chosen. Data analysis reports can be printed easily.

Normal and half normal probability plots are used to determine the important variables in your design. DESIGN-EASE makes it practical for non-statisticians to design and analyze their own experiments.

Residual analysis is done using a normal probability plot of the residuals and plots of the residuals versus predicted values, run order and the independent variables. If a transformation of the response is required, DESIGN-EASE has many available.

Interaction plots are used to interpret significant two-factor interactions. The response data is plotted against the two levels of one factor for both levels of the second factor. Lines that are not parallel show the nature of the interaction between the two factors. A cube plot can be used to illustrate the relationship between three factors. The response is averaged over the three factors chosen and those averages are plotted in the corners of a cube.

STAT-EASE, INC.  
Hennepin Square Suite 191  
2021 East Hennepin Avenue  
Minneapolis, MN 55413

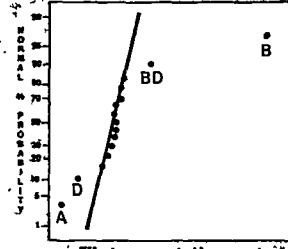
DESIGN-EASE ANALYSIS					
SOURCE	SS	DF	MEAN SQUARE	F	PROB > F
MODEL	2762.000000	4	690.500000	497.756	0.0001
ERROR	30.000000	11	2.727273		
TOTAL	2801.000000	15			

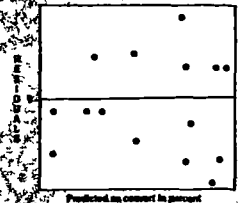
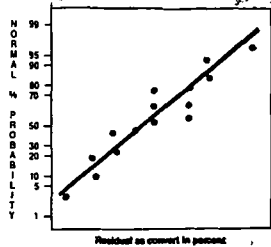
DESIGN-EASE ANALYSIS					
PARAMETER	ESTIMATE	SE	T	PROB >  T	CI
A	1.000000	0.100000	10.000000	0.0001	0.7999
B	0.500000	0.100000	5.000000	0.0005	0.3999
C	0.250000	0.100000	2.500000	0.0244	0.1999
D	0.125000	0.100000	1.250000	0.2238	0.1000

Run	A	B	C	D	Y				
1	1	1	10	240	80	10	1	1	
2	2	2	1	15	220	50	10	1	3
3	3	1	10	220	80	12	1	1	2
4	4	1	15	240	50	10	1	1	4
5	5	1	15	220	50	12	1	1	5
6	6	1	10	240	80	12	1	1	6
7	7	1	15	240	80	12	1	1	7
8	8	1	15	220	80	10	1	1	8
9	9	1	15	220	80	10	1	1	9
10	10	1	10	240	50	10	1	1	10
11	11	1	10	240	50	12	1	1	11
12	12	1	15	220	80	12	1	1	12
13	13	1	15	240	80	10	1	1	13
14	14	1	15	240	80	10	1	1	14
15	15	1	15	240	80	10	1	1	15

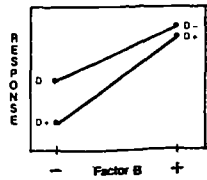
TYPICAL NORMAL PROBABILITY PLOT



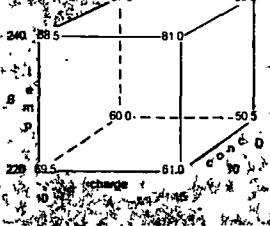
Effect as converted in percent



BD Interaction Plot



Cube plot of A, B and D



For More Information:  
Write or Call 612/378-9449

# DESIGN-EXPERT VERSION 2

Software for Response Surface and Mixture Experiments from STAT-EASE

## OPTIMIZE YOUR PRODUCT OR PROCESS



### POWERFUL YET EASY TO USE

DESIGN-EXPERT™ software helps you set up and analyze powerful experiments designed to optimize your product or process. Version 2 offers many useful designs for response surface and mixture experiments. Study up to 6 variables using the design that you select. Once you settle on the design, the program will generate worksheets with all experiments laid out and the runs randomized. Easy-to-use menus guide you through the set-up, analysis and report stages of your project. DESIGN-EXPERT provides high-resolution graphs and statistical summaries for your technical reports.

### MANY DESIGNS OFFERED

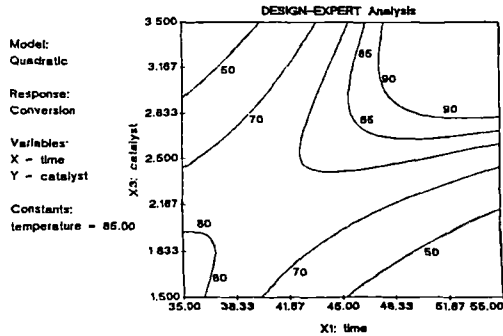
DESIGN-EXPERT provides great flexibility for the sophisticated experimenter. For response surface designs you can choose from factorial, central composite, pentagon, hexagon or Box-Behnken designs. If you work with mixtures, select from a menu that includes simplex lattice and simplex centroid designs (augmented or not), as well as distance based and d-optimal designs. You can modify any of these designs with the new design editor offered by DESIGN-EXPERT version 2.

### OPTIMIZE SEVERAL RESPONSES

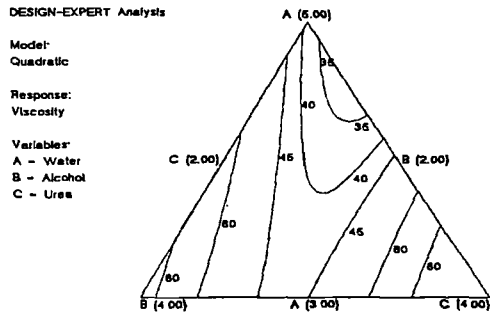
DESIGN-EXPERT provides complete least squares regression analysis to model your data. Choose linear, quadratic or cubic models for response surface analysis; and linear, quadratic or special cubic Scheffe polynomials for mixture component analysis. Display high resolution contour plots on your screen and/or your printer. The optimization module in DESIGN-EXPERT will even provide overlay plots of two (or more) responses, showing at a glance which conditions best meet your overall performance needs.

DESIGN-EXPERT: Main Menu	
C	- Configuration
S	- Design selection
D	- Design editing
R	- Response editing
A	-> Data analysis <
O	- Optimization
U	- Utilities
Esc	- Leave DESIGN-EXPERT

SAMPLE MENU - EASY TO FOLLOW



RESPONSE SURFACE PLOT



THREE-COMPONENT MIXTURE



## DESIGN-EXPERT VERSION 2

### USEFUL STATISTICAL DATA

DESIGN-EXPERT places the analysis of variance (ANOVA) data in a scrolling buffer. View and print the sections you wish to report. The analysis includes:

- model ANOVA
- predicted residual sum of squares
- sequential sum of squares table
- lack of fit tests.

These statistics aid in choosing the appropriate order polynomial for each response. To check residuals, you can now select from a variety of useful plots. DESIGN-EXPERT offers the features and flexibility you need to optimize your product, process or formulated mixture.

### TUTORIALS MAKE IT EASY

The DESIGN-EXPERT manual includes two complete tutorials that lead you through all the stages of a response surface and a mixture problem. In little more than an hour you can be up and running. You will find the menus to be laid out in a very logical sequence, so you can focus on designing your experiment, rather than looking up computer commands. The tutorials provide many helpful design tips. You also get a handy reference on the statistics used to analyze response surface and mixture designs.

### MANY NEW FEATURES

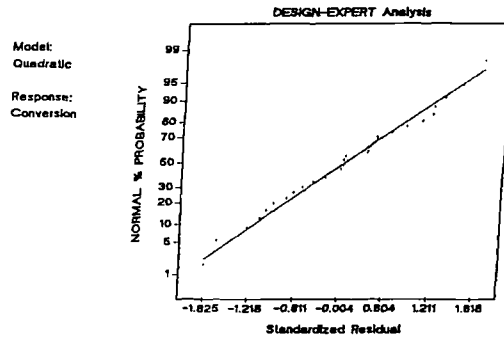
- Increase in variables from 4 to 6
- Easy-to-follow menuing system
- Many new designs to choose from
- Editing of design points allowed
- Scroll-back buffer that can be edited
- Comprehensive residual plots
- Enhanced reports and graphs

### HARDWARE REQUIREMENTS

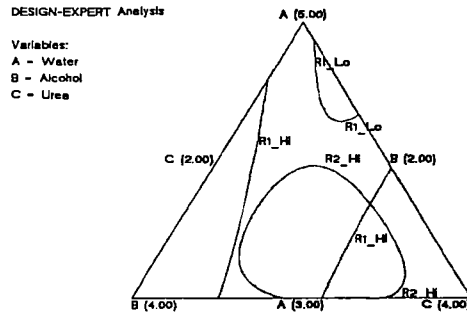
DESIGN-EXPERT runs on IBM personal computers and compatibles. It requires CGA, EGA, VGA or Hercules graphics, 512K of disk space (a hard disk is recommended) and 512K memory. Expanded memory (EMS) is supported.

Point Selection Method	
L - >	Simplex-lattice augmented <
S -	Simplex-lattice
A -	Simplex-centroid augmented
C -	Simplex-centroid
D -	Distance-based
O -	d-optimal
U -	User defined
Esc -	Return

### MENU - MIXTURE DESIGNS



### NORMAL PLOT RESIDUALS



### RESPONSE PLOTS OVERLAID

TO ORDER CALL 612/378-9449 OR WRITE

**STATBASE**  
INC.

Hennepin Square, Suite 191  
2021 East Hennepin Avenue  
Minneapolis, MN 55413

**30 DAY TRIAL.  
GIVE DESIGN-EXPERT  
A TRY!**

DESIGN - EASE ANALYSIS

	Run Order	1	2	3	4	5	6	7	8
	Block	1	1	1	1	1	1	1	1
	Standard Order	23	2	55	29	6	47	13	67
A -	MODE	-	TEMO	TEMO	-	TEMO	TEMO	TEMO	-
B -	SIDE ANG. DEGREES	10	0	5	0	0	10	0	5
C -	FOCUS mm	+1.0	-1.0	0	-1.0	+1.0	+1.0	+1.0	0
D -	SPEED mm/s	40	40	30	140	40	140	140	30
E -	POWER kW	3.5	1.5	2.5	3.5	1.5	1.5	1.5	2.5
F -	LENS mm	100	100	125	100	100	150	100	125
G -	POLARITY	-	CIRCULAR	LINEAR	-	CIRCULAR	CIRCULAR	LINEAR	CIRCULAR
H -	NORM ANG. DEGREES	5.5	0	-	5.5	0	5.5	5.5	-
R1 -	DEPTH mm	1.1800	0.8900	1.0700	1.0000	0.8500	0.4100	0.8100	1.0700
R2 -	HARDNESS HRB	271.0000	317.0000	271.0000	374.0000	289.0000	383.0000	321.0000	271.0000
R3 -	SPEC ENER J/mm2	701.0000	158.0000	200.0000	139.0000	158.0000	44.0000	66.0000	209.0000
R4 -	JOIN EFF. mm2/J	13.0000	24.0000	39.0000	40.0000	23.0000	38.0000	76.0000	39.0000
R5 -	MELT EFF. %	11.0000	16.0000	25.0000	16.0000	12.5000	19.0000	14.6000	20.0000
R6 -	w1 mm	1.3000	1.0600	0.8000	0.6500	0.8600	0.7500	0.2500	0.8000
R7 -	w2 mm	0.6000	0.5200	0.5000	0.2600	0.4100	0.0600	0.1700	0.5000

DESIGN - EASE ANALYSIS

	Run Order	9	10	11	12	13	14	15	16
	Block	1	1	1	1	1	1	1	1
	Standard Order	44	54	25	24	43	63	69	42
A -	MODE	-	TEMO	TEMO	TEMO	TEMO	TEMO	-	TEMO
B -	SIDE ANG. DEGREES	10	0	0	10	10	10	5	0
C -	FOCUS mm	-1.0	+1.0	-1.0	+1.0	-1.0	+1.0	0	-1.0
D -	SPEED mm/s	140	40	140	40	140	140	90	140
E -	POWER kW	1.5	3.5	3.5	3.5	1.5	3.5	2.5	1.5
F -	LENS mm	150	150	100	100	150	150	125	150
G -	POLARITY	-	LINEAR	CIRCULAR	LINEAR	LINEAR	CIRCULAR	LINEAR	-
H -	NORM ANG. DEGREES	0	0	0	0	5.5	0	-	5.5
R1 -	DEPTH mm	0.3200	0.9500	1.0000	1.0300	0.5000	0.9000	1.0700	0.3300
R2 -	HARDNESS HRB	457.0000	194.0000	303.0000	254.0000	275.0000	303.0000	281.0000	370.0000
R3 -	SPEC ENER J/mm2	40.0000	560.0000	200.0000	400.0000	44.0000	133.0000	200.0000	50.0000
R4 -	JOIN EFF. mm2/J	30.0000	14.0000	40.0000	11.0000	47.0000	36.0000	39.0000	40.0000
R5 -	MELT EFF. %	7.0000	13.0000	23.0000	10.0000	14.0000	15.0000	20.0000	15.0000
R6 -	w1 mm	0.4000	1.3000	1.0000	1.1000	0.5000	0.4500	0.3000	0.6000
R7 -	w2 mm	0.0000	0.8000	0.3300	0.8400	0.0600	0.4300	0.5000	0.0600

DESIGN-EASE ANALYSIS

	Run Order	17	18	19	20	21	22	23	24
Block	1	1	1	1	1	1	1	1	1
Standard Order	17	52	27	29	60	55	7	31	
A - MODE	-	TEM00	TEM01	TEM00	TEM01	TEM01	TEM00	TEM00	TEM00
B - SIDE ANG. DEGREES		0	10	10	10	10	10	10	10
C - FOCUS mm		-1.0	-1.0	-1.0	-1.0	-1.0	+1.0	+1.0	+1.0
D - SPEED mm/s		40	40	140	140	140	40	40	140
E - POWER kW		3.5	3.5	3.5	3.5	3.5	3.5	1.5	3.5
F - LENS mm		100	150	100	100	150	150	100	100
G - POLARITY	-	CIRCULAR	CIRCULAR	CIRCULAR	LINEAR	LINEAR	CIRCULAR	CIRCULAR	LINEAR
H - NORM ANG. DEGREES		0	5.5	5.5	0	5.5	0	0	5.5
R1 - DEPTH mm		1.1600	0.9200	0.5000	0.8100	0.9400	1.0700	1.0000	0.8300
R2 - MARGINES HRB		225.0000	271.0000	289.0000	382.0000	326.0000	159.0000	271.0000	362.0000
R3 - SPEC ENER J/mm2		541.0000	472.0000	200.0000	202.0000	89.0000	154.0000	232.0000	200.0000
R4 - JOIN EFF. mm2/J		13.0000	11.0000	20.0000	32.0000	38.0000	22.0000	25.0000	33.0000
R5 - MELT EFF. %		10.0000	7.0000	15.0000	28.0000	23.0000	17.0000	16.0000	14.0000
R6 - w1 mm		1.6000	1.1400	1.0000	0.5300	0.9000	1.6000	1.0000	1.6000
R7 - w2 mm		0.7400	0.7200	0.0000	0.2700	0.4500	0.8000	0.4100	0.3200

DESIGN-EASE ANALYSIS

	Run Order	25	26	27	28	29	30	31	32
Block	1	1	1	1	1	1	1	1	1
Standard Order	18	34	63	11	58	48	41	1	
A - MODE	-	TEM01	TEM01	-	TEM00	TEM01	TEM01	TEM00	TEM00
B - SIDE ANG. DEGREES		0	0	5	10	0	10	0	0
C - FOCUS mm		-1.0	-1.0	0	-1.0	-1.0	+1.0	-1.0	-1.0
D - SPEED mm/s		40	40	90	140	140	140	140	40
E - POWER kW		3.5	1.5	2.5	1.5	3.5	1.5	1.5	1.5
F - LENS mm		100	150	125	100	150	150	150	100
G - POLARITY	-	LINEAR	LINEAR	-	CIRCULAR	CIRCULAR	CIRCULAR	LINEAR	CIRCULAR
H - NORM ANG. DEGREES		5.5	5.5	-	0	0	0	0	5.5
R1 - DEPTH mm		0.9800	0.9100	1.0700	0.5000	0.5000	0.3500	0.2500	0.9000
R2 - MARGINES HRB		257.0000	250.0000	271.0000	386.0000	336.0000	390.0000	350.0000	362.0000
R3 - SPEC ENER J/mm2		466.0000	105.0000	200.0000	66.0000	30.0000	45.0000	30.0000	231.0000
R4 - JOIN EFF. mm2/J		11.0000	24.0000	39.0000	47.0000	20.0000	25.0000	30.0000	27.0000
R5 - MELT EFF. %		9.0000	20.0000	13.0000	14.0000	12.0000	15.0000	11.0000	10.0000
R6 - w1 mm		1.1000	1.2000	0.3000	0.5400	0.5300	0.6000	0.8000	0.7800
R7 - w2 mm		0.2800	0.5500	0.5000	0.0000	0.3500	0.0000	0.0000	0.3300

DESIGN - EASE ANALYSIS

	Run Order	33	34	35	36	37	38	39	40
	Block	1	1	1	1	1	1	1	1
	Standard Order	10	21	33	44	52	5	31	65
A -	MODE	-	TEM01	TEM00	TEM01	TEM01	TEM01	TEM00	TEM00
B -	SIDE ANG. DEGREES	0	0	10	0	10	0	10	0
C -	FOCUS mm	-1.0	+1.0	+1.0	+1.0	-1.0	+1.0	-1.0	0
D -	SPEED mm/s	140	40	40	140	140	40	40	90
E -	POWER kW	1.5	3.5	3.5	1.5	1.5	1.5	3.5	2.5
F -	LENS mm	100	100	150	100	100	100	150	125
G -	POLARITY	-	CIRCULAR	LINEAR	LINEAR	LINEAR	LINEAR	LINEAR	LINEAR
H -	NORM ANG. DEGREES	0	0	5.5	0	5.5	5.5	0	-
R1 -	DEPTH mm	0.4500	1.1500	0.9400	0.4000	0.9100	0.8500	1.0000	1.0000
R2 -	HARDNESS HRB	300.0000	333.0000	354.0000	362.0000	396.0000	330.0000	362.0000	271.0000
R3 -	SPEC ENER J/mm2	38.0000	701.0000	312.0000	80.0000	45.0000	231.0000	468.0000	200.0000
R4 -	JOIN EFF. mm2/J	35.0000	13.0000	11.0000	40.0000	85.0000	22.0000	11.0000	39.0000
R5 -	MELT EFF. %	14.0000	19.0000	9.0000	16.0000	29.0000	14.0000	11.0000	21.0000
R6 -	w1 mm	0.4200	1.0100	1.3000	0.3000	0.8300	0.8900	1.6100	0.8000
R7 -	w2 mm	0.0000	1.0000	0.6000	0.0000	0.2300	0.6800	0.9900	0.5000

DESIGN - EASE ANALYSIS

	Run Order	41	42	43	44	45	46	47	48
	Block	1	1	1	1	1	1	1	1
	Standard Order	37	36	4	45	50	22	16	35
A -	MODE	-	TEM00	TEM01	TEM01	TEM00	TEM01	TEM01	TEM00
B -	SIDE ANG. DEGREES	0	10	10	0	0	0	10	10
C -	FOCUS mm	+1.0	-1.0	-1.0	+1.0	-1.0	+1.0	+1.0	-1.0
D -	SPEED mm/s	40	40	40	140	40	40	140	40
E -	POWER kW	1.5	1.5	1.5	1.5	3.5	3.5	1.5	1.5
F -	LENS mm	150	150	100	150	150	100	100	150
G -	POLARITY	-	LINEAR	CIRCULAR	CIRCULAR	CIRCULAR	LINEAR	CIRCULAR	CIRCULAR
H -	NORM ANG. DEGREES	0	0	5.5	0	0	5.5	5.5	5.5
R1 -	DEPTH mm	0.6400	1.0000	1.1500	0.3000	0.9500	1.3000	1.0000	0.9600
R2 -	HARDNESS HRB	279.0000	254.0000	293.0000	395.0000	244.0000	278.0000	341.0000	271.0000
R3 -	SPEC ENER J/mm2	154.0000	374.0000	158.0000	150.0000	312.0000	465.0000	45.0000	154.0000
R4 -	JOIN EFF. mm2/J	27.0000	21.0000	31.0000	35.0000	11.0000	15.0000	31.0000	25.0000
R5 -	MELT EFF. %	17.0000	19.0000	22.0000	16.0000	11.0000	7.0000	29.0000	17.0000
R6 -	w1 mm	1.0000	1.1900	1.1200	0.5100	1.2900	1.3700	0.6500	1.1000
R7 -	w2 mm	0.7700	0.3800	0.4000	0.0000	0.9600	0.6500	0.1400	0.4500

DESIGN - EASE ANALYSIS

Run Order	50	51	52	53	54	55	55
Block	1	1	1	1	1	1	1
Standard Order	61	54	52	59	9	29	39
A - MODE	TEM00	TEM00	TEM01	TEM01	TEM00	TEM01	TEM00
B - SIDE ANG. DEGREES	0	10	0	0	10	10	10
C - FOCUS mm	+1.0	-1.0	+1.0	+1.0	-1.0	+1.0	+1.0
D - SPEED mm/s	140	140	140	140	140	40	140
E - POWER kW	2.5	3.5	3.5	3.5	3.5	1.5	3.5
F - LENS mm	150	150	150	150	150	100	100
G - POLARITY	CIRCULAR	LINEAR	CIRCULAR	LINEAR	CIRCULAR	LINEAR	CIRCULAR
H - NORM ANG. DEGREES	5.5	5.5	5.5	0	0	5.5	0
R1 - DEPTH mm	1.0500	0.9400	0.8600	1.0700	0.7700	0.9400	0.7500
R2 - HARDNESS HRB	254.0000	299.0000	374.0000	327.0000	279.0000	235.0000	341.0000
R3 - SPEC ENER J/mm2	133.0000	100.0000	135.0000	89.0000	133.0000	159.0000	200.0000
R4 - JOIN EFF. mm2/J	42.0000	37.0000	34.0000	43.0000	31.0000	25.0000	13.0000
R5 - MELT EFF. %	23.0000	26.0000	9.0000	21.0000	17.0000	17.0000	26.0000
R6 - w1 mm	0.8200	0.7300	0.4800	0.7500	0.9500	1.3000	0.8300
R7 - w2 mm	0.5600	0.2600	0.4200	0.4300	0.2800	0.5700	0.2500

DESIGN - EASE ANALYSIS

Run Order	57	58	59	60	61	62	63	64
Block	1	1	1	1	1	1	1	1
Standard Order	46	15	9	40	33	32	49	20
A - MODE	TEM01	TEM00	TEM00	TEM01	TEM00	TEM01	TEM00	TEM01
B - SIDE ANG. DEGREES	0	10	0	10	0	10	0	10
C - FOCUS mm	+1.0	+1.0	-1.0	+1.0	-1.0	+1.0	-1.0	-1.0
D - SPEED mm/s	140	140	140	40	40	140	40	40
E - POWER kW	1.5	1.5	1.5	1.5	1.5	3.5	3.5	3.5
F - LENS mm	150	100	100	150	150	100	150	100
G - POLARITY	LINEAR	LINEAR	LINEAR	LINEAR	CIRCULAR	CIRCULAR	CIRCULAR	CIRCULAR
H - NORM ANG. DEGREES	5.5	0	5.5	0	0	0	5.5	0
R1 - DEPTH mm	0.5200	0.8000	0.9200	0.8800	1.0000	1.0000	0.9100	1.1600
R2 - HARDNESS HRB	425.0000	390.0000	308.0000	332.0000	332.0000	351.0000	278.0000	275.0000
R3 - SPEC ENER J/mm2	39.0000	56.0000	80.0000	247.0000	154.0000	123.0000	468.0000	469.0000
R4 - JOIN EFF. mm2/J	43.0000	75.0000	36.0000	19.0000	25.0000	40.0000	10.0000	13.0000
R5 - MELT EFF. %	12.0000	26.0000	29.0000	13.0000	19.0000	17.0000	6.0000	11.0000
R6 - w1 mm	0.4000	0.6000	0.7200	1.5100	1.1500	0.8500	1.1400	1.4000
R7 - w2 mm	0.0600	0.1400	0.3400	0.5600	0.4900	0.4200	0.4900	0.8000

## **APPENDIX B**

**A summary of the statistical data analysis**

## STATISTICAL DEFINITIONS

An example of the output is given at the end of the appendix, in this instance the response is joining efficiency

**TREATMENT:** Terms estimating treatment effects.

**Sum of Squares:** Sum of variance of the treatment means from the overall mean

**Degrees of Freedom (DF):** The deviation of the treatment means from the overall average must be zero. Given three mean deviations, the remaining deviation can be determined. The DF for the deviation is, therefore, one less than the number of means. In this case 8.

**RESIDUAL:** Terms estimating the experimental error.

**Sum of Squares:** The sum of variance of response data points from their treatment means.

**Degrees of Freedom (DF):** The deviation from the treatment average must be zero. Summing the deviations for the treatment gives DF = number of data points - the number of treatments. Here, it is 60

**NULL HYPOTHESIS ( $H_0$ ):** That treatments do not differ for a given response and therefore, the model variance is equal to the error variance.

**F-VALUE:** Test for comparing treatment variance with error variance, given by treatment mean square/error mean square.

**PROB > F:** Probability of observed F value if  $H_0$  is true. Small values reject the null hypothesis. The observed F-value can be compared with the F-value with 8 and 60 DF in this case. The probability is the area of the tail of the F-distribution beyond the F-value.

**COR TOTAL:** Total sum of squares corrected for the mean.

**Sum of Squares:** Sum of variance of data points from the grand

average.

**Degrees of Freedom:** The deviations of the points from the grand mean must equal zero. DF is therefore the number of data points-1 = 68.

**ROOT MSE:** Square root of the mean square error. Standard deviation associated with experimental error.

**DEP MEAN:** Dependent mean, that is, overall mean of the response. Sum of the data points divided by the number of points.

**C.V.:** Coefficient of variation, the standard deviation as a percentage of the mean.

**R-SQUARED:** The multiple correlation coefficient. A measure of the amount of variation about the mean explained by the model.

**ADJ R-SQUARED:** Measure of the amount of variation about the mean explained by the model adjusted for the number of parameters in the model. Adjusted R-squared decreases as the number of parameters in the model increases relative to the number of design points.

**ESTIMATED MEAN:** The average response at each treatment.

**STANDARD ERROR OF TREATMENT:** Standard deviation of the data (ROOT MSE) divided by the square of the number of repetitions in a sample.

**ACTUAL VALUE:** The value of the data determined in the test.

**PREDICTED VALUE:** The value predicted by the model.

**RESIDUAL:** Difference between ACTUAL and PREDICTED values for each point in the design.

**STUDENTISED RESIDUAL:** Residual divided by the estimated deviation of that residual.

**COOK'S DISTANCE:** Measure of how much the regression changes if the case is



deleted. Large values should be investigated - they could be caused by recording errors, an incorrect model or a design point far from the remaining cases.

***OUTLIER T VALUE:*** The outlier t value statistic is the number of standard deviation between an actual data point and a predicted value at that point using the model based on all the data except this point. Checks if that data point is consistent with the other points in the model. Only extreme values ( $t=3-4$ ) should be considered as outliers.

ANOVA for Selected Model

SOURCE	SUM OF SQUARES	DF	MEAN SQUARE	F VALUE	PROB > F
MODEL	14126.250000	8	1765.7812500	13.068	0.0001
CURVATURE	316.848958	1	316.8489584	2.345	0.1310
ERROR	7972.234375	59	135.1226165		
RESIDUAL	7972.234375	55	144.9497159		
PURE ERR	0.000000	4	0.0000000		
COR TOTAL	22415.333333	68			
ROOT MSE	11.624225		R-SQUARED	0.6443	
DEP MEAN	30.734375		ADJ R-SQUARED	0.5901	
C. V.	37.82 %				

VARIABLE	PARAMETER ESTIMATE	DF	SUM OF SQUARES	t FOR H0 PARAMETER=0	PROB >  t
Intercept	30.734375	1		21.152	0.0001
A	-0.421675	1	11.390625	-0.290	0.7726
B	0.828125	1	43.890625	0.570	0.5709
C	0.828125	1	43.890625	0.570	0.5709
D	11.640625	1	8672.265625	8.011	0.0001
E	-7.828125	1	3921.890625	-5.387	0.0001
F	-3.078125	1	606.390625	-2.118	0.0384
G	-0.578125	1	21.390625	-0.398	0.6922
H	3.546875	1	805.140625	2.441	0.0177
Std ERROR	1.4530282				

Predicted Values and Residuals

Std Ord	ACTUAL VALUE	PREDICTED VALUE	RESIDUAL	STANDARDIZED RESIDUAL	COOK'S D	t VALUE	Ru Or
1	27.000000	31.734375	-4.734375	-0.4393	0.004	-0.436	32
2	24.000000	24.953125	-0.953125	-0.0884	0.000	-0.088	2
3	21.000000	27.453125	-6.453125	-0.5988	0.007	-0.596	67
4	31.000000	32.546875	-1.546875	-0.1435	0.000	-0.142	43
5	22.000000	34.546875	-12.546875	-1.1643	0.025	-1.168	38
6	23.000000	25.453125	-2.453125	-0.2276	0.001	-0.226	5
7	25.000000	27.953125	-2.953125	-0.2740	0.001	-0.272	23
8	25.000000	35.359375	-10.359375	-0.9613	0.017	-0.961	54
9	86.000000	56.171875	29.828125	2.7680	0.139	2.939	59
10	35.000000	47.078125	-12.078125	-1.1208	0.023	-1.123	33
11	47.000000	49.578125	-2.578125	-0.2392	0.001	-0.237	28
12	85.000000	56.984375	28.015625	2.5998	0.123	2.737	37
13	76.000000	56.671875	19.328125	1.7936	0.058	1.828	7
14	40.000000	49.890625	-9.890625	-0.9178	0.015	-0.917	36
15	75.000000	52.390625	22.609375	2.0981	0.080	2.161	58
16	93.000000	57.484375	35.515625	3.2958	0.197	3.611	47
17	13.000000	8.984375	4.015625	0.3726	0.003	0.370	17
18	11.000000	16.390625	-5.390625	-0.5002	0.005	-0.497	25
19	14.000000	18.890625	-4.890625	-0.4538	0.004	-0.451	66
20	13.000000	9.796875	3.203125	0.2972	0.002	0.295	64
21	13.000000	11.796875	1.203125	0.1116	0.000	0.111	34
22	15.000000	16.890625	-1.890625	-0.1754	0.001	-0.174	46
23	13.000000	19.390625	-6.390625	-0.5930	0.006	-0.590	1
24	11.000000	12.609375	-1.609375	-0.1493	0.000	-0.148	12
25	40.000000	33.421875	6.578125	0.6104	0.007	0.607	11
26	40.000000	36.515625	3.484375	0.1377	0.000	0.137	4
27	20.000000	41.015625	-21.015625	-1.9502	0.069	-1.998	19

Predicted Values and Residuals

Std Ord	ACTUAL VALUE	PREDICTED VALUE	RESIDUAL	STANDARDIZED RESIDUAL	COOK's D	t VALUE	Ru Or
28	32.000000	34.234375	-2.234375	-0.2073	0.001	-0.206	20
29	13.000000	33.921875	-20.921875	-1.9415	0.069	-1.989	55
30	26.000000	41.328125	-15.328125	-1.4224	0.037	-1.435	65
21	33.000000	43.828125	-10.828125	-1.0048	0.018	-1.005	24
32	40.000000	34.734375	5.265625	0.4886	0.004	0.486	62
33	25.000000	18.484375	6.515625	0.6046	0.007	0.601	61
34	24.000000	25.890625	-1.890625	-0.1754	0.001	-0.174	26
35	26.000000	28.390625	-2.390625	-0.2218	0.001	-0.220	48
36	27.000000	19.296875	7.703125	0.7148	0.009	0.712	42
37	27.000000	21.296875	5.703125	0.5292	0.005	0.526	41
38	31.000000	26.390625	4.609375	0.4277	0.003	0.425	68
39	27.000000	28.890625	-1.890625	-0.1754	0.001	-0.174	56
40	18.000000	22.109375	-4.109375	-0.3813	0.003	-0.379	60
41	30.000000	42.921875	-12.921875	-1.1991	0.026	-1.204	31
42	40.000000	48.015625	-8.015625	-0.7438	0.010	-0.741	16
43	47.000000	50.515625	-3.515625	-0.3262	0.002	-0.324	13
44	30.000000	43.734375	-13.734375	-1.2745	0.030	-1.281	9
45	35.000000	43.421875	-8.421875	-0.7815	0.011	-0.779	44
46	49.000000	50.828125	-1.828125	-0.1696	0.001	-0.168	57
47	38.000000	53.328125	-15.328125	-1.4224	0.037	-1.435	6
48	25.000000	44.234375	-19.234375	-1.7849	0.058	-1.819	30
49	10.000000	9.921875	0.078125	0.0072	0.000	0.007	63
50	11.000000	3.140625	7.859375	0.7293	0.010	0.726	45
51	11.000000	5.640625	5.359375	0.4973	0.004	0.494	39
52	11.000000	10.734375	0.265625	0.0246	0.000	0.024	18
53	15.000000	12.734375	2.265625	0.2102	0.001	0.209	69
54	14.000000	3.640625	10.359375	0.9613	0.017	0.961	10
55	22.000000	6.140625	15.859375	1.4717	0.039	1.487	22
56	11.000000	13.546875	-2.546875	-0.2363	0.001	-0.234	35
57	37.000000	34.359375	2.640625	0.2450	0.001	0.243	50
58	20.000000	25.265625	-5.265625	-0.4886	0.004	-0.486	29
59	31.000000	27.765625	3.234375	0.3001	0.002	0.298	53
60	38.000000	35.171875	2.828125	0.2624	0.001	0.260	21
61	42.000000	34.859375	7.140625	0.6626	0.008	0.660	49
62	43.000000	28.078125	14.921875	1.3847	0.035	1.396	52
63	36.000000	30.578125	5.421875	0.5031	0.005	0.500	14
64	34.000000	35.671875	-1.671875	-0.1551	0.000	-0.154	51

**APPENDIX C**  
Mechanical testing data

Profile	Sample No.	X section area (mm <sup>2</sup> )	Elongation (%)	Yield Strength MPa	Ultimate Tensile Strength MPa
	Blank	11.36	41.37	219.92	325.48
1	46 Bt	12.27	15.63	206	330
	38 Bt	12.40	40.44	150	305
1	69 Bt	11.13	25.00	188	305
2	1 Bt	11.38	34.40	175.67	307.42
2	23 Bt	12.25	7.04	193.47	292.24
2	28 Bt	12.25	38.17	159.18	310.20
2	35 Bt	12.12	39.12	160.82	305.15
3	2 Bt	12.25	26.25	146.94	292.24

**Table 1C** Results of tensile testing for the different weld profile categories (see section 3.2.2). Continued over page.

Profile	Sample No.	Thickness (mm)	Erichsen (mm)	Force (kN)	Energy (J)
3	9 Bt	0.99	10.47	1.965	0.887
3	49 Bt	0.98	10.83	1.947	0.981
3	41 Bt	1.01	10.54	1.787	0.872
3	52 Bt	1.01	11.36	1.947	1.053
3	64 Bt	0.99	10.02	1.788	0.832
4	12 Bt	0.99	9.81	1.697	0.738
4	24 Bt	0.99	11.06	1.929	1.034
4	4 Bt	0.99	10.47	1.822	0.893
4	11 Bop	0.99	10.56	2.000	0.963
4	66 Bt	0.98	7.57	1.106	0.427
4	22 Bt	0.97	9.95	1.751	0.822
5	5 Bt	0.97	6.69	0.929	0.269
5	59 Bt	0.97	10.21	1.822	0.870
5	19 Bt	1.00	5.44	0.393	0.126
5	27 Bt	1.00	3.89	0.286	0.075
5	65 Bt	1.00	4.75	0.536	0.126

Profile	Sample No.	X section area (mm <sup>2</sup> )	Elongation (%)	Yield Strength MPa	Ultimate Tensile Strength MPa
	Blank	11.36	41.37	219.92	325.48
1	46 Bt	12.27	15.63	206	330
	38 Bt	12.40	40.44	150	305
1	69 Bt	11.13	25.00	188	305
2	1 Bt	11.38	34.40	175.67	307.42
2	23 Bt	12.25	7.04	193.47	292.24
2	28 Bt	12.25	38.17	159.18	310.20
2	35 Bt	12.12	39.12	160.82	305.15
3	2 Bt	12.25	26.25	146.94	292.24

Table 2C The Erichsen testing results, divided into the five identified weld profiles (see section 3.2.2)

Profile	Sample No.	X section area (mm <sup>2</sup> )	Elongation (%)	Yield Strength MPa	Ultimate Tensile Strength MPa
4	12 Bop	12.05	40.04	136.88	302.80
4	12 Bt	12.20	33.80	233.69	336.04
4	22 Bt	11.17	36.55	187.97	313.28
4	38 Bt	12.02	40.44	149.65	299.30
4	50 Bt	12.4	34.7	153.23	305.57
5	59 Bt	12.15	36.80	160.47	308.59

Table 2CContinued



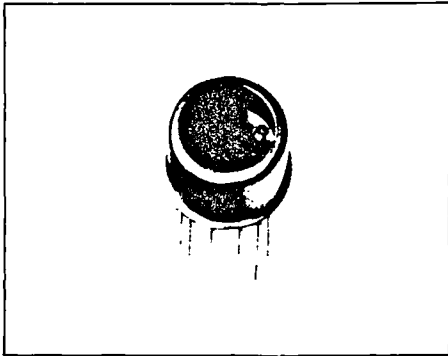
## **APPENDIX D**

**Quadrant sensor specification and circuit design.**

## Quadrant silicon photodiode

Stock number 652-027

A silicon photodiode containing four separate sensing elements (with commoned cathodes) arranged one per quadrant. The output voltage of each quadrant is available separately enabling null conditions to be detected with equal degrees of shading. The device is hermetically sealed in a TO5 package which incorporates the pcb pin connections.



### Absolute maximum ratings

dc reverse voltage	_____	15V
Peak pulse current (1 $\mu$ s, 1% duty cycle)	_____	200mA
Peak dc current	_____	10mA
Storage temperature range	_____	-45°C to +100°C
Operating temperature range	_____	-25°C to +75°C
Lead temperature soldering (5s)	_____	+200°C

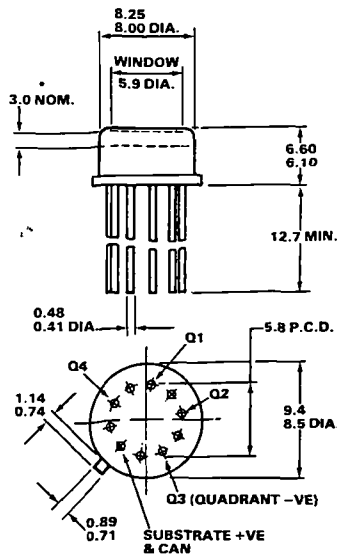
### Features

- High blue sensitivity and shunt resistance
- Suitable for low light level applications
- TO5 package incorporating pcb pin connections.

### Applications

- ▲ High accuracy position sensing
- ▲ Alignment
- ▲ Optical surveying.

### Pin connections and dimensions

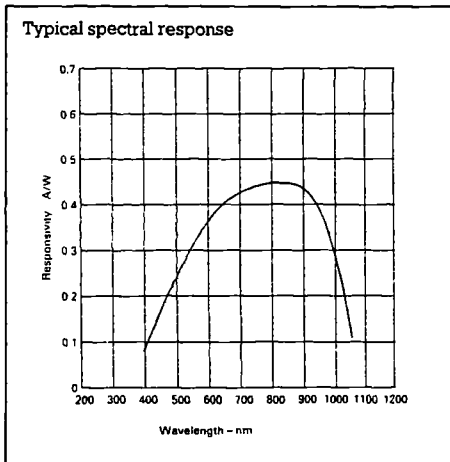


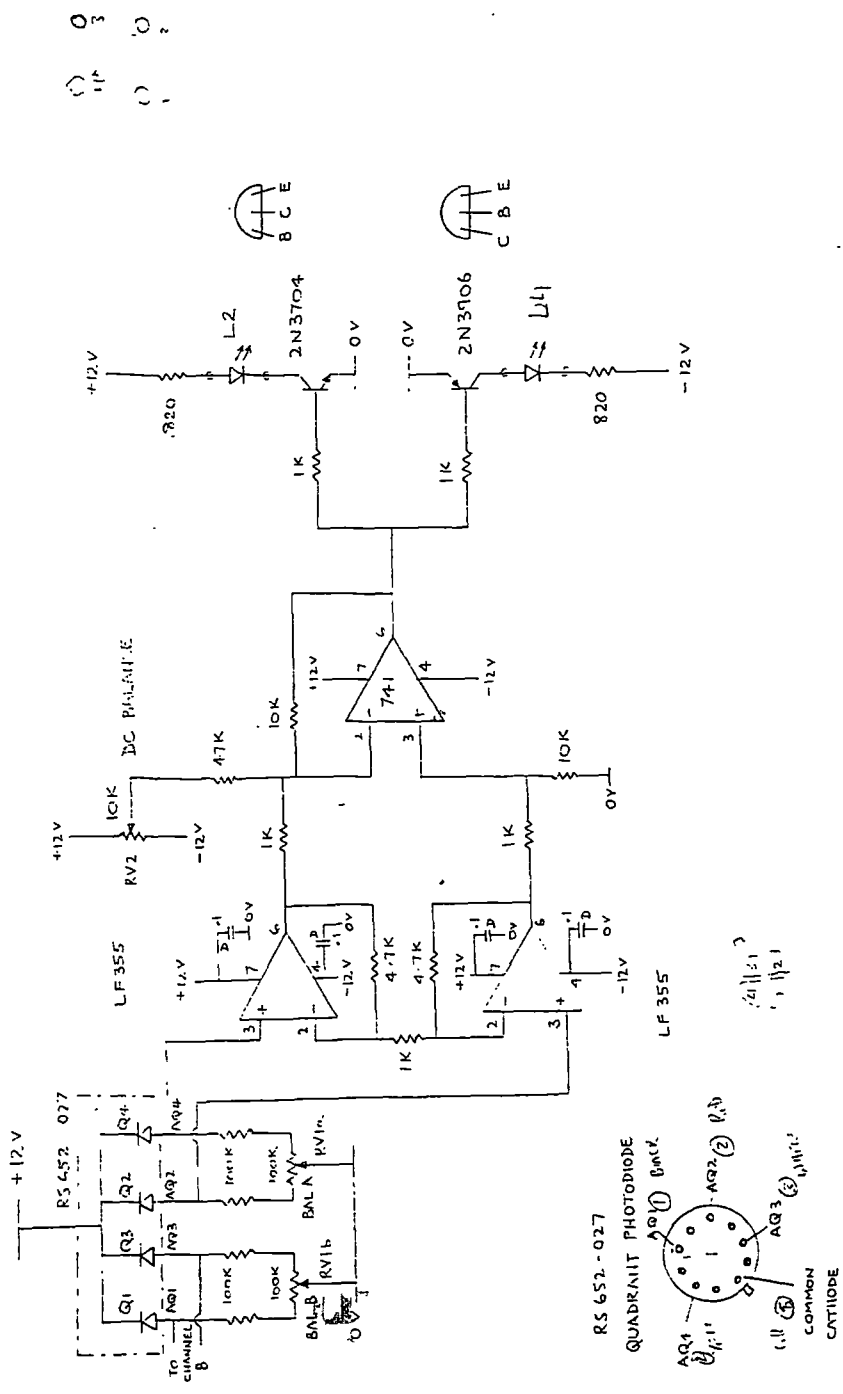
NOTE:  
DIMENSION\* REFERS TO DISTANCE  
BETWEEN WINDOW AND ACTIVE  
AREA. NO CONNECTION SHOULD BE MADE  
TO UNSPECIFIED PINS.

## RS Data Library

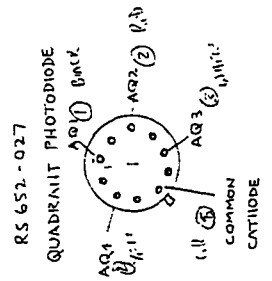
### Specification

Parameter	Conditions	Min.	Typ.	Max.	Units
Operating voltage				12	V
Dark current	$V_R=1V$		0.03	3	nA
Capacitance	$V_R=0V$		80	100	pF
Responsivity	900nm, $V_R=1V$	0.42	0.45		A/W
Rise time	0-70%, 864nm, $V_R=10V$ 100Ω load			<15	ns
Peak wavelength			820		nm
Spectral response range		430		900	nm
Noise equivalent power	900nm		$1 \times 10^{-13}$		WHz <sup>-1/2</sup>
Active diameter			3		mm
Total active area			7		mm <sup>2</sup>
Metallurgical separation			200		μm





( ) 0  
 ( ) 1  
 ( ) 2



PHOTODIODE AMPLIFIER

MEE 10416

ISS 1. 22. 10. 91

CHANNEL B IS IDENTICAL WITH CHANNEL A

① - 5.000000 160<sup>0</sup> 1111